

TEL AVIV UNIVERSITY



אוניברסיטת תל אביב

RAYMOND AND BEVERLY SACKLER
FACULTY OF EXACT SCIENCES
SCHOOL OF PHYSICS & ASTRONOMY

הפקולטה למדעים מדויקים
ע"ש ריימונד וברלי סאקלר
בית הספר לפיזיקה ולאסטרונומיה

**BEER analysis of *Kepler* and *CoRoT* light curves:
discovering binaries and exoplanets**

Thesis submitted for the degree “doctor of philosophy”

by

Simchon Faigler

Submitted to the senate of Tel Aviv University

February 2016

This work was carried out under the supervision of

Professor Tsevi Mazeh

To my family

Contents

Abstract	III
1 Introduction	1
2 The Papers	9
Paper I	10
Paper II	14
Paper III	22
Paper IV	32
Paper V	42
Paper VI	52
Paper VII	80
3 Discussion	95
3.1 The Papers	95
3.2 Astrophysical contributions	99
3.3 Into the future	100
Bibliography	103
Acknowledgments	107

Abstract

This thesis consists of seven scientific papers that cover the proof-of-concept, the development, and discoveries made through the use of the BEER (BEaming, Ellipsoidal, and Reflection) algorithm for searching for companions in the light curves from the *Kepler* and *CoRoT* space telescopes.

Paper I presents the detection of the ellipsoidal and the beaming effects in the *CoRoT* light curve of CoRoT-3, a system of a $22M_{\text{Jup}}$ brown dwarf orbiting an F star with an orbital period of 4.3 days. This work served as a proof-of-concept that these effects are detectable in the space light curves of systems with brown-dwarf or planetary secondaries, thus indicating that similar modulations may be detected in the light curves of non-transiting systems. As a follow-up to the first paper, Paper II presents the BEER algorithm for detecting *non-transiting* short-period low-mass companions, through the BEaming, Ellipsoidal and Reflection effects, in *Kepler* and *CoRoT* light curves. The paper also analyzes the expected performance of the algorithm and predicts that it should enable detection of secondaries with masses down to $5\text{--}10M_{\text{Jup}}$.

To establish the effectiveness of the BEER method, Paper III, and later Paper VI, present the discovery and radial velocity (RV) confirmation of seven, and seventy, non-eclipsing short-period binaries, in *Kepler* and *CoRoT* data, respectively. The papers illustrate that unlike eclipses searches, the BEER algorithm searches for *non-eclipsing* companions, and therefore can detect additional systems with lower inclination angles.

As envisioned by the previous papers, Paper IV presents the discovery of Kepler-76b, a $2M_{\text{Jup}}$ transiting hot Jupiter orbiting an F star with orbital period of 1.54 days. This planet was first identified by the BEER algorithm,

and then confirmed by RV follow-up observations. The Kepler-76 light curve also showed the first evidence in the *Kepler* band for superrotation. This phenomenon involves a phase shift of the planetary thermal-emission modulation, due to equatorial superrotating winds in the planet atmosphere, and was previously observed only in the infrared. Paper V extends the discovery of superrotation in Kepler-76b to two additional known hot Jupiters, HAT-P-7b and KOI-13b. These discoveries illustrate that detailed phase-curve studies, of precise space-surveys light curves, allow the investigation of atmospheric phenomena, such as thermal winds or reflective clouds, in multiple close-in exoplanets.

The last study, Paper VII, demonstrates the different strengths and utility of the BEER search algorithm. It presents the discovery of four short-period eclipsing binaries in the *Kepler* light curves, consisting of an A-star primary and a low-mass WD secondary (dA+WD). The systems show BEER phase modulations together with primary and secondary eclipses. These add to the 6 *Kepler*, and 18 WASP, previously known short-period eclipsing dA+WD binaries. The paper shows that three of the new systems harbor the smallest WDs detected so far in such binaries. These three binaries extend the previously known population to older systems with cooler and smaller WD secondaries, allowing to test binary evolution theories in a parameter region not observed before.

The seven papers illustrate the effectiveness of the BEER algorithm in finding both common stellar binaries and rare astrophysical objects. As such, the BEER tool can serve as an important component in the virtual astronomy toolbox for mining the vast astronomical data produced by current and future photometric surveys.

Chapter 1

Introduction

The *Kepler* and *CoRoT* space telescopes were launched with the primary mission of detecting extrasolar transiting planets, through the minute periodic transit dips they induce in the photometric light curves of their host stars (Borucki et al., 2010; Koch et al., 2010; Rouan et al., 1998; Baglin et al., 2006; Auvergne et al., 2009). As such, these missions produced hundreds of thousands of nearly uninterrupted, high precision light curves, with time spans of tens to more than a thousand days, and relative photometric precision of up to 10^{-3} – 10^{-4} per data point, depending on the stellar brightness. This exquisite photometry revolutionized exoplanet research, by enabling the detection of Earth size planets (and white dwarfs) with transit depths of $\sim 0.01\%$ (e.g., Léger et al., 2009; Batalha et al., 2011), a two orders of magnitudes improvement relative to the $\sim 1\%$ typical sensitivity of ground-based transit surveys (e.g., Butters et al., 2010; Udalski et al., 2015).

As of January 2016, analysis of the *CoRoT* light curves yielded the discovery of 30 exoplanets by the transit method, that were later confirmed by spectroscopic radial-velocity (RV) observations (Exoplanet Encyclopedia, 2016). More importantly, the analysis of the *Kepler* data has produced more

than 4600 planetary candidates, of which more than 1000 have been verified as planets by various methods (Batalha et al., 2013; Mullally et al., 2015; *Kepler* Exoplanet Archive, 2016). As a byproduct of this effort, the *Kepler* mission has also identified more than 2800 eclipsing binary (EB) systems¹ (Slawson et al., 2011).

For EB or transiting planets systems, the orbital period, inclination and the radii of the primary star and the companion, relative to the semi-major axis, are directly measurable through analysis of the eclipses/transit shape (e.g., Seager & Mallén-Ornelas, 2003). Yet, there are additional astrophysical effects that produce flux variations along the orbital phase of a binary system, which depend on, and thus probe, the mass of the companion, be it a stellar, brown dwarf, planet, or a compact object. Such out-of-eclipses phase modulations that are seen also in non-eclipsing systems, are the result of three main effects: reflection/emission, ellipsoidal, and beaming.

The reflection/emission effect (referred to here as the reflection modulation) is a result of each component’s light scattered off the facing hemisphere of its companion (“day side”), combined with light absorbed and later thermally re-emitted by the companion atmosphere, at different wavelengths (Vaz, 1985; Wilson, 1990; Maxted et al., 2002; Harrison et al., 2003; For et al., 2010; Reed et al., 2010). As such, this effect causes a modulation at the orbital period, and probes the companion radius relative to the semi-major axis, together with properties associated with the companion atmospheric response to its host-star radiation, such as the Bond albedo, scattered-light geometric albedo, and heat-redistribution parameters, among others.

The ellipsoidal modulation (Kopal, 1959; Morris, 1985) is a well-known and well-studied effect in close binaries, that is due to the tidal distortion

¹<http://keplerebs.villanova.edu/>

of the primary star by the gravity of the secondary (e.g., Loeb & Gaudi, 2003; Zucker, Mazeh & Alexander, 2007; Mazeh, 2008), resulting in a phase modulation at half the orbital period.

The beaming effect, sometimes called Doppler beaming or Doppler boosting, causes an increase (decrease) of the brightness of any light source approaching (receding from) the observer (Rybicki & Lightman, 1979; Loeb & Gaudi, 2003), with an amplitude proportional to the RV of the source. Therefore, the stellar RV modulation due to an orbiting companion will produce an RV like beaming phase modulation at the orbital period. The beaming amplitude is the result of a bolometric effect of $4V_r/c$, where V_r is the star RV and c is the speed of light, corrected by an α_{beam} factor that compensates for the stellar-spectrum shift into, or out of, the observed band-pass. The amplitudes of the beaming and the ellipsoidal modulations both depend, but in different ways, on the masses of the two components, that cannot be probed by the transit method. As such they can provide important complementary information about the basic astrophysical properties of the system.

While the reflection and the ellipsoidal effects are well known and studied in the field of short period binaries, the beaming modulation became observationally relevant only recently. Before the era of space photometry this effect has been noticed only once, by Maxted et al. (2000), who observed KPD 1930+2752, a binary with an orbital period a little longer than 2 hours, and an RV semi-amplitude of 350 km/s. The beaming effect of that system, on the order of 10^{-3} , was hardly seen in the photometric data. It was though anticipated that the high precision light curves of *CoRoT* and *Kepler* will detect each of the three modulations (e.g., Drake, 2003; Loeb & Gaudi, 2003; Zucker, Mazeh & Alexander, 2007), for binaries and planets

alike. As predicted, once the *Kepler* and *CoRoT* photometric light curves became available, several studies detected various combinations of the three effects in eclipsing binaries, for which the orbital period was well established from the space-obtained light curves. These detection were in eclipsing binaries with a white-dwarf secondary (van Kerkwijk et al., 2010; Carter et al., 2011; Bloemen et al., 2011, 2012; Breton et al., 2012; Rappaport et al., 2015; Faigler et al., 2015), and even in a few transiting brown-dwarfs and planetary secondaries (Snellen et al., 2009; Welsh et al., 2010; Mazeh & Faigler, 2010; Shporer et al., 2011; Mazeh et al., 2012; Barclay et al., 2012; Herrero et al., 2014).

However, space mission data can yield much more. In addition to eclipse events, The *CoRoT* and *Kepler* data can indicate the binarity of a system based on the beaming, ellipsoidal and reflection effects themselves. Loeb & Gaudi (2003) suggested that the beaming effect can be used to detect non-transiting exoplanets, and Zucker, Mazeh & Alexander (2007) extended this idea to binaries. Loeb & Gaudi (2003) (see also the discussion of Zucker, Mazeh & Alexander, 2007) showed that for relatively long-period orbits, of the order of 10–100 days, the beaming modulation is stronger than the ellipsoidal and the reflection effects, and therefore could be observed without interference from the other two modulations. However, the beaming modulation by itself might not be enough to render a star a good exoplanet candidate, as a pure sinusoidal modulation could be produced by other effects, stellar modulations in particular (e.g., Aigrain, Favata & Gilmore, 2004). The BEER search algorithm, therefore, searches for stars that show in their space-obtained light curves some *combination* of the BEaming, Ellipsoidal, and Reflection (BEER) modulations, with amplitudes and phases that are consistent with a low-mass companion.

This thesis consists of seven scientific papers that cover the proof-of-concept, the development, and discoveries made through the use of the BEER algorithm for searching for companions in the light curves of the *Kepler* and *CoRoT* space telescopes.

Spectroscopic RV confirmations in Papers III, IV and VII were performed mainly by the Tillinghast Reflector Echelle Spectrograph (TRES; Fűrész, 2008) mounted on the 1.5-m Tillinghast Reflector at the Fred Lawrence Whipple Observatory operated by the Smithsonian Astrophysical Observatory (SAO) on Mount Hopkins in Southern Arizona. This thesis relies on hundreds of TRES observations of ~ 180 target stars, led by Dave Latham from the Harvard-Smithsonian Center for Astrophysics, that contributed in a crucial way to the discoveries reported in the thesis papers.

Paper I (Mazeh & Faigler, 2010) describes the detection of the ellipsoidal and the beaming effects, through the use of a novel cosine-transform based detrending method, in the *CoRoT* light curve of CoRoT-3, a system of a $22M_{\text{Jup}}$ brown dwarf orbiting an F3 star in an orbital period of 4.3 days (Deleuil et al., 2008). This work, together with Snellen et al. (2009) and Welsh et al. (2010), served as a proof-of-concept that such modulations are indeed detectable in the space light curves of systems harboring brown-dwarf or planetary secondaries. These studies thus indicate that similar modulations may be detectable in the light curves of non-transiting systems.

Paper II (Faigler & Mazeh, 2011) describes the BEER algorithm for detection of non-transiting short-period low-mass companions, through the beaming, ellipsoidal and reflection effects, in *Kepler* and *CoRoT* light curves. The paper presents the algorithm, including an assignment of a likelihood factor to any possible detection, based on the expected ratio of the beaming and ellipsoidal effects. It then provides two examples of candidates found in the

light curves of the first *Kepler* quarter, with detected periodic amplitudes as small as 100 parts per million (ppm).

Paper III (Faigler et al., 2012) presents the first discoveries of seven non-eclipsing binaries in the *Kepler* light curves through the BEER method, that were confirmed by RV observations. Two of the detected binaries were the two candidates presented in Paper II. This work marks the first detections made through the use of the BEER algorithm.

Paper IV (Faigler et al., 2013) describes the discovery of Kepler-76b, a $2M_{\text{Jup}}$ hot Jupiter orbiting a 13.3 mag F star with orbital period of 1.54 days. This system that initially appeared in the *Kepler* EB catalog, was identified by the BEER algorithm, based on its amplitudes and phases of the three effects, as a system harboring a hot Jupiter. The paper covers the BEER algorithm detection of the hot Jupiter, RV observations confirmation of the companion mass, and first evidence in the *Kepler* band for superrotation in the atmosphere of Kepler-76b. Superrotation involves a phase shift of the planetary thermal-emission modulation, due to equatorial superrotating jets in the planet atmosphere. This phenomenon was predicted by Showman & Guillot (2002) and later observed by Knutson et al. (2007, 2009) in the infrared for HD 189733. In addition to TRES observations, part of the RV measurements presented in this paper were performed by the SOPHIE spectrograph (Perruchot et al., 2008; Bouchy et al., 2009, 2013) mounted on the 1.93-m telescope at Observatoire de Haute-Provence, France.

Paper V (Faigler & Mazeh, 2015) extends the discovery of superrotation in Kepler-76b to two additional known hot Jupiters, HAT-P-7b and KOI-13b, and presents the Lambertian superrotation BEER model, that enables estimating the masses of hot Jupiters from photometry alone. The paper concludes that hot Jupiter superrotation may be a common phenomenon

that is detectable in the visual-band *Kepler* light curves.

Paper VI (Tal-Or, Faigler & Mazeh, 2015) describes the discovery of seventy non-eclipsing binaries, detected by the BEER algorithm in *CoRoT* light curves, and confirmed by RV follow-up observations. The discoveries included two brown-dwarf candidates on a ~ 1 day period orbit. This was the first time non-eclipsing beaming binaries were detected in *CoRoT* data, and the paper estimates that ~ 300 such binaries can be detected in *CoRoT* long-run light curves. RV measurements presented in this paper were performed by the AAOmega multi-object spectrograph (Smith et al., 2004; Saunders et al., 2004) at the Anglo-Australian Telescope (AAT).

Paper VII (Faigler et al., 2015) presents the discovery of four short-period eclipsing systems in the *Kepler* light curves, consisting of an A-star primary and a low-mass WD secondary (dA+WD), through the BEER algorithm. These add to the 6 *Kepler*, and 18 WASP, previously known short-period eclipsing dA+WD binaries. Three of the new systems harbor the smallest WDs discovered so far in such binaries. These three binaries extend the previously known population to older systems with cooler and smaller WD secondaries.

Chapter 2

The Papers

L E

Detection of the ellipsoidal and the relativistic beaming effects in the CoRoT-3 lightcurve

T. Mazeh and S. Faigler

School of Physics and Astronomy, Raymond and Beverly Sackler Faculty of Exact Sciences, Tel Aviv University,
Tel Aviv 69978, Israel
e-mail: mazeh@post.tau.ac.il

Received 9 August 2010 / Accepted 21 September 2010

ABSTRACT

CoRoT-3b is a 22 Jupiter-mass massive-planet/brown-dwarf object, orbiting an F3-star with a period of 4.3 days. We analyzed the out-of-transit CoRoT-3 red-channel lightcurve obtained by the CoRoT mission and detected the ellipsoidal modulation, with half the orbital period and an amplitude of 59 ± 9 ppm (parts per million), and the relativistic beaming effect, with the orbital period and an amplitude of 27 ± 9 ppm. Phases and amplitudes of both modulations are consistent with our theoretical approximation.

Key words. methods: data analysis – planetary systems – stars: individual: CoRoT-3

1. Introduction

Close binary stellar systems display two well-known periodic photometric modulations – the ellipsoidal effect, due to the distortion of each component by the gravity of its companion (see a review by Mazeh 2008), and the reflection/heating effect (referred to here as the reflection effect), induced by the luminosity of each star, which affects only the close side of its companion (e.g., For et al. 2010). These two effects can be observed even for non-eclipsing binaries, but are much easier to study in eclipsing binaries, where the binarity of the system and the phases of the orbital motion are well known from the observations of the eclipses. Most algorithms that analyze lightcurves of eclipsing binaries, such as EBOP (Etzel 1980; Popper & Etzel 1981) and its derivative EBAS (Tamuz et al. 2008), WD (Wilson & Devinney 1971), and ELC (Orosz & Hauschildt 2000), include by default these two effects in their model of the out-of-eclipse lightcurve.

A much smaller and less studied photometric modulation is the relativistic beaming effect, sometimes also called Doppler boosting, induced by the stellar motion relative to the observer – V_{rel} , whose amplitude is on the order of V_{rel}/c , where c is the velocity of light. Before the era of space photometry this effect has been noticed only once, by Maxted et al. (2000), who observed KPD 1930+2752, a binary with a very short period, of little longer than 2 h, and a radial-velocity amplitude of 350 km s^{-1} . The beaming effect of that system, which should be on the order of 10^{-3} , was hardly seen in the photometric data.

Space photometry, which was developed to detect the minute transits of exoplanets, has substantially improved the precision of the produced lightcurves. The CoRoT (Rouan et al. 1998; Baglin et al. 2006; Auvergne et al. 2009) and Kepler (Borucki et al. 2010; Koch et al. 2010) missions are producing hundreds of thousands of continuous photometric lightcurves with timespan of tens and hundreds of days, with precision that can reach as high as 10^{-3} – 10^{-4} per measurement. It was therefore anticipated that CoRoT and Kepler should detect all three effects (e.g., Drake 2003), in particular the beaming effect for both planets (Loeb & Gaudi 2003) and eclipsing binaries (Zucker et al. 2007).

As predicted, van Kerkwijk et al. (2010) detected in the Kepler lightcurve the ellipsoidal and the beaming effect of two eclipsing binaries, KOI 74 and KOI 81 (Rowe 2010). They used the radial-velocity photometric beaming effect to derive the mass of the secondary in the two systems and showed that in both cases it was probably a white dwarf. Welsh et al. (2010) identified the ellipsoidal effect in the Kepler data of HAT-P-7, a system with a known planet of 1.8 Jupiter masses ($=M_{\text{Jup}}$) and a period of 2.2 days (Pál et al. 2008). Snellen et al. (2009) detected in the CoRoT data the reflection effect of CoRoT-1.

In this paper, we report the detection of the ellipsoidal and the beaming effects of CoRoT-3, induced by its massive-planet/brown-dwarf companion. CoRoT-3b (Deleuil et al. 2008) is a 22 Jupiter-mass object, orbiting an F3-star with a period of 4.26 days. The stellar rotation is probably synchronized with the orbital period. We analyzed the CoRoT-3 out-of-transit red-channel lightcurve and detected two modulations, one with the orbital period and the other with its first harmonic. We attributed the two modulations to the beaming and the ellipsoidal effects, respectively, as their phases and amplitudes were consistent with our order-of-magnitude approximation. Section 2 presents our data analysis, Sect. 3 compares our findings with theoretical approximations, and Sect. 4 summarizes our results.

2. Data analysis

CoRoT-3 was discovered (Deleuil et al. 2008) in the data obtained during the first long run of the CoRoT mission – LRc01, which lasted for 152.012 d, from May 26 until October 25, 2007 (for details about this run see Cabrera et al. 2009). The optics of the mission include a bi-prism that disperses the stellar light into three channels, *red*, *green*, and *blue*, the sum of which is called the *white* channel. For bright stars, including CoRoT-3, the light intensity coming through each of the three channels is available. We used the so-called N2 data level (Baudin et al. 2006) of CoRoT-3, which is now public.

As the modulations we searched for were quite small, we had to prepare and clean the data before searching for any periodic effect. We decided to concentrate on the red-channel data, because this channel included most of the stellar light detected

by CoRoT, and the other two channels only added noise to the data (see below). Snellen et al. (2009) adopted a similar strategy when analyzing the lightcurve of CoRoT-1. This section describes how we “cleaned” the data, removed the long-term variation, and searched for the periodic modulation with the orbital period and its harmonics.

2.1. Cleaning the lightcurve

The “cleaning” of the CoRoT-3 lightcurve had the following stages:

- rebinning: Corot-3b was detected before the CoRoT run was completed and therefore the cadence of the observations was changed during the run – the first part of the lightcurve is composed of 512 s exposures, while the later part contains 32 s exposures. Since we were interested in modulations with periods equal to or longer than half the orbital period, at about 2.1 d, the entire light curve was re-binned into 512 s bins. Altogether, we derived 22 072 valid measurements;
- removing transits: 1165 measurements taken during the transits of CoRoT-3 were removed from the analysis;
- jump removal: one “jump”, at CoRoT HJD of 2746.99, probably caused by a “hot pixel” event, was identified and corrected. The counts after the jump were adopted to the stellar flux before the jump, while 24 measurements following the jump were removed;
- outlier removal: we identified 106 outliers by calculating the running median and RMS around each point, and rejecting measurements that differed by 4σ or more from their corresponding median. We were left with 20 801 data points.

2.2. Long-term detrending with a cosine filter

The CoRoT-3 lightcurve clearly contained a long-term variation, as can be seen in Fig. 1, where we plot the *relative* red-channel flux, after subtracting and dividing the original flux by its median.

To remove this trend we used a discrete cosine transform (Ahmed et al. 1974), adopted to the unevenly spaced data we had in hand. We fitted the data with a linear combination of the first N low-frequency cosine functions

$$\left\{ f_i(t_j) = \cos\left(\frac{2\pi}{2T} i \times t_j\right); i = 0, N \right\}, \text{ where } N = \text{Round}\left(\frac{2T}{4P_{\text{orb}}}\right) = 18, \quad (1)$$

$T = 152.012 d$ is the timespan of the observations, $P_{\text{orb}} = 4.2568 d$ is the orbital period of CoRoT-3, and t_j is the timing of the j th measurement. The fitting finds the linear coefficient a_i for each of the cosine functions, so that the fitted model is

$$\mathcal{M}(t_j) = \sum a_i f_i(t_j). \quad (2)$$

We then subtracted the model $\mathcal{M}(t_j)$ from the lightcurve.

The general idea was to perform a high-pass filter, so we removed all the low-frequency cosine components of the lightcurve without altering the periodic modulation of the orbital period. In a similar manner we also removed the satellite and earth frequencies, which appeared in the N2 data (e.g., Mazeh et al. 2009).

Figure 1 shows the red-channel lightcurve before and after the removal of the long-term trend and the satellite and earth modulation. The RMS of the cleaned lightcurve is 904 ppm (parts per million). A similar analysis of the blue- and green-channel data yielded lightcurves with highly correlated noise, of an RMS of 1600 and 2000 ppm, respectively. The white-channel

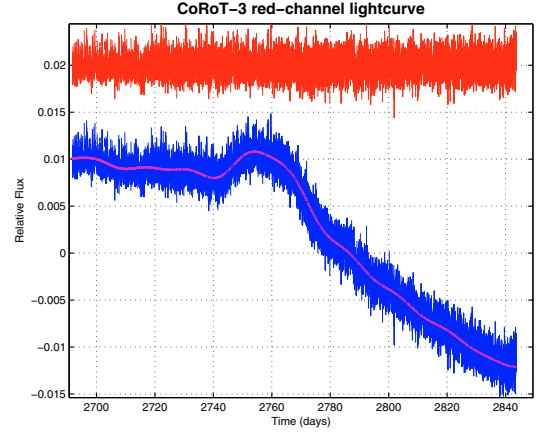


Fig. 1. The lightcurve of CoRoT-3, before (blue) and after (red) detrending. The long-term model is presented by the wide line. Time is the CoRoT time = BJD – 2 451 545.0. Flux is relative to the mean red-channel flux. The detrended lightcurve is shifted by 0.02.

lightcurve, which includes the blue and the green data, is affected by similar problems. These results supported our decision to consider the red-channel data only.

2.3. Fitting the amplitudes of the ellipsoidal, beaming, and reflection effects

We finally proceeded to fit a model that includes the ellipsoidal, beaming and reflection effects. We approximated each of the three effects using pure sine/cosine functions, relative to the middle of the transit, t_{tran} , denoted as phase zero. The reflection and the beaming effects were approximated by sine and cosine functions, respectively, with the orbital period, and the ellipsoidal effect by a cosine function with half the orbital period (see next section). In this approximation, we expressed the stellar flux modulation ΔF as a fraction of the averaged flux \bar{F} , and a function of $\hat{t} \equiv t - t_{\text{tran}}$:

$$\frac{\Delta F_{\text{ellip}}(\hat{t})}{\bar{F}} = -A_{\text{ellip}} \cos\left(\frac{2\pi}{P_{\text{orb}}/2} \hat{t}\right), \quad (3)$$

$$\frac{\Delta F_{\text{beam}}(\hat{t})}{\bar{F}} = A_{\text{beam}} \sin\left(\frac{2\pi}{P_{\text{orb}}} \hat{t}\right), \quad (4)$$

$$\frac{\Delta F_{\text{refl}}(\hat{t})}{\bar{F}} = -A_{\text{refl}} \cos\left(\frac{2\pi}{P_{\text{orb}}} \hat{t}\right), \quad (5)$$

where the coefficients, A_{ellip} , A_{beaming} , and A_{refl} are all positive.

We therefore fitted the cleaned, detrended lightcurve of CoRoT-3 with a 5-parameter model, \mathcal{M}_{ebr} , consisting of two frequencies

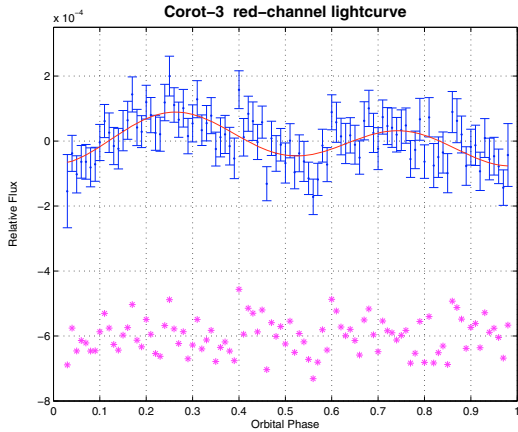
$$\mathcal{M}_{\text{ebr}}(t_j) = a_0 + a_{1c} \cos\left(\frac{2\pi}{P_{\text{orb}}} \hat{t}_j\right) + a_{1s} \sin\left(\frac{2\pi}{P_{\text{orb}}} \hat{t}_j\right) + a_{2c} \cos\left(\frac{2\pi}{P_{\text{orb}}/2} \hat{t}_j\right) + a_{2s} \sin\left(\frac{2\pi}{P_{\text{orb}}/2} \hat{t}_j\right), \quad (6)$$

as performed by Sirko & Paczyński (2003). The fitting process could find any value, positive or negative, for the five parameters. However, we did expect a_{1s} to represent the beaming effect and therefore be positive, a_{1c} to represent the reflection effect and therefore be negative, a_{2c} to represent the ellipsoidal

T. Mazeh and S. Faigler : Ellipsoidal and beaming effect in CoRoT-3

Table 1. The fitted coefficients and the theoretical expected amplitudes of the three effects of CoRoT-3.

Coefficient	Derived value (ppm)	Expected amplitude (ppm)	Effect
a_{1c}	-14 ± 9	$-\alpha_{\text{refl}}(7.2 \pm 0.3)$	Reflection
a_{1s}	27 ± 9	$\alpha_{\text{beam}}(29 \pm 0.5)$	Beaming
a_{2c}	-59 ± 9	$-\alpha_{\text{ellip}}(32 \pm 5)$	Ellipsoidal
a_{2s}	0.1 ± 9	–	–


Fig. 2. The folded cleaned lightcurve of CoRoT-3, binned into 100 bins, with the fitted model. The residuals are plotted at the bottom of the figure.

effect and therefore be negative, and a_{2s} to be close to zero. The last expectation is important because it ensures that the ellipsoidal modulation is detected with the correct phase. The a_0 parameter was induced to remove any DC component left in the data. Obviously, the expected absolute values of the three coefficients depended on the parameters of the CoRoT-3 system. Thus, *after* the analysis was performed we were able to verify our results by comparing them with the expected values.

The results of the fitting are given in Table 1 (with some order-of-magnitude theoretical expectations; see next section) and plotted in Fig. 2. In the figure one can easily discern the ellipsoidal modulation, with half the orbital period, and the beaming effect, which causes the difference between the two peaks. One indication of the consistency of our results with the expected modulations is the correct sign of the three first coefficients and that the fourth coefficient is smaller than the third one by at least one order of magnitude. This suggests a close agreement between the orbital phase of the ellipsoidal modulation and that of the transit. We note that the errors in the four coefficients are all 9 ppm, or somewhat smaller than 10^{-5} in relative flux. This precision does not allow a significant detection of the reflection modulation. However, the detection of both the ellipsoidal and the beaming effect is highly significant. A bootstrap test indicates that the probability of detecting the beaming modulation by chance is 2×10^{-4} .

3. Theoretical approximation

This section presents our theoretical approximations of the ellipsoidal, beaming, and the reflection effects. We are not interested in detailed calculations, which depend on specific models. For example, to calculate the ellipsoidal modulation one could integrate the light originating from the individual surface elements

of the rotating star, which is slightly deformed by the tidal force induced by its small companion (e.g., Orosz & Hauschildt 2000). Such an analysis was carefully performed very recently to model the Kepler lightcurve of HAT-P-7 (Welsh et al. 2010). Instead, we are interested here only in order-of-magnitude approximation, so we can check the consistency of the detected amplitudes with the theory. All our approximations are evaluated for an inclination angle i close to 90 deg, so we could ignore the $\sin i$ dependence of the three effects.

3.1. Ellipsoidal effect

To derive the order-of-magnitude of the ellipsoidal effect we used the analytical approximation of Morris & Naftilan (1993), who used the Kopal (1959) expansion of the periodic variation into discrete Fourier series with terms that depend on the ratio R_*/a , where R_* is the stellar radius and a is the semi-major axis of the orbit (see also Pfahl et al. 2008). Assuming R_*/a is small, the leading term of the stellar variation has a semi-amplitude of

$$A_{\text{ellip}} \approx \alpha_{\text{ellip}} \frac{m_p}{M_*} \left(\frac{R_*}{a} \right)^3, \quad (7)$$

where

$$\alpha_{\text{ellip}} = 0.15 \frac{(15 + u)(1 + g)}{3 - u} \quad (8)$$

is of order unity. In the above expression, m_p is the planetary mass, M_* is the stellar mass, g is the stellar gravity darkening coefficient, and u is its limb-darkening coefficient (e.g., Mazeh 2008).

3.2. Beaming effect

For a circular orbit, the amplitude of the beaming effect can be written as

$$A_{\text{beam}} = \alpha_{\text{beam}} 4 \frac{K_r}{c}, \quad (9)$$

where K_r is the stellar radial-velocity amplitude and c is the speed of light (Loeb & Gaudi 2003; Zucker et al. 2007), and α_{beam} is of order unity. The factor $4K_r/c$ represents the beaming effect for bolometric photometric observations, but ignores the Doppler shift photometric effect, which appears when the photometric observations are made in a specific bandpass, so that some of the stellar light is shifted out of or into the observed bandpass. The latter is accounted for by the α_{beam} factor, and we assume that for the CoRoT red bandpass it is of order unity.

3.3. Reflection effect

In our simplistic approximation we include in the reflection modulation the thermal emission from the dayside of CoRoT-3b, assuming both are modulated with the same phase (e.g., Snellen et al. 2009). The amplitude of the modulation of the reflected light alone is

$$A_{\text{refl}} = p_{\text{geo}} \left(\frac{r_p}{a} \right)^2, \quad (10)$$

where r_p is the planetary radius and p_{geo} is the geometrical albedo (e.g., Rowe et al. 2008). Rowe et al. (2008) found quite a small albedo, of 0.03, for HD 209458, but recent study (Cowan & Agol 2009) suggested that exoplanets may have a much larger albedo, of up to 0.5. We therefore write the amplitude of the reflection effect, including the thermal emission, as

$$A_{\text{refl}} = \alpha_{\text{refl}} 0.1 \left(\frac{r_p}{a} \right)^2, \quad (11)$$

where α_{refl} is of order unity.

Table 2. CoRoT-3 parameters, as derived by Deleuil et al. (2008) and Triaud et al. (2009).

Parameter	Derived value	Unit
a/R_*	7.8 ± 0.4	
r_p/R_*	$(663 \pm 9) \times 10^{-4}$	
m_p	21.7 ± 1.0	M_{Jup}
M_*	1.37 ± 0.09	M_{\odot}
T_s	6740 ± 140 K	deg
K_r	2170 ± 30	m s^{-1}

3.4. Application to CoRoT-3

Table 2 presents the relevant parameters of CoRoT-3. The first four parameters were derived by Deleuil et al. (2008), while the last parameter, the radial-velocity amplitude, was deduced by Triaud et al. (2009). From these parameters we derived the expected values of the amplitudes of the ellipsoidal, beaming, and reflection effects, which are given in Table 1.

We emphasize that in each of the three theoretical amplitudes given in Table 1, the main source of uncertainty is hidden in the α factor, which we did *not* calculate. The numerical values, with their relatively small errors, are only order-of-magnitude approximations for inclination angles close to 90 deg.

The amplitudes derived from the cleaned lightcurve of CoRoT-3, as shown in Table 1, are of the same order of magnitude as the expected values, based on our simplistic approximation. This is true in particular for the beaming effect, where the theoretical approximation was found to be quite accurate. We therefore propose that we have detected the ellipsoidal and beaming effects of CoRoT-3. Our results suggest that the α_{ellip} factor in CoRoT-3 is on the order of 2. The reflection effect was too small to ensure a significant detection, given the SNR of the lightcurve.

4. Discussion

Our analysis has demonstrated that the red-channel lightcurve of CoRoT-3 includes the ellipsoidal and beaming effects. This is the first time that the beaming effect has been detected for substellar companion. We have been able to detect the two effects, with 59 and 27 ppm amplitudes, respectively, because of a combination of three features:

- CoRoT-3 brightness: with r' -mag of 13.1, the star is among the brightest CoRoT targets, which are typically in the range of 11 to 16 in r' (Deleuil et al. 2008);
- the long observational run: the LRc01 lasted for 152 days, and the CCDs did not show yet any aging signals;
- the mass of CoRoT-3b: This massive-planet/brown-dwarf companion has one of the largest masses, $22 M_{\text{Jup}}$, discovered by CoRoT for substellar objects.

The last feature suggests that the stellar rotation has achieved synchronization with the orbital period of 4.3 days, without which the analysis of the ellipsoidal effect could have been more complicated.

Had this analysis been performed immediately after the discovery of the transits of CoRoT-3, and in particular before the radial-velocity confirmation of the planetary nature of the transiting object, we could have estimated the mass of the unseen object from the observed amplitudes of the ellipsoidal and beaming effects, provided we had been able to accurately derive their expected values. Such analysis could, in principle, save costly radial-velocity observations, or at least reduce to a minimum the

number of observed velocities needed to confirm the substellar mass of the transiting object.

Obviously, the analysis of lightcurves obtained by space missions is dramatically different from those obtained by ground-based photometry. For the latter, the appearance of the ellipsoidal modulation in the data of transit candidates was considered a sign that the transiting object was of stellar nature, as suggested by Sirko & Paczyński (2003), and applied, for example, by Kane et al. (2008) and Pietrukowicz et al. (2010). This is so because of the relatively high threshold of detection of the ellipsoidal modulation in the ground-based photometry. On the other hand, the present work, and the study of Welsh et al. (2010), suggest that the detection of the ellipsoidal modulation with a small amplitude in the CoRoT and Kepler data may indicate that the transiting object is a massive-planet/brown-dwarf object.

The present analysis suggests that, in principle, the three effects, or at least two of them, can be detected in the CoRoT lightcurves for some massive-planet/brown-dwarf objects, even without any transits, as suggested by Loeb & Gaudi (2003) and Zucker et al. (2007). The effects can be stronger for systems with shorter orbital periods, and therefore can be detected in stars fainter than CoRoT-3 in the CoRoT fields. Many objects similar to CoRoT-3 should also be detected by Kepler, because of both higher SNR and longer timespan of its lightcurves.

Acknowledgements. We thank Shay Zucker for helpful discussions, Antonio Claret and Edward Guinan for help with the theoretical estimation of the ellipsoidal modulation, and Avi Shporer for careful reading of the paper and helpful suggestions. This research was supported by the Israel Science Foundation (grant No. 655/07).

References

- Ahmed, N. T., Natarajan, T. K. R., & Rao, K. R. 1974, IEEE Trans. Computers, 90
- Auvergne, M., Bodin, P., Boissard, L., et al. 2009, A&A, 506, 411
- Baglin, A., Auvergne, M., Boissard, L., et al. 2006, 36th COSPAR Scientific Assembly, 36, 3749
- Baudin, F., Baglin, A., Orcesi, J.-L., et al. 2006, ESA Spec. Pub., 1306, 145
- Borucki, W. J., Koch, D., Basri, G., et al. 2010, Science, 327, 977
- Cabrera, J., Fridlund, M., Ollivier, M., et al. 2009, A&A, 506, 501
- Cowan, N. B., & Agol, E. 2009, ApJ, submitted [arXiv:1001.0012]
- Deleuil, M., Deeg, H. J., Alonso, R., et al. 2008, A&A, 491, 889
- Drake, A. J. 2003, ApJ, 589, 1020
- Etzel, P. B. 1980, EBOP User's Guide, 3rd edn., UCLA A&A
- For, B.-Q., Green, E. M., Fontaine, G., et al. 2010, ApJ, 708, 253
- Kane, S. R., Clarkson, W. I., West, R. G., et al. 2008, MNRAS, 384, 1097
- Koch, D. G., Borucki, W. J., Basri, G., et al. 2010, ApJ, 713, L79
- Kopal, Z. 1959, Close binary systems, The International Astrophysics Series (London: Chapman & Hall)
- Loeb, A., & Gaudi, B. S. 2003, ApJ, 588, L117
- Maxted, P. F. L., Marsh, T. R., & North, R. C. 2000, MNRAS, 317, L41
- Mazeh, T. 2008, EAS Pub. Ser., 29, 1
- Mazeh, T., Guterman, P., Aigrain, S., et al. 2009, A&A, 506, 431
- Morris, S. L., & Nafilan, S. A. 1993, ApJ, 419, 344
- Orosz, J. A., & Hauschildt, P. H. 2000, A&A, 364, 265
- Pál, A., Bakos, G. Á., Torres, G., et al. 2008, ApJ, 680, 1450
- Pfahl, E., Arras, P., & Paxton, B. 2008, ApJ, 679, 783
- Pietrukowicz, P., Minniti, D., Díaz, R. F., et al. 2010, A&A, 509, A4
- Popper, D. M., & Etzel, P. B. 1981, AJ, 86, 102
- Rouan, D., Baglin, A., Copet, E., et al. 1998, Earth Moon and Planets, 81, 79
- Rowe, J. F., Matthews, J. M., Seager, S., et al. 2008, ApJ, 689, 1345
- Sirko, E., & Paczyński, B. 2003, ApJ, 592, 1217
- Snellen, I. A. G., de Mooij, E. J. W., & Albrecht, S. 2009, Nature, 459, 543
- Tamuz, O., Mazeh, T., & North, P. 2006, MNRAS, 367, 1521
- Triaud, A. H. M. J., Queloz, D., Bouchy, F., et al. 2009, A&A, 506, 377
- van Kerkwijk, M. H., Rappaport, S. A., Breton, R. P., et al. 2010, ApJ, 715, 51
- Welsh, W. F., Orosz, J. A., Seager, S., et al. 2010, ApJ, 713, L145
- Wilson, R. E., & Devinney, E. J. 1971, ApJ, 166, 605
- Zucker, S., Mazeh, T., & Alexander, T. 2007, ApJ, 670, 1326



Photometric detection of non-transiting short-period low-mass companions through the beaming, ellipsoidal and reflection effects in *Kepler* and *CoRoT* light curves

S. Faigler[★] and T. Mazeh¹*School of Physics and Astronomy, Raymond and Beverly Sackler Faculty of Exact Sciences, Tel Aviv University, Tel Aviv 69978, Israel*

Accepted 2011 May 4. Received 2011 April 28; in original form 2011 February 21

ABSTRACT

We present a simple algorithm, BEER, to search for a combination of the BEaming, Ellipsoidal and the Reflection/heating periodic modulations, induced by short-period *non-transiting* low-mass companions. The beaming effect is due to the increase (decrease) in the brightness of any light source approaching (receding from) the observer. To first order, the beaming and the reflection/heating effects modulate the stellar brightness at the orbital period, with phases separated by a quarter of a period, whereas the ellipsoidal effect is modulated with the orbital first harmonic. The phase and harmonic differences between the three modulations allow the algorithm to search for a combination of the three effects and identify stellar candidates for low-mass companions. The paper presents the algorithm, including an assignment of a likelihood factor to any possible detection, based on the expected ratio of the beaming and ellipsoidal effects, given an order-of-magnitude estimate of the three effects. As predicted by Loeb & Gaudi and by Zucker, Mazeh & Alexander, the *Kepler* and the *CoRoT* light curves are precise enough to allow detection of massive planets and brown-dwarf/low-mass-stellar companions with orbital period up to 10–30 days. To demonstrate the feasibility of the algorithm, we present two examples of candidates found in the first 33 days of the Q1 *Kepler* light curves. Although we used a relatively short time-span, the light curves were precise enough to enable the detection of periodic effects with amplitudes as small as one part in 10^4 of the stellar flux.

Key words: methods: data analysis – binaries: eclipsing – binaries: general.

1 INTRODUCTION

We present a simple algorithm, BEER, to search for a combination of the BEaming, Ellipsoidal and the Reflection/heating periodic modulations, induced by short-period *non-transiting* low-mass companions, using precise photometric stellar light curves. Two of the modulations are well known for many years from the study of close binary stellar systems. These are the ellipsoidal variation (Morris 1985), due to the tidal distortion of each component by the gravity of its companion (see a review by Mazeh 2008), and the reflection/heating variation (referred to here as the reflection modulation), induced by the luminosity of each component that falls only on the close side of its companion (e.g. Maxted et al. 2002; Harrison et al. 2003; For et al. 2010; Reed et al. 2010).

A much smaller and less studied photometric modulation is the beaming effect, sometimes called Doppler boosting, induced by the stellar radial motion. This effect causes an increase (decrease) in

the brightness of any light source approaching (receding from) the observer (e.g. Rybicki & Lightman 1979). Before the era of space photometry this effect has been noticed only once, by Maxted, Marsh & North (2000), who observed KPD 1930+2752, a binary with a very short period, of little longer than 2 h, and a radial-velocity amplitude of 350 km s^{-1} . The beaming effect of that system, which should be of the order of 10^{-3} , was hardly seen in the photometric data.

The beaming effect became relevant only recently, when space photometry, aimed to detect transits of exoplanets, has substantially improved the precision of the produced light curves. The *CoRoT* (Rouan et al. 1998; Baglin et al. 2006; Auvergne et al. 2009) and *Kepler* (Borucki et al. 2010; Koch et al. 2010) missions are producing hundreds of thousands of continuous photometric light curves with time-spans of tens and hundreds of days, at a relative precision level that can get to 10^{-3} – 10^{-4} per measurement, depending on the stellar brightness. It was therefore anticipated that *CoRoT* and *Kepler* will detect each of the three modulations (e.g. Drake 2003; Loeb & Gaudi 2003; Zucker, Mazeh & Alexander 2007), for binaries and planets alike.

[★]E-mail: simchonf@mail.tau.ac.il

As predicted, already in the Q1 *Kepler* data, which spanned over only 33 d, van Kerkwijk et al. (2010) detected the ellipsoidal and the beaming effect of two eclipsing binaries, KOI-74 and KOI-81 (Rowe et al. 2010). Carter, Rappaport & Fabrycky (2011) detected the ellipsoidal, beaming and reflection effects in the *Kepler* light curve of the eclipsing binary KIC 10657664, and derived the system parameters from the amplitudes of the three effects, determining the system to be comprised of a low-mass, thermally bloated, hot white dwarf orbiting an A star. The effects were discovered even for brown-dwarf secondaries and planets. Welsh et al. (2010) identified the ellipsoidal effect in the *Kepler* data of HAT-P-7, a system with a known planet of $1.8 M_{\text{Jup}}$ and a period of 2.2 d (Pál et al. 2008). Snellen, de Mooij & Albrecht (2009) detected in *CoRoT* data the reflection effect of *CoRoT*-1b. Mazeh & Faigler (2010) detected the ellipsoidal and the beaming effect induced by *CoRoT*-3b, a $22 M_{\text{Jup}}$ massive-planet/brown-dwarf companion with a period of 4.3 d (Deleuil et al. 2008).

However, space mission data can yield much more. In addition to eclipse events, *CoRoT* and *Kepler* are producing data that can indicate the binarity of a system based on the evidence coming only from the beaming, ellipsoidal and reflection effects themselves. Loeb & Gaudi (2003) suggested that the beaming effect can be used to detect non-transiting exoplanets, and Zucker et al. (2007) extended this idea to binaries. Loeb & Gaudi (2003) (see also the discussion of Zucker et al. 2007) showed that for relatively long-period orbits, of the order of 10–100 d, the beaming modulation is stronger than the ellipsoidal and the reflection effects, and therefore could be observed without the interference of the other two modulations. However, the beaming modulation by itself might not be enough to render a star a good exoplanet candidate, as the pure sinusoidal modulation could be produced by other effects, stellar modulations in particular (e.g. Aigrain, Favata & Gilmore 2004). The BEER detection algorithm, therefore, searches for stars that show in their space-obtained light curves some *combination* of the three modulations, the ellipsoidal and the beaming effects in particular.

The *CoRoT* mission, and certainly the *Kepler* satellite, have the required precision to reveal the ellipsoidal and even the beaming modulations for massive planets and brown-dwarf/low-mass stellar companions with short enough orbital periods. This was demonstrated by Mazeh & Faigler (2010) for the aforementioned *CoRoT*-3b, for which they detected the two modulations with amplitudes of about 60 and 30 ppm (parts per million), respectively.

Searching for an unknown orbital period is more difficult than looking for a modulation with a known period and phase. However, the combination of at least two of the modulations, and their relative amplitudes and *phases*, can suggest the presence of a small non-transiting companion. Like in the transit searches, the candidates found must be followed by radial velocity (RV) observations in order to confirm the existence of the low-mass companion, and to reject the other possible interpretations of the photometric modulations.

This paper presents the details of the BEER algorithm. Section 2 presents the theoretical approximation of the beaming, ellipsoidal and reflection effects. Section 3 explains the details and the performance estimate of the algorithm itself. Section 4 presents two candidates found in the *Kepler* Q1 data, with a companion mass of up to the sine of the orbital inclination, $\sim 70 M_{\text{Jup}}$. In a separate paper (Faigler & Mazeh et al., in preparation) we will present RV observations that confirm the existence of the two companions. Section 5 summarizes our results and argues that the BEER algorithm can discover short-period brown-dwarf companions and even massive planets, given the *CoRoT* and *Kepler* data accuracy.

2 THEORETICAL APPROXIMATION OF THE THREE EFFECTS

To perform the search for massive planets and brown-dwarf/low-mass-stellar companions we need order-of-magnitude approximations for the three effects. For the BEER algorithm, we use the expressions listed by Mazeh & Faigler (2010) for circular orbits, assuming that the companion is much smaller than the primary star, and therefore ignoring its luminosity. The expressions for a $10 M_{\text{Jup}}$ companion become

$$A_{\text{beam}} = \alpha_{\text{beam}} 4 \frac{K_{\text{RV}}}{c} = 27 \alpha_{\text{beam}} \left(\frac{M_*}{M_{\odot}} \right)^{-2/3} \left(\frac{P_{\text{orb}}}{1 \text{ d}} \right)^{-1/3} \times \left(\frac{m_2 \sin i}{10 M_{\text{Jup}}} \right) \text{ ppm}, \quad (1)$$

$$A_{\text{ellip}} = \alpha_{\text{ellip}} \frac{m_2 \sin i}{M_*} \left(\frac{R_*}{a} \right)^3 \sin i = 128 \alpha_{\text{ellip}} \sin i \left(\frac{R_*}{R_{\odot}} \right)^3 \times \left(\frac{M_*}{M_{\odot}} \right)^{-2} \left(\frac{P_{\text{orb}}}{1 \text{ d}} \right)^{-2} \left(\frac{m_2 \sin i}{10 M_{\text{Jup}}} \right) \text{ ppm}, \quad (2)$$

$$A_{\text{refl}} = \alpha_{\text{refl}} 0.1 \left(\frac{r_2}{a} \right)^2 \sin i = 57 \alpha_{\text{refl}} \sin i \left(\frac{M_*}{M_{\odot}} \right)^{-2/3} \times \left(\frac{P_{\text{orb}}}{1 \text{ d}} \right)^{-4/3} \left(\frac{r_2}{R_{\text{Jup}}} \right)^2 \text{ ppm}. \quad (3)$$

In the above expressions, m_2 and r_2 are the companion mass and radius, M_* and R_* are the primary mass and radius, P_{orb} and a are the orbital period and semimajor axis, K_{RV} is the semi-amplitude of the stellar RV modulation induced by the companion, i is the orbital inclination relative to our line of sight, and c is the speed of light.

The α values represent order-of-unity coefficients that necessitate a more detailed model to evaluate as follows.

(i) The expression for the beaming effect includes two factors. The $4K_{\text{RV}}/c$ factor represents the beaming effect for bolometric photometric observations, but ignores the Doppler shift photometric effect, which appears when the photometric observations are made in a specific bandpass, so that some of the stellar light is shifted out of or into the observed bandpass. The latter is accounted for by the α_{beam} factor. We assume here a blackbody stellar radiation model that yields for the *CoRoT* and the *Kepler* bandpasses and for F-G-K spectral-type stars, α_{beam} value between 0.8 and 1.2.

(ii) The α_{ellip} factor represents the response of the stellar surface to the tidal effect induced by the companion, and to first order can be written (Morris 1985) as

$$\alpha_{\text{ellip}} \simeq 0.15 \frac{(15 + u)(1 + g)}{3 - u}, \quad (4)$$

where g is the stellar gravity darkening coefficient, whose expected range is 0.3–1.0, and u is the limb-darkening coefficient, whose range is 0–1 and is typically ≈ 0.6 for solar-like stars (see, for example Mazeh 2008). Thus, we estimate that for the F-G-K spectral-type stars, the α_{ellip} value is between 1.0 and 2.4.

Note that the expression for A_{ellip} includes an extra $\sin i$ factor, in addition to the one that appears in the $m_2 \sin i$ factor of equation (2). This reflects a stronger dependence of the ellipsoidal modulation on the inclination angle. If we know well enough all the other factors of α_{ellip} and α_{beam} and derive A_{ellip} and A_{beam} , we can, at least in principle, estimate both $m_2 \sin i$ and $\sin i$.

(iii) In our simplistic approximation we include in the reflection modulation the thermal emission from the dayside of the

companion, assuming that both are modulated with the same phase (e.g. Snellen et al. 2009). This approximation does not model the small phase shift of the reflection modulation that can be present if the companion is not tidally locked, or if there is advection of heat away from the substellar point, as shown by Knutson et al. (2007). The amplitude of the modulation of the reflected light alone is

$$A_{\text{refl}} = p_{\text{geo}} \left(\frac{r_2}{a} \right)^2 \sin i, \quad (5)$$

where p_{geo} is the geometrical albedo. Rowe et al. (2008) found quite a small albedo, of 0.03, for HD 209458b, but a recent study (Cowan & Agol 2011) suggested that exoplanets could have much larger albedo, up to 0.5. We therefore estimate, somewhat arbitrarily, the geometrical albedo coefficient by $p_{\text{geo}} = 0.1\alpha_{\text{refl}}$, and estimate that the value of α_{refl} can be between 0.2 and 5.

3 THE BEER ALGORITHM

3.1 Two-harmonic search

Before searching for small periodic effects in any stellar light curve, we have to prepare and clean the data. This is done in two stages. In the first one we remove jumps and outliers, and in the second stage we identify and subtract the long-term variation of the light curve with the discrete cosine transform (Ahmed, Natarajan & Rao 1974), adopted to unevenly spaced data. This is done by subtracting from the data a linear model of all cosine functions with frequencies from 0 to 0.1 d^{-1} , with a frequency separation of $1/(2T)$, T being the total time-span of the light curve (see the details of our approach in Mazeh & Faigler 2010).

We then proceed to fit the data with a model that includes the ellipsoidal, beaming and reflection effects for every possible period, P_{orb} . The algorithm approximates each of the three effects by a pure sine/cosine function, relative to phase zero taken at the time of conjunction, t_{conj} , when the small companion is in front of the stellar component of the system. This fiducial point replaces the time of transit, t_{tran} , used when modelling transiting planets and eclipsing binaries (e.g. Mazeh & Faigler 2010). The reflection and the beaming effects are approximated by cosine and sine functions, respectively, with the orbital period, and the ellipsoidal effect by a cosine function with half the orbital period. In this approximation we express the stellar flux modulation ΔF as a fraction of the averaged flux \bar{F} , and as a function of $\hat{t} \equiv t - t_{\text{conj}}$:

$$\frac{\Delta F_{\text{ellip}}(\hat{t})}{\bar{F}} = -A_{\text{ellip}} \cos \left(\frac{2\pi}{P_{\text{orb}/2}} \hat{t} \right), \quad (6)$$

$$\frac{\Delta F_{\text{beam}}(\hat{t})}{\bar{F}} = A_{\text{beam}} \sin \left(\frac{2\pi}{P_{\text{orb}}} \hat{t} \right), \quad (7)$$

$$\frac{\Delta F_{\text{refl}}(\hat{t})}{\bar{F}} = -A_{\text{refl}} \cos \left(\frac{2\pi}{P_{\text{orb}}} \hat{t} \right), \quad (8)$$

where the coefficients A_{ellip} , A_{beam} and A_{refl} are all positive.

We note that contrary to the case of transiting planets, like *CoRoT-3b*, we do *not* know a priori the time of t_{conj} . The algorithm therefore fits the cleaned, detrended light curve with a linear five-parameter model, consisting of two frequencies:

$$\mathcal{M}(\bar{t}) = a_0 + a_{1c} \cos \left(\frac{2\pi}{P_{\text{orb}}} \bar{t} \right) + a_{1s} \sin \left(\frac{2\pi}{P_{\text{orb}}} \bar{t} \right) + a_{2c} \cos \left(\frac{2\pi}{P_{\text{orb}/2}} \bar{t} \right) + a_{2s} \sin \left(\frac{2\pi}{P_{\text{orb}/2}} \bar{t} \right), \quad (9)$$

where \bar{t} is the time relative to some arbitrary zero time. Since in this model the amplitudes are free to be either positive or negative, the usual bias of overestimating a sinusoid's amplitude when fitting noisy data is not present.

As explained, we expect a_{2s} to be close to zero and a_{2c} to be negative relative to the time of conjunction, so after the fitting is done we find t_{conj} that results in $a_{2s} = 0$ and a_{2c} being negative. This time is when the first harmonic model

$$\mathcal{M}_2(\bar{t}) = a_{2c} \cos \left(\frac{2\pi}{P_{\text{orb}/2}} \bar{t} \right) + a_{2s} \sin \left(\frac{2\pi}{P_{\text{orb}/2}} \bar{t} \right) \quad (10)$$

has its minimum. We note that because \mathcal{M}_2 presents the first harmonic component of the model, it has two minima per period. The algorithm choice between the two minima is detailed below.

The algorithm then performs a new linear fit with a four-parameter model:

$$\mathcal{M}(\hat{t}) = \hat{a}_0 + \hat{a}_{1c} \cos \left(\frac{2\pi}{P_{\text{orb}}} \hat{t} \right) + \hat{a}_{1s} \sin \left(\frac{2\pi}{P_{\text{orb}}} \hat{t} \right) + \hat{a}_{2c} \cos \left(\frac{2\pi}{P_{\text{orb}/2}} \hat{t} \right), \quad (11)$$

which is our final model for that period.

3.2 A likelihood parameter

So far, the search performs a regular double-harmonic search (e.g. Shporer & Mazeh 2006), and therefore the fitting process could find any values for the three amplitudes. We now exercise our astrophysical expectations for the amplitudes and phases of the three effects, and assign to each period a likelihood factor that expresses how likely are the derived ratio between the amplitudes of the beaming and the ellipsoidal effects, and the phase difference between the beaming and the reflection effects.

If indeed the modulation, with its double harmonic components, is induced by a low-mass companion with negligible luminosity, we expect \hat{a}_{1s} to represent the beaming effect and therefore to be positive and \hat{a}_{1c} to represent the reflection effect and therefore be negative. The \hat{a}_{1c} coefficient is negative by our definition of t_{conj} .

The algorithm therefore distinguishes between two cases as follows.

(i) The beaming and the reflection coefficients, \hat{a}_{1s} and \hat{a}_{1c} , respectively, have opposite signs. In this case the algorithm chooses (between the two options, see above) t_{conj} so that \hat{a}_{1s} is positive and \hat{a}_{1c} is negative.

(ii) The beaming and the reflection coefficients, \hat{a}_{1s} and \hat{a}_{1c} , respectively, have the same sign. In such a case the algorithm chooses (between the two options, see above) t_{conj} such that the more significant coefficient has the correct sign. The other coefficient is then set to zero.

Our model is therefore composed of two or three components, depending on the relative signs of the sine and cosine components of the fitting. Because we are looking for a system that displays *both* beaming and ellipsoidal modulations, we consider as our model goodness-of-fit parameter the rms of the smaller one of these two fitted modulations. To scale the goodness-of-fit we divide the model rms by that of the residuals relative of the total model. This definition implies that a prominent peak in the periodogram indicates that *both* modulations, the ellipsoidal *and* the beaming ones, are significant at the specific peak period. This ratio, derived for every possible period, marks the first stage of our periodogram.

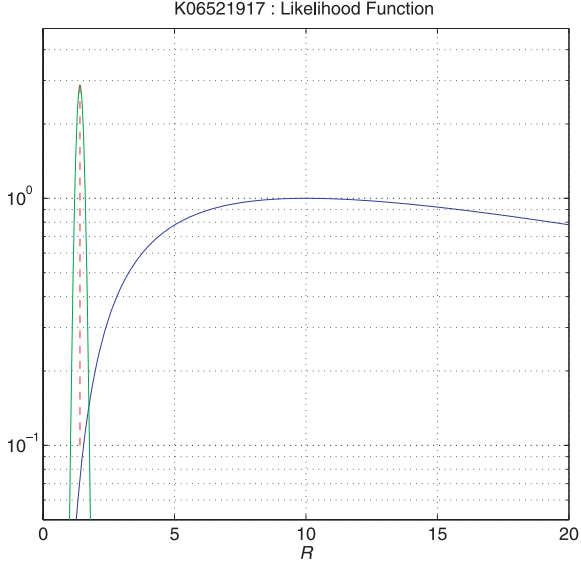


Figure 1. The likelihood function of the expected value of \mathcal{R}_{exp} (blue) and the probability distribution of the observed value of \mathcal{R}_{obs} (green) for the *Kepler* star K06521917, derived for a period of 1.345 d. The likelihood function peaks at $\mathcal{R} = 10.01$, and the probability distribution peaks at $\mathcal{R} = 1.4$, denoted by a vertical dashed line.

We now proceed to assign a likelihood factor to the model. Using equations (1) and (2) we get the following for the ratio between the amplitudes of the ellipsoidal and the beaming effects:

$$\mathcal{R} \equiv \frac{A_{\text{ellip}}}{A_{\text{beam}}} = 5 \frac{\alpha_{\text{ellip}}}{\alpha_{\text{beam}}} \left(\frac{M_*}{M_{\odot}} \right)^{-4/3} \left(\frac{R_*}{R_{\odot}} \right)^3 \left(\frac{P_{\text{orb}}}{1 \text{ d}} \right)^{-5/3} \sin i. \quad (12)$$

We note that the amplitude ratio of the two effects depends only on parameters associated with the stellar properties of the primary star and the orbital period and inclination, and does not depend on the companion mass. As such, this ratio can serve as the basis for comparing and validating the relevance of the detected amplitudes.

To do that, we distinguish between the *expected* ratio

$$\mathcal{R}_{\text{exp}} \equiv 5 \frac{\alpha_{\text{ellip}}}{\alpha_{\text{beam}}} \left(\frac{M_*}{M_{\odot}} \right)^{-4/3} \left(\frac{R_*}{R_{\odot}} \right)^3 \left(\frac{P_{\text{orb}}}{1 \text{ d}} \right)^{-5/3} \sin i, \quad (13)$$

and the *observed* ratio, $\mathcal{R}_{\text{obs}} \equiv |\hat{a}_{2c}|/|\hat{a}_{1s}|$. Obviously, \mathcal{R}_{obs} is not known exactly, but can be described by a probability distribution, $P_{\text{obs}}(\mathcal{R})$, which depends on the precision of the two derived amplitudes.

Furthermore, our expectation for \mathcal{R}_{exp} also does not have a single value, due to the lack of a precise knowledge of its factors. However, we can generate for every star and period a likelihood function $\mathcal{F}_{\text{exp}}(\mathcal{R})$, which assigns a likelihood value to a range of possible values of \mathcal{R} . This function reflects the random distribution of the inclination, together with our prior distributions of the mass and radius of the given star, and the prior likelihood, depending on the theory, of a range of values of α_{beam} and α_{ellip} . The function $\mathcal{F}_{\text{exp}}(\mathcal{R})$ thus, in essence, encompasses our expectations of the system, and serves as a prior, defined such that its maximum is unity and minimum is zero.

To demonstrate the situation we plot the two functions in Fig. 1 for the *Kepler* star K06521917, derived for a period of 1.345 d. In this example, the most probable \mathcal{R}_{exp} value is 10.01 while $\mathcal{R}_{\text{obs}} = 1.4 \pm 0.14$. The likelihood in this case is quite small, 0.07.

For a given period, the value of the likelihood factor, defined as

$$\mathcal{L}(P) = \int \mathcal{F}_{\text{exp}}(\mathcal{R}) \times P_{\text{obs}}(\mathcal{R}) d\mathcal{R}, \quad (14)$$

determines how likely are the two modulations to be caused by a low-mass companion for any given period. The likelihood factor is derived by integration over the probability distribution of \mathcal{R}_{obs} , weighted by the likelihood function. The final periodogram is the goodness-of-fit of the model multiplied by the likelihood factor $\mathcal{L}(P)$, generated for a range of periods. The highest peak of each periodogram is our best estimate for the orbital period of the presumed low-mass companion.

3.3 Significance and detection limit

For any derived periodogram with its highest peak, we have to answer the following two questions.

- (i) Is this peak significant, representing a real periodic modulation, or is it a result of random noise?
- (ii) If the peak is real and the stellar light curve does contain a periodic modulation, is this modulation induced by a low-mass companion?

The significance of a period detection can be estimated, for example, by the ratio of the highest peak to the second highest one in the periodogram, not including the harmonics of the highest peak. We choose to put our threshold detection when this ratio is 2. Bootstrap simulations of 10 118 *Kepler* Q1 stars with a magnitude within the 12–13 range, and with a radius smaller than $3 R_{\odot}$, did not yield a single false detection using the factor of 2 threshold, indicating a 99.99 per cent significance. If a peak above this threshold is derived, we consider the corresponding star as a *candidate* host of a low-mass companion, with the orbital period corresponding to the peak frequency.

Unfortunately, answering the second question is more difficult. Even with a highly significant peak at the periodogram, at this point we cannot rule out false positive detections, which can rise from stellar modulations of some kind. Therefore, in order to confirm the detection of a low-mass companion, we do need follow-up RV observations. As the presumed period is known, a few measurements should be enough to confirm or reject the low-mass conjecture.

We now turn to roughly estimate our detection rate for the bright-star light curves of *Kepler*. To do that we took the actual Q1 light curves and added to them simulated beaming, ellipsoidal and reflection effects of binaries with a period of 3.2 d and randomly chosen phases. In this way, we used the real noise characteristics of the *Kepler* light curves to estimate the detection performance of the algorithm. The sample was composed of the 10 118 *Kepler* Q1 stars with a magnitude within the 12–13 range, and with a radius smaller than $3 R_{\odot}$, and the simulated effects were prepared with $\alpha_{\text{beam}} = 1$, $\alpha_{\text{ellip}} = 1.5$, $\alpha_{\text{refl}} = 1$, and $\sin i = \pi/4$, using the stellar masses and radii available from the *Kepler* catalogue, all with the same secondary mass. We repeated the simulation for six different secondary masses – 10/20/40/80/160/320 M_{Jup} . In each simulation we applied the BEER algorithm and counted the stars for which the highest periodogram peak was at least twice as much higher than the next one, and we could detect both the beaming and the ellipsoidal modulations with 5σ significance. If the highest peak in our periodogram did not have the inserted period, we did not consider that star as a detection.

The results are given in Fig. 2, which indicates the fraction of systems that have been detected in the simulations as a function of

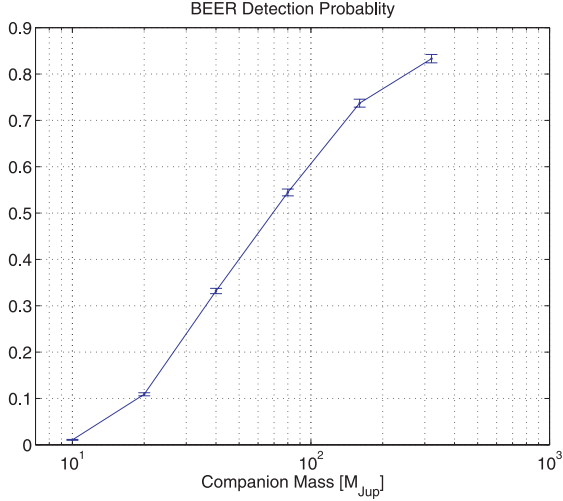


Figure 2. Percentage of 5σ detections of the BEER algorithm in our simulations, as a function of the secondary mass. Each of the simulations included a set of 10,118 *Kepler* Q1 stars, with a magnitude within the 12–13 range, and with a radius smaller than $3 R_{\odot}$ (see text).

the mass of the inserted modulation. We note that while the algorithm detected only one per cent of the simulated massive planets, with masses of $10 M_{\text{Jup}}$, almost all the simulated modulations corresponding to a secondary mass of $\sim 0.3 M_{\odot}$ were detected. The detection rate derived in this way indicates the potential of the BEER algorithm. We note that some of the non-detections may be caused by systems with *real* companions with different periods, with masses higher than the ones inserted by the simulation. This is especially true for the simulated $10 M_{\text{Jup}}$ cases.

4 TWO SIMPLE EXAMPLES

In order to demonstrate the effectiveness of the BEER algorithm, this section presents the detection of both the beaming and the ellipsoidal modulations in two different *Kepler* light curves, induced by two low-mass companions. The two stars, KIC 08016222 (hereafter K6222) and KIC 010848064 (hereafter K8064), were found by the BEER algorithm, applied to the 11 249 brightest stars in the *Kepler* public light curves data base (<http://archive.stsci.edu/kepler/>), with available stellar mass and radius estimate. In both the light curves BEER detected periodic modulations, which we attributed in both the cases to variations induced by a low-mass companion estimated, up to $\sin i$, at $\sim 70 M_{\text{Jup}}$. We chose to give these two examples to demonstrate the precision of the *Kepler* mission, which allows detecting with high significance a companion with mass that could be in the lower end of the stellar mass range.

Fig. 3 shows the obtained *Kepler* flux variation of the two stars, each of which is divided by its own mean flux. The light curves include only the Q1 released data, which lasted for 33 days, from 2009 May 13 until 2009 June 15.

In both the light curves one can see a clear periodic modulation superposed on a long-term variability of the stellar flux. Fig. 4 shows the BEER periodograms of the two stars, using the cleaned detrended light curves (see Section 3.1). Both the periodograms show a prominent peak, indicating the presence of a low-mass companion.

Fig. 5 presents the likelihood function of the two stars for the best period found by the periodogram. The likelihood factor, based on equation (14), is 0.99 and 0.97 for K8064 and K6222, respectively, implying that the detected periodic modulation *could* have been induced by a low-mass companion. Fig. 6 presents the folded cleaned light curves, with phase zero defined to coincide with t_{conj} found by our algorithm for each star, together with the fitted BEER model.

Table 1 presents some details of the primaries of the two stars – the estimated mass and radius and their *Kepler* magnitudes (<http://archive.stsci.edu/kepler/>) – and presents the periods and derived amplitudes of the three effects found by the BEER algorithm for the two systems. It also gives the derived masses of the unseen companions and the expected amplitude of the RV modulation.

One can see in Table 1 that the relative strength of the beaming and the ellipsoidal effects is quite different in the two stars. While for K8064 the derived amplitude of the ellipsoidal effect is larger than that of the beaming modulation, in the case of K6222, the derived beaming effect is almost three times the ellipsoidal modulation. This difference changes the appearance of the folded light curves. This is so because the ellipsoidal effect is symmetric around phase 0.5 while the beaming effect is antisymmetric. Therefore, the shape of the folded light curve of K8064 looks almost symmetric while in the case of K6222 the symmetric appearance is completely lost.

The different ratio of the two amplitudes is rooted in equation (12), which shows that this ratio depends on the stellar parameters of the primary, on the stellar radius to the third power in particular, and on the orbital period. As the *Kepler* estimate of the radius of K8064 is larger than that of K6222 and the derived orbital period is shorter, we expect the amplitude ratio of the two effects to be different for the two stars.

We opt not to give in this paper error estimates of the derived RV amplitudes and the inferred companion masses. Although the formal error of the RV amplitude can be derived from the error on the beaming amplitude, the true error is much larger, as we have to include the error coming from the inaccuracy of determining the orbital phase. This requires a further analysis, which we defer to the paper that presents our analysis of all the *Kepler* light curves (Faigler & Mazeh et al., in preparation). The companion mass error is even lesser known, as it depends not only on the amplitudes of the beaming and ellipsoidal effects, but also on the stellar primary mass, which is not well known at this stage. When we obtain spectra of the stars, we can better estimate the primary masses and give better constraints on the companion masses.

For both the stars, the detection of the ellipsoidal and the beaming modulations was highly significant. The reflection effect, on the other hand, was less secure, as the amplitude of the detected modulations was only five and three times their respective formal errors (see the discussion in the previous paragraph). However, as the two main effects were significantly detected, we estimated these detections as being secure, and considered these stars as candidates for hosting a low-mass companion. In a separate paper (Faigler & Mazeh et al., in preparation) we present RV observations that confirm the existence of the two low-mass companions, and demonstrate a good agreement between the BEER predicted period and the velocity amplitude, and the RV ones.

The analysis of K8064 and K6222 presented here was based on Q1 data only. After the BEER analysis and the performance of the RV observations that confirmed the photometric detection, the *Kepler* Q2 data were released. The Q2 light curves, with a time-span with an additional 120 d, confirmed the detection of the photometric modulation. In particular, the newly derived photometric periods for both the stars were consistent with the present photometric periods

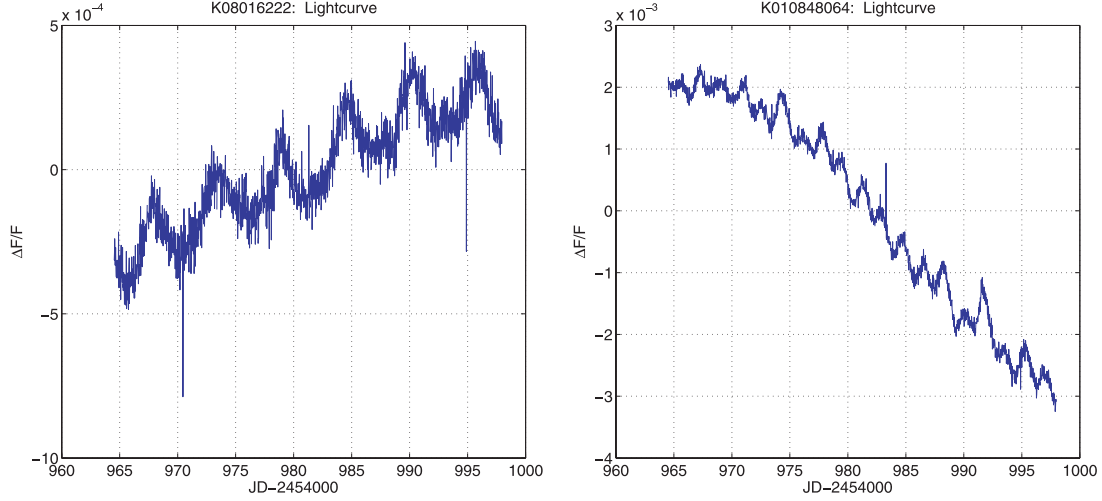
3926 *S. Faigler and T. Mazeh*


Figure 3. The original Q1 *Kepler* light curves of K6222 and K8064. The flux variation of each star is divided by its own mean. Left: K6222. Right: K8064. (Note the scale difference between the two panels.)

and the RV ones. The whole photometric data and RV measurements will be presented in the coming paper (Faigler & Mazeh et al., in preparation). Here we present only the Q1 data and analysis, to show how we actually discovered the two stars, in order to demonstrate the potential of the BEER algorithm.

5 DISCUSSION

We presented here a simple algorithm to detect candidates for low-mass *non-transiting* companions, using the *Kepler* and *CoRoT* light curves. The algorithm searches for the beaming effect, together with the ellipsoidal and the reflection modulations. The algorithm uses our prior knowledge of the stellar mass and radius, and the theory of tidal and beaming modulations, to verify that the ratio between the amplitudes of the beaming and ellipsoidal effects is as expected, and that the three effects have the correct relative phases. We expect the amplitudes of the effect to be of the order of 10–1000 ppm.

At the level of precision needed for this work, stellar activity will contaminate the signal, and worse yet, it will do so at a time-scale that is comparable to the signals of interest, i.e. the orbital period. The associated flux modulations due to star-spots can easily be larger than the expected beaming/ellipsoidal/reflection signal, and since the orbital period of the candidate is not known before time, variations in the stellar rotation period can easily be of the correct duration to confound the BEER method. Therefore the BEER method can find only *candidates*, and RV observations are absolutely required for any confirmation. This is similar to transiting searches, where RV follow-up measurements are crucial. To estimate statistically the yield of the BEER algorithm, the algorithm can be run on subsets of the data. RV follow-up observations of the candidates found in the subsets can help in the determination of the false alarm rate as a function of spectral type and magnitude.

The present version of the algorithm searches for a small-mass companion with a circular orbit. Obviously, an eccentric orbit will

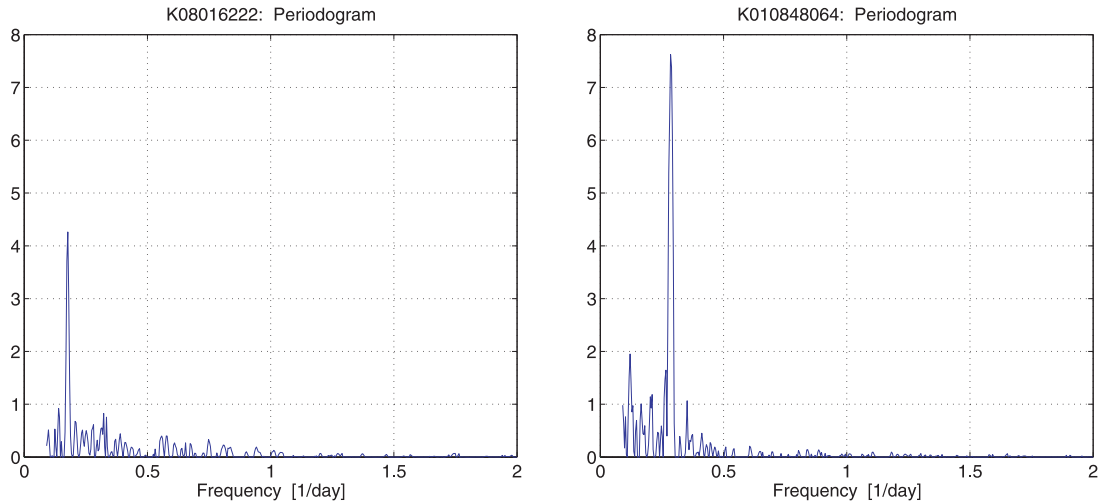


Figure 4. The derived periodograms of the BEER algorithm for the cleaned detrended light curves. Left: K6222. Right: K8064.

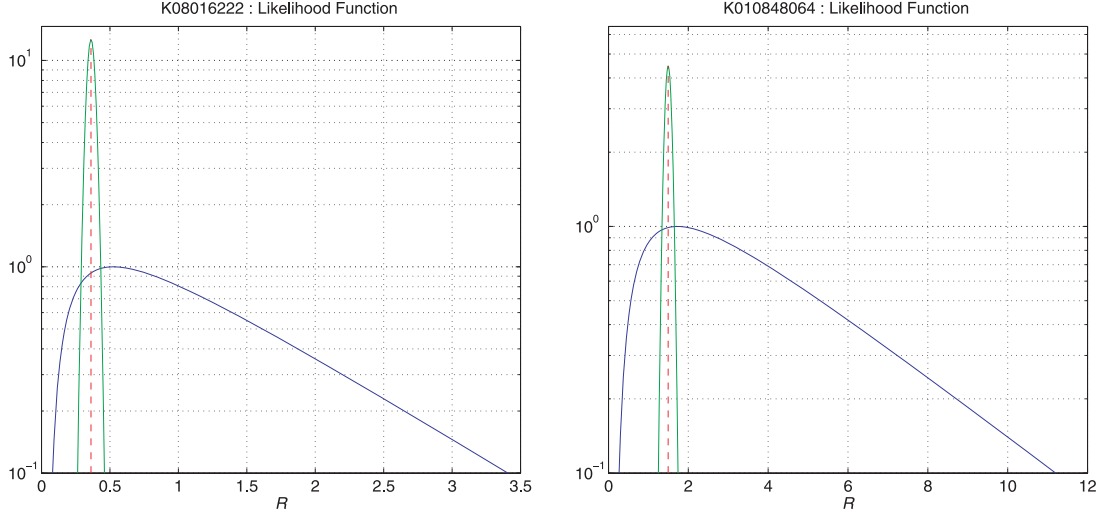


Figure 5. The likelihood function of the expected value of \mathcal{R}_{exp} (blue) and the probability distribution of the observed value of \mathcal{R}_{obs} (green), for the two examples. Left: K6222. Right: K8064. (Note the scale difference between the two panels.)

complicate the analysis, introducing higher harmonics of the orbital frequency. The RV modulation of an eccentric orbit is a well-understood effect, but the ellipsoidal modulation has still to be modelled carefully. Therefore, we assume in our analysis that the eccentricity contribution is small and we leave a more thorough analysis to the next stage of the development of the algorithm.

The two examples presented here demonstrated the potential of the *Kepler* light curves. The detection was done by using only the *Kepler* Q1 data, with a time-span of only 33 d. We note that the detections were highly significant – the derived amplitudes of the beaming effect in both the stars were of the order of 100 ppm, while the formal errors on the modulation amplitudes were 2 and 5 ppm for K6222 and K8064, respectively (but see the discussion

in the previous section). If we ignore the stellar correlated noise (for its implication, see, for example Pont, Zucker & Queloz 2006), we could expect the efficiency of the BEER algorithm to improve for longer light curves by up to \sqrt{n} , where n is the number of observations. Therefore, we can expect to be able to detect a periodic modulation with an amplitude of a few ppm when we will have access to more of *Kepler* data, at least for stars with the same noise level as that of K6222 and K8064. Thus, it might be possible in the near future to find candidates for planets with mass as small as $5\text{--}10 M_{\text{Jup}}$. Mazeh & Faigler (2010) showed that the *CoRoT* data are also accurate enough to detect the beaming and the ellipsoidal effects induced by a brown-dwarf companion.

The long time-span of *Kepler* observations has one more advantage. If an analysis discovers an interesting candidate, follow-up

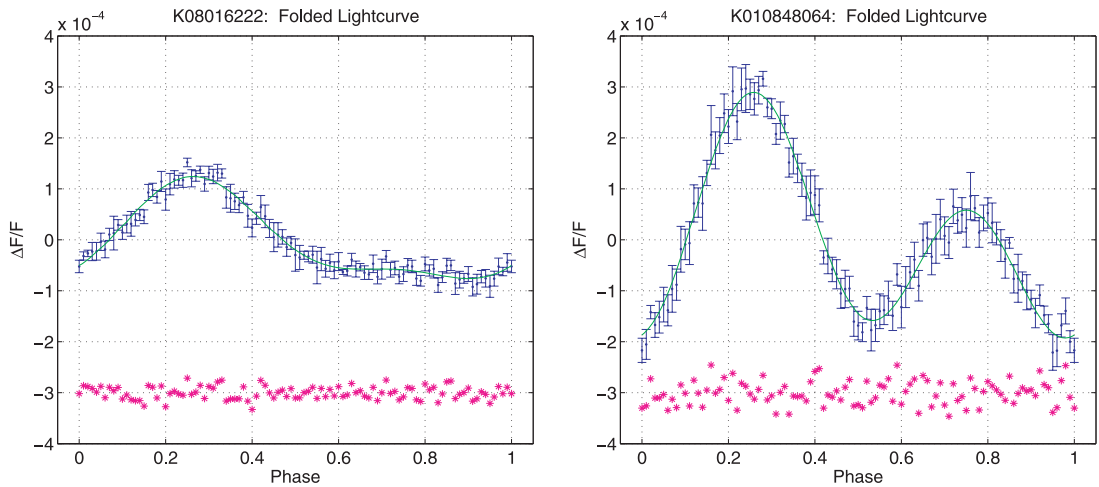


Figure 6. The folded cleaned light curves, binned into 100 bins, with the fitted model. The errors of each bin represent the 1σ scatter of the measurements in each bin. The continuous line presents the BEER model. The residuals from this model are plotted at the bottom of the figure. Both the panels have the same scale. Left: K6222. Right: K8064.

Table 1. The derived parameters of the three effects for K6222 and K8064.

	K6222	K8064	
M_*	1.1	1.2	M_\odot
R_*	1.3	1.5	R_\odot
Kp ^a	11.6	12.1	mag
Period	5.6 ± 0.2	3.53 ± 0.07	d
Ellipsoidal	34 ± 2	170 ± 5	ppm
Beaming	96 ± 2	116 ± 5	ppm
Reflection	11 ± 2	17 ± 5	ppm
$m_2 \sin i$	~70	~70	M_{Jup}
Expected K_{RV}	7	9	km s ⁻¹

^aKp is the stellar Kepler magnitude.

RV measurements of this candidate can be obtained while the *Kepler* observations are still going on. This will enable the observer to compare not only the amplitude and period of the photometric beaming modulation with the RV observations, but also the phase of the detected beaming effect with the RV phase, confirming the existence of the low-mass companion with only very few RV observations. Furthermore, if enough RV measurements were obtained and an independent RV phase can be established, comparing the phase of the follow-up RV observations with that of the ellipsoidal modulation can give us some access to a possible lag between the two, which might indicate how the star is lagging after the tidal force has been exerted by its companion.

The attractiveness of the proposed approach is based on the fact that we have at hand of the order of a quarter of a million light curves (*CoRoT* and *Kepler* together) with precision high enough to detect low-mass companions, depending on the stellar brightness. It is almost equivalent of having an RV survey of many thousands of stars with a precision of 1–5 km s⁻¹. This precision is enough to detect short-period low-mass-stellar, brown-dwarf companions, and even sometimes massive planets. Our simulations indicate that in the *Kepler* Q1 data we can detect about 30 per cent of the brown-dwarfs with 40 M_{Jup} for stars with a magnitude between 12 and 13 and stellar radii smaller than 3 R_\odot (see Fig. 2). We might expect that when we have at hand 3 years of *Kepler* data, with a time-span of ~1000 d instead of ~30 d, our detection threshold will improve by $\sim \sqrt{1000/30} \simeq 5$. This might be equivalent to having a modulation of $5 \times 40 M_{\text{Jup}}$ star in the present data set. Consequently, we might expect that we will be able to detect 75 per cent of the brown-dwarf secondaries of that sample. In the upcoming papers (Faigler & Mazeh et al., in preparation) we list all the candidates found in the *CoRoT* and the *Kepler* data. These candidates, after confirmed, will increase the number of known low-mass-stellar/brown-dwarf companions and even of massive planets.

The approach presented here could have been conceived only because of the vision of Loeb & Gaudi (2003) and Zucker et al. (2007), who anticipated such detections to happen well before the launch of *CoRoT* and *Kepler*. We feel deeply indebted to the authors of these two papers and to the teams of the *CoRoT* and *Kepler* satellites, who built and are maintaining these missions, enabling us to search and analyse their unprecedented photometric data.

ACKNOWLEDGMENTS

We are indebted to Shay Zucker for helpful discussions and suggestions. We thank Dave Latham and Avi Shporer for a careful reading of a previous version of the paper and illuminating comments. We thank the anonymous referee whose comments and suggestions are highly appreciated.

All the photometric data presented in this paper were obtained from the Multimission Archive at the Space Telescope Science Institute (MAST). STScI is operated by the Association of Universities for Research in Astronomy, Inc., under NASA contract NAS5-26555. Support for MAST for non-*HST* data is provided by the NASA Office of Space Science via grant NNX09AF08G and by other grants and contracts.

This research was supported by the Israel Science Foundation (grant no. 655/07).

REFERENCES

- Ahmed N. T., Natarajan T., Rao K. R., 1974, *IEEE Trans. Comput.*, 90
 Aigrain S., Favata F., Gilmore G., 2004, *A&A*, 414, 1139
 Auvergne M. et al., 2009, *A&A*, 506, 411
 Baglin A. et al., 2006, 36th COSPAR Sci. Assembly, 36, 3749
 Borucki W. J. et al., 2010, *Sci*, 327, 977
 Carter J. A., Rappaport S., Fabrycky D., 2011, *ApJ*, 728, 139
 Cowan N. B., Agol E., 2011, *ApJ*, 726, 82
 Deleuil M. et al., 2008, *A&A*, 491, 889
 Drake A. J., 2003, *ApJ*, 589, 1020
 For B.-Q. et al., 2010, *ApJ*, 708, 253
 Harrison T. E., Howell S. B., Huber M. E., Osborne H. L., Holtzman J. A., Cash J. L., Gelino D. M., 2003, *AJ*, 125, 2609
 Knutson H. A. et al., 2007, *Nat*, 447, 183
 Koch D. G. et al., 2010, *ApJ*, 713, L79
 Loeb A., Gaudi B. S., 2003, *ApJ*, 588, L117
 Maxted P. F. L., Marsh T. R., North R. C., 2000, *MNRAS*, 317, L41
 Maxted P. F. L., Marsh T. R., Heber U., Morales-Rueda L., North R. C., Lawson W. A., 2002, *MNRAS*, 333, 231
 Mazeh T., 2008, *EAS Publ. Series*, 29, 1
 Mazeh T., Faigler S., 2010, *A&A*, 521, L59
 Morris S. L., 1985, *ApJ*, 295, 143
 Pál A. et al., 2008, *ApJ*, 680, 1450
 Pont F., Zucker S., Queloz D., 2006, *MNRAS*, 373, 231
 Reed M. D. et al., 2010, *Ap&SS*, 329, 83
 Rouan D., Baglin A., Copet E., Schneider J., Barge P., Deleuil M., Vuillemin A., Léger A., 1998, *Earth Moon Planets*, 81, 79
 Rowe J. F. et al., 2008, *ApJ*, 689, 1345
 Rowe J. F. et al., 2010, *ApJ*, 713, L150
 Rybicki G. B., Lightman A. P., 1979, *Radiative Processes in Astrophysics*. Wiley, New York
 Shporer A., Mazeh T., 2006, *MNRAS*, 370, 1429
 Snellen I. A. G., de Mooij E. J. W., Albrecht S., 2009, *Nat*, 459, 543
 van Kerkwijk M. H., Rappaport S. A., Breton R. P., Justham S., Podsiadlowski P., Han Z., 2010, *ApJ*, 715, 51
 Welsh W. F., Orosz J. A., Seager S., Fortney J. J., Jenkins J., Rowe J. F., Koch D., Borucki W. J., 2010, *ApJ*, 713, L145
 Zucker S., Mazeh T., Alexander T., 2007, *ApJ*, 670, 1326

This paper has been typeset from a $\text{\TeX}/\text{\LaTeX}$ file prepared by the author.

SEVEN NEW BINARIES DISCOVERED IN THE *KEPLER* LIGHT CURVES THROUGH THE BEER METHOD
CONFIRMED BY RADIAL-VELOCITY OBSERVATIONSS. FAIGLER¹, T. MAZEH¹, S. N. QUINN², D. W. LATHAM², AND L. TAL-OR¹¹ School of Physics and Astronomy, Raymond and Beverly Sackler Faculty of Exact Sciences, Tel Aviv University, Tel Aviv 69978, Israel² Harvard-Smithsonian Center for Astrophysics, 60 Garden St., Cambridge, MA 02138, USA

Received 2011 August 25; accepted 2011 December 9; published 2012 February 6

ABSTRACT

We present seven newly discovered *non-eclipsing* short-period binary systems with low-mass companions, identified by the recently introduced BEER algorithm, applied to the publicly available 138-day photometric light curves obtained by the *Kepler* mission. The detection is based on the beaming effect (sometimes called Doppler boosting), which increases (decreases) the brightness of any light source approaching (receding from) the observer, enabling a prediction of the stellar Doppler radial-velocity (RV) modulation from its precise photometry. The BEER algorithm identifies the BEaming periodic modulation, with a combination of the well-known Ellipsoidal and Reflection/heating periodic effects, induced by short-period companions. The seven detections were confirmed by spectroscopic RV follow-up observations, indicating minimum secondary masses in the range 0.07–0.4 M_{\odot} . The binaries discovered establish for the first time the feasibility of the BEER algorithm as a new detection method for short-period non-eclipsing binaries, with the potential to detect in the near future non-transiting brown-dwarf secondaries, or even massive planets.

Key words: binaries: spectroscopic – brown dwarfs – methods: data analysis – planets and satellites: detection

Online-only material: color figures

1. INTRODUCTION

In a recent paper, Faigler & Mazeh (2011) presented a new way to discover short-period non-eclipsing binaries with low-mass companions by using highly precise photometric light curves obtained by space missions such as *CoRoT* and *Kepler* (Rouan et al. 1998; Baglin et al. 2006; Borucki et al. 2010). The algorithm, BEER, based on an idea suggested by Loeb & Gaudi (2003) and Zucker et al. (2007), searches for the beaming effect, sometimes called Doppler boosting, induced by stellar radial motion. This effect causes an increase (decrease) of the brightness of any light source approaching (receding from) the observer (Rybicki & Lightman 1979), on the order of $4v_r/c$, where v_r is the radial velocity (RV) of the source and c is the velocity of light. Therefore, periodic modulation of the stellar velocity due to a companion in a binary orbit will produce a corresponding periodic beaming modulation of the stellar photometry.

For short-period binaries the beaming effect is extremely small, on the order of 100–300 ppm (parts per million). Therefore the effect has become relevant only recently, when *CoRoT* and *Kepler*—the two presently operating satellites that search for transiting exoplanets—started producing hundreds of thousands of uninterrupted light curves with high precision (Auvergne et al. 2009; Koch et al. 2010).

As predicted, several studies detected the beaming effect in eclipsing binaries and transiting planets, for which the orbital period was well established from the space-obtained light curves (van Kerkwijk et al. 2010; Rowe et al. 2010; Carter et al. 2010; Mazeh & Faigler 2010; Bloemen et al. 2011; Kipping & Spiegel 2011). Yet, space mission data can yield much more. Evidence of the binarity of a stellar system can be found from detecting the beaming effect without any eclipse or transit (Loeb & Gaudi 2003; Zucker et al. 2007). However, the beaming modulation by itself might not be enough to render a star a good binary

candidate, as periodic modulations could be produced by other effects, stellar variability in particular (Aigrain et al. 2004).

The BEER detection algorithm (Faigler & Mazeh 2011), therefore, searches for stars that show in their light curves a combination of the BEaming effect with two other effects induced by the presumed companion—the Ellipsoidal and the Reflection modulation. The ellipsoidal variation (Morris 1985) is due to the tidal distortion of each component by the gravity of its companion (see a review by Mazeh 2008), while the reflection/heating variation (referred to herein as the reflection modulation) is induced by the luminosity of each component that falls only on the close side of its companion (Vaz 1985; Wilson 1990; Maxted et al. 2002; Harrison et al. 2003; For et al. 2010; Reed et al. 2010). Detecting the beaming effect together with the ellipsoidal and reflection modulations, with the expected relative amplitudes and *phases* in particular, can suggest the presence of a small non-transiting companion.

Just as in transit searches, the candidates found by the BEER algorithm have to be followed by RV observations in order to confirm the existence of the low-mass companion and to reject other possible interpretations of the photometric modulation.

This paper presents the discovery of the first seven new binaries with low-mass secondaries, in the range 0.07–0.4 M_{\odot} , detected by using the BEER algorithm and confirmed by RV spectroscopic follow-up measurements. Section 2 presents the photometric analysis of the *Kepler* light curves, Section 3 provides the details and results of the RV observations, Section 4 summarizes and compares the results of the photometric analysis and the RV measurements, and Section 5 discusses the implications of, and conclusions from, the findings of this paper.

2. PHOTOMETRIC ANALYSIS

We used the publicly available *Kepler* raw light curves of the Q0, Q1, and Q2 quarters, spanning 138 days. To avoid

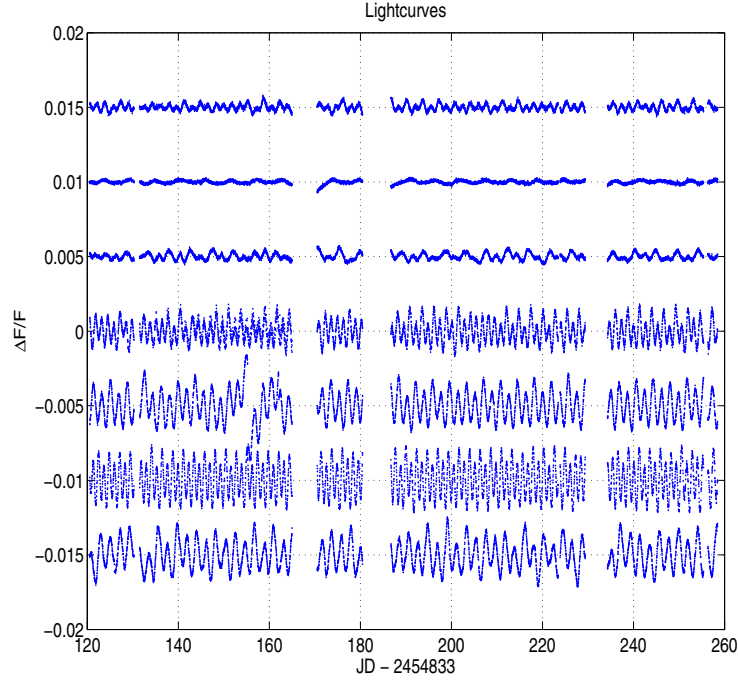


Figure 1. Light curves of the seven detections, after outlier removal and long-term detrending. Top to bottom: K10848064, K08016222, K09512641, K07254760, K05263749, K04577324, and K06370196. For clarity, each light curve was shifted by 5000 ppm relative to the previous one. The periodic modulation can be seen in all seven light curves. The light curves show several discontinuities: end of Q0 at day 131, end of Q1 around day 166, Q2 first safe mode event at day 183, and Q2 second safe mode event at day 232. In addition there is a single discontinuity at day 155 in the K05263749 light curve.

(A color version of this figure is available in the online journal.)

Table 1
Coordinates, Magnitudes, Stellar Properties, and Photometric Analysis Results of the Seven Candidates

	K10848064	K08016222	K09512641	K07254760	K05263749	K04577324	K06370196
R.A.	19:01:21.24	19:06:48.03	18:58:39.91	18:42:28.78	19:12:59.00	19:42:35.91	19:35:00.36
Decl.	48:16:32.90	43:48:32.90	46:08:52.80	42:49:31.90	40:26:42.30	39:38:00.80	41:47:59.60
K_p^a (mag)	12.13	11.65	11.66	12.04	11.53	11.98	11.97
R^a (R_\odot)	1.5	1.3	1.7	1.5	1.9	1.3	2.1
M^b (M_\odot)	1.2	1.1	1.2	1.2	1.3	1.2	1.3
Photometry results							
Period (days)	3.49 ± 0.01	5.60 ± 0.02	4.65 ± 0.02	2.66 ± 0.01	3.73 ± 0.01	2.33 ± 0.01	4.23 ± 0.01
Ellipsoidal (ppm)	201 ± 3	30 ± 2	172 ± 10	845 ± 7	1222 ± 5	1489 ± 4	1210 ± 10
Beaming (ppm)	118 ± 3	97 ± 2	185 ± 5	356 ± 6	358 ± 5	436 ± 4	382 ± 7
Reflection (ppm)	0 ± 3	6 ± 2	36 ± 4	150 ± 6	158 ± 5	245 ± 4	174 ± 7
Cleaned data rms (ppm)	204	106	227	807	1184	1408	1141
Residuals rms (ppm)	128	68	113	268	200	168	328

Notes.

^a From Kepler Input Catalog.

^b Calculated from Kepler Input Catalog $\log g$ and R .

systematic variations, we ignored all data points within 1 day after the beginning of Q2, and all data points within 1 day before, to 3 days after, each of the two safe mode events in Q2. We also corrected two systematic jumps at *Kepler* time (JD – 2,454,833) of 200.32 and 246.19 days. We then applied the BEER algorithm to 14,685 stars brighter than 13th mag, with Kepler Input Catalog (Brown et al. 2011) radius smaller than $3 R_\odot$, calculating the BEER periodogram (Faigler & Mazeh 2011) with period range of 0.5–20 days for each star. Next, we identified the periodograms whose highest peak was at least three times higher than the next highest one. For these stars we used the peak period to estimate the system secondary

mass and radius, assuming the periodicity is induced by a secondary star. We then selected 25 candidates with secondary mass smaller than $0.5 M_\odot$ and implied albedo smaller than 0.4, suggesting a significant probability for a low-mass companion. These candidates were then followed by RV observations, which we describe in detail in the next section. In a forthcoming paper, we will report on the false alarm cases and analyze the false alarm frequency of our candidates. Here, we report on the first seven clear detections.

Table 1 lists for each of the seven stars its coordinates, the stellar properties estimates from the Kepler Input Catalog (Brown et al. 2011), the photometric periods and amplitudes

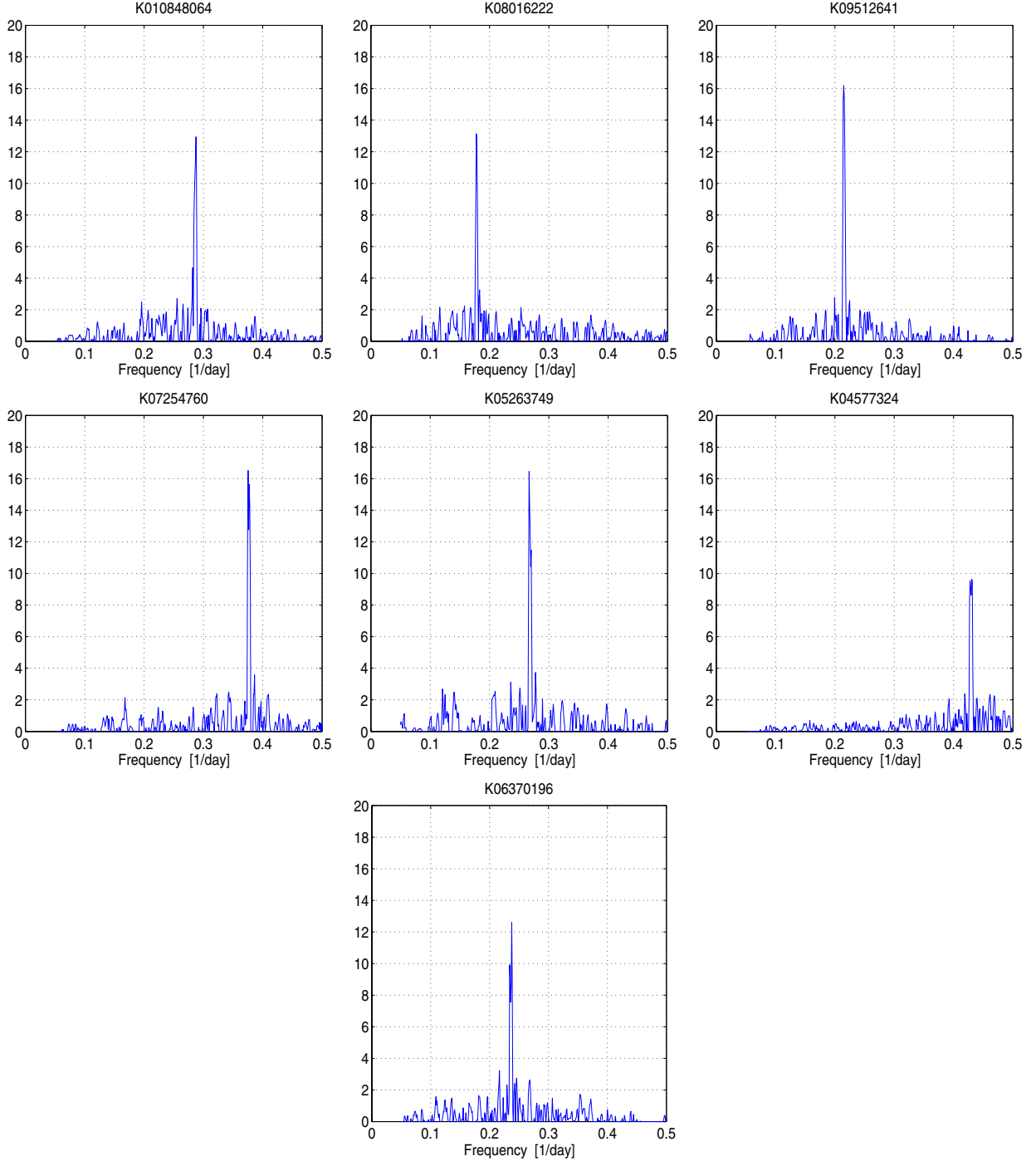


Figure 2. BEER periodograms of the seven candidates. The peak frequency corresponds to the suspected orbital period. The periodograms were calculated for the period range 0.5–20 days. For clarity, only the period range 2–20 days is plotted, since no significant peak was found for periods smaller than 2 days in any of the periodograms. The periodograms are normalized so that the rms of the 100 noise points on two sides of the peak (50 on each side) is set to one. (A color version of this figure is available in the online journal.)

of the three effects found by the BEER algorithm, and the rms of the data before and after subtraction of the BEER model.

We order the stars according to the detected RV amplitude, presented in the next section. Figure 1 presents the “cleaned”

(Mazeh & Faigler 2010; Faigler & Mazeh 2011) photometric data of the seven detections, Figure 2 presents the BEER periodograms for the detections, and Figure 3 shows the light curves folded with the detected period. In fact, the quality of the *Kepler* data is so high that the periodic modulation can be seen

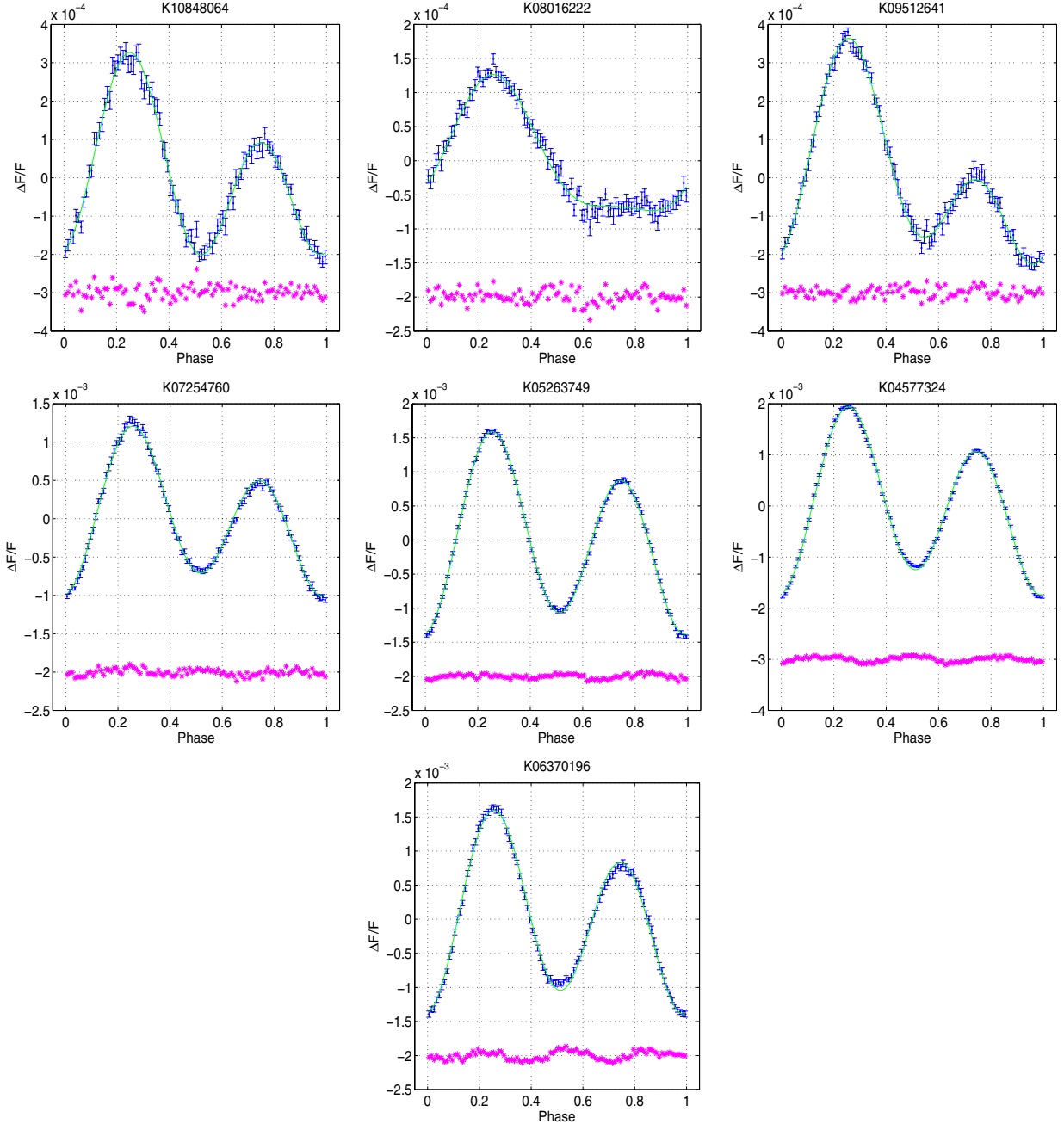


Figure 3. Folded cleaned light curves, binned into 100 bins, of the seven candidates. Phase zero is when the presumed companion is closest to the observer, while phase 0.5 is when the primary is closest to the observer. The errors of each bin represent the 1σ estimate of the bin average value. The line presents the BEER model. The model residuals are plotted at the bottom of each figure.

(A color version of this figure is available in the online journal.)

directly from the cleaned data, plotted in Figure 1, even without consulting the BEER periodogram.

It is interesting to compare the shape of the BEER modulation of the seven candidates, presented in Figure 3. In six of them the two peaks, at phase of 0.25 and 0.75, are similar, although the latter is somewhat smaller, due to the beaming effect (Faigler & Mazeh 2011). In one case, K08016222, the second peak completely disappeared, because in this case the

beaming amplitude is more than three times higher than that of the ellipsoidal, while for the rest of the candidates the ellipsoidal amplitude is significantly higher than the beaming amplitude. This is a clear result of the long orbital period and small stellar radius of this system, relative to the other systems, since the ellipsoidal amplitude to beaming amplitude ratio is proportional to $R_*^3/P_{\text{orb}}^{5/3}$ (Faigler & Mazeh 2011; Zucker et al. 2007).

Table 2
Spectra-derived Stellar Properties of the Seven Binaries

	K10848064	K08016222	K09512641	K07254760	K05263749	K04577324	K06370196
T_{eff} (K)	6209 ± 131	5919 ± 128	6348 ± 214	6377 ± 133	6328 ± 119	6515 ± 145	6213 ± 168
$\log g$ (dex)	3.68 ± 0.16	4.29 ± 0.14	4.04 ± 0.23	4.04 ± 0.23	3.54 ± 0.14	3.71 ± 0.14	3.91 ± 0.13
$[m/H]$ (dex)	-0.24 ± 0.11	-0.14 ± 0.11	-0.37 ± 0.15	-0.04 ± 0.11	-0.21 ± 0.10	-0.08 ± 0.11	-0.26 ± 0.16
$v \sin i$ (km s $^{-1}$)	14.26 ± 0.45	3.37 ± 0.24	9.47 ± 0.24	14.96 ± 0.52	21.50 ± 0.16	28.90 ± 0.36	20.93 ± 0.45

3. RADIAL-VELOCITY OBSERVATIONS

The RV observations were performed between 2010 September 25 and 2011 June 15 with the Tillinghast Reflector Echelle Spectrograph (TRES; Fűrész 2008) mounted on the 1.5 m Tillinghast Reflector at the Fred Lawrence Whipple Observatory operated by the Smithsonian Astrophysical Observatory on Mount Hopkins in Southern Arizona, using the medium fiber at a spectral resolution of 44,000, covering a spectral range from 385 to 910 nm. Exposures of a thorium–argon hollow-cathode lamp immediately before and after each exposure were used for wavelength calibration. The spectra were extracted and rectified to intensity versus wavelength using standard procedures developed by Lars Buchhave (Buchhave et al. 2010).

To derive precise relative radial velocities, we performed a cross-correlation between each observed spectrum and a template spectrum constructed by shifting and co-adding all the observed spectra. In addition to the template constructed by shifting and co-adding all the observed spectra, we also tried using the strongest individual exposure of each object as the observed template. The two approaches gave essentially indistinguishable results, with slightly better residuals from the orbital fits for the shifted and co-added template. We also derived absolute velocities using the library of synthetic templates and found the same orbits, although with somewhat larger residuals.

We did not include spectral orders that were significantly contaminated by telluric lines from Earth’s atmosphere, nor did we include the bluest orders with the lowest signal-to-noise ratio and a few red orders with known problems. The error of each relative velocity was estimated using the standard deviation of the velocities from the 21 individual orders, but the velocities themselves were derived by first co-adding the correlation functions from the 21 orders to get a natural weighting of the contribution from each order.

Using the shifted and co-added template can distort the cross-correlation peak because the noise in each spectrum correlates with the same noise that is still present in the averaged template, and therefore can lead to underestimated uncertainties of the velocities. To correct this effect we later inflated the uncertainties of the orbital elements (see χ_{red}^2 discussion below).

We used a library of synthetic spectra, calculated by John Laird for a grid of Kurucz model atmospheres, using a line list developed by Jon Morse (Carney et al. 1987; Latham et al. 2002), to estimate values for the effective temperature, surface gravity, metallicity, and rotational velocity of the seven primaries. This was done by cross-correlating each co-added observed template spectrum against a grid of synthetic templates surrounding the one that gave the best correlation. Our library of synthetic spectra has a spacing of 250 K in effective temperature, T_{eff} ; 0.5 in \log surface gravity, $\log g$; 0.5 in the \log of the metallicity compared to the Sun, $[m/H]$; and has a progressive spacing for rotational velocity, v_{rot} . Because the grid is coarse, we used the correlation peak heights to interpolate between grid points

to arrive at a more precise classification. Three TRES spectral orders overlap with the synthetic spectra, so we performed this cross-correlation and interpolation in each order. The mean values, weighted by the cross-correlation peak height in each order, and rms errors are reported in Table 2. Note that because of the degeneracies between T_{eff} , $\log g$, and $[m/H]$ in the stellar spectra, correlated systematic errors may dominate. For this reason, and based on our experience in other surveys, we have inflated the errors by adding 100 K in T_{eff} and 0.1 dex in $\log g$ and $[m/H]$ in quadrature to the formal order-to-order rms errors.

The relative velocities were adjusted by a constant offset to a system of absolute velocities using observations of the nearby IAU Radial Velocity Standard Star HD 182488, whose absolute velocity was assumed to be -21.508 km s $^{-1}$. This adjustment utilized our library of synthetic templates, from which we picked the synthetic template that gave the best match to the observations of each star in the spectral order centered on the Mg b feature near 518 nm. This approach should avoid the problem of possible template mismatch between the various target stars and HD 182488. The uncertainty in the zero point of our absolute velocities is probably limited by the uncertainty in the absolute velocity of HD 182488, which could be as large as 100 m s $^{-1}$. Table 3 lists the RV measurements and their uncertainties.

For all seven candidates discussed here the first RV measurements showed clear variability. We therefore obtained enough RVs to allow orbital solutions completely independent of the BEER analysis. To determine the orbital elements of each target, independent of the BEER results, we ran a Markov Chain Monte Carlo (MCMC) analysis of the radial velocities. We adopted values for the epoch (T), period (P), systemic velocity (γ), orbital semi-amplitude (K), eccentricity (e), and argument of periastron (ω) corresponding to the median values of the posterior distributions. The errors listed in the tables are those corresponding to the 16th and 84th percentiles of the posterior distributions. The reported error on γ , however, includes contributions both from the formal error from the MCMC posterior and from the uncertainty in the TRES absolute zero-point offset.

When the orbit is circular, the epoch reported is T_{max} , the time of maximum velocity, and when the orbit is eccentric, we report T_{peri} , the time of periastron passage. In six of the seven cases, either the orbital phase coverage was not sufficient to adequately constrain the eccentricity or e was statistically indistinguishable from zero. In these cases, we fixed $e = 0$ and reran the MCMC chains, adopting T_{max} , P , γ , and K from this solution. In one case, K08016222, the orbital phase coverage is good and e is significantly non-zero.

Figure 4 shows the RV follow-up measurements for each of the seven binaries, folded with the period found, and Table 4 lists the orbital elements derived. The table also lists χ_{red}^2 , the reduced χ^2 of the model, and the time span of the observations. For two binaries the derived χ_{red}^2 value is close to unity, as expected, but for the others its value is relatively large. This

Table 3
Radial Velocities of the Seven Binaries

Time (HJD–2,455,000)	RV (m s ⁻¹)	σ (m s ⁻¹)	Time (HJD–2,455,000)	RV (m s ⁻¹)	σ (m s ⁻¹)
K10848064:			K07254760:		
464.710256	-8835	119	694.814729	37083	39
469.624378	-17974	76	695.834208	-11894	46
488.634305	-16743	77	697.807122	15727	61
489.574441	-6552	123	699.779976	46148	83
490.617670	-17742	83	702.796583	36412	47
498.599389	-23508	57	703.815335	-11560	54
513.639601	-9108	170	704.799619	39179	51
692.888788	-13130	124	705.802918	14063	89
722.832949	-14423	43	K05263749:		
723.863233	-7328	56	694.829973	20947	69
724.857438	-21205	28	696.825053	13787	141
K08016222:			697.826976	45095	68
465.787007	-31819	63	699.974074	-12159	61
466.613973	-37012	39	701.980887	34841	87
467.723417	-33482	96	705.958593	23622	73
469.613641	-18312	42	722.851562	10492	63
485.603398	-23367	37	723.875349	45267	46
490.579108	-29588	63	724.846275	10122	75
498.591317	-22720	47	K04577324:		
722.843084	-21815	86	695.982214	-22723	166
K09512641:			697.845760	8912	99
658.935318	6324	22	703.971684	38803	87
669.855208	33915	29	722.871612	46652	99
693.803705	34608	67	723.895443	-22140	103
694.822698	16733	54	724.869757	34694	124
696.815346	17503	50	726.867639	5528	96
697.816773	34761	48	727.847462	33003	91
698.934501	27404	39	K06370196:		
701.814582	24838	40	694.852291	20398	58
702.805990	36143	39	697.835776	-13709	144
703.826109	22562	59	702.968624	22603	41
704.813460	6060	65	722.861284	-35084	114
705.813161	11855	43	723.884266	17354	76
			724.826295	8740	72
			726.857187	-47080	95
			727.797595	4696	132

Table 4
Orbital Model Elements of the Seven Binaries

	K10848064	K08016222	K09512641	K07254760	K05263749	K04577324	K06370196
$T_{\max} - 2,455,000$ (HJD)	465.1289 ± 0.0060	464.6288 ^a ± 0.0029	642.3690 ± 0.0052	702.4395 ± 0.0126	466.7071 ± 0.0124	466.7005 ± 0.0079	698.8374 ± 0.0035
P (days)	3.49318 ± 0.00099	5.60864 ± 0.00017	4.64588 ± 0.00044	2.65642 ± 0.00068	3.72665 ± 0.00019	2.328663 ± 0.000070	4.23371 ± 0.00067
γ (km s ⁻¹)	-15.670 ± 0.219	-28.078 ± 0.048	20.518 ± 0.110	17.092 ± 0.177	13.862 ± 0.060	11.325 ± 0.119	-17.168 ± 0.454
K (km s ⁻¹)	9.107 ± 0.073	9.495 ± 0.018	15.519 ± 0.023	29.024 ± 0.061	31.428 ± 0.040	35.316 ± 0.043	40.222 ± 0.131
e	0 (fixed)	0.0439 \pm 0.0022	0 (fixed)	0 (fixed)	0 (fixed)	0 (fixed)	0 (fixed)
ω (deg)		36.2 \pm 2.6					
χ^2_{red}	11.0	1.0	4.3	11.6	2.6	1.2	12.6
Span (days)	260.1	257.1	46.9	11.0	30.0	31.9	32.9

Note. ^a For K08016222 the T_{\max} value is the time of periastron passage.

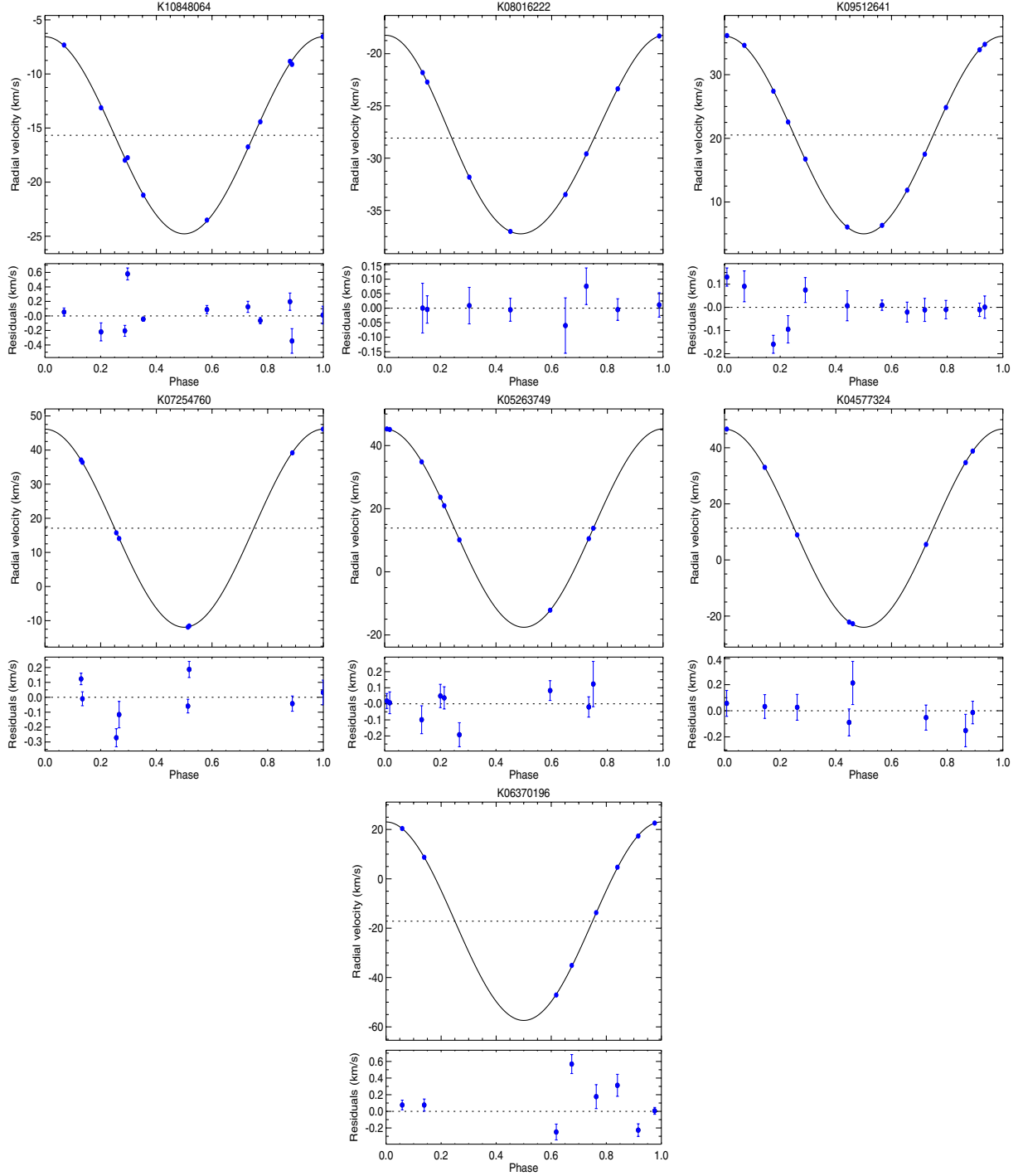


Figure 4. RV measurements of the seven stars folded at the derived orbital period. The line presents the orbital RV model. The residuals are plotted at the bottom of each figure. Note the different scale of the upper and lower panels for each star. The error bars are too small to be seen in the upper panels. (A color version of this figure is available in the online journal.)

could indicate either that for those binaries our RV uncertainties are underestimated, or that our RV model is too simple, due to some stellar noise, for example. In order to get more realistic uncertainties for the model elements, we inflated the parameter

uncertainties of each target by its $\sqrt{\chi_{\text{red}}^2}$, which is equivalent to inflating the RV errors of that star by the same factor. The resulting uncertainties in the orbital model elements are listed in Table 4.

Table 5
Derived Photometric RV Period and Semi-amplitude Together with RV Observations Period and Semi-amplitude for Each of the Seven Binaries

	K10848064	K08016222	K09512641	K07254760	K05263749	K04577324	K06370196
Photometry results:							
Period (days)	3.49 ± 0.01	5.60 ± 0.02	4.65 ± 0.02	2.66 ± 0.01	3.73 ± 0.01	2.33 ± 0.01	4.23 ± 0.01
α_{beam}	0.944 ± 0.025	1.012 ± 0.023	0.912 ± 0.036	0.921 ± 0.024	0.921 ± 0.022	0.887 ± 0.025	0.936 ± 0.030
K_{beam} (km s ⁻¹)	9.37 ± 0.34	7.19 ± 0.22	15.21 ± 0.72	28.97 ± 0.89	29.14 ± 0.81	36.86 ± 1.10	30.61 ± 1.12
RV results:							
N_{obs}	11	8	12	8	9	8	8
Period (days)	3.49318 ± 0.00099	5.60864 ± 0.00017	4.64588 ± 0.00044	2.65642 ± 0.00068	3.72665 ± 0.00019	2.328663 ± 0.000070	4.23371 ± 0.00067
K_{RV} (km s ⁻¹)	9.107 ± 0.073	9.495 ± 0.018	15.519 ± 0.023	29.024 ± 0.061	31.428 ± 0.040	35.316 ± 0.043	40.223 ± 0.131
Minimum secondary mass (M_{Jup})	76 ± 5	90 ± 6	147 ± 10	222 ± 15	279 ± 19	253 ± 17	376 ± 25

4. RESULTS

Table 5 lists for each of the seven newly discovered binaries the period derived from the photometry, the calculated α_{beam} , the expected RV semi-amplitude, K_{beam} , derived from α_{beam} , and the photometric beaming amplitude. The α_{beam} factor includes one component that originates from the fact that the stellar spectrum is Doppler shifted relative to the observed band. To estimate this factor for each of the seven detected binaries we numerically shifted spectra from the library of Castelli & Kurucz (2004) models that were close to the estimated temperature, metallicity, and gravity of each of the seven stars. The values adopted were derived by interpolation of the α_{beam} values between the available models of the library. The α_{beam} uncertainties were estimated by calculating the interpolated α_{beam} values within the T_{eff} , $\log g$, and $[m/H]$ error ranges. The error on the expected K_{beam} was estimated by combining the photometric beaming amplitude error and the α_{beam} error. The table then reports the number of RV measurements, their derived RV period and semi-amplitude, and the minimal secondary mass, up to $\sin i$. For all cases we *independently* derived the period of the RV modulation, and found it to be consistent with the photometric period, indicating that the orbital period was reliably derived by the BEER algorithm, solely from the photometric data.

In six of the binaries the eccentricity was too small to be derived significantly, so we assumed circular orbits. Because these are short-period stellar binaries, the expected circularization timescale is short, so finding in most cases that $e = 0$ is consistent with our expectations. For K08016222 we find $e = 0.0439 \pm 0.0022$. Interestingly, this is the binary with the longest period, so its lifetime might have been too short to achieve circularization (Mathieu & Mazeh 1988).

Out of the seven binaries, the measured RV amplitudes of five cases were consistent with those predicted by the photometric analysis. For the other two stars, K08016222 and K06370196, the predicted amplitudes were 24% smaller than the observed ones. This could be due to underestimation of the photometric amplitude. Another possible explanation may be an inaccurate translation of the photometric amplitude to the expected RV amplitude, which depends on the assumed stellar spectral type. We need more confirmed binaries to understand this effect.

5. DISCUSSION

The RV observations presented here demonstrate the ability of the BEER algorithm to discover short-period binaries with

minimum secondary masses in the range $0.07\text{--}0.4 M_{\odot}$ in the publicly available *Kepler* data.

The original goal of the *Kepler* and *CoRoT* missions was to search for transiting planets. Such projects are limited to planets with orbital inclinations close to 90° . The serendipitous discoveries of eclipsing binaries in the *Kepler* photometry (Prša et al. 2011) are suffering from the same limitation. The BEER algorithm, on the other hand, is searching for *non-transiting* companions, and therefore can detect many more systems with much lower inclination angles. Searching with BEER is effectively equivalent to performing an RV survey that is not limited to nearly face-on inclinations. Applying the BEER algorithm to the hundreds of thousands of already available light curves of *Kepler* and *CoRoT* is like performing an RV survey of a huge sample that is composed of these stars.

Therefore, we expect BEER to discover many hundreds of new binaries with short periods. Furthermore, whereas in RV studies the actual mass of the companion depends on the unknown inclination angle, detecting *both* the ellipsoidal and the beaming effects will enable BEER to derive, or at least estimate, the mass of the small companion in certain cases. As pointed out by Faigler & Mazeh (2011), this can become possible because the two effects have different dependencies on the orbital inclination, and therefore the derived ratio of the amplitudes of the two effects can, *in principle*, remove the degeneracy between the secondary mass and the inclination.

Obviously, at this stage of the BEER search, detecting a candidate is not enough—the candidates have to be confirmed by follow-up RV observations. However, when we accumulate enough observations we will be able to estimate the false alarm probability, which might be a function of the amplitude of the photometric modulation and the stellar mass, radius, and temperature. Therefore, we will be able to derive the statistical features of the short-period binaries without confirming each detection with RV observations.

The seven cases presented here were based on the *Kepler* Q0–Q2 data. Faigler & Mazeh (2011) suggested that once the full *Kepler* data set is available, we should be able to detect brown-dwarf secondaries and even massive planets. Moreover, the other stellar modulations that contribute now to the false alarm frequency are not expected to be so stable on timescales of years, whereas the three BEER effects are strictly periodic and stable. Therefore, we expect the false alarm frequency to decrease when we have access to longer data sets. The

unprecedentedly large sample size and data quality, together with a knowledge of the false alarm probability, could serve as a tool to study accurately the frequency of low-mass secondaries in short-period binaries on the high- and low-mass ends of the brown-dwarf desert (Raghavan et al. 2010; Udry 2010; Sahlmann et al. 2011).

We are indebted to Shay Zucker and Ehud Nakar for helpful discussions. We thank the anonymous referee for highly illuminating comments and suggestions.

We feel deeply indebted to the team of the *Kepler* mission that enabled us to search and analyze their unprecedentedly accurate photometric data.

All the photometric data presented in this paper were obtained from the Multimission Archive at the Space Telescope Science Institute (MAST). STScI is operated by the Association of Universities for Research in Astronomy, Inc., under NASA Contract NAS5-26555. Support for MAST for non-*HST* data is provided by the NASA Office of Space Science via grant NNX09AF08G and by other grants and contracts.

We thank the *Kepler* mission for partial support of the spectroscopic observations under NASA Cooperative Agreement NNX11AB99A with the Smithsonian Astrophysical Observatory; PI: D. W. L.

This research was supported by the Israel Science Foundation (grant no. 655/07).

Facility: FLWO:1.5m (TRES)

REFERENCES

- Aigrain, S., Favata, F., & Gilmore, G. 2004, *A&A*, **414**, 1139
 Auvergne, M., Bodin, P., Boisnard, L., et al. 2009, *A&A*, **506**, 411
 Baglin, A., Auvergne, M., Boisnard, L., et al. 2006, in 36th COSPAR Scientific Assembly, *Abstract 3749*
 Bloemen, S., Marsh, T. R., Østensen, R. H., et al. 2011, *MNRAS*, **410**, 1787
 Borucki, W. J., Koch, D., Basri, G., et al. 2010, *Science*, **327**, 977
 Brown, T. M., Latham, D. W., Everett, M. E., & Esquerdo, G. A. 2011, *AJ*, **142**, 112
 Buchhave, L. A., Bakos, G. Á., Hartman, J. D., et al. 2010, *ApJ*, **720**, 1118
 Carney, B. W., Laird, J. B., Latham, D. W., & Kurucz, R. L. 1987, *AJ*, **93**, 116
 Carter, J. A., Rappaport, S., & Fabrycky, D. 2011, *ApJ*, **728**, 139
 Castelli, F., & Kurucz, R. L. 2004, arXiv:astro-ph/0405087
 Faigler, S., & Mazeh, T. 2011, *MNRAS*, **415**, 3921
 For, B.-Q., Green, E. M., Fontaine, G., et al. 2010, *ApJ*, **708**, 253
 Fűrész, G. 2008, PhD thesis, Univ. Szeged, Hungary
 Harrison, T. E., Howell, S. B., Huber, M. E., et al. 2003, *AJ*, **125**, 2609
 Kipping, D. M., & Spiegel, D. S. 2011, *MNRAS*, **417**, L88
 Koch, D. G., Borucki, W. J., Basri, G., et al. 2010, *ApJ*, **713**, L79
 Latham, D. W., Stefanik, R. P., Torres, G., et al. 2002, *AJ*, **124**, 1144
 Loeb, A., & Gaudi, B. S. 2003, *ApJ*, **588**, L117
 Mathieu, R. D., & Mazeh, T. 1988, *ApJ*, **326**, 256
 Maxted, P. F. L., Marsh, T. R., Heber, U., et al. 2002, *MNRAS*, **333**, 231
 Mazeh, T. 2008, in Tidal Effects in Stars, Planets and Disks, ed. M.-J. Goupil & J.-P. Zahn, EAS Publications Series, Vol. 29 (Les Ulis, France: EDP Sciences), 1
 Mazeh, T., & Faigler, S. 2010, *A&A*, **521**, L59
 Morris, S. L. 1985, *ApJ*, **295**, 143
 Prša, A., Batalha, N., Slawson, R. W., et al. 2011, *AJ*, **141**, 83
 Raghavan, D., McAlister, H. A., Henry, T. J., et al. 2010, *ApJS*, **190**, 1
 Reed, M. D., Terndrup, D. M., Østensen, R., et al. 2010, *Ap&SS*, **329**, 83
 Rouan, D., Baglin, A., Copet, E., et al. 1998, *Earth Moon Planets*, **81**, 79
 Rowe, J. F., Borucki, W. J., Koch, D., et al. 2010, *ApJ*, **713**, L150
 Rybicki, G. B., & Lightman, A. P. 1979, *Radiative Processes in Astrophysics* (New York: Wiley)
 Sahlmann, J., Ségransan, D., Queloz, D., & Udry, S. 2011, in IAU Symposium 276, The Astrophysics of Planetary Systems: Formation, Structure, and Dynamical Evolution, ed. A. Sozzetti, M. G. Lattanzi, & A. P. Boss (Cambridge: Cambridge Univ. Press), 117
 Udry, S. 2010, in Proc. Conf. In the Spirit of Lyot 2010: Direct Detection of Exoplanets and Circumstellar Disks, ed. A. Boccaletti
 van Kerkwijk, M. H., Rappaport, S. A., Breton, R. P., et al. 2010, *ApJ*, **715**, 51
 Vaz, L. P. R. 1985, *Ap&SS*, **113**, 349
 Wilson, R. E. 1990, *ApJ*, **356**, 613
 Zucker, S., Mazeh, T., & Alexander, T. 2007, *ApJ*, **670**, 1326

BEER ANALYSIS OF *KEPLER* AND *CoRoT* LIGHT CURVES. I. DISCOVERY OF KEPLER-76b: A HOT JUPITER WITH EVIDENCE FOR SUPERROTATIONS. FAIGLER¹, L. TAL-OR¹, T. MAZEH¹, D. W. LATHAM², AND L. A. BUCHHAVE³¹ School of Physics and Astronomy, Raymond and Beverly Sackler Faculty of Exact Sciences, Tel Aviv University, Tel Aviv 69978, Israel² Harvard-Smithsonian Center for Astrophysics, 60 Garden Street, Cambridge, MA 02138, USA³ Niels Bohr Institute, University of Copenhagen, DK-2100 Copenhagen, Denmark

Received 2013 February 18; accepted 2013 April 25; published 2013 June 12

ABSTRACT

We present the first case in which the BEER algorithm identified a hot Jupiter in the *Kepler* light curve, and its reality was confirmed by orbital solutions based on follow-up spectroscopy. The companion Kepler-76b was identified by the BEER algorithm, which detected the BEaming (sometimes called Doppler boosting) effect together with the Ellipsoidal and Reflection/emission modulations (BEER), at an orbital period of 1.54 days, suggesting a planetary companion orbiting the 13.3 mag F star. Further investigation revealed that this star appeared in the *Kepler* eclipsing binary catalog with estimated primary and secondary eclipse depths of 5×10^{-3} and 1×10^{-4} , respectively. Spectroscopic radial velocity follow-up observations with Tillinghast Reflector Echelle Spectrograph and SOPHIE confirmed Kepler-76b as a transiting $2.0 \pm 0.26 M_{\text{Jup}}$ hot Jupiter. The mass of a transiting planet can be estimated from either the beaming or the ellipsoidal amplitude. The ellipsoidal-based mass estimate of Kepler-76b is consistent with the spectroscopically measured mass while the beaming-based estimate is significantly inflated. We explain this apparent discrepancy as evidence for the superrotation phenomenon, which involves eastward displacement of the hottest atmospheric spot of a tidally locked planet by an equatorial superrotating jet stream. This phenomenon was previously observed only for HD 189733b in the infrared. We show that a phase shift of $10:3 \pm 2:0$ of the planet reflection/emission modulation, due to superrotation, explains the apparently inflated beaming modulation, resolving the ellipsoidal/beaming amplitude discrepancy. Kepler-76b is one of very few confirmed planets in the *Kepler* light curves that show BEER modulations and the first to show superrotation evidence in the *Kepler* band. Its discovery illustrates for the first time the ability of the BEER algorithm to detect short-period planets and brown dwarfs.

Key words: binaries: spectroscopic – methods: data analysis – planets and satellites: detection – planets and satellites: individual (KIC 4570949b, Kepler-76b)

Online-only material: color figures

1. INTRODUCTION

CoRoT and *Kepler* have produced hundreds of thousands of nearly uninterrupted high-precision light curves (Auvergne et al. 2009; Koch et al. 2010) that enable detection of minute astrophysical effects. One of these is the beaming effect, sometimes called Doppler boosting, induced by stellar radial velocity (RV). The effect causes a decrease (increase) of the brightness of any light source receding from (approaching) the observer (Rybicki & Lightman 1979) on the order of $4v_r/c$, where v_r is the RV of the source and c is the velocity of light. Thus, periodic variation of the stellar RV due to an orbiting companion produces a periodic beaming modulation of the stellar flux. Loeb & Gaudi (2003) and Zucker et al. (2007) suggested using this effect to identify non-eclipsing binaries and exoplanets in the light curves of *CoRoT* and *Kepler*. The precision of the two satellites is needed because even for short-period binaries with large RV orbital amplitudes, the beaming effect is small, on the order of 100–500 ppm (parts per million).

As predicted, several studies identified the beaming effect in short-period known eclipsing binaries (van Kerkwijk et al. 2010; Rowe et al. 2011; Carter et al. 2011; Kipping & Spiegel 2011; Bloemen et al. 2011, 2012; Breton et al. 2012). Yet, space missions data can be used to identify non-eclipsing binaries through detection of the beaming effect (Loeb & Gaudi 2003; Zucker et al. 2007). However, the beaming modulation by itself might not be enough to identify a binary star, as

periodic modulations could be produced by other effects, stellar variability in particular (e.g., Aigrain et al. 2004).

To overcome this problem, the BEER algorithm (Faigler & Mazeh 2011) searches for stars that show in their light curves a combination of the BEaming effect with two other effects that are produced by a short-period companion—the Ellipsoidal and the Reflection modulations. The ellipsoidal variation (e.g., Morris 1985) is due to the tidal interaction between the two components (see a review by Mazeh 2008), while the reflection/heating variation (referred to herein as the reflection modulation) is caused by the luminosity of each component that falls on the facing half of its companion (e.g., Wilson 1990; Maxted et al. 2002; Harrison et al. 2003; For et al. 2010; Reed et al. 2010). Detecting the beaming effect together with the ellipsoidal and reflection periodic variations, with the expected relative amplitudes and phases, can indicate the presence of a small non-eclipsing companion. Recently, Faigler et al. (2012) reported RV confirmation of seven new non-eclipsing short-period binary systems in the *Kepler* field, with companion minimum masses in the range 0.07–0.4 M_{\odot} , that were discovered by the BEER algorithm.

For brown dwarfs or planetary companions the beaming effect is even smaller, on the order of 2–50 ppm. Interestingly, several studies were able to detect this minute effect in systems with transiting brown dwarfs and planets (Mazeh & Faigler 2010; Shporer et al. 2011; Mazeh et al. 2012; Jackson et al. 2012; Mislis et al. 2012; Barclay et al. 2012), indicating it may be

Table 1
Coordinates, Magnitude, Stellar Properties, and BEER Results

R.A.	19:36:46.11	Right ascension
Decl.	39:37:08.4	Declination
K_p^a (mag)	13.3	<i>Kepler</i> band magnitude
T_{eff}^a (K)	6196	KIC effective temperature
T_{eff}^b (K)	6409 ± 95	Revised effective temperature
$\log g^a$ (dex)	4.388	Surface gravity
$[m/H]^a$ (dex)	-0.033	Metallicity
R_*^a (R_\odot)	1.12	Primary radius
M_*^c (M_\odot)	1.12	Primary mass
f_3^a	0.056	Average third light fraction
BEER model:		With transit and occultation points masked out
Period (days)	1.5449 ± 0.0007	Orbital period
$T_0 - 2455000^d$ (BJD)	737.49 ± 0.19	Orbital zero phase ephemeris
Ellipsoidal (ppm) ^e	21.5 ± 1.7	Ellipsoidal semi-amplitude
Beaming (ppm) ^e	15.6 ± 2.2	Beaming semi-amplitude
Reflection (ppm) ^e	56.0 ± 2.5	Lambertian reflection/emission semi-amplitude
rms cleaned data (ppm)	133	Root mean square of the cleaned and detrended data
rms residuals (ppm)	127	Root mean square of residuals of data from BEER model

Notes.

^a From Kepler Input Catalog.

^b Revised T_{eff} from Pinsonneault et al. (2012).

^c Calculated from Kepler Input Catalog $\log g$ and R .

^d T_0 is the time in which the companion is closest to the observer, assuming a circular orbit.

^e Corrected for third light.

possible to detect such non-transiting objects by identifying these effects in their host star light curves.

This paper presents the discovery of Kepler-76b, the first hot Jupiter detected by the BEER algorithm that was subsequently confirmed by Tillinghast Reflector Echelle Spectrograph (TRES) and SOPHIE RV spectroscopy. It was identified by the BEER algorithm as a high-priority planetary candidate. Visual inspection of its light curve revealed a V-shaped primary transit and a minute secondary eclipse, combined with beaming, ellipsoidal, and reflection amplitudes, consistent with a massive-planet companion. We noticed later that this star was listed in the *Kepler* eclipsing binary catalog (Prša et al. 2011; Slawson et al. 2011). Based on this information, spectroscopic follow-up observations were initiated for this target, which in turn confirmed its planetary nature.

Section 2 presents the BEER search and the initial analysis of the *Kepler* light curve, Section 3 provides the details and results of the spectroscopic observations, Section 4 describes the details and results of the light curve transits and occultations analysis, Section 5 presents the detection of evidence for superrotation in the light curve, and Section 6 discusses the implications of, and conclusions from, the findings of this paper.

2. THE PHOTOMETRIC BEER SEARCH

To identify candidates for low-mass companions, we analyzed the *Kepler* raw light curves of the Q2 to Q10 quarters, spanning 831 days. We visually identified 22 time segments that showed instrumental artifacts in the photometry, and ignored data points within those segments, removing a total of 59.9 days of data from the light curves. We also corrected two systematic jumps at *Kepler* times (BJD – 2454833) of 200.32 and 246.19 days. For each light curve, outliers were then removed by 4σ clipping and detrending was performed using a cosine-transform filter, adapted to unevenly spaced data (Mazeh & Faigler 2010; Mazeh et al. 2012), resulting in a cleaned and detrended light curve. We then applied the BEER algorithm to 41,782 stars brighter than

13.7 mag, with Kepler Input Catalog (Brown et al. 2011) radius smaller than $4 R_\odot$, calculating the fast Fourier transform (FFT)-based power spectrum of the cleaned and detrended light curve of each star, interpolated over the gaps. Next, in order to avoid spurious peaks at long periods, we divided the full period range of each power spectrum into five sub-ranges: [0.3–1], [1–2], [2–5], [5–10], and [10–20] days, and identified the highest peak within each sub-range. For each of the five peaks, we derived the BEER amplitudes and the estimated mass and albedo of the candidate companion (Faigler & Mazeh 2011), assuming the peak corresponds to either the orbital period (beaming and reflection) or half the orbital period (ellipsoidal). The BEER amplitudes were calculated by fitting the data with the modified BEER model suggested by Mazeh et al. (2012), which uses a Lambertian reflection/emission function.

We then selected 26 candidates with the highest signal-to-noise ratio for the ellipsoidal and beaming amplitudes, and with estimated secondary mass smaller than $60 M_{\text{Jup}}$ and implied albedo smaller than 0.5. One of these candidates was Kepler-76 (Kepler Input Catalog number 4570949), for which visual inspection revealed primary and secondary eclipses with depths of about 5×10^{-3} and 1×10^{-4} , respectively. This candidate was also identified as a member of the *Kepler* eclipsing binary catalog (Prša et al. 2011). Follow-up spectroscopic observations confirmed the companion as a hot Jupiter. In forthcoming papers, we will report on our observations of the 26 candidates, additional confirmation of a possible brown dwarf, and the false-positive rate of this sample.

We report here the BEER analysis results for the light curve of Kepler-76 after masking out the transit and occultation data points. We note that in our initial detection, the BEER analysis was performed on the unmasked data, but the use of a robust-fit function (Holland & Welsch 1977) that identified the transit points as outliers resulted in similar measured BEER amplitudes. Table 1 lists for Kepler-76 the coordinates and stellar properties from the Kepler Input Catalog (Brown et al. 2011), the revised effective temperature estimate from Pinsonneault et al.

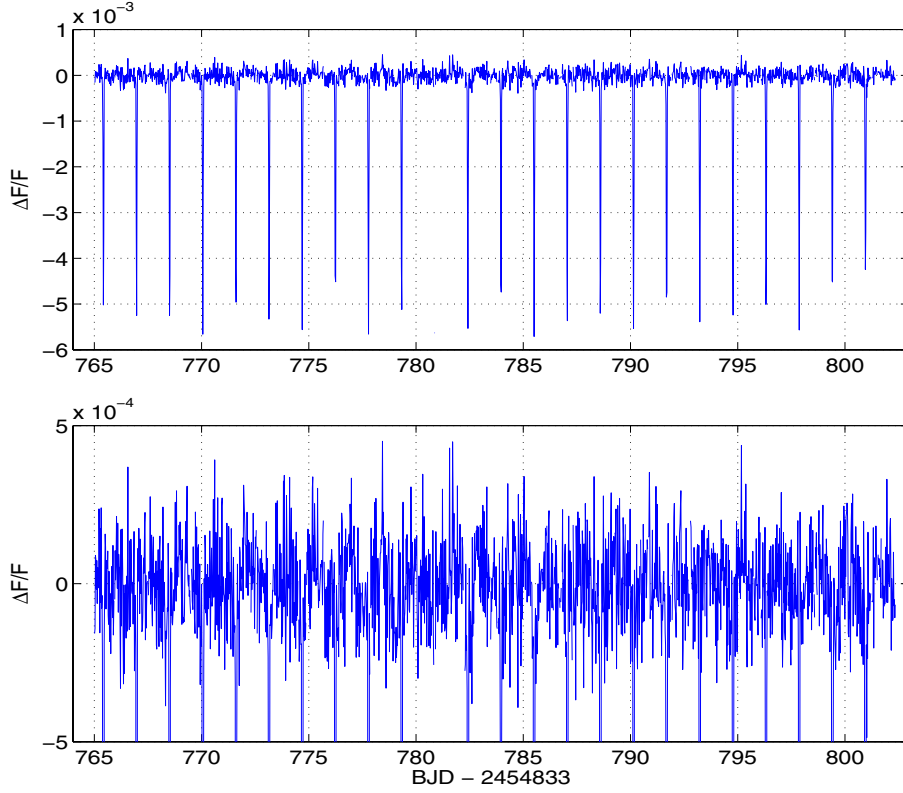


Figure 1. Light curve of Kepler-76 for a selected time span of 37 days, after outlier removal and long-term detrending. Top: the untruncated light curve, showing the full depth of the transits. Bottom: the light curve with the core of the transit events truncated. Note the different scales of the two plots. (The transit missing at time 780.9 fell in a short gap in the raw data.)

(A color version of this figure is available in the online journal.)

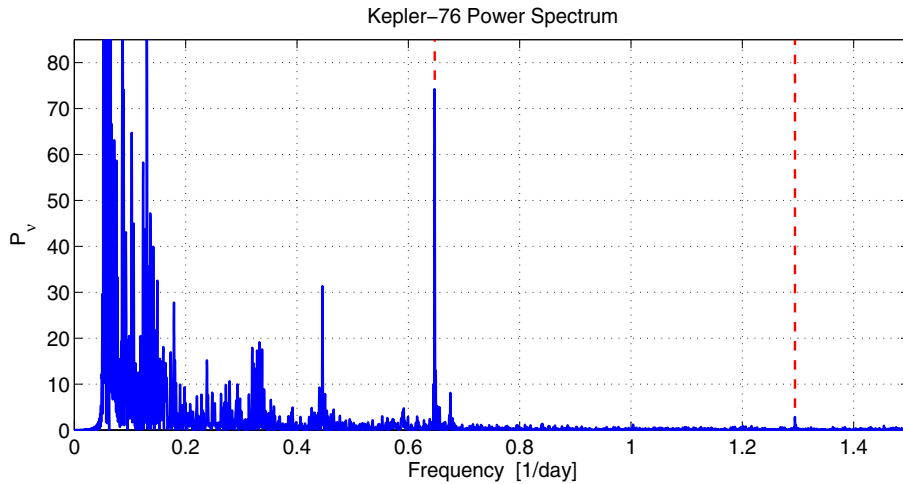


Figure 2. FFT-based power spectrum of the detection. The orbital period and half-orbital period peaks are marked by vertical dashed lines. For clarity, only the frequency range of 0–1.5 day⁻¹ is plotted, since no significant peak was found for frequencies higher than 1.5 day⁻¹.

(A color version of this figure is available in the online journal.)

(2012), and the results of the BEER analysis. Figure 1 presents a short section of the “cleaned” (Mazeh & Faigler 2010; Faigler & Mazeh 2011) photometric data of the host star, Figure 2 presents the FFT-based power spectrum, and Figure 3 shows the light curve folded with the detected period. It is interesting to

note, by inspecting the cleaned light curves (Figure 1) and the data and residuals rms (Table 1), that the effects are significantly smaller than the light curve noise, to the point that the detected modulations almost cannot be recognized by eye. However, deriving the BEER photometric power spectrum from data with

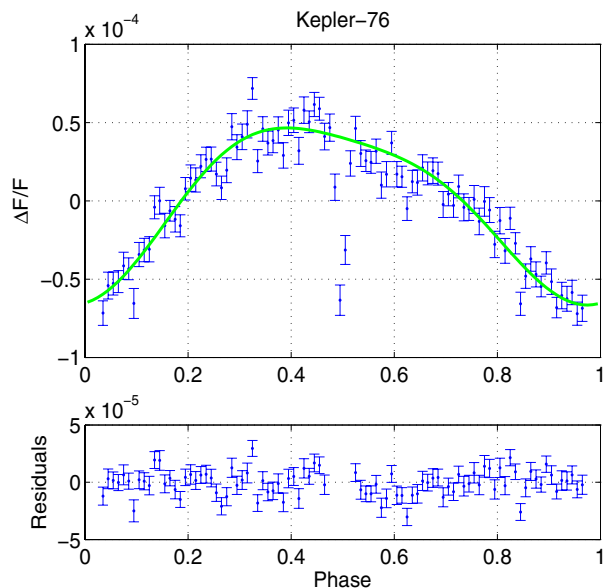


Figure 3. Folded cleaned light curve binned into 100 bins. Phase zero is when the companion is closest to the observer, while phase 0.5 is when the primary is closest to the observer, assuming a circular orbit. The error bars represent 1σ uncertainties of the median value of each bin, based on the scatter of data points within that bin. The line represents the BEER model. The residuals of the data from the model are plotted in the bottom panel. For clarity, the primary eclipse was removed. The secondary eclipse is clearly visible at phase 0.5 of the plot. (A color version of this figure is available in the online journal.)

time spans of hundreds of days produces a prominent detectable peak at the orbital period (Figure 2).

3. SPECTROSCOPIC OBSERVATIONS

Spectroscopic observations of the candidate were obtained between May 29 and 2012 October 6 with the TRES (Fűrész 2008) mounted on the 1.5 m Tillinghast Reflector at the Fred Lawrence Whipple Observatory operated by the Smithsonian Astrophysical Observatory on Mount Hopkins in Southern Arizona, using the medium resolution fiber at a spectral resolution of 44,000, covering a spectral range from 385 to 910 nm. Exposures of a thorium–argon hollow-cathode lamp immediately before and after each exposure were used for wavelength calibration. The spectra were extracted and rectified to intensity versus wavelength using standard procedures developed by Lars Buchhave (Buchhave et al. 2010).

Additional spectroscopic observations were obtained between July 17 and 2012 August 1 with the SOPHIE spectrograph (Perruchot et al. 2008; Bouchy et al. 2009, 2013) mounted on the 1.93 m telescope at Observatoire de Haute-Provence, France, using the High Efficiency mode ($R \sim 39,000$ at 550 nm) of the instrument. Spectra were extracted with the online standard pipeline.

Following a method similar to the Stellar Parameter Classification method (Buchhave et al. 2012), the atmospheric parameters of Kepler-76 were determined from the SOPHIE spectra by cross-correlating the observed spectral regions not affected by telluric lines against a library of synthetic spectra (Hauschildt et al. 1999), with varying values of effective temperature T_{eff} , surface gravity $\log g$, metallicity $[m/H]$, and rotational velocity $v \sin i$. For each of the observed spectra, we derived the best

Table 2
Atmospheric Parameters of Kepler-76

T_{eff} (K)	6300 ± 200
$\log g$ (dex)	4.2 ± 0.3
$[m/H]$ (dex)	-0.1 ± 0.2
$v \sin i$ (km s^{-1})	6.5 ± 2
M_* (M_{\odot})	1.2 ± 0.2

set of parameters that yielded the highest correlation. This was done by fitting a second-degree polynomial to the maximum correlation as a function of each parameter around the synthetic spectrum that yielded the best correlation. The final parameter values for a star were taken as the mean of the parameter values derived for each observed spectrum of that star, weighted proportionally to the inverse of the scatter of the maximum around the fitted polynomial.

The Phoenix library of synthetic spectra we used spans the following intervals in atmospheric parameters: $3000 \text{ K} < T_{\text{eff}} < 10,000 \text{ K}$, $-0.5 < \log g < 5.5$ (cgs), and $-1.5 < [m/H] < +0.5$. The spacing in T_{eff} is 100 K for $T_{\text{eff}} < 7000 \text{ K}$, and 200 K elsewhere. The spacing in $\log g$ and $[m/H]$ is 0.5 dex. The interval and spacing of the $v \sin i$ values in our algorithm are free parameters set by the user, since each synthetic spectrum chosen from the library is convolved with a rotational profile $G(v)$ (e.g., Gray 2005, p. 465; Santerne et al. 2012) and a Gaussian representing the instrumental broadening of the lines, just before calculating the cross-correlation function (CCF).

The cross-correlation was performed using TODMOR (Zucker & Mazeh 1994; Zucker et al. 2003, 2004)—a two-dimensional correlation algorithm, assuming the light contribution of the secondary is negligible. In TODMOR, the CCFs are calculated separately for each echelle order, and then combined to a single CCF according to the scheme proposed by Zucker et al. (2003). The atmospheric parameters found this way are listed in Table 2. The relatively large uncertainties result mainly from the addition of possible systematic errors (see, e.g., Bruntt et al. 2010, 2012; Torres et al. 2012).

The primary mass was estimated using the atmospheric parameters derived from the spectra and a grid of Y^2 stellar isochrones (Yi et al. 2001; Demarque et al. 2004). This was done by taking into account all age and mass values that fall into the ellipsoid in the (T_{eff} , $\log g$, $[\text{Fe}/\text{H}]$) space defined by the atmospheric parameters and their errors. To illustrate the process, Figure 4 shows two sets of Y^2 stellar isochrones of 0.2, 0.4, 1, 2, 4, 8, and 10 Gyr—one for $[\text{Fe}/\text{H}] = 0.05$ (solid lines) and one for $[\text{Fe}/\text{H}] = -0.27$ (dashed lines). The ellipse defined by the estimated T_{eff} and $\log g$ and their uncertainties is also shown. A lower limit of 0.2 Gyr on the stellar age was set to ignore possible pre-main-sequence solutions. This procedure yielded a mass estimate of $1.20 \pm 0.09 M_{\odot}$. Following Basu et al. (2012), we have conservatively doubled the mass errors to take into account possible uncertainties in the stellar model parameters.

RVs were derived for the TRES observations in two different ways, as described in detail by Faigler et al. (2012). First, we derived absolute velocities using cross-correlations of the observed spectra against the template from our library of synthetic spectra that yielded the best match (with $T_{\text{eff}} = 6000 \text{ K}$, $\log g = 4.0$ cgs, $v \sin i = 12 \text{ km s}^{-1}$, and solar metallicity). The absolute velocity analysis used just the spectral order containing the MgIb triplet and was calibrated using IAU RV standard stars. With the goal of achieving better precision, we also derived velocities

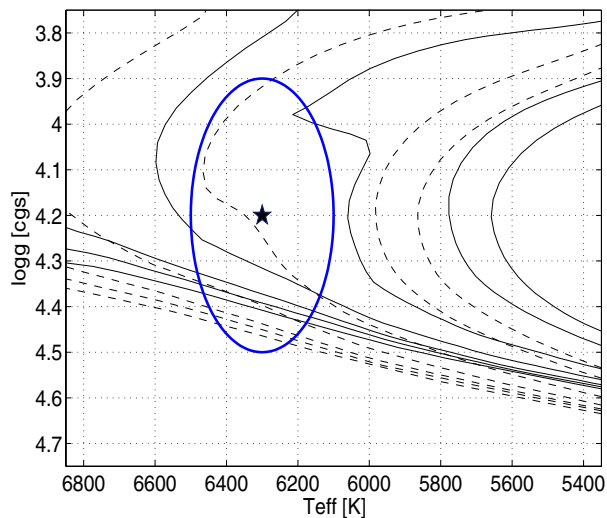


Figure 4. Y^2 stellar isochrones, from Demarque et al. (2004), of 0.2–10 Gyr for metallicities $[\text{Fe}/\text{H}] = 0.05$ (solid lines) and $[\text{Fe}/\text{H}] = -0.27$ (dashed lines). The estimated T_{eff} and $\log g$ of Kepler-76 with their uncertainties are marked by a star and an ellipse.

(A color version of this figure is available in the online journal.)

using about two dozen spectral orders, correlating the individual observations against a template based on the strongest exposure. Thus, the multi-order velocities are relative to the observation chosen as the template. They are reported in Table 3.

For the SOPHIE observations, RVs were derived by computing the weighted CCF of the spectra with a numerical spectral mask of a G2V star (Baranne et al. 1996; Pepe et al. 2002). For the last five exposures, which were contaminated by scattered moon light, we subtracted the sky using the fiber B spectrum (Santerne et al. 2009), before deriving the RVs. Table 3 lists the RV measurements and their uncertainties.

The first RV measurements of Kepler-76 showed variability consistent with the photometric orbital phase, so we continued observations in order to allow an orbital solution independent of the BEER analysis. The derived eccentricity of the solution was statistically indistinguishable from zero, so we reran the solution with eccentricity fixed to zero. Figure 5 shows the follow-up RV

Table 3
Radial Velocity Measurements

Time (BJD–2456000)	RV (km s^{-1})	σ (km s^{-1})	Instrument
76.930366	0.581	0.069	TRES
83.895818	0.161	0.110	TRES
84.868623	0.546	0.072	TRES
87.836880	0.607	0.103	TRES
107.916759	0.586	0.098	TRES
115.796005	0.727	0.114	TRES
117.775394	0.100	0.082	TRES
207.682884	0	0.069	TRES
126.378842	–4.999	0.036	SOPHIE
128.575439	–5.597	0.036	SOPHIE
129.562543	–5.081	0.056	SOPHIE
130.416149	–5.560	0.091	SOPHIE
131.389038	–5.341	0.061	SOPHIE
137.536798	–5.196	0.132	SOPHIE
138.488304	–5.194	0.057	SOPHIE
139.470933	–5.615	0.080	SOPHIE
140.470516	–4.992	0.114	SOPHIE
141.450747	–5.171	0.082	SOPHIE

measurements and the velocity curve for the orbital solution, folded with the period found, and the top section of Table 4 lists the derived orbital elements for the independent RV solution. The center-of-mass velocities γ_T and γ_S for the independent RV sets from TRES and SOPHIE differ by 5.68 km s^{-1} . This is because the TRES velocities are relative to the strongest observation, while the SOPHIE velocities are meant to be on an absolute scale. If the absolute TRES velocities derived using the Mg b order are used instead of the relative velocities, then $\gamma_T = -5.18 \text{ km s}^{-1}$, quite close to the SOPHIE value of $\gamma_S = -5.31 \text{ km s}^{-1}$. For the joint analysis reported below, the two independent velocity sets were shifted to a common zero point using the γ velocities reported in Table 4.

Next, in order to obtain a combined solution from photometry and RV measurements, we reran the RV model using the photometric period and ephemeris, with their uncertainties, as priors. The bottom section of Table 4 lists the orbital elements derived from this photometry-constrained RV solution, and the estimated minimum secondary mass, $M_p \sin i$.

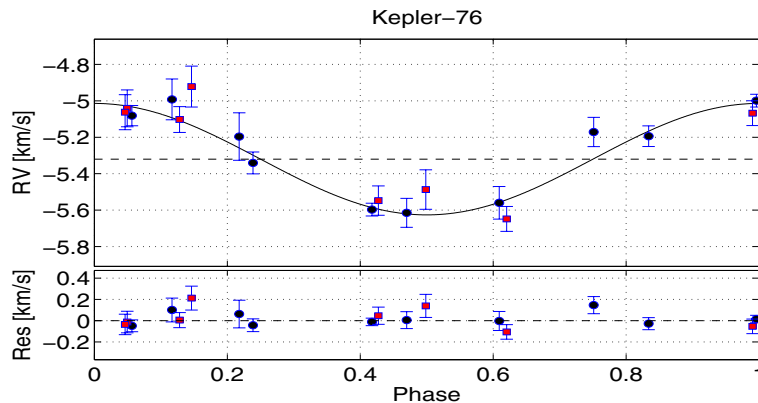


Figure 5. RV measurements folded at the derived orbital period. In the top panel, the solid line represents the photometry-constrained orbital RV model and the horizontal-dashed line indicates the center-of-mass velocity. Circles denote SOPHIE RV points and squares denote TRES RV points. The residuals are plotted at the bottom panel. Note the different scales of the upper and lower panels.

(A color version of this figure is available in the online journal.)

Table 4
Orbital Elements Based on RV Measurements

N	18	Number of RV measurements
Span (days)	130.8	Time span of measurements
Independent RV solution		
$T_0 - 2456000^a$ (BJD)	126.76 ± 0.03	Orbital ephemeris
P (days)	1.5474 ± 0.0021	Orbital period
γ_T (km s^{-1})	0.365 ± 0.042	Zero-point velocity of TRES
γ_S (km s^{-1})	-5.315 ± 0.019	Zero-point velocity of SOPHIE
K_{RV} (km s^{-1})	0.308 ± 0.020	Radial velocity semi-amplitude
RV solution constrained by the photometric period and ephemeris		
$T_0 - 2456000^a$ (BJD)	126.77 ± 0.023	Orbital ephemeris
P (days)	1.5450 ± 0.0005	Orbital period
γ_T (km s^{-1})	0.328 ± 0.032	Zero-point velocity of TRES
γ_S (km s^{-1})	-5.320 ± 0.020	Zero-point velocity of SOPHIE
K_{RV} (km s^{-1})	0.306 ± 0.020	Radial velocity semi-amplitude
$M_p \sin i$ (M_{Jup})	1.96 ± 0.25	Minimum companion mass

Note. ^a T_0 is the time in which the companion is closest to the observer.

Table 5
Photometric Light Curve Transit and Occultation Model

Parameter	Median and 1σ Uncertainty	
Priors		
M_* (M_\odot)	1.2 ± 0.2	Primary mass
a_*	0.313	Star linear limb darkening coefficient
b_*	0.304	Star quadratic limb darkening coefficient
a_p	0.5	Planet linear limb darkening coefficient
b_p	0	Planet quadratic limb darkening coefficient
f_3	0.056	Average third light fraction (From KIC)
Posteriors		
T_0 (BJD)	$2454966.54811 \pm 0.00007$	Time of primary transit
Period (days)	$1.54492875 \pm 0.00000027$	Orbital period
i (deg)	78.0 ± 0.2	Orbital inclination
R_*/a	0.221 ± 0.003	Fractional primary radius
R_p/a	0.0214 ± 0.0008	Fractional planet radius
d_2 (ppm)	98.9 ± 7.1	Occultation depth
ρ_*/ρ_\odot	0.522 ± 0.019	Primary density relative to the Sun density
R_* (R_\odot)	1.32 ± 0.08	Primary radius
R_p (R_{Jup})	1.25 ± 0.08	Planet radius
b	0.944 ± 0.011	Impact parameter

4. PHOTOMETRIC MODELING OF THE LIGHT CURVE

For a more complete photometric analysis of this transiting hot Jupiter we used the *Kepler* light curves of the Q2 to Q13 quarters, spanning 1104 days. First, we fitted the cleaned and detrended data with the BEER model while masking out data points in or around the transits and occultations. The fitted amplitudes, after correction for a third light using the KIC estimate, are listed in Table 6. We then subtracted the BEER model from the data and analyzed the data points in and around the transits and occultations. For that we ran a Markov chain Monte Carlo (MCMC) analysis, while fitting the transit data points using a long-cadence-integrated Mandel & Agol (2002) model with quadratic limb darkening, assuming a circular orbit. The model limb darkening coefficients could not be constrained, so we kept them fixed at values interpolated from Claret & Bloemen (2011) using the stellar parameters derived from spectroscopy. We then fitted the occultation data keeping the geometric parameters derived from the transit fixed, and assuming a linear limb darkening coefficient of 0.5 for the planet, while looking for the occultation depth that best fits the data.

Figure 6 presents the cleaned and detrended data points and the best-fit Mandel & Agol (2002) model combined with the BEER model, both folded at the orbital period. Table 5 lists the priors and the MCMC medians and 1σ uncertainties of the posterior parameters. We note here that the orbital period P and time of primary transit T_0 listed in Table 5 were derived from the transit data points, thus yielding high-accuracy estimates. The same parameters, listed in Table 1, were derived from the out-of-transit data, and thus yielded much lower-accuracy estimates. The T_0 values listed in both tables were not corrected for the *Kepler* timing error (http://archive.stsci.edu/kepler/timing_error.html), which should be taken in account when comparing them to non-*Kepler* observations.

5. INFLATED BEAMING AMPLITUDE AND PLANET EQUATORIAL SUPERROTATING JET

The spectroscopic RV observations and the light curve transit and occultation analysis yielded independent orbital solutions with ephemeris and period nicely consistent with the BEER ephemeris and period. To compare the measured RV amplitude

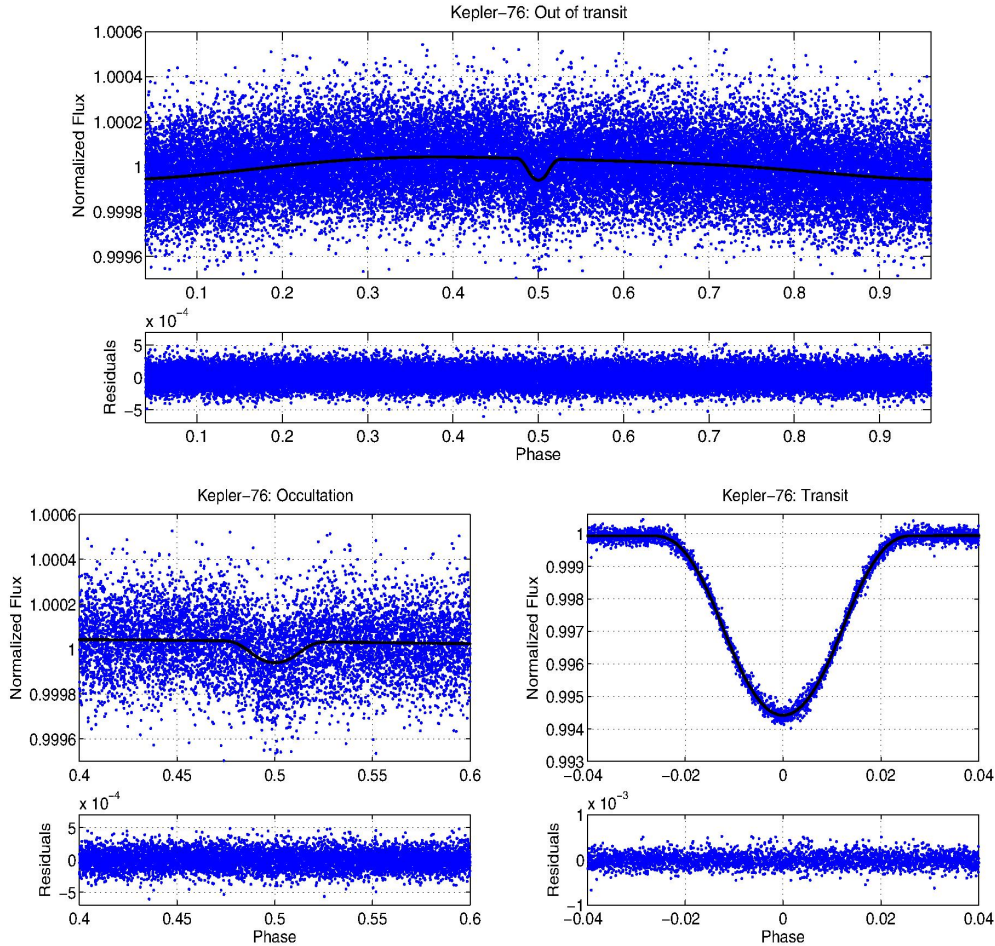


Figure 6. Kepler-76 cleaned and detrended data points and best-fit model, both folded at the orbital period. In the top panel of each plot, the solid line represents the best-fit model, and the dots represent the data points. The residuals are plotted in the bottom panel. Note the different scales of the upper and lower panels of each plot. (A color version of this figure is available in the online journal.)

with the beaming-based predicted RV amplitude, one needs to evaluate the α_{beam} factor, which corrects for the Doppler shift of the stellar spectrum relative to the observed band of the telescope (Rybicki & Lightman 1979; Faigler & Mazeh 2011).

To estimate the α_{beam} value, we used spectra from the library of the Castelli & Kurucz (2004) models close to the estimated temperature, metallicity, and gravity of the primary star, numerically shifting them relative to the *Kepler* response function, while taking into account the photon counting nature of *Kepler* (Loeb & Gaudi 2003; Bloemen et al. 2011; Faigler et al. 2012). For clarity, we note that by definition $\alpha_{\text{beam}} = (3 - \alpha/4) = ((B)/4)$, where α is the power-law index used by Loeb & Gaudi (2003) and (B) is the photon-weighted bandpass-integrated beaming factor used by Bloemen et al. (2011). The result of this calculation gave $\alpha_{\text{beam}} = 0.92 \pm 0.04$, resulting in an RV semi-amplitude of $K_{\text{beamed}} = 1.11 \pm 0.17 \text{ km s}^{-1}$. The RV semi-amplitude predicted from the beaming effect was 3.5 times larger than the measured amplitude, with a difference significance of about 4.5σ between the two.

A possible explanation for this inflated photometric beaming amplitude might be a phase shift of the reflection signal,

due to the superrotation phenomenon, which involves eastward advection of gas by an equatorial superrotating jet within the atmosphere of a corotating companion. Showman & Guillot (2002) predicted through a three-dimensional atmospheric circulation model that tidally locked, short-period planets develop a fast eastward, or *superrotating*, jet stream that extends from the equator to latitudes of typically 20° – 60° . They showed that in some cases (depending on the imposed stellar heating and other factors) this jet causes an eastward displacement of the hottest regions by 10° – 60° longitude from the substellar point, resulting in a phase shift of the thermal emission phase curve of the planet. This prediction was confirmed by Knutson et al. (2007, 2009) through *Spitzer* infrared observations of HD 189733, which indicated a phase shift of $16^\circ \pm 6^\circ$ in the $8 \mu\text{m}$ band and 20° – 30° in the $24 \mu\text{m}$ band.

In general, what we call a reflection modulation is actually the light scattered off the planet in combination with radiation absorbed and later thermally re-emitted at different wavelengths. The two processes are controlled by the Bond albedo, $0 < A_B < 1$, and the day–night heat redistribution efficiency, $0 < \epsilon < 1$, which can be constrained only if observations

Table 6
BEER Amplitudes, Planetary Mass, and Superrotation Phase-shift Angle

BEER model		
Ellipsoidal (ppm) ^a	21.1 ± 1.7	Ellipsoidal semi-amplitude
Beaming (ppm) ^a	13.5 ± 2.0	Beaming semi-amplitude
Reflection (ppm) ^a	50.4 ± 2.0	Reflection semi-amplitude
a_{2s} (ppm) ^a	−2.7 ± 1.0	sin 2 ϕ coefficient
$M_{p,beam}$ (M_{Jup})	7.2 ± 1.4	Planetary mass derived from beaming
$M_{p,ellip}$ (M_{Jup})	2.1 ± 0.4	Planetary mass derived from ellipsoidal
$M_{p,RV}$ (M_{Jup})	2.00 ± 0.26	Planetary mass measured by spectroscopic RV
Superrotation phase-shift model solution		
$M_{p,SR}$ (M_{Jup})	2.1 ± 0.4	Planetary mass
δ_{SR} (deg)	10.3 ± 2.0	Superrotation phase-shift angle
A_g	0.23 ± 0.02	Geometric albedo
N	31468	Number of data points
χ^2	31465	χ^2 of a model allowing for a phase shift
χ^2_{null}	31555	χ^2 of a zero phase-shift model (null model)

Note. ^a Corrected for third light.

of the phase modulation or the secondary eclipse are available in different wavelengths (Cowan & Agol 2011). This makes it impossible to distinguish between reflected and re-radiated photons from the single-band *Kepler* light curve we have in hand. Cowan & Agol (2011) discuss HAT-P-7 as an example, and show that its *Kepler* light curve can be explained as mostly reflected light at one limit, to mostly thermal emission at the other limit, with an entire range of models between them being consistent with the light curve. This is important for the current discussion, as we expect superrotation to shift only the thermal re-emission, while leaving the scattered light component unshifted.

To estimate the maximum fraction of the reflection amplitude originating from thermal re-emission in our case, we follow Cowan & Agol (2011) and estimate the no albedo, no redistribution, effective dayside temperature $T_{\epsilon=0} \approx 2670$ K, which translates in the *Kepler* band to a maximum reflection amplitude $A_{ref} \approx 37$ ppm. This means that the measured amplitude of ≈ 50 ppm can be explained mostly by thermal re-emission. The actual fraction of thermal emission in this case is probably smaller, but this calculation illustrates that the fraction of thermal emission in the visual *Kepler* light curve phase modulation may be significant, making it a worthy effort to look for a superrotation phase shift in the light curve.

We suggest here, that if such a phase shift is present in the *Kepler* light curve, it will show up in our phase curve model mainly as an inflated beaming amplitude. To illustrate that, we consider a simple superrotation model consisting of a phase-shifted geometric reflection/emission combined with a beaming modulation,

$$\begin{aligned} \mathcal{M}_{SR} &= -A_{ref} \cos(\phi + \delta_{SR}) + A_{beam} \sin \phi \\ &= -A_{ref} \cos \delta_{SR} \cos \phi + (A_{beam} + \underline{A_{ref} \sin \delta_{SR}}) \sin \phi, \end{aligned} \quad (1)$$

where A_{ref} is the reflection/emission semi-amplitude, A_{beam} is the beaming semi-amplitude, ϕ is the orbital phase relative to mid-transit, and δ_{SR} is the superrotation phase shift angle. This model suggests that if a phase shift is present *and* the reflection amplitude is larger than, or of the order of, the beaming amplitude, then the underlined term in Equation (1)

may add substantially to the amplitude of the sin ϕ modulation, mimicking an inflated beaming effect.

To test our conjecture that the beaming/ellipsoidal inconsistency is a result of a superrotation phase shift of the reflection/emission phase modulation, we fitted the data using the derived system parameters (Tables 2 and 5) and the BEER effects equations (Faigler & Mazeh 2011), while looking for the planetary mass, geometric albedo, and phase shift of the Lambertian phase function that minimized the χ^2 of the fit. Adding the phase-shift parameter to the model resulted in a decrease of the χ^2 value by 90, relative to the no-phase-shift model, indicating a substantially better agreement of the data with a model that combines beaming, ellipsoidal, and a phase-shifted Lambertian reflection. An F -test shows that fitting the data while allowing for a phase shift, as opposed to the no-phase-shift null model, yields a better fit with a confidence level better than 9σ . Table 6 lists the amplitudes derived by the BEER analysis, the planetary mass derived directly from the beaming versus the ellipsoidal amplitudes, and the spectroscopic RV derived planetary mass. The table then lists the planetary mass, phase-shift angle, and geometric albedo resulting from the superrotation model. The superrotation phase-shift estimate is small and well within the theoretical limit of 60° predicted by Showman & Guillot (2002). In addition, the derived planetary mass estimate is well within the 1σ range of the RV measured planetary mass, indicating that assuming superrotation resolves the inconsistency and provides a good estimate for the planetary mass, derived *solely* from the *Kepler* photometry, given a good stellar model.

6. DISCUSSION

This paper presents a new hot-Jupiter companion, Kepler-76b, initially identified by the BEER algorithm, and later confirmed by spectroscopic observations. The BEER detection was based on the photometrically measured amplitudes of the BEaming, Ellipsoidal, and Reflection effects, which were consistent with a planetary companion. This is just the third confirmed planet in the *Kepler* field, after HAT-P-7b (Welsh et al. 2010) and TrES-2b (Barclay et al. 2012), for which its host light curve exhibits the three phase curve effects, and is the faintest of the three stars. It is also one of a few confirmed grazing exoplanets, showing a V-shaped transit and a partial occultation.

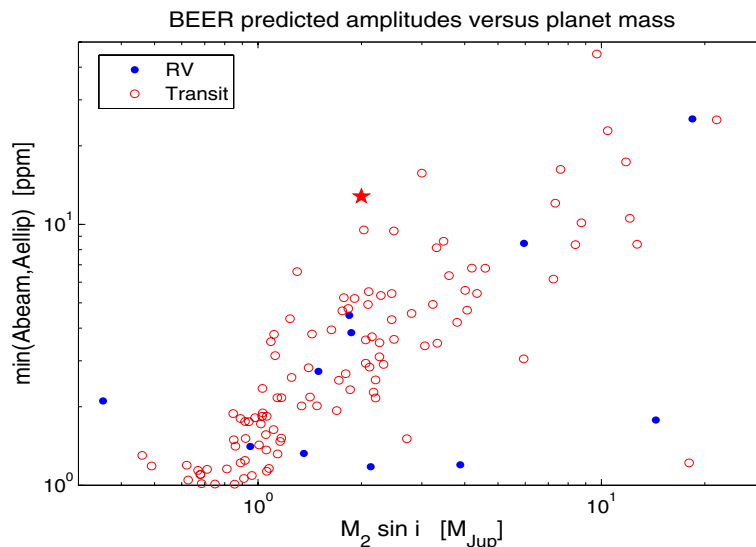


Figure 7. Minimum of the predicted beaming and ellipsoidal semi-amplitudes, as a function of the secondary mass, for known exoplanets of mass higher than $0.5 M_{\text{Jup}}$ and period shorter than 30 days. Blue dots mark exoplanets detected by RV, red circles mark exoplanets detected by transit, and the red star marks the measured amplitude of Kepler-76b.

(A color version of this figure is available in the online journal.)

We have identified an inconsistency between the beaming amplitude and the spectroscopically measured RV. Similar inconsistencies between the planetary mass derived from the beaming amplitudes and the mass derived from the ellipsoidal amplitude were noticed previously by several authors for KOI-13 (Mazeh et al. 2012; Shporer et al. 2011) and TrES-2 (Barclay et al. 2012). We suggest here that these inconsistencies can be explained by a phase shift of the planetary thermal modulation due to the equatorial superrotation phenomena predicted by Showman & Guillot (2002) and later observed by Knutson et al. (2007, 2009) in the infrared for HD 189733. In such cases, we should be able to measure the superrotation phase-shift angle from the visual-band *Kepler* light curve of the system. As we do not expect scattered light to exhibit such a phase shift, visual band detection of the superrotation phase shift may yield a constraint on the ratio of scattered light to thermally re-emitted light from the planet.

Finally, we wish to briefly comment on the sensitivity of the BEER algorithm. The detection presented here exhibits the lowest-mass companion identified so far by the algorithm, indicating its possible current detection limit. As we require that a BEER candidate must show statistically significant beaming and ellipsoidal effects to be considered valid, we choose here the minimum of the semi-amplitudes of the two effects as the BEER detectability parameter of a planet. To estimate our ability to detect more planets and brown dwarfs, Figure 7 presents the calculated value of this parameter, using the Faigler & Mazeh (2011) equations, for known exoplanets of mass higher than $0.5 M_{\text{Jup}}$ and period shorter than 30 days, as of 2013 January (<http://exoplanet.eu/>), together with the measured value for Kepler-76b. The figure shows that there are six transiting and one RV detected planets with calculated amplitudes higher than that of Kepler-76b, suggesting that these systems could have been detected by the BEER algorithm, if their stellar and instrumental noise were similar to that of Kepler-76. It is also apparent that further enhancement of the algorithm

sensitivity could significantly increase the number of potentially detectable planets. Given the fact that BEER can detect similar non-transiting objects, we expect to find more objects once we improve our detection threshold.

We are indebted to Shay Zucker for numerous helpful discussions, and to Ignasi Ribas for discussing the thermal phase shift. We thank the referee Steven Bloemen for his valuable remarks and suggestions, and especially for his comment about the α_{beam} calculation. The research leading to these results has received funding from the European Research Council under the EU’s Seventh Framework Programme (FP7/(2007-2013)/ERC grant Agreement No. 291352). This research was supported by the ISRAEL SCIENCE FOUNDATION (grant No. 1423/11). We feel deeply indebted to the team of the *Kepler* mission that enabled us to search and analyze their unprecedentedly accurate photometric data. All the photometric data presented in this paper were obtained from the Multimission Archive at the Space Telescope Science Institute (MAST). STScI is operated by the Association of Universities for Research in Astronomy, Inc., under NASA contract NAS5-26555. Support for MAST for non-*HST* data is provided by the NASA Office of Space Science via grant NNX09AF08G and by other grants and contracts. We thank the *Kepler* mission for partial support of the spectroscopic observations under NASA Cooperative Agreement NNX11AB99A with the Smithsonian Astrophysical Observatory, DWL PI. We are indebted to Andrew H. Szentgyorgyi, who led the TRES project, and to Gabor Fűrész for his many contributions to the success of the instrument. We thank Robert P. Stefanik, Perry Berlind, Gilbert A. Esquerdo, and Michael L. Calkins for obtaining the TRES observations, and Allyson Bieryla and Jessica Mink for help with the data analysis. This paper is based in part on observations made at Observatoire de Haute Provence (CNRS), France. We are grateful to the OHP director and team for the allocation of the SOPHIE observing time. We are also thankful for the help of the night assistants

that enabled us to obtain the spectra presented here. OHP observations were supported by the OPTICON network. OPTICON has received research funding from the European Community's Seventh Framework Programme.

Facilities: FLWO:1.5m(TRES), OHP:1.93m(SOPHIE)

REFERENCES

- Aigrain, S., Favata, F., & Gilmore, G. 2004, *A&A*, 414, 1139
- Auvergne, M., Bodin, P., Boissard, L., et al. 2009, *A&A*, 506, 411
- Baranne, A., Queloz, D., Mayor, M., et al. 1996, *A&AS*, 119, 373
- Barclay, T., Huber, D., Rowe, J. F., et al. 2012, *ApJ*, 761, 53
- Basu, S., Verner, G. A., Chaplin, W. J., & Elsworth, Y. 2012, *ApJ*, 746, 76
- Bloemen, S., Marsh, T. R., Degroote, P., et al. 2012, *MNRAS*, 422, 2600
- Bloemen, S., Marsh, T. R., Østensen, R. H., et al. 2011, *MNRAS*, 410, 1787
- Bouchy, F., Díaz, R. F., Hébrard, G., et al. 2013, *A&A*, 549, A49
- Bouchy, F., Hébrard, G., Udry, S., et al. 2009, *A&A*, 505, 853
- Breton, R. P., Rappaport, S. A., van Kerkwijk, M. H., & Carter, J. A. 2012, *ApJ*, 748, 115
- Brown, T. M., Latham, D. W., Everett, M. E., & Esquerdo, G. A. 2011, *AJ*, 142, 112
- Bruntt, H., Basu, S., Smalley, B., et al. 2012, *MNRAS*, 423, 122
- Bruntt, H., Bedding, T. R., Quirion, P.-O., et al. 2010, *MNRAS*, 405, 1907
- Buchhave, L. A., Bakos, G. Á., Hartman, J. D., et al. 2010, *ApJ*, 720, 1118
- Buchhave, L. A., Latham, D. W., Johansen, A., et al. 2012, *Natur*, 486, 375
- Carter, J. A., Rappaport, S., & Fabrycky, D. 2011, *ApJ*, 728, 139
- Castelli, F., & Kurucz, R. L. 2004, arXiv:astro-ph/0405087
- Claret, A., & Bloemen, S. 2011, *A&A*, 529, A75
- Cowan, N. B., & Agol, E. 2011, *ApJ*, 729, 54
- Demarque, P., Woo, J.-H., Kim, Y.-C., & Yi, S. K. 2004, *ApJS*, 155, 667
- Faigler, S., & Mazeh, T. 2011, *MNRAS*, 415, 3921
- Faigler, S., Mazeh, T., Quinn, S. N., Latham, D. W., & Tal-Or, L. 2012, *ApJ*, 746, 185
- For, B.-Q., Green, E. M., Fontaine, G., et al. 2010, *ApJ*, 708, 253
- Fűrész, G. 2008, PhD thesis, Univ. Szeged, Hungary
- Gray, D. F. 2005, in *The Observations and Analysis of Stellar Photospheres*, ed. D. F. Gray (3rd ed.; Cambridge: Cambridge Univ. Press)
- Harrison, T. E., Howell, S. B., Huber, M. E., et al. 2003, *AJ*, 125, 2609
- Hauschildt, P. H., Allard, F., & Baron, E. 1999, *ApJ*, 512, 377
- Holland, P. W., & Welsch, R. E. 1977, *Commun. Stat.: Theory Methods*, A6, 813
- Jackson, B. K., Lewis, N. K., Barnes, J. W., et al. 2012, *ApJ*, 751, 112
- Kipping, D. M., & Spiegel, D. S. 2011, *MNRAS*, 417, L88
- Knutson, H. A., Charbonneau, D., Allen, L. E., et al. 2007, *Natur*, 447, 183
- Knutson, H. A., Charbonneau, D., Cowan, N. B., et al. 2009, *ApJ*, 690, 822
- Koch, D. G., Borucki, W. J., Basri, G., et al. 2010, *ApJL*, 713, L79
- Loeb, A., & Gaudi, B. S. 2003, *ApJL*, 588, L117
- Mandel, K., & Agol, E. 2002, *ApJL*, 580, L171
- Maxted, P. F. L., Marsh, T. R., Heber, U., et al. 2002, *MNRAS*, 333, 231
- Mazeh, T. 2008, in *EAS Publications Series, Tidal Effects in Stars, Planets, and Disks*, Vol. 29, ed. M. J. Goupil & J. P. Zahn (Cambridge: Cambridge Univ. Press), 1
- Mazeh, T., & Faigler, S. 2010, *A&A*, 521, L59
- Mazeh, T., Nachmani, G., Sokol, G., Faigler, S., & Zucker, S. 2012, *A&A*, 541, A56
- Mislis, D., Heller, R., Schmitt, J. H. M. M., & Hodgkin, S. 2012, *A&A*, 538, A4
- Morris, S. L. 1985, *ApJ*, 295, 143
- Pepe, F., Mayor, M., Galland, F., et al. 2002, *A&A*, 388, 632
- Perruchot, S., Kohler, D., Bouchy, F., et al. 2008, *Proc. SPIE*, 7014, 70140J
- Pinsonneault, M. H., An, D., Molenda-Zakowicz, J., et al. 2012, *ApJS*, 199, 30
- Prša, A., Batalha, N., Slawson, R. W., et al. 2011, *AJ*, 141, 83
- Reed, M. D., Terndrup, D. M., Østensen, R., et al. 2010, *Ap&SS*, 329, 83
- Rowe, J., Borucki, W. J., Howell, S. B., et al. 2011, *BAAS*, 43, 103.04
- Rybicki, G. B., & Lightman, A. P. 1979, *Radiative Processes in Astrophysics* (New York: Wiley)
- Santerne, A., Moutou, C., Barros, S. C. C., et al. 2012, *A&A*, 544, L12
- Santerne, A., Moutou, C., Bouchy, F., Hébrard, G., & Deleuil, M. 2009, in *SF2A-2009: Proc. Annual Meeting of the French Society of Astronomy and Astrophysics*, ed. M. Heydari-Malayeri, C. Reyl, & R. Samadi, 21
- Showman, A. P., & Guillot, T. 2002, *A&A*, 385, 166
- Shporer, A., Jenkins, J. M., Rowe, J. F., et al. 2011, *AJ*, 142, 195
- Slawson, R. W., Prša, A., Welsh, W. F., et al. 2011, *AJ*, 142, 160
- Torres, G., Fischer, D. A., Sozzetti, A., et al. 2012, *ApJ*, 757, 161
- van Kerkwijk, M. H., Rappaport, S. A., Breton, R. P., et al. 2010, *ApJ*, 715, 51
- Welsh, W. F., Orosz, J. A., Seager, S., et al. 2010, *ApJL*, 713, L145
- Wilson, R. E. 1990, *ApJ*, 356, 613
- Yi, S., Demarque, P., Kim, Y.-C., et al. 2001, *ApJS*, 136, 417
- Zucker, S., & Mazeh, T. 1994, *ApJ*, 420, 806
- Zucker, S., Mazeh, T., & Alexander, T. 2007, *ApJ*, 670, 1326
- Zucker, S., Mazeh, T., Santos, N. C., Udry, S., & Mayor, M. 2003, *A&A*, 404, 775
- Zucker, S., Mazeh, T., Santos, N. C., Udry, S., & Mayor, M. 2004, *A&A*, 426, 695

BEER ANALYSIS OF *KEPLER* AND *CoRoT* LIGHT CURVES. II. EVIDENCE FOR SUPERROTATION IN THE PHASE CURVES OF THREE *KEPLER* HOT JUPITERS

S. FAIGLER AND T. MAZEH

School of Physics and Astronomy, Raymond and Beverly Sackler Faculty of Exact Sciences, Tel Aviv University, Tel Aviv 69978, Israel
Received 2014 July 8; accepted 2014 December 12; published 2015 February 10

ABSTRACT

We analyzed the *Kepler* light curves of four transiting hot Jupiter systems—KOI-13, HAT-P-7, TrES-2, and Kepler-76, which show BEaming, Ellipsoidal, and Reflection (BEER) phase modulations. The mass of the four planets can be estimated from either the beaming or the ellipsoidal amplitude, given the mass and radius of their parent stars. For KOI-13, HAT-P-7, and Kepler-76 we find that the beaming-based planetary mass estimate is larger than the mass estimated from the ellipsoidal amplitude, consistent with previous studies. This apparent discrepancy may be explained by equatorial superrotation of the planet atmosphere, which induces an angle shift of the planet reflection/emission phase modulation, as was suggested for Kepler-76 in the first paper of this series. We propose a modified BEER model that supports superrotation, assuming either a Lambertian or geometric reflection/emission phase function, and provides a photometry-consistent estimate of the planetary mass. Our analysis shows that for Kepler-76 and HAT-P-7, the Lambertian superrotation BEER model is highly preferable over an unshifted null model, while for KOI-13 it is preferable only at a 1.4σ level. For TrES-2 we do not find such preference. For all four systems the Lambertian superrotation model mass estimates are in excellent agreement with the planetary masses derived from, or constrained by, radial velocity measurements. This makes the Lambertian superrotation BEER model a viable tool for estimating the masses of hot Jupiters from photometry alone. We conclude that hot Jupiter superrotation may be a common phenomenon that can be detected in the visual light curves of *Kepler*.

Key words: methods: data analysis – planets and satellites: fundamental parameters – planets and satellites: individual (KOI-13b, HAT-P-7b, TrES-2b, Kepler-76b)

1. INTRODUCTION

The *Kepler* space telescope has produced more than 150,000 nearly uninterrupted high-precision light curves (Koch et al. 2010) that enable detection of minute astrophysical effects. As of 2014 June, analysis of these light curves yielded the discovery of more than 4200 planetary candidates (*Kepler* Exoplanet Archive 2014) through detection by the transit method (Batalha et al. 2013), of which more than 900 have been verified as planets by various methods (Exoplanet Encyclopedia 2014). For such transiting planets, the orbital period, inclination, and radii of the star and planet, relative to the semimajor axis, are directly measurable through analysis of the transit shape (e.g., Seager & Mallén-Ornelas 2003). However, there are additional astrophysical effects that produce flux variations along the orbital phase of a star–planet system, which depend on, and thus probe, additional properties of the planet. Such out-of-transit phase modulations are the result of three main stellar and planetary effects: BEaming, Ellipsoidal, and Reflection (BEER). The beaming effect, sometimes called Doppler boosting, causes an increase (decrease) of the brightness of any light source approaching (receding from) the observer (Rybicki & Lightman 1979; Loeb & Gaudi 2003), with an amplitude proportional to the radial velocity (RV) of the source. Therefore, the stellar RV modulation due to a circular-orbit planet will produce a sine-like beaming phase modulation at the orbital period, if midtransit is defined as the phase zero point. The ellipsoidal effect (Kopal 1959; Morris 1985) is due to the tidal distortion of the star by the gravity of the planet (e.g., Loeb & Gaudi 2003; Zucker et al. 2007; Mazeh 2008), resulting in a cosine-like phase modulation at half the orbital period, for a circular-orbit planet under the same phase-zero definition. The amplitudes of the beaming and the ellipsoidal modulations for a transiting planet are *both* proportional to the planet mass, which cannot

be probed by the transit method, thus providing an important insight into the planet composition. The reflection/emission variation, on the other hand, is a result of light scattered off the planet dayside combined with light absorbed and later thermally reemitted by the planet atmosphere at different wavelengths (Vaz 1985; Wilson 1990; Maxted et al. 2002; Harrison et al. 2003; For et al. 2010; Reed et al. 2010). This effect probes properties associated with the planet atmosphere response to its host-star radiation, such as the Bond albedo, scattered light geometric albedo, and heat redistribution parameters, among others. The reflection/emission phase modulation is expected to behave approximately as a cosine wave at the orbital period for a circular orbit.

In case the beaming, reflection, and ellipsoidal effects modulate as sine and cosine at the orbital period and cosine at half the orbital period, respectively, their functions are orthogonal along the orbital phase, thus enabling the measuring of each of the effects amplitudes without interference from the other effects. As a result, the mass of a transiting planet can be independently estimated by either the beaming or the ellipsoidal amplitudes. Such a derivation was performed for KOI-13 (Shporer et al. 2011; Mazeh et al. 2012; Esteves et al. 2013), HAT-P-7 (Esteves et al. 2013), TrES-2 (Barclay et al. 2012; Esteves et al. 2013), and Kepler-76b (Faigler et al. 2013). Interestingly, in all cases, except for the Esteves et al. (2013) analysis of TrES-2, the beaming-derived planetary mass estimate was significantly higher than the ellipsoidal-derived estimate. In addition, RV measurements, available for HAT-P-7, TrES-2, and Kepler-76 (Winn et al. 2009; O’Donovan et al. 2006; Faigler et al. 2013), show spectroscopic RV amplitudes that are significantly smaller than the beaming-derived RV ones, pointing to puzzling inflated beaming amplitudes.

Faigler et al. (2013) suggested that the inflated photometric beaming amplitude of Kepler-76 may be the result of a

phase shift of the reflection signal, due to the superrotation phenomenon. Showman & Guillot (2002) predicted, through three-dimensional atmospheric circulation model and simulations, that tidally locked, short-period planets develop fast eastward, or *superrotating*, equatorial jet streams that in some cases displace the hottest regions by 10° – 60° longitude from the substellar point, resulting in a phase shift of the thermal emission phase curve of the planet. The existence of such a phase shift, due to superrotating equatorial jets, was confirmed through infrared phase curve observations of HD 189733 (Knutson et al. 2007, 2009, 2012) that showed that the maximum flux occurred several hours before secondary eclipse. Later, this phenomenon was further demonstrated by many numerical simulations (e.g., Showman et al. 2008, 2009; Thrastarson & Cho 2010; Dobbson-Dixon et al. 2010; Leconte et al. 2013). In recent years significant progress has been made in understanding the superrotation phenomenon through semianalytic and linear approximation models (e.g., Gu & Ogilvie 2009; Gu & Hsieh 2011; Watkins & Cho 2010; Showman & Polvani 2011; Tsai et al. 2014). Alternatively, high-altitude optically reflective clouds located westward of the substellar point may result in opposite-direction phase shift, as detected and explained by Demory et al. (2013) for Kepler-7b and also by Angerhausen et al. (2014) for Kepler-12b and Kepler-43b. Close to the submission date of this paper Esteves et al. (2014) published a comprehensive phase curve analysis of 14 *Kepler* hot Jupiters and found that in 7 of them a phase shift of the planetary light offsets its peak from the substellar point. They concluded that eastward phase shifts dominate light from hotter planets (Kepler-76b and HAT-P-7b), while westward phase shifts dominate light from cooler planets (Kepler-7b, Kepler-8b, Kepler-12b, Kepler-41b, and Kepler-43b).

The present paper extends the superrotation hypothesis by Faigler et al. (2013) and suggests that in addition to Kepler-76 this idea may be applicable to KOI-13, HAT-P-7, and TrES-2. We show that if such a superrotation-induced phase shift is present in the *Kepler* light curve, it should show up in the basic BEER phase curve model mainly as an apparently inflated beaming amplitude. We present the details and results of the new superrotation BEER model that provides a photometry-consistent estimate of the planetary mass.

This paper is organized as follows. Section 2 presents the basic BEER model of a transiting planet assuming either a geometric or Lambertian reflection/emission phase function, and Section 3 presents the superrotation BEER model, which models also the superrotation-induced phase shift of the reflection/emission modulation. Section 4 then describes the analysis of the *Kepler* light curves of KOI-13, HAT-P-7, TrES-2, and Kepler-76; Section 5 lists the parameters of the systems from the literature used in this paper and describes how additional stellar and planetary parameters were derived from them; and Section 6 presents the results of the superrotation BEER models for the four systems. Section 7 follows by discussing the relation between the *Kepler*-band-derived phase shift and the thermal emission phase shift, Section 8 compares our results with those of previous studies, and Section 9 summarizes and discusses the findings of this work.

2. THE BASIC BEER MODEL OF A TRANSITING PLANET

We start with modeling the phase modulation of a circular-orbit transiting planet. For such a planet we define the BEER model as a modification to the method described by Faigler &

Mazeh (2011). First we define the orbital phase as

$$\phi = \frac{2\pi}{P_{\text{orb}}} (t - T_0), \quad (1)$$

where P_{orb} is the orbital period and T_0 is the midtransit time. We then calculate, using a robust linear fit (Holland & Welsch 1977), the first five Fourier series coefficients of the cleaned and detrended light curve (Mazeh & Faigler 2010),

$$\mathcal{M}(\phi) = a_0 - a_{1c} \cos \phi + a_{1s} \sin \phi - a_{2c} \cos 2\phi - a_{2s} \sin 2\phi; \quad (2)$$

where the signs are defined so that the coefficients are expected to be positive, though the fit can result in any sign for them.

In our approximation we express the relative flux modulation of the system due to a circular-orbit planet, as a result of the BEER effects, as

$$\frac{\Delta F}{F} = a_0 + A_{\text{ref}} \frac{\Phi(z)}{\sin i} + A_{\text{beam}} \sin \phi - A_{\text{ellip}} \cos 2\phi, \quad (3)$$

where a_0 is the relative flux zero point; i is the orbital inclination angle; z is the star–planet–observer angle; $\Phi(z)$ is the reflection/thermal emission phase function, which includes a $\sin i$ dependence; and A_{ref} , A_{beam} , and A_{ellip} are the reflection/emission, beaming, and ellipsoidal semi-amplitudes, respectively, which are expected to be positive. For the BEER effect amplitudes we use (Faigler & Mazeh 2011; Zucker et al. 2007; Loeb & Gaudi 2003; Morris & Naftilan 1993)

$$A_{\text{ref}} = \alpha_{\text{ref1}} \left(\frac{R_p}{a} \right)^2 \sin i,$$

$$A_{\text{beam}} = \alpha_{\text{beam}} 4 \frac{K_{\text{RV}}}{c} = 2.7 \alpha_{\text{beam}} \left(\frac{M_*}{M_\odot} \right)^{-2/3} \left(\frac{M_p}{M_{\text{Jup}}} \right) \times \left(\frac{P_{\text{orb}}}{1 \text{ day}} \right)^{-1/3} \sin i \text{ (ppm)}, \quad (4)$$

$$A_{\text{ellip}} = \alpha_{\text{ellip}} \frac{M_p}{M_*} \left(\frac{R_*}{a} \right)^3 \sin^2 i,$$

where K_{RV} is the star RV semi-amplitude; a is the orbital semimajor axis; M_* , R_* , M_p , and R_p are the mass and radius of the star and planet, respectively; and α_{ref1} , α_{beam} , and α_{ellip} are the reflection/emission, beaming, and ellipsoidal coefficients, respectively. It is important to note that α_{ref1} encapsulates two distinct and different planet luminosity sources. One is due to the planet dayside geometric albedo resulting in reflected-light phase modulation, and the other is due to the planet day–night temperature contrast, resulting in thermal-emission phase modulation. While we expect both modulations to be proportional to $(R_p/a)^2$, it is only a simplifying assumption to use for both the same phase function $\Phi(z)$.

The reflection/emission phase function depends on the z angle, defined as the star–planet–observer angle, which is related to the ϕ phase through

$$\begin{aligned} \cos z &= -\sin i \cos \phi \\ \Rightarrow \cos 2z &= \sin^2 i \cos 2\phi + \text{constant term}, \end{aligned} \quad (5)$$

where throughout this discussion we ignore constant terms that are not phase dependent, as these add up to the total flux and are not measurable from the data.

A possible choice for the phase function is the geometric reflection function, which assumes that the received flux is proportional to the projected area on the sky plane of the illuminated half-sphere of the planet, as seen by the observer. Following a notation similar to Mislis et al. (2012), the geometric reflection phase function is

$$\frac{\Phi_{\text{geo}}(z)}{\sin i} = \frac{\cos z}{\sin i} = -\cos \phi. \quad (6)$$

Under this definition of the phase function, the BEER amplitudes (Equation (3)) are directly related to the Fourier coefficients measured from the light curve (Equation (2)) through

$$\{A_{\text{ref}} = a_{1c}, A_{\text{beam}} = a_{1s}, A_{\text{ellip,geo}} = a_{2c}, a_{2s} = 0\}. \quad (7)$$

It is more common, however, to model the planet as a Lambert sphere (Russell 1916; Sobolev 1975; Demory et al. 2011), which assumes that the planet surface is an ideal diffuse reflector, i.e., of equal reflection to all directions in the half-sphere facing the star, regardless of the incident light direction. The resulting Lambertian reflection phase function is

$$\Phi_{\text{Lam}} = \frac{2}{\pi} (\sin |z| + (\pi - |z|) \cos |z|), \quad \{-\pi \leq z \leq \pi\}, \quad (8)$$

where we have defined Φ_{geo} and Φ_{Lam} with the same peak-to-peak amplitude. Evaluating the Fourier series expansion of Φ_{Lam} , we realize that for all integers n the $\sin n z$ coefficients equal zero, as this function is symmetric about the $z = 0$ point. Therefore, expanding with the cosine functions, we get

$$\begin{aligned} \Phi_{\text{Lam}} = & \frac{8}{\pi^2} + \cos z + \frac{16}{9\pi^2} \cos 2z \\ & + \frac{16}{225\pi^2} \cos 4z + \text{smaller terms}. \end{aligned} \quad (9)$$

Ignoring all harmonics higher than $\cos 2z$ provides accuracy better than 1%, which gives, after translating from the z angle to the ϕ angle,

$$\frac{\Phi_{\text{Lam}}}{\sin i} \approx -\cos \phi + 0.18 \sin i \cos 2\phi + \text{a constant term}. \quad (10)$$

The resulting Φ_{Lam} form shows that geometric reflection is simply a first harmonic approximation of Lambertian reflection and that Lambertian reflection has a cosine component in the *second* harmonic. Next, from Equations (3) and (10) we get

$$\begin{aligned} \frac{\Delta F_{\text{Lam}}}{F} = & a_0 - A_{\text{ref}} \cos \phi + A_{\text{beam}} \sin \phi \\ & - (A_{\text{ellip,Lam}} - 0.18 A_{\text{ref}} \sin i) \cos 2\phi, \end{aligned} \quad (11)$$

which enables deriving the relations between the BEER amplitudes and the measured Fourier coefficients, resulting in

$$\begin{aligned} \{A_{\text{ref}} = a_{1c}, A_{\text{beam}} = a_{1s}, A_{\text{ellip,Lam}} = a_{2c} + 0.18 a_{1c} \sin i, \\ a_{2s} = 0\}. \end{aligned} \quad (12)$$

We see that the apparent unnatural definition of the reflection term in Equation (3) actually leads to a simple form for the BEER effect amplitudes, resulting in the same A_{ref} value for geometric and Lambertian reflection, representing half the peak-to-peak variation of the reflection effect in both cases. On the other hand, as demonstrated by Mislis et al. (2012), the Lambertian reflection assumption results in a larger ellipsoidal semi-amplitude $A_{\text{ellip,Lam}}$, relative to $A_{\text{ellip,geo}}$ in the geometric case. In this paper we consider the two alternative ellipsoidal semi-amplitudes using Equations (7) and (12).

3. THE SUPERROTATION BEER MODEL OF A TRANSITING PLANET

To model the superrotation-induced phase shift, we follow the model suggested by Faigler et al. (2013), while extending it to either geometric or Lambertian phase functions. To account for superrotation in our analysis, we adopt a simplistic model for the total reflection/emission modulation that is the sum of a scattered-light phase function and a *phase-shifted* emission phase function. In this model we represent the total reflection/emission modulation in the *Kepler* band as a phase-shifted Lambertian or geometric phase function. While accurate for geometric scattered-light and emission phase functions, it is only an approximation for Lambertian phase functions. Under these model assumptions, we simply need to replace ϕ with $\phi + \delta_{\text{sr}}$ in the geometric or Lambertian phase function (Equation (6) or (10)), where δ_{sr} is the phase shift in the *Kepler* band due to superrotation, assumed to be positive. Inserting each shifted phase function into Equation (3), we have for geometric reflection

$$\begin{aligned} \frac{\Delta F_{C,SR}}{F} = & a_0 - A_{\text{ref}} \cos \delta_{\text{sr}} \cos \phi + (A_{\text{beam}} + A_{\text{ref}} \sin \delta_{\text{sr}}) \\ & \times \sin \phi - A_{\text{ellip}} \cos 2\phi, \\ \implies \{ & A_{\text{ref}} \cos \delta_{\text{sr}} = a_{1c}, \quad A_{\text{beam}} + A_{\text{ref}} \sin \delta_{\text{sr}} = a_{1s}, \\ & A_{\text{ellip}} = a_{2c}, \quad a_{2s} = 0\}, \end{aligned} \quad (13)$$

or for Lambertian reflection

$$\begin{aligned} \frac{\Delta F_{L,SR}}{F} = & a_0 - A_{\text{ref}} \cos \delta_{\text{sr}} \cos \phi \\ & + (A_{\text{beam}} + A_{\text{ref}} \sin \delta_{\text{sr}}) \sin \phi \\ & - (A_{\text{ellip}} - 0.18 A_{\text{ref}} \cos 2\delta_{\text{sr}} \sin i) \cos 2\phi \\ & - 0.18 A_{\text{ref}} \sin 2\delta_{\text{sr}} \sin i \sin 2\phi, \\ \implies \{ & A_{\text{ref}} \cos \delta_{\text{sr}} = a_{1c}, \\ & A_{\text{beam}} + A_{\text{ref}} \sin \delta_{\text{sr}} = a_{1s}, \\ & A_{\text{ellip}} - 0.18 A_{\text{ref}} \cos 2\delta_{\text{sr}} \sin i = a_{2c}, \\ & 0.18 A_{\text{ref}} \sin 2\delta_{\text{sr}} \sin i = a_{2s}\}. \end{aligned} \quad (14)$$

We see that for both phase functions, a phase shift in the reflection modulation results in the additional underlined term of $A_{\text{ref}} \sin \delta_{\text{sr}}$, which inflates the $\sin \phi$ coefficient and might be wrongly interpreted as an inflated beaming amplitude. In addition, assuming Lambertian reflection yields additional smaller corrections to the $\cos 2\phi$ coefficient and to the previously assumed-to-be-zero $\sin 2\phi$ coefficient (see Equation (11) versus Equation (14)). As a summary, Table 1 lists, for the different BEER model types, the relations between the astrophysical effect amplitudes $\{A_{\text{beam}}, A_{\text{ellip}}, A_{\text{ref}}\}$ and the measured Fourier coefficients $\{a_{1c}, a_{1s}, a_{2c}, a_{2s}\}$.

4. PHOTOMETRIC ANALYSIS

In this section we describe the analysis of the *Kepler* long-cadence Pre-search Data Conditioning (PDC) light curves of the Q2 to Q16 quarters, spanning 1302 days, for KOI-13, HAT-P-7, TrES-2, and Kepler-76. The data were first cleaned and detrended following the methods described by Mazeh & Faigler (2010) and Faigler et al. (2013). We then fitted the data using Equation (2) and derived the Fourier coefficients, while masking out data points in or around the transits and occultations. To test the robustness of our process, we performed

Table 1
Relations between BEER Model Amplitudes and Fourier Coefficients

Fourier coefficients →	$\cos \phi$	$\sin \phi$	$\cos 2\phi$	$\sin 2\phi$
BEER models ↓	$(-a_{1c})$	(a_{1s})	$(-a_{2c})$	$(-a_{2s})$
Geometric Reflection	$-A_{\text{ref}}$	A_{beam}	$-A_{\text{ellip}}$	0
Lambert Reflection	$-A_{\text{ref}}$	A_{beam}	$-A_{\text{ellip}}$ $+0.18A_{\text{ref}} \sin i$	0
Geometric Superrotation	$-A_{\text{ref}} \cos \delta_{\text{sr}}$	$A_{\text{beam}} + A_{\text{ref}} \sin \delta_{\text{sr}}$	$-A_{\text{ellip}}$	0
Lambert Superrotation	$-A_{\text{ref}} \cos \delta_{\text{sr}}$	$A_{\text{beam}} + A_{\text{ref}} \sin \delta_{\text{sr}}$	$-A_{\text{ellip}}$ $+0.18A_{\text{ref}} \cos 2\delta_{\text{sr}} \sin i$	$-0.18A_{\text{ref}} \sin 2\delta_{\text{sr}} \sin i$

the same analysis on the raw *Kepler* light curves of the four systems, yielding no significant differences between the results of the two analyses.

We have paid special attention in the fitting process to deriving realistic uncertainties for the Fourier coefficients. To do that, we performed the fitting for each *Kepler* quarter separately, and we report the best-fit coefficient as $a = \text{median}\{a_q\}$, where $\{a_q\}$ are the fit results over the *Kepler* quarters. Next, we estimated the uncertainty from the scatter of $\{a_q\}$, using a modification to the Median Absolute Deviation method, as $\sigma_a = 1.253 \times \text{mean}\{|a_q - a|/\sqrt{N_q}\}$, where N_q is the number of *Kepler* quarters for which data are available. This calculation should result in uncertainties similar to linear fitting for uncorrelated Gaussian noise, while providing more realistic uncertainties for correlated noise or systematic effects. Considering the quarter-to-quarter variation is supported by Van Eylen et al. (2013), who measured seasonal variations of about 1% of the transit depth of HAT-P-7 over the *Kepler* quarters. Even more relevant to our case of periodic modulations, they also measured about 1% seasonal variations of the pulsation amplitude of the RR Lyr star KIC 6936115. In both cases Van Eylen et al. (2013) showed that the seasonal variations were over an order of magnitude larger than the naive uncertainties derived from fitting the combined *Kepler* light curve of all available quarters. Although we do not see any correlation in amplitudes measured in same season quarters (i.e., separated by 1 yr), we do measure quarter-to-quarter variations that are significantly larger than the fitting process uncertainties. Indeed, our reported uncertainties, which are derived from the quarter-to-quarter variations, are usually larger than those reported by other authors for the same quantities, but we believe that they better capture the uncertainty embedded in the data.

For KOI-13 we inflated the amplitudes by a third-light factor of 1.82 that was estimated by Szabó et al. (2011), while for the other systems we used the Kepler Input Catalog (KIC) third-light estimates. The KIC third-light average estimates for HAT-P-7, TrES-2, and Kepler-76 are 0.2%, 0.8%, and 5.7%, respectively, and incorporating or ignoring them had negligible effect on our results.

The fitted Fourier coefficients of the first two orbital-period harmonics, after correction for third light, are listed in Table 2.

5. SYSTEMS PARAMETERS FROM THE LITERATURE

For transiting planets the orbital period P_{orb} , inclination angle i , and ratio of primary radius to orbital semimajor axis R_*/a are directly measurable from the transit light curve. When combined with a stellar model for the primary mass M_* and

the effect coefficients α_{beam} and α_{ellip} , which also depend on the stellar parameters, the planetary mass can be independently estimated from either the beaming or the ellipsoidal amplitude, using Equation (4). To estimate the planetary mass from the different models, we used the systems parameters available in the literature. The upper section of Table 3 lists the parameter values used from the literature for the four systems. The lower section of the table lists additional parameters that we derived from the literature parameters listed in the upper section.

We estimated α_{beam} by numerically shifting spectra from the library of Castelli & Kurucz (2004) models against the *Kepler* response function following Faigler et al. (2012), while taking into account the photon-counting nature of *Kepler* (Bloemen et al. 2011). The α_{ellip} coefficient was estimated using the interpolated limb and gravity darkening coefficients from Claret & Bloemen (2011) and the stellar parameters, with the Morris & Naftilan (1993) equation (see Mazeh & Faigler 2010).

To estimate the maximum fraction of the reflection/emission amplitude originating from thermal reemission, we follow Cowan & Agol (2011) and derive the no-albedo, no-redistribution, effective dayside temperature $T_{\epsilon=0}$, which translates in the *Kepler* band to the maximum emission amplitude $A_{\text{ref}, \epsilon=0}$, both listed in Table 3 for the four systems.

KOI-13 is a hierarchical triple stellar system, where KOI-13A and KOI-13B are common proper-motion fast-rotating A-type stars ($V_A = 9.9$, $V_B = 10.2$) with $\sim 1.2'$ angular separation, and KOI-13C is a $0.4-1 M_{\odot}$ star on a 65.8 day orbit around KOI-13B (Aitken 1904; Dommangeat & Nys 1994; Szabó et al. 2011; Santerne et al. 2012). KOI-13b is a $\sim 1.4 R_{\text{Jup}}$ planet on a 1.76 day orbit around the system main component KOI-13A (Szabó et al. 2011; Barnes et al. 2011; Santerne et al. 2012; Batalha et al. 2013; Shporer et al. 2014). Santerne et al. (2012) determined, through spectroscopic RV observations of the system, a 3σ upper limit of $14.8 M_{\text{Jup}}$ for the mass of KOI-13b. For this system we used the transit derived parameters from Barnes et al. (2011), which successfully modeled the asymmetry of the KOI-13 transit light curve assuming a gravity-darkened rapidly rotating host star in order to constrain the system's spin-orbit alignment and transit parameters.

HAT-P-7b is a $1.8 M_{\text{Jup}}$, $1.5 R_{\text{Jup}}$ planet on a 2.2 day retrograde orbit around a 9.7 mag evolved F6 star (Pál et al. 2008; Winn et al. 2009). For this system we used the transit derived parameters from Welsh et al. (2010) and the stellar parameters derived through asteroseismology by Christensen-Dalsgaard et al. (2010).

TrES-2b is the first transiting planet discovered in the *Kepler* field (O'Donovan et al. 2006). It is a $1.17 M_{\text{Jup}}$, $1.16 R_{\text{Jup}}$ planet on a 2.47 day orbit around a 11.3 mag G0V star.

Table 2
Derived Fourier Coefficients

Fourier coefficients → System ↓	$\cos \phi$ ($-a_{1c}$)	$\sin \phi$ (a_{1s})	$\cos 2\phi$ ($-a_{2c}$)	$\sin 2\phi$ ($-a_{2s}$)	
KOI-13	-71.0 ± 0.7	8.2 ± 0.7	-55.9 ± 0.8	-2.0 ± 1.1	ppm
HAT-P-7	-32.2 ± 0.9	6.6 ± 1.1	-14.8 ± 1.2	-0.4 ± 0.6	ppm
TrES-2	-1.5 ± 1.1	1.9 ± 1.3	-2.9 ± 0.6	-0.6 ± 0.6	ppm
Kepler-76	-54.4 ± 2.3	13.1 ± 1.3	-12.7 ± 1.6	-2.8 ± 0.8	ppm

Table 3
System Parameters from the Literature

	KOI-13	HAT-P-7	TRES-2	Kepler-76	
T_{eff} (K)	8500 ± 400^a	6350 ± 80^c	5850 ± 50^i	6300 ± 200^l	Host star effective temperature
M_* (M_{\odot})	$2.05 \pm 0.2^{a,b}$	1.53 ± 0.04^f	0.94 ± 0.05^j	1.2 ± 0.2^l	Host star mass
[m/H] (dex)	$0.2 \pm 0.1^{a,b}$	0.3 ± 0.1^c	-0.1 ± 0.1^i	-0.1 ± 0.2^l	Host star metallicity
R_*/a	0.2237 ± 0.0041^m	0.241 ± 0.001^h	0.126 ± 0.001^j	0.2209 ± 0.0027^l	Fractional primary radius
R_p/a	0.0189 ± 0.0004^m	0.0187 ± 0.0001^h	0.0158 ± 0.0001^j	0.0214 ± 0.0008^l	Fractional planet radius
Inclination (deg)	85.9^m	83.1^h	83.9^j	78.0^l	Orbital inclination
Period (days)	1.7635877^c	2.20473^h	2.47061320^j	1.54492875^l	Orbital period
K_{RV} (ms^{-1})	$< 1.3^d$	212 ± 5^e	181.3 ± 2.6^k	306 ± 20^l	Spectroscopic RV semiamplitude
$M_{p,RV}$ (M_{Jup})	$< 14.8^d$	1.82 ± 0.05	1.17 ± 0.04	2.0 ± 0.26	Planet mass derived from RV
α_{beam}	0.63 ± 0.05	0.91 ± 0.04	0.99 ± 0.04	0.92 ± 0.04	Beaming coefficient
α_{ellip}	1.53 ± 0.08	1.21 ± 0.03	1.31 ± 0.03	1.22 ± 0.03	Ellipsoidal coefficient
$T_{\epsilon=0}$ (K)	3630	2800	1880	2670	Planet max. dayside temperature
$A_{\text{ref},\epsilon=0}$ (ppm)	82	34	3.4	37	Planet max. emission semiamplitude

Notes.

- ^a Szabó et al. (2011).
- ^b Uncertainties added by authors.
- ^c Batalha et al. (2013).
- ^d 3σ upper limit (Santerne et al. 2012).
- ^e Pál et al. (2008).
- ^f Christensen-Dalsgaard et al. (2010).
- ^g Winn et al. (2009).
- ^h Welsh et al. (2010).
- ⁱ Sozzetti et al. (2007).
- ^j Barclay et al. (2012).
- ^k O’Donovan et al. (2006).
- ^l Faigler et al. (2013).
- ^m Barnes et al. (2011).

For this system we used the transit-derived parameters and the asteroseismology-derived stellar parameters from Barclay et al. (2012).

Kepler-76b is a $2 M_{\text{Jup}}$, $1.25 R_{\text{Jup}}$ planet orbiting a 13.3 mag F star in 1.55 days. For this system we used the transit-derived parameters and spectroscopic stellar parameters from Faigler et al. (2013).

6. RESULTS

We are now in a position to estimate the planetary mass using the different models and compare it with the mass estimate derived from the RV semiamplitude $M_{p,RV}$. For the unshifted geometric/Lambert reflection models, the beaming/ellipsoidal-based mass estimates can be derived directly from their respective semiamplitudes using Equation (4), Table 1, and Table 2. For the geometric/Lambert superrotation models we fitted the light-curve Fourier coefficients, using the system parameters and the superrotation model equations, while deriving the planetary mass $M_{p,sr}$, reflection coefficient $\alpha_{\text{ref}1}$, and phase shift δ_{sr} , which minimize the χ^2 of the fit. Table 4 lists the planetary masses, phase-shift angles, and reflection coefficient estimates assuming the different models and their corresponding χ^2 values. For Kepler-76, HAT-P-7, and KOI-13, χ^2 -tests show that the

Lambert superrotation BEER model is preferable over a zero-phase-shift null model, with confidence levels of 7.4σ , 3.3σ , and 1.4σ , respectively. For TrES-2 the Lambert superrotation model is not preferable over the unshifted model, resulting in a phase shift that is consistent with zero. For the three detections the resulting superrotation phase shift angle is small and well within the theoretical limit of 60° predicted by Showman & Guillot (2002). Also, for all four systems the mass estimate derived from the Lambert superrotation BEER model is consistent with the RV-based planetary mass, indicating that the Lambert superrotation model resolves the inconsistency and provides a good photometric estimate for the planet mass, derived *solely* from the *Kepler* photometry, given a good stellar model.

The χ^2 -tests are valid in these cases as we assume that our measured amplitude uncertainties are well estimated (see Section 4). To verify this claim, we also fitted the same BEER models to the out-of-transit data points and calculated the *F*-test confidence levels of the fits. For the three detections KOI-13, HAT-P-7, and Kepler-76 the *F*-test confidence levels were better than the χ^2 -test confidence levels, both indicating preference for the superrotation models.

Interestingly, Table 4 shows that the planetary mass derived by the superrotation model $M_{p,sr}$ is very close to the mass derived directly from the ellipsoidal amplitude $M_{p,\text{ellip}}$. This is because

Table 4
Planetary Mass Estimates and Superrotation Phase-shift Angle

	KOI-13	HAT-P-7	TRES-2	Kepler-76	
$M_{p,RV} (M_{Jup})$	$<14.8^f$	1.82 ± 0.05	1.17 ± 0.04	2.0 ± 0.26	Planet mass derived from RV
Geometric reflection					
$M_{p,beam} (M_{Jup})$	9.4 ± 1.3	4.6 ± 0.8	0.90 ± 0.66	7.0 ± 1.2	Planet mass from beaming
$M_{p,ellip} (M_{Jup})$	7.0 ± 0.9	1.42 ± 0.12	1.11 ± 0.23	1.25 ± 0.28	Planet mass from ellipsoidal
χ^2_{null}	14.1	17.5	7.7	74.1	χ^2 of unshifted null model
Lambert reflection					
$M_{p,beam} (M_{Jup})$	9.4 ± 1.3	4.6 ± 0.8	0.90 ± 0.66	7.0 ± 1.2	Unshifted Lambert reflection
$M_{p,ellip} (M_{Jup})$	8.6 ± 1.1	1.97 ± 0.14	1.22 ± 0.25	2.21 ± 0.43	Planet mass from ellipsoidal
χ^2_{null}	4.2	12.2	1.4	55.5	χ^2 of unshifted null model
Geometric superrotation					
$M_{p,sr} (M_{Jup})$	7.0 ± 0.9	1.42 ± 0.13	1.11 ± 0.23	1.25 ± 0.28	Shifted geometric reflection
δ_{sr} (deg)	1.7 ± 0.8	8.0 ± 2.0	-12 ± 51	11.2 ± 1.5	Planetary mass
α_{refl}	0.20 ± 0.01	0.093 ± 0.003	0.006 ± 0.004	0.12 ± 0.01	phase shift angle
χ^2	6.2	0.5	6.9	13.2	Reflection coefficient
P	$4.7E - 3 (2.8\sigma)$	$3.7E - 5 (4.1\sigma)$	$3.8E - 1 (0.9\sigma)$	$5.9E - 15 (7.8\sigma)$	χ^2 of the model
					χ^2 -test confidence level
Lambert superrotation					
$M_{p,sr} (M_{Jup})$	8.6 ± 1.1	1.97 ± 0.14	1.13 ± 0.24	2.18 ± 0.42	Shifted Lambert reflection
δ_{sr} (deg)	0.8 ± 0.9	5.4 ± 1.5	13 ± 54	9.2 ± 1.3	Planetary mass
α_{refl}	0.20 ± 0.01	0.092 ± 0.003	0.006 ± 0.004	0.12 ± 0.01	phase shift angle
χ^2	2.4	1.5	1.24	0.1	Reflection coefficient
P	$1.8E - 1 (1.4\sigma)$	$1.1E - 3 (3.3\sigma)$	$7.3E - 1 (0.4\sigma)$	$9.8E - 14 (7.4\sigma)$	χ^2 of the model
					χ^2 -test confidence level

introducing the additional phase-shift parameter δ_{sr} into the model can significantly modify the beaming amplitude A_{beam} while keeping the ellipsoidal amplitude A_{ellip} unchanged for geometric phase function, or almost unchanged for Lambertian phase function (see Table 1). As a result, the superrotation model best fit will converge to a phase-shift value that modifies the beaming amplitude so that its resulting planetary mass aligns with the ellipsoidal-derived mass.

Figure 1 presents the cleaned and detrended data points, folded at the orbital period and grouped into 50 phase bins, and the best-fit preferred models of the four systems. The figure also shows the Lambert reflection/emission, beaming, and ellipsoidal models and marks the phase of the maximum reflection/emission modulation, which for Kepler-76, HAT-P-7, and KOI-13 is smaller than 0.5 owing to the superrotation phase shift. Note, however, that the model fitting was performed on the derived Fourier coefficients and not directly on the data points. The folded and binned light-curve data are plotted here for illustrating the periodic modulation.

7. THE SUPERROTATION PHASE SHIFT

The *Kepler*-band reflection/emission modulation is a combination of light scattered off the planet surface (reflection), together with radiation absorbed and later thermally reemitted (emission). This point is important, as we expect superrotation to shift only the thermal reemission, while leaving the scattered-light component unshifted. For the four systems the measured reflection/emission amplitude is smaller than, or similar to, the maximum thermal emission amplitude $A_{ref,\epsilon=0}$ listed in Table 3, suggesting that the fraction of thermal emission in the visual *Kepler* light-curve phase modulation is probably significant. Nevertheless, the superrotation phase shift that we derive in the *Kepler* band can serve only as a lower limit for the emission phase shift, while its actual value depends on the ratio

$$\mathcal{R} = \frac{a_{scatter}}{a_{1c}}, \quad (15)$$

where $a_{scatter}$ is the scattered-light amplitude parameter and a_{1c} is the derived total *unshifted* reflected/emitted amplitude, in the *Kepler* band. The [0–1] range of \mathcal{R} , resulting from the [0– a_{1c}] range of the $a_{scatter}$ parameter, covers the entire range of emission-only to scatter-only planet irradiance, and any mixed emission/scattering in between, and is related to the thermal emission phase shift $\delta_{emission}$ through

$$\tan(\delta_{emission}) = \frac{\tan(\delta_{sr})}{1 - \mathcal{R}}. \quad (16)$$

Figure 2 presents for the three detections Kepler-76, HAT-P-7, and KOI-13 the dependence of the thermal emission phase shift on \mathcal{R} , given the derived phase shifts in the *Kepler* band, and assuming geometric phase functions for both the scattered light and the emission modulations. The figure also marks the expected values for \mathcal{R} at several dayside temperatures. The \mathcal{R} value at each temperature was derived by estimating the emission amplitude as blackbody emission in the *Kepler* band from the dayside, assuming no heat redistribution, i.e., a dark nightside.

8. DETAILED COMPARISON WITH PREVIOUS STUDIES

In this section we compare our results with those of previous phase modulation studies and discuss specific features of each system.

8.1. KOI-13

Shporer et al. (2011), Mazeh et al. (2012), Esteves et al. (2013), and Angerhausen et al. (2014) analyzed the *Kepler* light curve of KOI-13 and derived BEER amplitudes that are all within 1.4σ of the amplitudes we report here, except for the beaming amplitude that was not detected by Angerhausen et al. (2014). We also find a significant third harmonic amplitude of 7.4 ± 0.5 ppm with a phase shift of 1.1 rad (see the KOI-13 residuals in Figure 1), which is consistent with the KOI-13 third harmonic modulation detected by Esteves

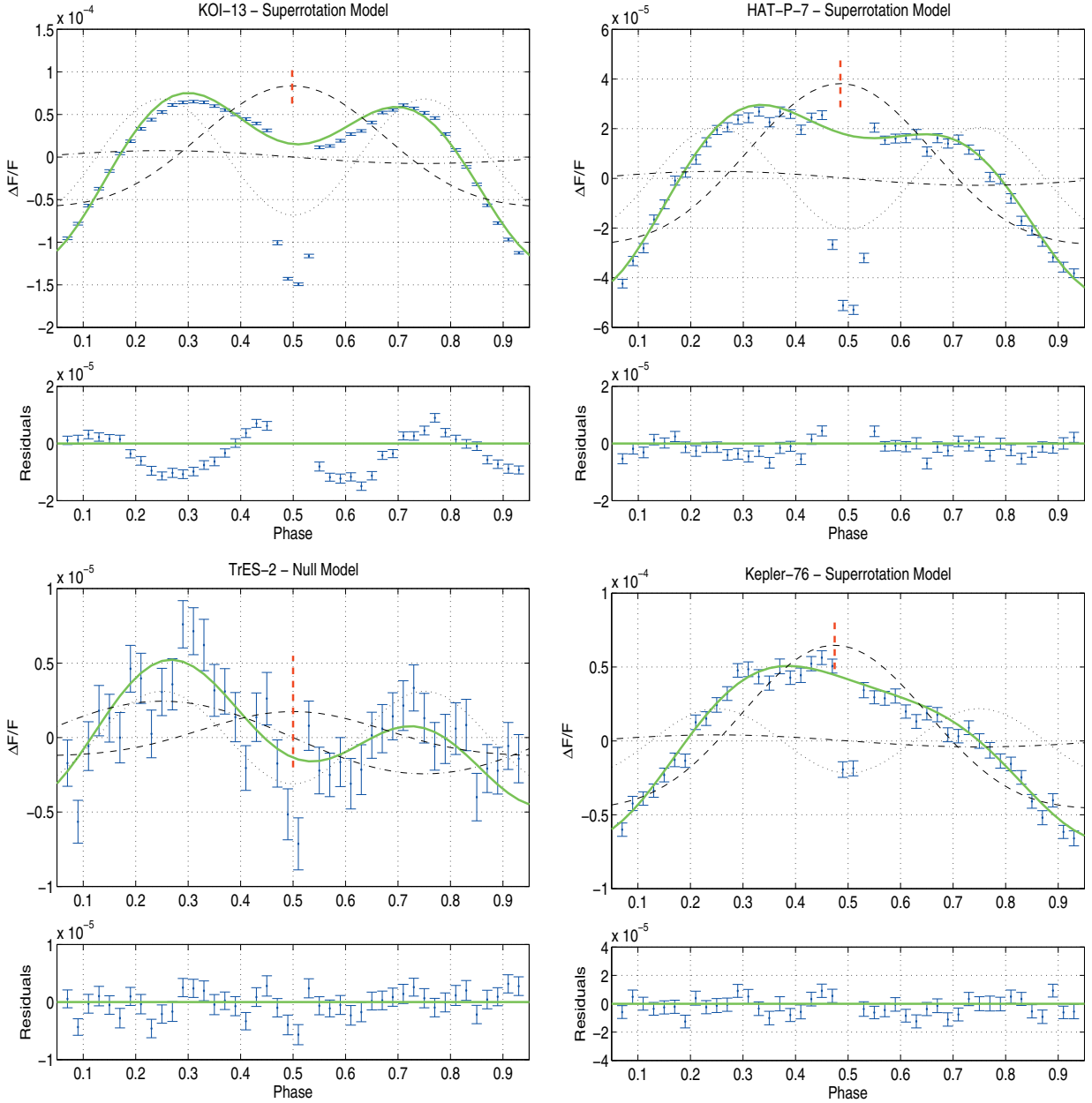


Figure 1. Binned, cleaned, and detrended data points and best-fit preferred model of the four systems, folded at the orbital period. In the top panel of each plot, the solid line presents the Lambert superrotation model for Kepler-76, HAT-P-7, and KOI-13 and the unshifted BEER model for TrES-2, and the dots with error bars present the binned data points. The dashed, dot-dashed, and dotted lines present the Lambert reflection/emission, beaming, and ellipsoidal models, respectively. The vertical red dashed lines mark the phases of maximum reflection/emission, which are 0.474, 0.485, and 0.498 for Kepler-76, HAT-P-7, and KOI-13, respectively. The residuals are plotted in the bottom panel. Note the different scales of the top and bottom panels of each plot.

et al. (2013). They suggest that this modulation may be a result of the gravity darkening of the fast-rotating host star KOI-13A. For the planetary mass, Mazeh et al. (2012) and Esteves et al. (2013) report an inflated-beaming-based mass estimate, by 1.8σ and 2.2σ respectively, relative to the mass derived from the ellipsoidal amplitude, which are consistent with the findings of this work. Esteves et al. (2013) and Angerhausen et al. (2014) also derived dayside brightness temperatures for KOI-13b of 3706 K and 3421 K, respectively, which are close to our estimate of 3630 K for $T_{\epsilon=0}$. Such day-

side temperatures are consistent with an emission-only, zero-scattered-light phase function ($\mathcal{R} = 0$), resulting in an emission phase shift δ_{emission} that is identical to the phase shift derived from the visual *Kepler* light curve, assuming a cold nightside (see Figure 2).

8.2. HAT-P-7

As one of the most studied systems in the *Kepler* field, there are multiple studies of the HAT-P-7 *Kepler* light-curve

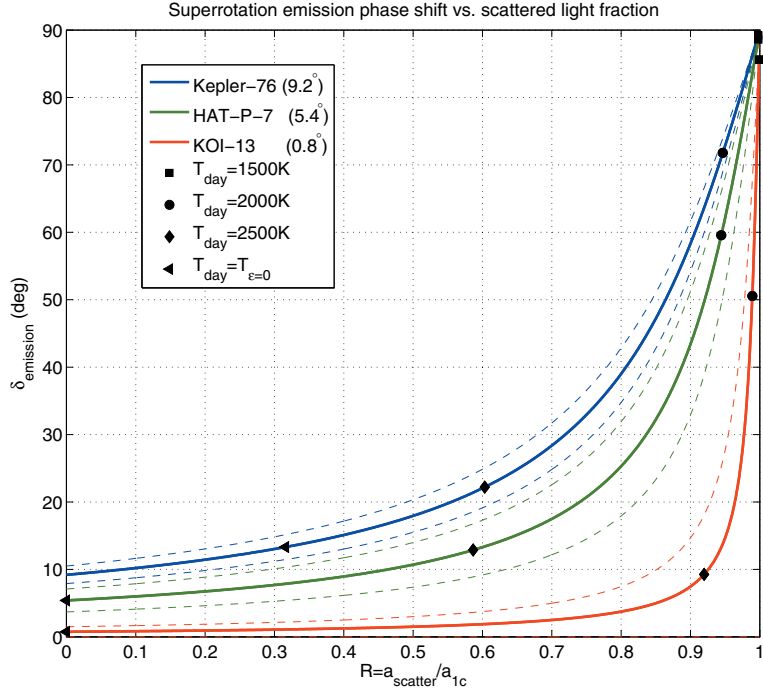


Figure 2. Expected thermal emission phase-shift angle δ_{emission} as a function of the ratio of scattered light to total unshifted reflected/emitted light $\mathcal{R} = a_{\text{scatter}}/a_{1c}$ in the *Kepler* band for the three detections Kepler-76, HAT-P-7, and KOI-13. The dashed lines represent the 1σ range of the same color plot. The black markers show the expected system position on each plot for several dayside temperature values, assuming blackbody emission from the dayside and a dark nightside. $T_{\epsilon=0}$ is the no albedo, no redistribution, effective dayside temperature listed in Table 3.

phase modulations (Borucki et al. 2009; Welsh et al. 2010; Esteves et al. 2013; Angerhausen et al. 2014). Esteves et al. (2013) analyzed the short-cadence Q0–Q14 *Kepler* light curve of HAT-P-7 and derived amplitudes that are within up to 1.2σ of the amplitudes we report here. They also derived an ellipsoidal-based planetary mass estimate that is consistent at the 1.6σ level with the RV-derived mass, while reporting a significantly inflated-beaming-based mass estimate that is more than 13σ larger than the RV-based estimate, a behavior that is consistent with the finding of this work. Angerhausen et al. (2014) analyzed the short-cadence Q0–Q15 *Kepler* light curve of HAT-P-7 but report amplitudes that differ by 1.2σ – 3.0σ relative to the amplitudes we derive, a difference that may be a result of underestimated uncertainties. Esteves et al. (2013) also derived a dayside brightness temperature of 2846 K, which is close to our estimate of 2800 K for $T_{\epsilon=0}$. Such temperatures are again consistent with a fully thermal, zero-scattered-light phase function ($\mathcal{R} = 0$) and a thermal-emission phase shift δ_{emission} that is identical to the visual *Kepler* light-curve phase shift, assuming a cold nightside.

8.3. *TrES-2*

Barclay et al. (2012), Esteves et al. (2013), and Angerhausen et al. (2014) used the short-cadence *Kepler* light curve of *TrES-2* to derive its phase curve amplitudes, which are all within up to 1.2σ of the amplitudes we report here. We note, though, that our amplitude uncertainties, which are derived from the quarter-to-quarter variations, are 2–4 times larger than the uncertainties they report. For the planetary mass, Barclay et al. (2012) report about 2σ difference between the mass derived from the ellipsoidal and the beaming amplitude, while Esteves et al. (2013) report consistent planetary mass derived from the two

effects. Consistent with Esteves et al. (2013), our analysis for *TrES-2* shows no preference for a superrotation model, making our derived reflection/emission phase shift for this system consistent with zero. Esteves et al. (2013) and Angerhausen et al. (2014) also derived dayside brightness temperatures of 1910 K and 1947 K, respectively, which are close to our estimate of 1880 K for $T_{\epsilon=0}$. Such temperatures are consistent with zero scattered light ($\mathcal{R} = 0$), yielding thermal-emission phase shift δ_{emission} that is consistent with zero, based on our analysis of the *Kepler* light curve.

8.4. *Kepler-76*

In the planet discovery paper, Faigler et al. (2013) derived BEER amplitudes from the *Kepler* raw light curves of Q2–Q13 that are within 1.3σ of the amplitudes derived here. Angerhausen et al. (2014) used the *Kepler* PDC light curves of Q0–Q15 to derive the phase curve amplitudes and the occultation depth of *Kepler-76*. Their derived amplitudes are again consistent within 1.3σ with the amplitudes we report. They also obtained a planet brightness temperature of 2780 K, which is close to our estimate of 2670 K for $T_{\epsilon=0}$. Figure 2 shows that the derived $T_{\epsilon=0}$ yields minimum scattered-light ratio \mathcal{R} of 0.32 and minimum emission phase shift δ_{emission} of $13^{\circ}3$.

9. SUMMARY AND DISCUSSION

Several authors detected inconsistencies between planetary mass derived from the beaming amplitude and the one derived from the ellipsoidal amplitude for the four transiting hot Jupiters: KOI-13b, HAT-P-7b, *TrES-2*b, and *Kepler-76*b (Mazeh et al. 2012; Shporer et al. 2011; Esteves et al. 2013; Barclay et al. 2012; Faigler et al. 2013). In addition, RV measurements,

available for HAT-P-7, TrES-2, and Kepler-76 (Winn et al. 2009; O’Donovan et al. 2006; Faigler et al. 2013), show spectroscopic RV amplitudes that are significantly smaller than the beaming-derived RV ones, pointing to inflated beaming amplitudes. In their discovery paper, Faigler et al. (2013) suggested that the inconsistency of the Kepler-76 beaming amplitude can be explained by a phase shift of the reflection/emission modulation due to the hot Jupiter superrotation phenomenon predicted by Showman & Guillot (2002) and later observed by Knutson et al. (2007, 2009, 2012) in the infrared. Here we extend and test this model also for KOI-13b, HAT-P-7b, and TrES-2b.

To allow the BEER model to account for superrotation, we developed analytic approximations for the amplitudes of the first two harmonics of the BEER modulation of a hot Jupiter system, assuming

1. a circular orbit;
2. that planetary mass is negligible relative to the star mass;
3. a first-order approximation for the ellipsoidal variation;
4. a superrotation-induced phase-shifted Lambertian or geometric reflection/emission phase function.

For Kepler-76 and HAT-P-7 χ^2 -tests show that the Lambert superrotation BEER model yields a better fit to the data and is highly preferred over the unshifted null model, while for KOI-13 it is preferable only at the 1.4σ level. For TrES-2 we find no preference for the superrotation model. Nevertheless, for all four systems the planet mass estimate derived from the Lambert superrotation BEER model is highly consistent with the planetary mass derived or constrained by RV studies, suggesting that the Lambertian superrotation model yields a good photometric estimate for the planet mass, given a good stellar model.

Initially, the phase-shifted emission modulation was identified in the *Kepler* band owing to its “leakage” into the a_{1s} coefficient, resulting in an apparently inflated beaming amplitude. It is interesting to check the dependence of this “leakage” phenomenon on the planetary parameters of the system. Using the relations in Table 1, the relative addition to the A_{beam} amplitude, due to phase-shifted emission, is

$$\frac{A_{\text{ref}} \sin \delta_{\text{sr}}}{A_{\text{beam}}} \propto \frac{R_p^2}{M_p P_{\text{orb}}} \quad (17)$$

while the right-hand side of the equation results from Equation (4). Considering that over the secondary-mass range of $1\text{--}100 M_{\text{Jup}}$, covering Jupiters to late M dwarfs, the radius remains almost unchanged at about $1 R_{\text{Jup}}$, the dependence above suggests that the relative inflation of the beaming amplitude is at maximum at the $1 M_{\text{Jup}}$ end of the range. Adding to that the P_{orb} dependence, we conclude that close-in, hot Jupiters are expected to show the most apparent inflated beaming amplitude. It is then not a surprise that this phenomenon was initially discovered in hot Jupiters and is in agreement with the phase-shifted reflection/emission modulations of Kepler-76, HAT-P-7, and KOI-13 reported by this study.

Detailed phase curve studies, such as the one we present here and alike (e.g., Esteves et al. 2014), open the opportunity to estimate the mass and investigate the atmospheric properties of multiple close-in exoplanets, through analysis of the precise photometric light curve produced by space telescopes like *CoRoT* and *Kepler*. Such analyses of photometric light curves of future missions, like TESS and PLATO, cannot only discover nontransiting stellar binaries and exoplanets (Faigler et al. 2012,

2013) but also provide consistent planetary mass and density estimates of transiting exoplanets, and even identify close-in planets with unique, or nonordinary, phase curve behavior, as targets for spectroscopic and IR follow-up. These phase curve studies can serve as a highly efficient filter for focusing the research on transiting exoplanet systems with the most intriguing mass, radius, density, and phase curve features, so that future IR observations and transmission-spectroscopy resources are efficiently assigned to systems that are most valuable for our understanding of planetary atmospheres.

We are indebted to Shay Zucker for numerous helpful discussions. We thank the anonymous referee for his highly valuable remarks and suggestions. The research leading to these results has received funding from the European Research Council under the EU’s Seventh Framework Programme (FP7/ (2007-2013)/ERC Grant Agreement No. 291352). This research was supported by the Israel Science Foundation (grant No. 1423/11) and the Israeli Centers Of Research Excellence (I-CORE, grant No. 1829/12). We feel deeply indebted to the team of the *Kepler* mission, which enabled us to search and analyze their unprecedentedly accurate photometric data. All the photometric data presented in this paper were obtained from the Multimission Archive at the Space Telescope Science Institute (MAST). STScI is operated by the Association of Universities for Research in Astronomy, Inc., under NASA contract NAS5-26555. Support for MAST for non-*HST* data is provided by the NASA Office of Space Science via grant NNX09AF08G and by other grants and contracts.

REFERENCES

- Aitken, R. G. 1904, *LicOB*, 3, 6
- Angerhausen, D., DeLarme, E., & Morse, J. A. 2014, arXiv:1404.4348
- Barclay, T., Huber, D., Rowe, J. F., et al. 2012, *ApJ*, 761, 53
- Barnes, J. W., Linscott, E., & Shporer, A. 2011, *ApJS*, 197, 10
- Batalha, N. M., Rowe, J. F., Bryson, S. T., et al. 2013, *ApJS*, 204, 24
- Bloemen, S., Marsh, T. R., Ostensen, R. H., et al. 2011, *MNRAS*, 410, 1787
- Borucki, W. J., Koch, D., Jenkins, J., et al. 2009, *Sci*, 325, 709
- Castelli, F., & Kurucz, R. L. 2004, arXiv:astro-ph/0405087
- Christensen-Dalsgaard, J., Kjeldsen, H., Brown, T. M., et al. 2010, *ApJL*, 713, L164
- Claret, A., & Bloemen, S. 2011, *A&A*, 529, A75
- Cowan, N. B., & Agol, E. 2011, *ApJ*, 729, 54
- Demory, B.-O., de Wit, J., Lewis, N., et al. 2013, *ApJL*, 776, LL25
- Demory, B.-O., Seager, S., Madhusudhan, N., et al. 2011, *ApJL*, 735, LL12
- Dobbs-Dixon, I., Cumming, A., & Lin, D. N. C. 2010, *ApJ*, 710, 1395
- Dommanget, J., & Nys, O. 1994, *CoORB*, 115, 1
- Esteves, L. J., De Mooij, E. J. W., & Jayawardhana, R. 2013, *ApJ*, 772, 51
- Esteves, L. J., De Mooij, E. J. W., & Jayawardhana, R. 2014, arXiv:1407.2245
- Exoplanet Encyclopedia. 2014, The Extrasolar Planets Encyclopaedia, <http://exoplanet.eu/>
- Faigler, S., & Mazeh, T. 2011, *MNRAS*, 415, 3921
- Faigler, S., Mazeh, T., Quinn, S. N., Latham, D. W., & Tal-Or, L. 2012, *ApJ*, 746, 185
- Faigler, S., Tal-Or, L., Mazeh, T., Latham, D. W., & Buchhave, L. A. 2013, *ApJ*, 771, 26
- For, B.-Q., Green, E. M., Fontaine, G., et al. 2010, *ApJ*, 708, 253
- Gu, P.-G., & Hsieh, H.-F. 2011, *Eur. Phys. J. Web Conf.*, 16, 04003
- Gu, P.-G., & Ogilvie, G. I. 2009, *MNRAS*, 395, 422
- Harrison, T. E., Howell, S. B., Huber, M. E., et al. 2003, *AJ*, 125, 2609
- Holland, P. W., & Welsch, R. E. 1977, *Commun. Stat.: Theory Methods*, A6, 813
- Kepler Exoplanets Archive. 2014, <http://exoplanetarchive.ipac.caltech.edu/>
- Knutson, H. A., Charbonneau, D., Allen, L. E., et al. 2007, *Natur*, 447, 183
- Knutson, H. A., Charbonneau, D., Cowan, N. B., et al. 2009, *ApJ*, 690, 822
- Knutson, H. A., Lewis, N., Fortney, J. J., et al. 2012, *ApJ*, 754, 22
- Koch, D. G., Borucki, W. J., Basri, G., et al. 2010, *ApJL*, 713, L79

Paper V – Hot-Jupiters Superrotation

THE ASTROPHYSICAL JOURNAL, 800:73 (10pp), 2015 February 10

FAIGLER & MAZEH

- Kopal, Z. 1959, *The International Astrophysics Series: Close Binary Systems* (London: Chapman & Hall)
- Leconte, J., Forget, F., Charnay, B., et al. 2013, *A&A*, 554, A69
- Loeb, A., & Gaudi, B. S. 2003, *ApJL*, 588, L117
- Maxted, P. F. L., Marsh, T. R., Heber, U., et al. 2002, *MNRAS*, 333, 231
- Mazeh, T. 2008, in *Tidal Effects in Stars, Planets, & Disks*, ed. M.-J. Goupil & J.-P. Zahn (EAS Pub. Series 29; Les Ulis: EDP), 1
- Mazeh, T., & Faigler, S. 2010, *A&A*, 521, L59
- Mazeh, T., Nachmani, G., Sokol, G., Faigler, S., & Zucker, S. 2012, *A&A*, 541, A56
- Mislis, D., Heller, R., Schmitt, J. H. M. M., & Hodgkin, S. 2012, *A&A*, 538, A4
- Morris, S. L. 1985, *ApJ*, 295, 143
- Morris, S. L., & Nafilan, S. A. 1993, *ApJ*, 419, 344
- O'Donovan, F. T., Charbonneau, D., Mandushev, G., et al. 2006, *ApJL*, 651, L61
- Pál, A., Bakos, G. Á., Torres, G., et al. 2008, *ApJ*, 680, 1450
- Reed, M. D., Terndrup, D. M., Ostensen, R., et al. 2010, *Ap&SS*, 329, 83
- Russell, H. N. 1916, *ApJ*, 43, 173
- Rybicki, G. B., & Lightman, A. P. 1979, *Radiative Processes in Astrophysics* (New York: Wiley)
- Santerne, A., Moutou, C., Barros, S. C. C., et al. 2012, *A&A*, 544, L12
- Seager, S., & Mallén-Ornelas, G. 2003, *ApJ*, 585, 1038
- Showman, A. P., Cooper, C. S., Fortney, J. J., & Marley, M. S. 2008, *ApJ*, 682, 559
- Showman, A. P., Fortney, J. J., Lian, Y., et al. 2009, *ApJ*, 699, 564
- Showman, A. P., & Guillot, T. 2002, *A&A*, 385, 166
- Showman, A. P., & Polvani, L. M. 2011, *ApJ*, 738, 71
- Shporer, A., Jenkins, J. M., Rowe, J. F., et al. 2011, *AJ*, 142, 195
- Shporer, A., O'Rourke, J. G., Knutson, H. A., et al. 2014, *ApJ*, 788, 92
- Sobolev, V. V. 1975, *Light Scattering in Planetary Atmospheres* (Oxford: Pergamon)
- Sozzetti, A., Torres, G., Charbonneau, D., et al. 2007, *ApJ*, 664, 1190
- Szabó, G. M., Szabó, R., Benkő, J. M., et al. 2011, *ApJL*, 736, L4
- Thrustarson, H. T., & Cho, J. Y. 2010, *ApJ*, 716, 144
- Tsai, S.-M., Dobbs-Dixon, I., & Gu, P.-G. 2014, *ApJ*, 793, 141
- Van Eylen, V., Lindholm Nielsen, M., Hinrup, B., Tingley, B., & Kjeldsen, H. 2013, *ApJL*, 774, LL19
- Vaz, L. P. R. 1985, *Ap&SS*, 113, 349
- Watkins, C., & Cho, J. Y.-K. 2010, *ApJ*, 714, 904
- Welsh, W. F., Orosz, J. A., Seager, S., et al. 2010, *ApJL*, 713, L145
- Wilson, R. E. 1990, *ApJ*, 356, 613
- Winn, J. N., Johnson, J. A., Albrecht, S., et al. 2009, *ApJL*, 703, L99
- Zucker, S., Mazeh, T., & Alexander, T. 2007, *ApJ*, 670, 1326

BEER analysis of *Kepler* and *CoRoT* light curvesIII. Spectroscopic confirmation of seventy new beaming binaries discovered in *CoRoT* light curves[★]

L. Tal-Or, S. Faigler, and T. Mazeh

School of Physics and Astronomy, Raymond and Beverly Sackler Faculty of Exact Sciences, Tel Aviv University, Tel Aviv, Israel
e-mail: levta1o@post.tau.ac.il

Received 28 April 2015 / Accepted 20 May 2015

ABSTRACT

Context. The BEER algorithm searches stellar light curves for the BEaming, Ellipsoidal, and Reflection photometric modulations that are caused by a short-period companion. These three effects are typically of very low amplitude and can mainly be detected in light curves from space-based photometers. Unlike eclipsing binaries, these effects are not limited to edge-on inclinations.

Aims. Applying the algorithm to wide-field photometric surveys such as *CoRoT* and *Kepler* offers an opportunity to better understand the statistical properties of short-period binaries. It also widens the window for detecting intrinsically rare systems, such as short-period brown-dwarf and massive-planetary companions to main-sequence stars.

Methods. Applying the search to the first five long-run center *CoRoT* fields, we identified 481 non-eclipsing candidates with periodic flux amplitudes of 0.5–87 mmag. Optimizing the Anglo-Australian-Telescope pointing coordinates and the AAOmega fiber-allocation with dedicated softwares, we acquired six spectra for 231 candidates and seven spectra for another 50 candidates in a seven-night campaign. Analysis of the red-arm AAOmega spectra, which covered the range of 8342–8842 Å, yielded a radial-velocity precision of $\sim 1 \text{ km s}^{-1}$. Spectra containing lines of more than one star were analyzed with the two-dimensional correlation algorithm TODCOR.

Results. The measured radial velocities confirmed the binarity of seventy of the BEER candidates – 45 single-line binaries, 18 double-line binaries, and 7 diluted binaries. We show that red giants introduce a major source of false candidates and demonstrate a way to improve BEER’s performance in extracting higher fidelity samples from future searches of *CoRoT* light curves. The periods of the confirmed binaries span a range of 0.3–10 days and show a rise in the number of binaries per $\Delta \log P$ toward longer periods. The estimated mass ratios of the double-line binaries and the mass ratios assigned to the single-line binaries, assuming an isotropic inclination distribution, span a range of 0.03–1. On the low-mass end, we have detected two brown-dwarf candidates on a ~ 1 day period orbit.

Conclusions. This is the first time non-eclipsing beaming binaries are detected in *CoRoT* data, and we estimate that ~ 300 such binaries can be detected in the *CoRoT* long-run light curves.

Key words. binaries: spectroscopic – binaries: eclipsing – brown dwarfs – techniques: photometric – techniques: spectroscopic – techniques: radial velocities

1. Introduction

The space-based photometric surveys *CoRoT* (Rouan et al. 1998; Baglin 2003) and *Kepler* (Borucki et al. 2010) were designed mainly to detect minute exoplanetary transits. Each of these missions has provided over 160 000 continuous stellar light curves with time-spans of tens to hundreds of days and a photometric precision of 10^{-3} – 10^{-4} per measurement (Auvergne et al. 2009; Koch et al. 2010). Hundreds of transiting planets were indeed detected (e.g., Moutou et al. 2013; Rowe et al. 2014), but the unprecedented quality of the light curves also enabled the detection of other flux variations of astrophysical origins. One such variation is the relativistic beaming effect.

Rybicki & Lightman (1979) showed that several factors contribute to the beaming effect, which increase (decrease) the observed brightness of any approaching (receding) light source by $\sim |4v_R/c|$, where v_R is the radial velocity (RV) of the source and c is the speed of light. Thus, for short-period

(1–10 days) brown-dwarfs (BDs) or massive planetary companions ($M_p \sin i \gtrsim 5 M_J$) of solar-like stars, the beaming amplitudes are in the range of 10^{-4} – 10^{-5} . Loeb & Gaudi (2003) have predicted that *Kepler*’s photometric precision would be sufficient to detect such companions. For stellar binaries with typical RV semi-amplitudes of 10 – 100 km s^{-1} , the beaming amplitudes are in the range of 10^{-3} – 10^{-4} . For this reason, Zucker et al. (2007) have predicted that *CoRoT* and *Kepler* will also detect hundreds of non-eclipsing binaries of this type, and create a new observational category: beaming binaries.

Soon after the first *Kepler* light curves became available, several studies measured the beaming effect of a few eclipsing binaries (EBs) detected by *Kepler* (e.g., van Kerkwijk et al. 2010; Carter et al. 2011). However, as mentioned by Loeb & Gaudi (2003) and by Zucker et al. (2007), for short-period binaries and planets, the amplitude of the beaming effect might be comparable to (or even smaller than) another two photometric effects – the ellipsoidal and the reflection light variations. The ellipsoidal variation is caused by tidal interactions between the two components of the binary (e.g., Morris 1985; Mazeh 2008). The reflection variation is caused by the brightness difference between

[★] Full Tables 2, 4, and 5 are only available at the CDS via anonymous ftp to cdsarc.u-strasbg.fr (130.79.128.5) or via <http://cdsarc.u-strasbg.fr/viz-bin/qcat?J/A+A/580/A21>

the “day” side and the “night” side of each component (e.g., Wilson 1990; Harrison et al. 2003). By accounting for the three effects, several studies succeeded to detect the weak beaming effect caused by a transiting BD or even a transiting massive planet in *CoRoT* and *Kepler* light curves (e.g., Mazeh & Faigler 2010; Shporer et al. 2011; Mazeh et al. 2012; Jackson et al. 2012; Mislis et al. 2012).

To find non-eclipsing short-period beaming binaries, Faigler & Mazeh (2011) introduced the BEER algorithm, which searches light curves for a combination of the three photometric effects caused by a short-period companion – the BEaming, Ellipsoidal, and Reflection periodic modulations. BEER approximates each of the three effects by a sine/cosine function relative to phase zero taken at the time of conjunction – when the lighter component is in front of the heavier one. The reflection and the beaming effects can then be approximated by cosine and sine functions with the orbital period, respectively, while the ellipsoidal effect can be approximated by a cosine function with half the orbital period.

Detection of BEER-like modulations in a stellar light curve does not yet prove the binary nature of the star, since sinusoidal flux modulations could be produced by other effects as well (e.g., Aigrain et al. 2004). To confirm BEER detections, one needs to perform RV follow-up observations (Faigler & Mazeh 2011). The first RV confirmation of non-eclipsing beaming binaries was reported by Faigler et al. (2012). Candidate binaries for that study were detected with BEER in Q0-Q2 *Kepler* light curves, and seven of them were confirmed using RV measurements.

Paper I of the current series (Faigler et al. 2013) reported the discovery of Kepler-76b – the first hot Jupiter discovered with BEER. In Paper II, Faigler & Mazeh (2015) showed evidence for equatorial superrotation of three hot Jupiters measured by *Kepler* – KOI-13, HAT-P-7, and Kepler-76b.

In this paper we present RV confirmation of seventy new beaming binaries found by BEER in *CoRoT* light curves. The targets were selected from the first five long-run center *CoRoT* fields and were confirmed using the AAOmega multi-object spectrograph (Lewis et al. 2002). Section 2 presents the BEER search applied to the *CoRoT* light curves, Sect. 3 describes the spectroscopic follow-up observations, Sect. 4 details the spectral analysis and derivation of RVs from the spectra, Sect. 5 explains the orbital solutions performed and the statistical methods applied to separate true BEER binaries from false detections, Sect. 6 discusses the use of the findings to evaluate the BEER algorithm performance, Sect. 7 focuses on the mass ratio and orbital-period distributions of the new binaries, and Sect. 8 summarizes the findings.

2. BEER photometric search for binaries

To detect beaming-binary candidates, we analyzed the ~40 000 white light curves of the *CoRoT* fields LRc01, LRc02, LRc03, LRc04, and LRc05. We did not use the red, green, or blue light curves of targets having chromatic information (e.g., Aigrain et al. 2008; Deleuil et al. 2011) due to their lower signal-to-noise ratio (S/N).

The light curve analysis consisted of several steps. First, oversampled light curves (Surace et al. 2008) were rebinned to 512 s. Then, we corrected for jumps in all light curves. Jumps were identified by calculating a median filter to each light curve and detecting outliers in its derivative. The correction was made by subtracting the median filter from the light curve around the identified jump epoch. A cosine-transform-based detrending and 4σ outliers removal were then performed using ROBUSTFIT

(Holland & Welsch 1977). Next, a fast Fourier-transform (FFT)-based power spectrum (PS) was calculated for each light curve, and the five most prominent peaks were identified and analyzed following Faigler et al. (2013). As detailed there, for each of the five peaks we derived the BEER amplitudes and the estimated mass and albedo of the presumed companion by fitting the amplitudes with a BEER model, assuming that the orbit is circular and the peak corresponds to either the orbital period or half the orbital period. Hence, for each light curve we evaluated ten possible orbital periods.

After fitting a circular BEER model to each light curve at each of its suspected periods, we assigned each fit a score in the 0–1 range, with 1 being the best. The score of each fit was calculated as

$$S_{\text{Total}} = S_{\text{BEER,S/N}} S_{\text{min,S/N}} S_{\chi^2} S_{\sin i} S_{\text{Albedo}}, \quad (1)$$

where $S_{\text{BEER,S/N}}$ is the BEER model S/N score, $S_{\text{min,S/N}}$ is the score of the minimum S/N of the two BEER harmonics, S_{χ^2} is the fit χ^2 score, $S_{\sin i}$ is the score of the model-derived $\sin i$, and S_{albedo} is the score of the model-derived geometric albedo. Each of these partial scores is the result of a dedicated scoring function that gives a score in the range of 0–1 for its associated parameter. The scoring functions we used were

$$S_{\text{BEER,S/N}} = 1 - \exp\left(-\frac{\text{BEER,S/N}}{C_{\text{BEER,S/N}}}\right), \quad (2)$$

$$S_{\text{min,S/N}} = 1 - \exp\left(-\frac{\text{min,S/N}}{C_{\text{min,S/N}}}\right), \quad (3)$$

$$S_{\chi^2} = \exp\left(-\frac{\chi^2}{C_{\chi^2}}\right), \quad (4)$$

$$S_{\sin i} = 1 - \exp\left(-\frac{\sin i}{C_{\sin i}}\right), \text{ and} \quad (5)$$

$$S_{\text{Albedo}} = \exp\left(-\frac{\max(\text{Albedo} - C_{\text{alb,m}}, 0)}{C_{\text{alb,s}}}\right), \quad (6)$$

where $C_{\text{BEER,S/N}}$, $C_{\text{min,S/N}}$, C_{χ^2} , $C_{\sin i}$, $C_{\text{alb,m}}$, and $C_{\text{alb,s}}$ are constants that calibrate the behavior of the scoring functions. The most likely orbital period of each light curve was selected as the period with the highest total score S_{Total} out of its ten evaluated periods.

As an illustration, Figs. 1 and 2 show the light curve analysis of *CoRoT* 105962436 and *CoRoT* 104674562, respectively. We present 70-day-long parts of the original and detrended light curves, the entire light curve power spectra, and the entire phase-folded and binned light curves, with the best-fit BEER models superposed. We note that the most prominent peak in Fig. 1 at 1.11 day^{-1} is caused by the ellipsoidal effect, whose frequency is twice the orbital frequency (i.e., the predicted orbital period is 1.8 days). Figure 2 shows that the BEER modulation of *CoRoT* 104674562 at a period of 4.6 days is almost buried in the noise, and from the PS it seems that the modulation at ~20.4 days is more evident. Nevertheless, thanks to its period-selection process, BEER found the correct orbital period in this case as well (as we show in Sect. 5).

After the score assignment and the best-period selection, we visually inspected the 200 highest score candidates of each field and assigned priorities of 1–3 to targets that we deemed viable binary candidates, with priority 1 assigned to the best candidates. These priorities were assigned through visual inspection

L. Tal-Or et al.: Seventy new *CoRoT* BEER binaries

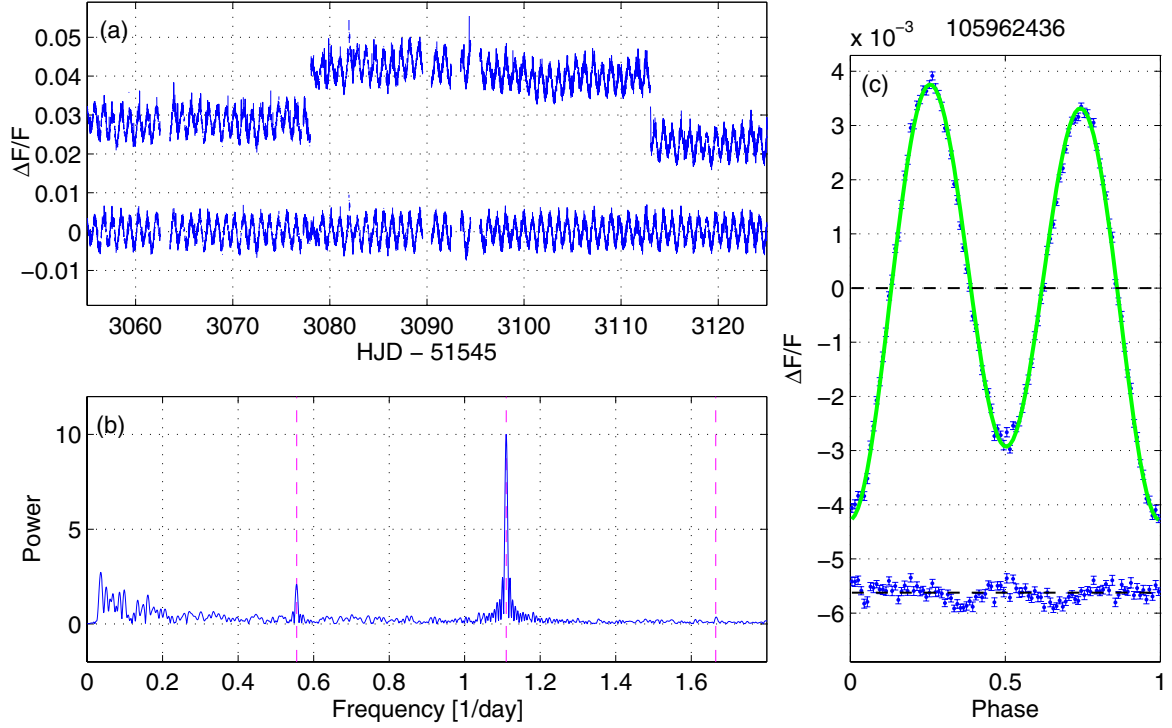


Fig. 1. BEER light curve analysis of *CoRoT* 105962436 **a)** A 70-day long part of the *CoRoT* white light curve, normalized by its median. For clarity, the original light curve was shifted upward by 0.03 relative to the cleaned and detrended one. The cleaned light curve demonstrates the jumps correction, outlier removal, and detrending functionality. **b)** FFT-based power spectrum of the detrended light curve, with its maximum value normalized to 10. Vertical dashed lines mark the first three harmonics of the candidate orbital frequency. **c)** Phase-folded and binned light curve (blue) and the best-fit BEER models assuming a circular orbit (green). The residuals were shifted downward for clarity.

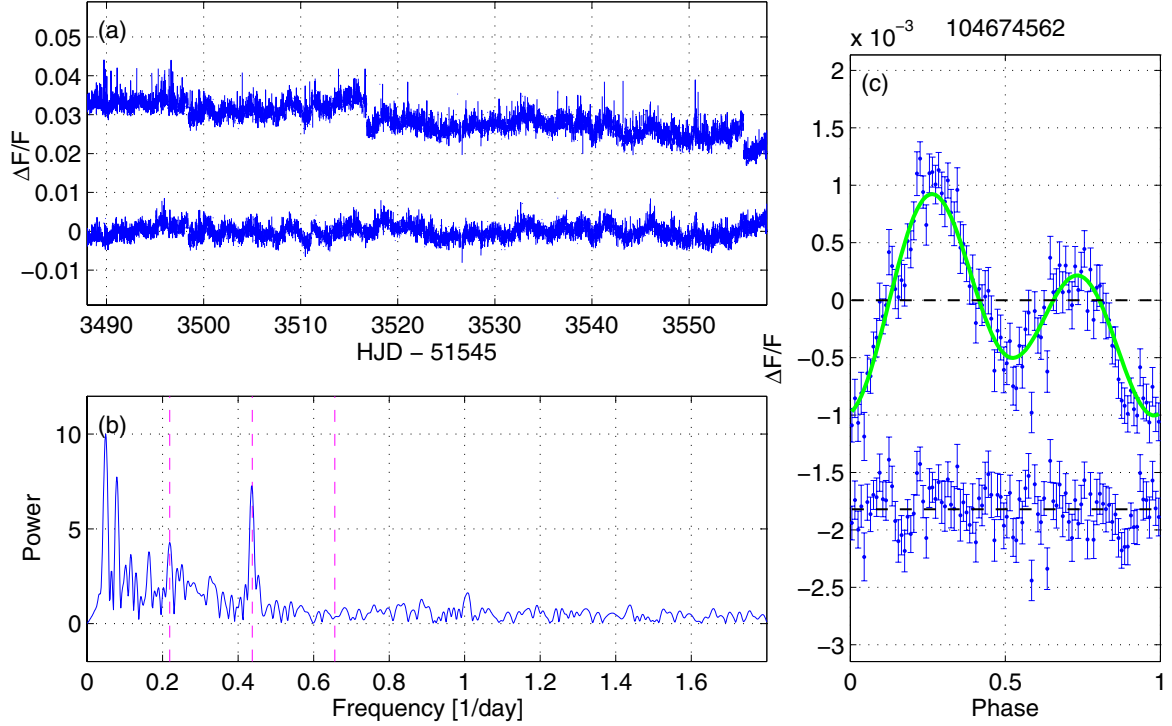


Fig. 2. BEER light curve analysis of *CoRoT* 104674562. The panels are the same as in Fig. 1.

Table 1. Selected pointing ephemeris of the five *CoRoT* fields, and the number of targets observed in each field.

Field	Mean RA (J2000)	Mean Dec (J2000)	Science targets	BEER targets
LRc01	19:26:25.34	+01:12:00.5	211	41
LRc02	18:41:52.44	+06:37:03.9	292	55
LRc03	18:32:27.45	−06:21:52.7	362	50
LRc04	18:33:50.89	+08:49:58.9	359	68
LRc05	18:39:19.29	+04:28:21.6	165	67

of the photometric power spectrum, the goodness-of-fit of the BEER model, the correlation structure of the time-domain residuals, and other target specific features. Naturally, the visual inspection method and the resulting target priorities are subjective and prone to human bias and errors, but we nevertheless used it for lack of a better software-based method at this stage.

In this way, we selected a total of 481 candidates for RV follow-up from all five fields. The assigned priorities of these candidates were later used by the AAOmega fiber-allocation software to prioritize between them in cases of conflict. The selected candidates span a range of 0.1–17 days in predicted orbital periods and of 0.3–87 mmag in photometric amplitudes. As we show below, the confirmed candidates span somewhat narrower ranges of 0.3–10 days in orbital period and of 0.5–87 mmag in photometric amplitudes.

3. AAOmega follow-up observations

We performed RV follow-up observations with the AAOmega multi-object spectrograph (e.g., [Lewis et al. 2002](#); [Smith et al. 2004](#); [Saunders et al. 2004](#)) at the Anglo-Australian Telescope (AAT). The AAOmega two-degree field of view, its three-magnitudes dynamic range, and its ability to simultaneously record up to 392 spectra are ideal for our purpose. These features enabled us to observe the majority of BEER candidates in each of the *CoRoT* fields in a single pointing. We used the AAOmega software CONFIGURE (e.g., [Lewis et al. 2002](#); [Miszalski et al. 2006](#))¹ to optimize the pointing and fibre allocation. Table 1 lists for each field the selected pointing ephemeris, the number of BEER targets observed, and the total number of science targets observed. The observed stars span the range of 12.5–16 in *V* magnitude.

In total, we observed 281 out of the 481 selected BEER candidates. Most of the candidates that were selected for follow-up but were not observed are from the LRc01 and LRc02 fields. These two fields were observed by *CoRoT* with two $1.4^\circ \times 1.4^\circ$ detectors, as opposed to the LRc03, LRc04, and LRc05 fields that were observed by *CoRoT* with only one such detector ([Moutou et al. 2013](#)). Nevertheless, to maximize the number of priority 1 candidates observed each night, we used only one pointing per field. Table 2 lists the coordinates, magnitudes, photometric ephemeris, and amplitudes of the three BEER effects for the candidates observed with AAOmega. For convenience, the confirmed binaries are indicated in the rightmost column of Table 2. To make the best use of available observing resources, we also observed several hundred *CoRoT* EBs. In this paper, however, we report only on observing non-eclipsing BEER candidates and on confirming seventy of them. We leave the EBs spectra analysis to a separate paper.

¹ Available at <http://www.aao.gov.au/science/software/configure>

The observations took place on seven consecutive nights, starting on August 02, 2012. Between two and five fields were observed each night, depending on the available time and weather conditions. We acquired six spectra for 231 candidates and seven spectra for another 50 candidates in a seven-night AAOmega campaign. Table 3 lists for each field the heliocentric Julian dates (HJDs) of mid-exposure, calculated for the mean ephemeris presented in Table 1.

We used the 1700D grating on the red arm since it was reported to give good RV precision (e.g., [Lane et al. 2011](#)). We used the 1700B grating on the blue arm since it covers several Balmer lines and also enables RV measurements of hot stars. The nominal spectral coverage is 8342–8842 Å on the red arm and 3803–4489 Å on the blue arm, but the actual coverage is smaller by up to ~ 60 Å and is different for different fibers, depending on their position on the detector.

Observations and data reduction were performed similarly to previously reported works (see e.g., [Sebastian et al. 2012](#)). In short, the observing sequence at each new pointing usually consisted of a flat and two arc frames followed by three or two exposures of 20 or 30 min, respectively.

Data reduction used the dedicated software 2DFDR ([Taylor et al. 1996](#))². The spectrum from each fiber and each subexposure was first normalized by its flat and was wavelength calibrated using the arc frames, rebinning the data onto the same linear wavelength scale to facilitate combining the subexposures. The throughput of each fiber in each subexposure was calculated using sky emission lines. An average sky spectrum was subtracted from the data using dedicated sky fibres. Finally, the subexposures were combined to give a single calibrated 60-minute exposure, weighting each subexposure by its flux level and rejecting cosmic ray hits.

Most of the exposures were made under bright sky, so the sky subtraction procedure left some residuals of telluric emission lines in the spectra. In addition, a few pixels in each spectrum were affected by bad columns of the detector. We replaced the values of the telluric-line residuals and the bad pixels with a smoothed version of the same spectrum, which was calculated using a moving median filter, 21-pixel wide. Additional 6σ outliers were later replaced the same way.

4. Spectral analysis

4.1. Non-composite spectra analysis

To derive the most precise RVs, we first searched for an optimal theoretical template spectrum for each candidate by maximizing the cross-correlation values between the candidate’s observed spectra and a set of synthetic Phoenix spectra ([Hauschildt et al. 1999](#)), calculated on a grid of effective temperature (T_{eff}), surface gravity ($\log g$), and metallicity ($[M/H]$). Line broadening due to the projected rotational velocity was added to each synthetic spectrum by convolving it with a rotational profile $G(v)$ (e.g., [Santerne et al. 2012](#); [Gray 2005](#)). To account for the instrumental broadening of the lines, each synthetic spectrum was also convolved with a Gaussian of $\sigma = 20.5 \text{ km s}^{-1}$.

Figures 3 and 4 illustrate the data and the optimization process. Figure 3 shows co-added AAOmega spectra and cross-correlation functions (CCFs) of four slowly rotating candidates (rotational broadening $\lesssim 20 \text{ km s}^{-1}$), which have different T_{eff} values and non-composite spectra. The narrow metal

² Available at <http://www.aao.gov.au/science/software/2dfdr>

L. Tal-Or et al.: Seventy new *CoRoT* BEER binaries

Table 2. Coordinates and photometric parameters of the BEER candidates observed at AAOmega.

CoRoT ID	RA (deg)	Dec (deg)	V (mag)	Orbital period (day)	Orbital phase (HJD-2 451 545)	Ellipsoidal amplitude (ppm)	Beaming amplitude (ppm)	Reflection amplitude (ppm)	Conf. flag ^d
100537909	290.7709	1.2476	13.1	5.75 0.19	2828.9 2.5	-641 267	406 207	-216 204	1
100576007	290.8286	1.6783	15.1	0.319485 0.000074	2833.575 0.017	-902 27	227 21	-187 44	0
100604403	290.8710	1.6941	13.7	3.094 0.021	2832.39 0.50	-164 24	327 17	120 26	0
100637229	290.9165	1.4645	13.8	8.73 0.17	2829.7 1.4	-675 45	480 90	-148 88	0
100677124	290.9786	0.9625	15.7	0.41720 0.00015	2833.533 0.026	-9014 67	650 581	-1291 420	0

Notes. This table is available in its entirety in a machine-readable form in <ftp://wise-ftp.tau.ac.il/pub/corotAAO> and at the CDS. A portion of the table is shown here for guidance regarding its form and content. Each line of parameters is followed by a line of uncertainties. ^(a) conf. flag: 0 – false alarm; 1 – confirmed BEER binary.

Table 3. Mid-exposure HJD–2 456 141 days.

LRc01	LRc02	LRc03	LRc04	LRc05
1.070956	–	0.998684	–	–
2.050900	1.942608	1.888283	1.996221	2.103633
3.045416	2.936347	2.882764	2.989653	3.098236
4.053797	3.942036	3.887762	3.995172	4.110621
5.104335	4.942736	4.889214	4.996094	5.049920
6.109585	5.946059	5.889688	6.001038	6.055340
–	6.950716	6.899660	7.009869	7.059933

lines weaken and wide hydrogen lines become stronger with increasing T_{eff} . Accordingly, the CCF peaks of cool stars ($T_{\text{eff}} \lesssim 7000$ K) are narrower than those of hot stars. Figure 4 shows the T_{eff} optimization plot of the coolest candidate presented in Fig. 3. The best T_{eff} for each exposure was estimated from the interpolation of its maximum-CCF versus T_{eff} curve. The best global T_{eff} for each candidate was taken as the weighted mean of the different T_{eff} values from the different exposures, taking the squares of the maximum-CCF values as weights. Surface gravity, metallicity, and projected rotational velocity were estimated for each candidate the same way. For each candidate, the nearest synthetic spectrum to its estimated spectral parameters was chosen as its best template.

The analysis, including RV derivation and orbital solutions, was independently performed both for the red-arm and blue-arm spectra. However, the results presented from this point onward are based on the red-arm spectra alone, since we generally found them to have better S/N and stability than the blue-arm spectra. For instance, Fig. 3 shows that the blue-arm CCF peaks are wider and lower than the red-arm CCF peaks of the same stars. This is partially due to the lower resolution and lower S/N of blue-arm spectra. Red-arm spectra thus provided better RV precision than blue-arm spectra, even for the hottest stars in the sample ($T_{\text{eff}} \gtrsim 8000$ K).

After optimizing the templates, we derived RVs and errors from each spectrum by calculating the CCF with the best template. At this stage, we carefully inspected the CCFs, looking for a signature of a secondary star, and identified 26 stars that present composite spectra (i.e., spectra containing lines of more than one star). Table 4 lists the 255 non-composite spectrum candidates observed and the template parameters used to derive

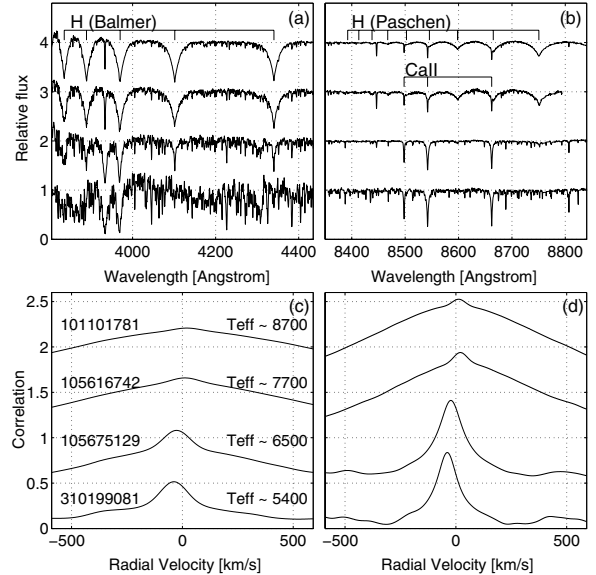


Fig. 3. Co-added AAOmega spectra (panels a) and b)) and CCFs (panels c) and d)) of four BEER candidates with different effective temperatures. For clarity, successive spectra were shifted upward by 1 and successive CCFs were shifted upward by 0.55. CoRoT IDs and estimated temperatures of the four candidates are indicated in panel c). Blue-arm spectra and their CCFs are shown on the left (panels a) and c)), while red-arm spectra and their CCFs are shown on the right (panels b) and d)). Wavelengths of Ca II and hydrogen lines are taken from Kramida et al. (2013).

their RVs. For convenience, the rightmost column identifies the confirmed BEER single-line binaries (SB1s), 45 of which were identified in that list (as explained in Sect. 5). The measured RVs of all non-composite spectrum candidates are given in machine-readable form³.

4.2. Composite spectra analysis

Composite spectra were analyzed with TODCOR (Zucker & Mazeh 1994; Mazeh & Zucker 1994) – the two-dimensional

³ <ftp://wise-ftp.tau.ac.il/pub/corotAAO>

A&A 580, A21 (2015)

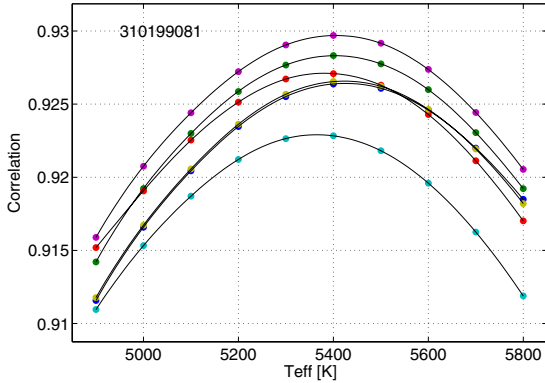


Fig. 4. T_{eff} optimization plot of CoRoT 310199081. Colored dots show the maximum-CCF values, cross-correlating its red-arm AAOmega spectra with synthetic Phoenix spectra of different T_{eff} . Solid black lines show for each exposure a SPLINE interpolation of its maximum-CCF versus T_{eff} curve.

Table 4. Template parameters of non-composite spectrum candidates.

CoRoT ID	T_{eff} (K)	$\log g$ (cgs)	[m/H] (dex)	Rot. broad. (km s $^{-1}$)	Conf. flag
100537909	6500	5.0	0.0	7	1
100576007	5400	4.0	-0.5	1	0
100604403	7000	4.5	0.0	9	0
100637229	6500	4.5	0.0	16	0
100677124	6000	4.0	+0.5	102	0

Notes. This table is available in its entirety in machine-readable form at <ftp://wise-ftp.tau.ac.il/pub/corotAAO> and at the CDS. A portion of the table is shown here for guidance regarding its form and content.

correlation algorithm. The templates were optimized in several steps. First, we searched for the best primary template (i.e., the template for the more luminous component in the spectrum) similarly to the search performed for non-composite spectra. By inspecting the CCFs and the derived RVs, we then identified for each candidate the exposures made at times when the separation between the primary and secondary sets of lines was relatively large. Using only these exposure subsets, we optimized the primary- and secondary-template T_{eff} and rotational broadening, also optimizing the flux ratio between the primary and the secondary components (TODCOR's α parameter). Metallicity and $\log g$ of the secondary template (i.e., the template for the less luminous component in the spectrum) for each candidate were fixed assuming the secondary is a dwarf ($\log g = 4.5$) with the same metallicity as its primary.

After optimizing the templates, we used TODCOR to derive the primary and secondary RVs and errors from each spectrum, fixing α to its best value. As an illustration, Fig. 5 shows a spectrum and the TODCOR plots for one of the AAOmega exposures of CoRoT 105962436 – probably an A5V–G0V double-line binary (SB2) with $\alpha \sim 0.25$. The splitting of the Ca II lines can be seen in the upper panel. The middle panel shows the corresponding TODCOR two-dimensional correlation function. The lower panel of the figure shows the primary and secondary cuts through the two-dimensional correlation function, which run through the two-dimensional correlation peak parallel to the primary and secondary RV axes (Zucker & Mazeh 1994). The correlation in

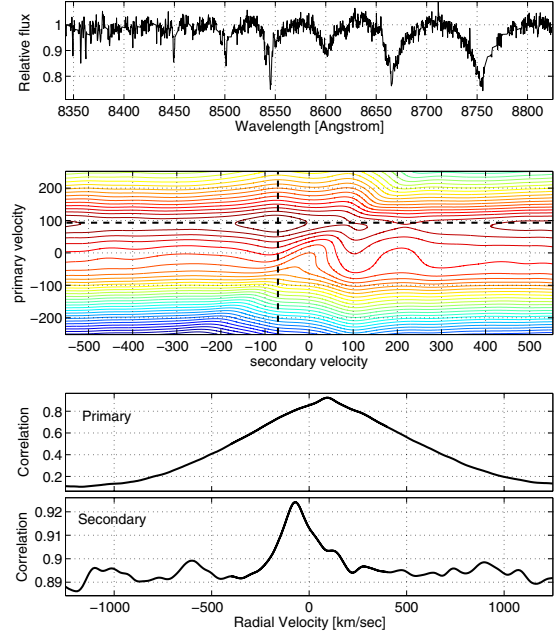


Fig. 5. Upper panel: red-arm AAOmega spectrum of the double-line BEER binary 105962436 from August 05, 2012. Middle panel: TODCOR two-dimensional correlation function for that spectrum, using the templates whose parameters are specified in Table 5. Colored solid lines connect points of equal correlation. The black dashed lines run through the two-dimensional correlation peak parallel to the primary and secondary RV axes. Bottom panel: primary and secondary cuts through the two-dimensional correlation peak.

Table 5. Template parameters of the composite-spectrum candidates.

CoRoT ID	T_{eff} (K)	$\log g$ (cgs)	[m/H] (dex)	Rot. broad. (km s $^{-1}$)	Flux ratio (α)
100688131 A	6100	4.5	0.0	13	–
100688131 B	5900	4.5	0.0	6	0.62
100906796 A	7000	4.5	0.0	60	–
100906796 B	5100	4.5	0.0	71	0.15
100976101 A	7400	4.5	0.0	1	–
100976101 B	4800	4.5	0.0	16	0.09
101177998 A	7200	4.5	0.0	41	–
101177998 B	5000	4.5	0.0	14	0.17
103833966 A	6200	5.0	+0.5	1	–
103833966 B	5600	4.5	+0.5	21	0.27

Notes. This table is available in its entirety in machine-readable form at <ftp://wise-ftp.tau.ac.il/pub/corotAAO> and at the CDS. A portion of the table is shown here for guidance regarding its form and content.

the secondary cut drops only by ~ 0.03 when moving away from the peak because we changed the velocity of the secondary template, which only contributes $\sim 25\%$ of the light, and the primary velocity was kept at its best value. Nevertheless, the secondary peak is prominent, which means that the RV of the secondary star can be measured despite the broad hydrogen lines of the primary and the relatively low flux ratio.

Table 5 lists the template parameters and α values used for the composite-spectrum BEER candidates. We only use the nomenclature “A” and “B” (both here and later in Table 8) to

denote the more and less luminous components, respectively. The measured RVs and errors of both components are given in machine-readable form⁴.

5. Orbital solutions

5.1. Confirming BEER binaries with non-composite spectra

To separate true BEER binaries from false detections (which we call false alarms for simplicity, or FAs), and to derive the orbital parameters of the true BEER SB1s, we fitted the derived RVs of non-composite spectrum candidates with a circular Keplerian model. We calculated two χ^2 statistics – χ_{null}^2 and χ_{orb}^2 , for the null hypothesis (constant RV star) and for the circular orbital solution, respectively. We took the BEER period and phase as priors by treating them as additional measurements, meaning that their squares of residuals, scaled by their error estimates, were added to χ_{orb}^2 in the search for the best fit. For the best-fit orbital parameters we also calculated the following F -statistic:

$$F = \frac{(\chi_{\text{null}}^2 - \chi_{\text{orb}}^2) / \text{DOF}_{\text{orb}}}{\chi_{\text{orb}}^2 / \text{DOF}_{\text{orb}}}, \quad (7)$$

where DOF_{null} and DOF_{orb} are the numbers of degrees of freedom of the null hypothesis and the orbital solution, respectively. Since the only free parameter of the null hypothesis is an RV offset, $\text{DOF}_{\text{null}} = N_{\text{RV}} - 1$, where N_{RV} is the number of RV points. For the orbital solution $\text{DOF}_{\text{orb}} = N_{\text{RV}} + 2 - p_{\text{orb}}$, where p_{orb} is the number of free parameters of the orbital solution, since we treated the BEER period and phase as additional measurements. For a circular orbit $p_{\text{orb}} = 4$.

To obtain a good distinction between true BEER SB1s and FAs, we used both the χ_{null}^2 -test and the F -test. The χ_{null}^2 -test was used first to screen all candidates that showed no significant RV variability within the observing run. Then the F -test was applied to candidates that passed the χ_{null}^2 -test to check the compatibility of their RVs with a circular Keplerian model at the BEER-predicted period and phase. Only candidates that passed both tests were considered as confirmed BEER SB1s.

After visual inspection of the results, particularly of a few borderline cases, we chose the critical p -values to be 10^{-6} and 0.003 for the χ_{null}^2 - and F -tests, respectively. As a consequence, 54 out of the 255 non-composite spectrum candidates passed the χ_{null}^2 -test, and 45 of them also passed the F -test and were classified as confirmed BEER SB1s. The nine candidates that passed the χ_{null}^2 -test but not the F -test might be true variables at a different orbital period, or their spectra suffer from some systematics causing RV outliers.

Another possible reason for a true BEER binary to fail our F -test is an eccentric orbit. Therefore, we also fitted each RV curve with an eccentric Keplerian model, for which $p_{\text{orb}} = 6$. The fact we have only 6–7 RV points for most of our candidates makes the DOF_{orb} of an eccentric solution as small as 2–3. Since an F -test fails at such a low number of DOF, we required a p -value improvement of at least a factor of 10 to prefer the eccentric solution over the circular one. None of the candidates fulfilled this requirement, meaning we could not find significant eccentricity in any of the confirmed SB1s.

Figure 6 shows (on a log-scale) p -value histograms of the χ_{null}^2 - and F -statistics for the 255 non-composite spectrum BEER candidates. The solid black lines represent the expected p -value distributions for RV measurements of constant-RV stars normally distributed for each star around its RV. The expected and

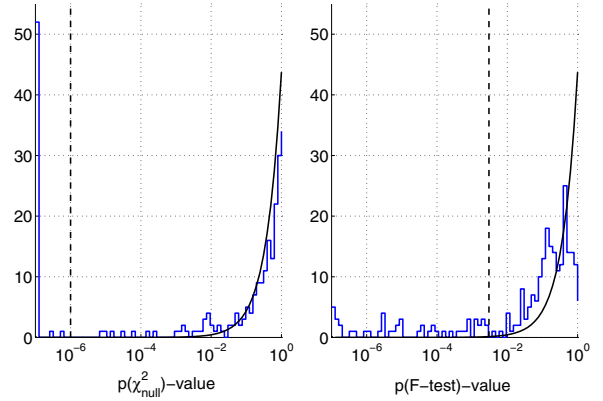


Fig. 6. Test statistics p -value histograms of the 255 non-composite spectrum BEER candidates, solving for their red-arm AAOmega RVs. The solid black lines represent a flat distribution between 0 and 1 scaled so that its integral is equal to the number of FAs. The dashed black lines mark the critical values that were chosen to separate possible BEER SB1s (to the left of the lines) from FAs (to the right of the lines). The histograms were truncated at 10^{-7} , so that the leftmost columns contain all candidates with p -values $< 10^{-7}$.

observed histograms agree fairly well, particularly for the χ_{null}^2 -statistics. The dashed black lines mark the critical values that were chosen to separate possible BEER SB1s from FAs. Only candidates found to the left of the lines in both plots were considered as confirmed BEER SB1s.

Table 6 lists the orbital parameters of the confirmed BEER SB1s. Figure 12 shows their measured AAOmega RVs and the best-fit circular Keplerian model. Their orbital periods span a range of 0.4–10 days, and their RV semi-amplitudes span a range of 6–115 km s^{-1} . Two of the confirmed BEER SB1s with the smallest RV semi-amplitudes are *CoRoT* 105659320 and 101044188 – possibly two BDs on a ~ 1 -day period orbit around F-G stars.

5.2. Confirming BEER binaries with composite spectra

There are three possible scenarios for a composite-spectrum candidate. (1) The two components in the candidate’s spectra belong to the primary and secondary stars in a short-period SB2 at the BEER-predicted period and phase. (2) One of the components belongs to a binary at the BEER-predicted period and phase, while the other component belongs to another star, either bound or unbound to the binary (i.e., a diluted BEER binary). (3) Neither of the components belongs to the BEER-predicted binary. We classified a composite-spectrum BEER candidate as confirmed if the RVs of at least one of its components was compatible with a Keplerian model at the BEER-predicted period and phase.

To assign the correct scenario to each composite-spectrum candidate and (in case of a true BEER binary) to derive its orbital parameters, we separately fitted a circular Keplerian model to its primary and secondary RVs and also calculated the p -value of the F -test in Eq. (7). Candidates in which both component’s SB1-model got a p -value < 0.001 were considered as confirmed BEER SB2s. If the SB1 model of only one of the components got a p -value < 0.001 , the candidate was considered as a diluted BEER binary. If both component’s SB1-model got a p -value > 0.001 , we considered the candidate as an FA. Similarly to non-composite spectrum candidates, the selected

⁴ <ftp://wise-ftp.tau.ac.il/pub/corotAAO>

Table 6. Orbital parameters of the 45 confirmed BEER SB1s.

CoRoT ID	P (day)	T_0 (HJD-2 456 141)	K (km s ⁻¹)	γ (km s ⁻¹)	F -test p -value	χ^2_{orb}
103924393	6.851 0.021	5.906 0.021	49.93 0.75	42.90 0.60	1.3E – 08	1.6
105767195	4.0526 0.0022	3.139 0.019	27.99 0.85	2.01 0.60	3.4E – 08	0.7
105810223	0.5929447 0.0000029	3.87271 0.00097	115.0 1.4	4.31 0.93	4.0E – 08	4.5
104674562	4.5804 0.0071	5.895 0.021	30.55 0.96	17.73 0.66	4.5E – 08	0.7
310222016	2.08218 0.00047	5.725 0.020	29.3 1.7	-30.61 0.65	4.9E – 08	3.8
310210722	6.975 0.020	7.165 0.025	47.7 1.2	11.02 0.78	1.1E – 07	7.6
105818861	1.301182 0.000054	6.0599 0.0037	57.5 1.0	9.82 0.73	1.2E – 07	3.5
101029997	3.57665 0.00044	3.361 0.011	41.42 0.88	36.17 0.59	1.3E – 07	2.7
105844488	0.554937 0.000095	2.9081 0.0021	90.2 2.1	-7.7 1.5	1.4E – 07	2.4
310215106	3.23943 0.00032	4.099 0.016	33.58 0.91	-0.07 0.69	1.7E – 07	7.4
310176634	1.26221 0.00058	5.877 0.013	17.1 1.1	-26.82 0.81	3.5E – 07	0.5
105336757	2.356960 0.000096	6.059 0.011	32.78 0.86	-7.64 0.64	3.8E – 07	3.0
105712106	3.4521 0.0020	7.165 0.010	47.04 0.78	-2.58 0.59	7.7E – 07	10.4
105403147	2.9136 0.0019	5.876 0.012	35.37 0.79	22.14 0.59	1.1E – 06	7.0
105706604	2.26769 0.00017	6.978 0.012	32.4 1.2	-17.00 0.69	2.2E – 06	4.8
105714214	3.1309 0.0051	1.950 0.012	36.57 0.82	-10.49 0.60	2.4E – 06	10.0
104295292	2.8685 0.0043	2.751 0.015	26.09 0.86	7.83 0.60	2.8E – 06	5.1
110567660	1.238837 0.000091	3.9782 0.0054	49.5 1.5	-8.1 1.0	2.9E – 06	6.0
101177265	0.6419480 0.0000050	4.0489 0.0038	36.4 1.5	35.2 1.0	3.0E – 06	3.4
101014035	0.4596816 0.0000015	4.0441 0.0021	55.3 1.7	1.9 1.2	4.1E – 06	7.6
100889978	10.160 0.026	0.734 0.093	27.38 0.80	7.84 0.98	5.4E – 06	9.4
105661774	2.22043 0.00013	2.094 0.023	31.3 2.3	26.2 1.4	6.2E – 06	2.0
105618890	2.6219 0.0012	1.774 0.013	39.5 1.1	21.24 0.81	6.5E – 06	11.0
105802223	1.414011 0.000040	3.826 0.014	18.0 1.2	34.40 0.85	7.6E – 06	2.0
100880613	0.893171 0.000018	1.9956 0.0069	36.0 1.3	59.9 1.1	8.0E – 06	8.3
105760939	1.53138 0.00042	3.847 0.012	22.7 1.4	36.56 0.89	8.3E – 06	2.6
104113878	2.22939 0.00024	3.085 0.024	15.70 0.97	-25.11 0.59	2.5E – 05	6.5
103782315	5.372 0.012	6.737 0.070	15.9 1.3	-46.68 0.90	3.1E – 05	2.9
310169750	0.6321732 0.0000065	2.8879 0.0058	40.5 2.0	-3.8 1.5	3.4E – 05	8.0
103922738	7.901 0.037	7.92 0.19	6.2 1.4	12.64 0.87	5.3E – 05	0.5
104648865	1.446104 0.000097	5.045 0.041	32.6 5.9	-21.2 4.3	6.3E – 05	0.8
104536524	3.12477 0.00100	2.108 0.052	10.8 1.1	60.34 0.79	6.7E – 05	2.6

Notes. Each line of parameters is followed by a line of uncertainties.

Table 6. continued.

CoRoT ID	P (day)	T_0 (HJD-2 456 141)	K (km s ⁻¹)	γ (km s ⁻¹)	F -test p -value	χ^2_{orb}
101058035	0.7647344 0.0000057	6.1885 0.0079	21.3 1.3	10.57 0.95	8.6E – 05	9.1
105378453	3.2362 0.0075	5.099 0.021	19.77 0.83	–14.99 0.58	1.5E – 04	23.1
105597526	0.920035 0.000029	2.934 0.023	39.0 3.7	–55.7 5.8	2.0E – 04	7.1
104667709	0.6984611 0.0000056	3.0336 0.0071	25.1 1.9	–34.8 1.1	3.5E – 04	13.1
105154613	4.587 0.026	1.459 0.064	9.36 0.88	38.69 0.59	5.0E – 04	8.6
100537909	4.8190 0.0094	2.534 0.023	24.41 0.83	31.81 0.56	5.6E – 04	67.6
105659320	0.706141 0.000026	4.986 0.018	6.91 0.94	–1.18 0.72	6.7E – 04	4.7
101044188	1.368287 0.000075	4.969 0.021	8.19 0.94	39.32 0.62	7.1E – 04	6.9
104279119	10.161 0.051	7.63 0.24	14.8 1.5	12.5 1.7	7.3E – 04	15.2
104598628	2.75207 0.00061	4.264 0.056	19.1 2.8	96.2 1.8	1.3E – 03	6.5
105164611	3.50481 0.00066	4.532 0.056	23.8 2.9	4.0 1.8	1.4E – 03	9.0
100851348	0.854818 0.000012	4.027 0.023	13.5 2.5	19.0 2.0	1.7E – 03	4.0
105472536	0.4066543 0.0000092	6.8778 0.0050	34.0 6.4	–36.8 2.4	2.1E – 03	4.8

critical p -value of 0.001 originates in a visual inspection of the results, particularly of a few borderline cases.

In our sample of 26 composite-spectrum candidates we found 18 BEER SB2s, 7 diluted BEER binaries, and one FA (CoRoT 310186704). For the confirmed BEER SB2s we then also fitted circular SB2 Keplerian model for the two sets of RVs together. Together with the 45 confirmed BEER SB1s, we have thus confirmed 70 new non-eclipsing BEER binaries.

In addition to a circular model, we also fitted each RV curve with an eccentric Keplerian model. Requiring an improvement of a factor 10 in the F -test p -value, we found no SB2s that show measurable eccentricity. We found two diluted-binary candidates (104626523 A and 103833966 A) to have slightly eccentric orbits. However, the low eccentricities (~ 0.3) found for these two cases might also be spurious or at least inflated (e.g., Lucy & Sweeney 1971). The preference for an eccentric orbital solution might also be a result of systematic RV errors caused by the presence of the second component in the spectra.

Table 7 lists the orbital parameters of the confirmed BEER SB2s, sorted by ascending F -test p -value of the primary. Table 8 lists the orbital parameters of the variable components in the diluted BEER binaries, sorted by ascending F -test p -value.

Figure 13 shows the measured AAOmega RVs and the best-fit Keplerian models of the confirmed BEER SB2s listed in Table 7. Figure 14 shows the measured AAOmega RVs and the best-fit Keplerian models of the variable components in the confirmed BEER diluted binaries listed in Table 8.

Figure 15 shows the phase-folded and binned light curves of all 70 confirmed BEER binaries, together with the best-fit

circular BEER model. For convenience, the order of the plots in Fig. 15 is the same as in Figs. 12–14.

6. Performance of the BEER search algorithm

We are now in a position to evaluate the performance of the BEER algorithm in detecting short-period binaries in the light curves of CoRoT long runs. This is possible in view of the large sample of confirmations and FAs that are reported here.

6.1. BEER-model priority, $M_2 \sin i$, and period

We start by considering the priority classes that we manually assigned to candidates during the visual inspection stage. The left-hand side of Table 9 lists the number of binary confirmations and FAs per priority class within our sample. As expected, BEER did not perform that well with its priority 3 candidates. They were not considered to be good candidates in the first place and were included in the observational campaign only due to the availability of fibers on the AAOmega spectrograph. Therefore, we decided to ignore priority 3 candidates in our performance analysis, and only concentrated on priority 1 and 2 candidates.

Two other parameters that determine the success of the BEER detection are the secondary mass and the orbital period because the BEER amplitudes mostly depend on these two parameters (Faigler & Mazeh 2011). We therefore plot in Fig. 7 the BEER-model $M_2 \sin i$ as a function of the photometric period for priority 1 and 2 targets. As expected, shorter-period modulations

Table 7. Orbital parameters of the 18 confirmed BEER SB2s.

CoRoT ID	P (day)	T_0 (HJD-2 456 141)	K_1 (km s ⁻¹)	K_2 (km s ⁻¹)	γ (km s ⁻¹)	F -test p -value A	F -test p -value B	χ_{orb}^2
105962436	1.8020 0.0062	5.917 0.012	83.5 1.2	133.8 3.0	27.74 0.78	5.6E – 09	8.0E – 05	20.3
106024478	3.013 0.012	4.1436 0.0068	65.25 0.98	66.2 1.1	-22.33 0.57	2.0E – 07	5.4E – 08	9.9
105649738	3.604 0.010	2.7189 0.0064	87.6 1.1	87.7 1.2	-7.47 0.57	2.0E – 07	2.2E – 07	8.4
105928477	1.6509 0.0048	4.9285 0.0063	74.3 1.2	74.7 2.3	-2.18 0.80	2.3E – 07	1.6E – 06	3.1
100688131	6.984 0.098	2.518 0.023	38.12 0.77	43.20 0.95	-13.84 0.47	1.7E – 06	2.3E – 06	25.1
310198235	1.713 0.011	6.873 0.019	99.7 2.8	113.4 3.7	7.55 0.61	2.0E – 06	6.3E – 07	74.8
100976101	4.738 0.025	0.856 0.018	67.22 0.73	113.0 2.9	-9.00 0.55	2.3E – 06	2.2E – 05	68.7
104369937	6.093 0.061	5.699 0.020	56.37 0.81	72.8 1.7	-16.58 0.54	2.6E – 06	2.2E – 04	54.7
105963904	6.048 0.044	5.062 0.010	67.26 0.76	81.7 1.5	-36.46 0.53	2.8E – 06	4.7E – 05	99.9
104181232	4.138 0.027	4.025 0.012	58.15 0.87	83.2 3.5	-0.64 0.65	4.0E – 06	1.9E – 04	34.1
105506915	0.6542 0.0048	3.083 0.016	25.50 0.98	123.4 5.0	-72.51 0.96	2.0E – 05	4.8E – 05	22.8
310136399	6.146 0.098	2.826 0.027	73.2 1.9	76.0 1.7	-7.10 0.97	3.3E – 05	2.0E – 05	96.8
101177998	1.6103 0.0044	4.0305 0.0056	26.5 1.7	156.8 4.1	40.59 0.91	2.8E – 04	2.4E – 04	32.7
310212616	0.35918 0.00047	3.8372 0.0016	96.7 3.6	149.0 3.7	-12.0 2.0	3.4E – 04	1.1E – 05	105.1
103838038	6.238 0.061	4.758 0.016	42.98 0.88	44.0 1.0	-8.99 0.48	3.8E – 04	4.4E – 05	192.2
310173237	0.29882 0.00033	2.0277 0.0025	85.5 3.9	132.2 4.6	-38.6 2.1	4.7E – 04	3.9E – 04	177.7
104432741	0.43955 0.00053	4.0074 0.0018	86.5 2.7	166.1 4.1	9.7 2.0	6.0E – 04	1.3E – 05	29.8
105583867	0.8567 0.0037	2.049 0.017	54.4 2.7	141.5 7.0	10.2 2.0	6.1E – 04	1.4E – 04	47.2

Notes. Each line of parameters is followed by a line of uncertainties.

with larger BEER-model $M_2 \sin i$ have higher chances of being true BEER modulations than FAs. For instance, there are no confirmations with BEER-model $M_2 \sin i < 0.25 M_{\odot}$. The vertical dashed line in Fig. 7 marks $P = 1.4$ days, and it is explained next.

From this stage onward we continue the performance analysis while ignoring all targets with BEER-model $M_2 \sin i < 0.25 M_{\odot}$. The summary of the remaining targets as a function of their priority is listed in the central columns of Table 9.

6.2. Spectral type

Another parameter that can influence the success of the BEER detection is the candidate’s spectral type. To check this option, we plot in Fig. 8 the BEER score as a function of the spectral type for priority 1 and 2 candidates with BEER-model $M_2 \sin i > 0.25 M_{\odot}$. The spectral type is taken from EXODAT⁵,

⁵ cesam.oamp.fr/exodat

and it was obtained using the SED analysis described by [Deleuil et al. \(2009\)](#). The advantage of using EXODAT is its availability regardless of any follow-up observations. Figure 8 shows that there is a larger fraction of FAs for late-type candidates than for early-type candidates. Particularly if we draw a line at a spectral type of G7 ($T_{\text{eff}} \sim 5600$ K), we find that the fraction of FAs is $\sim 54\%$ (69/128) to the left of that line and $\sim 77\%$ (20/26) to the right of that line.

In Fig. 7 we also mark with open circles candidates of spectral type later than G7. A close examination of these cool candidates, with BEER-model $M_2 \sin i > 0.25 M_{\odot}$, reveals that the confirmed binaries differ from the FAs in yet another way. By drawing a line at $P = 1.4$ days, we find most of the cool FAs (18/20) to the right of that line, and most of the confirmed cool binaries (5/6) to the left of that line.

To explain this phenomenon, we plot in Fig. 9 the spectral parameters of the observed candidates, which were derived in Sect. 4. Since spectral type is a proxy of T_{eff} , we place T_{eff} at the abscissa. Similarly to Fig. 8, there is an excess of cool

L. Tal-Or et al.: Seventy new *CoRoT* BEER binaries

Table 8. Orbital parameters of the variable component in the seven confirmed diluted BEER binaries.

CoRoT ID	P (day)	T_0^a (HJD-2 456 141)	K (km s ⁻¹)	γ (km s ⁻¹)	F -test p -value	χ_{orb}^2
310205770 B	5.543 0.014	5.218 0.019	56.8 1.5	3.51 0.94	4.9E – 07	12.6
310193013 B	0.2801751 0.0000021	5.8446 0.0013	193.3 3.9	–0.3 3.3	1.5E – 05	32.0
104791410 B	1.04457 0.00051	6.757 0.021	108 18	0 18	2.0E – 05	5.2
104626523 A	7.354 0.052	2.99 0.22	28.2 1.6	4.7 1.5	8.7E – 05	0.1
105423352 B	4.712 0.018	3.668 0.040	56.5 2.5	–24.0 1.8	2.6E – 04	10.8
100906796 B	0.8974124 0.0000046	5.0351 0.0043	180.0 4.8	–6.9 3.2	3.5E – 04	39.7
103833966 A	10.80 0.11	7.75 0.92	72 47	1 22	6.1E – 04	0.4

Notes. Each line of parameters is followed by a line of uncertainties. ^(a) For the eccentric binaries 104626523 A and 103833966 A the third column shows the periastron time. The eccentricity of 104626523 A is 0.33 ± 0.09 and its longitude of periastron is 242 ± 15 deg. The eccentricity of 103833966 A is 0.32 ± 0.16 and its longitude of periastron is 121 ± 40 deg.

Table 9. Confirmations and FAs per priority class by applying different filters to the sample.

Filter:	All candidates		$M_2 \sin i > 0.25 M_{\odot}$		$M_2 \sin i > 0.25 M_{\odot}$ and spectral type earlier than G7 for $P > 1.4$ day	
	Confirmations	FAs	Confirmations	FAs	Confirmations	FAs
Priority 1	30	26	30	18	30	17
Priority 2	35	108	35	71	34	54
Priority 3	5	77	5	70	4	35

Notes. See text for the justifications of the chosen filters.

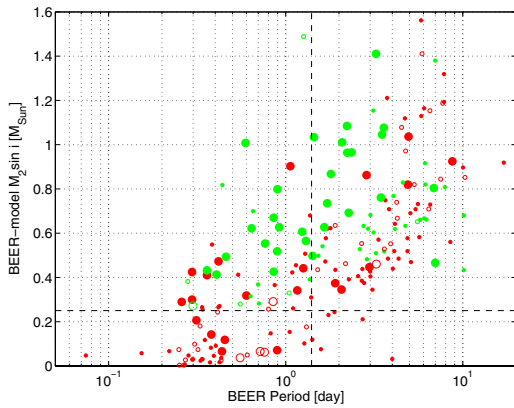


Fig. 7. BEER-model $M_2 \sin i$ as a function of the BEER period. Large and small circles represent priority 1 and 2 targets, respectively. Green circles represent confirmations, while red circles represent FAs. Open circles represent candidates of spectral type later than G7. The horizontal dashed line marks $M_2 \sin i = 0.25 M_{\odot}$, below which there are no confirmed targets. The vertical dashed line marks $P = 1.4$ days, to the right of which there are 18 FAs of spectral type later than G7, but only one confirmed binary (see Sect. 6.2).

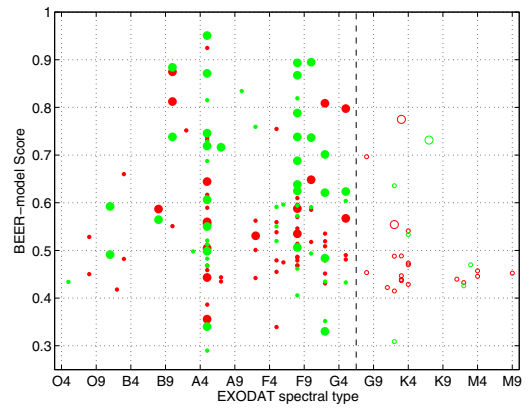


Fig. 8. BEER score as a function of the EXODAT spectral type for candidates with $M_2 \sin i > 0.25 M_{\odot}$. The symbols are the same as in Fig. 7. The vertical dashed line marks a spectral type of G7.

lower metallicity. Even though our spectral-parameter measurement technique is prone to systematic biases (e.g., Torres et al. 2012), such a strong bimodality suggests that most cool FAs are possibly red giant stars.

FAs ($T_{\text{eff}} \lesssim 5600$ K), with just a few confirmed binaries in that temperature regime. In addition, cool FAs seem to constitute a distinct sample of slowly rotating stars with lower gravity and

We propose that the main reason that red giants introduce false candidates with photometric periods of $\gtrsim 1.4$ day is related to solar-like oscillations. Using *Kepler* data, Mosser et al. (2013)

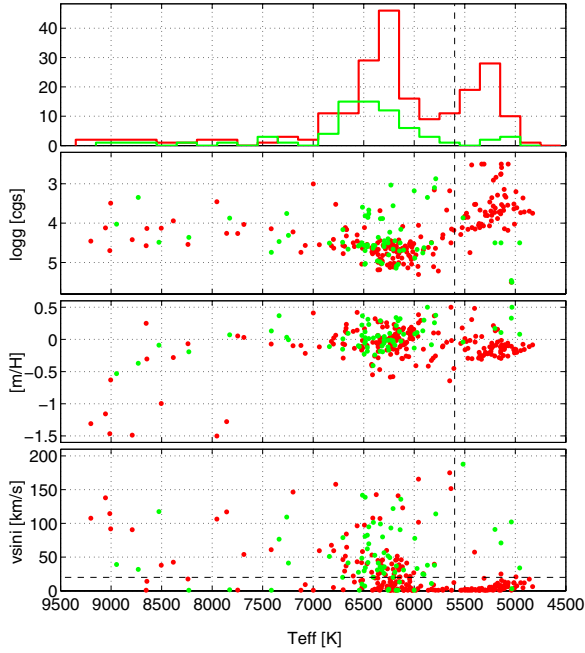


Fig. 9. Spectral parameters derived in Sect. 4. Confirmed BEER binaries are represented in green, while FAs are represented in red. For SB2s, only the spectral parameters of the primary are shown. For diluted BEER binaries, only the spectral parameters of the variable component are shown. The upper panel shows the two T_{eff} histograms. The lower three panels show the $T_{\text{eff}}\text{-log } g$, $T_{\text{eff}}\text{-metallicity}$, and $T_{\text{eff}}\text{-rotational broadening}$ scatter plots. The vertical dashed lines mark $T_{\text{eff}} = 5600$ K – the approximate temperature of a G7V star. The horizontal dashed line in the lower panel indicates a rotational broadening of 20 km s^{-1} , below which the measured values are unreliable as a result of the medium resolution of the spectrograph (see Sect. 4).

have shown that solar-like oscillations of $1\text{--}2 M_{\odot}$ red giants have frequencies of $1\text{--}10 \mu\text{Hz}$ (periods of $1.2\text{--}12$ days), amplitudes (A_{max}) of $0.1\text{--}1$ mmag, and that the amplitude increases with the period as a power law. For BEER binaries, the photometric amplitude decreases with the period (Zucker et al. 2007). However, it appears that for periods of about $1\text{--}10$ days, these two phenomena might have similar photometric amplitudes. A large fraction of the stars observed by CoRoT are indeed giants, particularly in the CoRoT-center fields (e.g., Deleuil et al. 2009; Gazzano et al. 2010). Although solar-like oscillations are semi-regular in nature, given the typical length and S/N of long-run CoRoT data, BEER might have interpreted the variability of some red giants as an indication for the presence of a short-period companion.

To check whether filtering out red candidates with periods of >1.4 days improves BEER’s performance, we list in the right-hand side of Table 9 the number of binary confirmations and FAs per priority class, after removing candidates with BEER-model $M_2 \sin i < 0.25 M_{\odot}$, and also candidates of spectral type later than G7 with photometric periods of >1.4 days. These two filters applied to the candidate list lowers the fraction of FAs to $\sim 1/3$ for priority 1 candidates, and to $\sim 2/3$ for priority 2 candidates.

6.3. BEER-model score

To evaluate the BEER performance as a function of its score, we counted the targets with scores higher than some threshold T

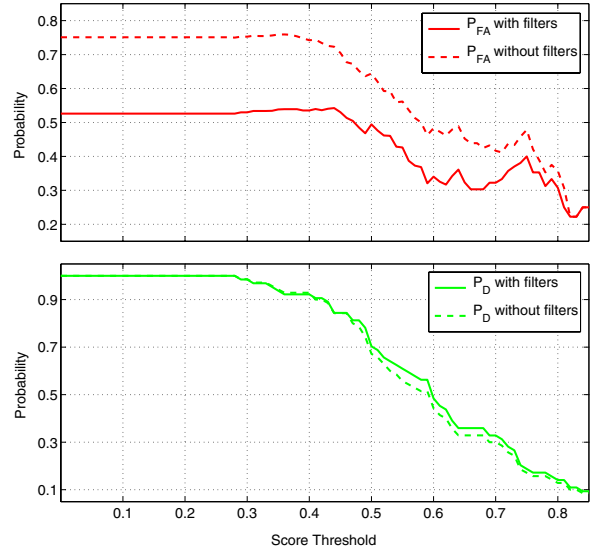


Fig. 10. Upper panel: false-alarm probability as a function of the BEER score threshold. Lower panel: the detection probability as a function of the BEER score threshold. The dashed lines show the probabilities for the whole sample of 281 candidates observed, while the solid lines show the probabilities for the remaining 135 candidates, after applying the three filters discussed in the text (see also the first two rows of the right-hand side of Table 9). The plot was truncated at a score threshold of 0.85 since only 8 candidates got a higher score.

and obtained the detection probability $P_D(T)$ and the false-alarm probability $P_{\text{FA}}(T)$ of the algorithm as

$$P_D = \frac{\text{Number of confirmations with score } > T}{\text{Total number of confirmations}}, \quad (8)$$

$$P_{\text{FA}} = \frac{\text{Number of false alarms with score } > T}{\text{Total number of targets with score } > T}. \quad (9)$$

To illustrate the algorithm performance, Fig. 10 plots P_D and P_{FA} as a function of T for two sets of targets – the whole sample of 281 candidates observed, and the remaining 135 candidates, after filtering out priority 3 candidates, candidates with BEER-model $M_2 \sin i < 0.25 M_{\odot}$, and candidates of spectral type later than G7 with photometric periods of >1.4 day. The addition of these three filters lowers P_{FA} and raises P_D for any given T , hence improves the algorithm performance.

Estimating the two probabilities for any selected threshold level might be useful in estimating the results of future CoRoT-based BEER searches. If such a search would yield N targets with scores higher than some predefined threshold T , then using the P_D and P_{FA} that correspond to T , we expect to have

$$N_C = N(1 - P_{\text{FA}}), \quad (10)$$

$$N_{\text{FA}} = NP_{\text{FA}}, \text{ and} \quad (11)$$

$$N_{\text{CC}} = \frac{N(1 - P_{\text{FA}})}{P_D}, \quad (12)$$

where N_C is the number of expected confirmations within the N candidates, N_{FA} is the number of expected FAs within the N candidates, and N_{CC} is the estimated number of binaries that can be discovered by BEER in the original sample of CoRoT targets. For instance, using the solid lines in Fig. 10, for $T = 0.6$ we

L. Tal-Or et al.: Seventy new *CoRoT* BEER binaries

get $P_{\text{FA}} \sim 1/3$ and $P_{\text{D}} \sim 1/2$. This means that, for $T = 0.6$, we expect about two thirds of the selected sample to be true BEER binaries and the total number of BEER binaries in the original sample of *CoRoT* targets to be about $(4/3)N$.

7. Mass ratio and orbital period distribution of the BEER *CoRoT* sample

To discuss the mass ratio and period distribution of the sample of confirmed BEER binaries, we wish to plot an estimate of the mass ratio of each system as a function of its orbital period. For SB2s this is straightforward, since the mass ratio ($q \equiv M_2/M_1 = K_1/K_2$) can be measured directly from the orbital parameters. For SB1s, however, the mass ratio depends not only on the orbital parameters, but also on the primary mass and orbital inclination, and can be found using the relation

$$(M_1 f^{-1} \sin^3 i) q^3 - q^2 - 2q - 1 = 0, \quad (13)$$

where M_1 is the estimated mass of the primary, f is the mass function derived analytically from the orbital parameters, and i is the inclination.

To estimate M_1 of the confirmed binaries, we used the empiric relations given in [Torres et al. \(2010\)](#), which express the stellar mass and radius in terms of its observed spectral parameters. As an input, we used the spectral parameters that were derived for the primary component of the confirmed SB1s and SB2s in Sect. 4. To estimate the mass uncertainties, we took equal uncertainties of 300 K in T_{eff} , 0.4 dex in $\log g$, and 0.3 dex in $[m/H]$ to all primary stars. For most of the observed stars these uncertainties are larger than the scatter of the best spectral parameters between consecutive exposures (see for instance Fig. 4), but taking into account the possible systematic errors (e.g., [Torres et al. 2012](#)), they are probably reasonable. The intrinsic scatter from the empiric relations ([Torres et al. 2010](#)) was added in quadrature to the mass uncertainties.

To assign an inclination for each SB1 we considered three options – to use the inclination estimated from its light curve by BEER, to derive its inclination distribution using the algorithm developed by [Mazeh & Goldberg \(1992\)](#), or to assume an isotropic inclination distribution. While using the BEER-model $\sin i$ estimates could sound appealing, we decided not to use them because we do not know their actual uncertainties, including possible systematic biases. Deriving inclination distributions using the algorithm of [Mazeh & Goldberg \(1992\)](#) would probably be the correct way to proceed, but it is beyond the scope of this paper. We therefore, somewhat arbitrarily, assigned a value of $\sin i = 0.866^{+0.121}_{-0.326}$, taking the median of an isotropic inclination distribution and the confidence limits to cover the central 68.3% of the distribution (e.g., [Ho & Turner 2011](#); [Lopez & Jenkins 2012](#)).

Table 10 lists the spectral parameters, primary mass, and the assigned mass ratio of the confirmed BEER SB1s. Table 11 lists the primary spectral parameters, primary mass, and the estimated mass ratio of the confirmed BEER SB2s. For convenience, the order of Tables 10 and 11 is the same as of Tables 6 and 7. We did not estimate the masses of the seven diluted BEER binaries since their spectral parameters might have been biased by the presence of the third star.

Figure 11 shows the assigned mass ratio of the 45 confirmed SB1s and the estimated mass ratio of the 18 confirmed SB2s as a function of their orbital period. The period and the mass-ratio histograms are plotted as well. The solid red line in the

Table 10. Spectral parameters, primary mass, and the assigned mass ratio of the 45 confirmed BEER SB1s.

CoRoT ID	T_{eff} (K)	$\log g$ (cgs)	$[m/H]$ (dex)	Primary mass (M_{\odot})	Mass ratio (M_2/M_1)
103924393	6500	4.6	-0.1	1.20 ± 0.16	$0.69^{+0.70}_{-0.12}$
105767195	6400	4.6	-0.4	1.07 ± 0.13	$0.28^{+0.22}_{-0.04}$
105810223	6500	3.8	0.0	1.59 ± 0.38	$0.62^{+0.61}_{-0.11}$
104674562	6500	4.6	-0.2	1.15 ± 0.15	$0.32^{+0.25}_{-0.05}$
310222016	6800	4.5	-0.1	1.28 ± 0.17	$0.21^{+0.16}_{-0.03}$
310210722	7800	3.9	0.1	2.02 ± 0.46	$0.52^{+0.48}_{-0.09}$
105818861	6400	4.6	-0.2	1.12 ± 0.15	$0.41^{+0.36}_{-0.06}$
101029997	6600	4.6	-0.1	1.20 ± 0.15	$0.41^{+0.35}_{-0.06}$
105844488	5000	5.5	+0.3	1.01 ± 0.23	$0.53^{+0.50}_{-0.09}$
310215106	6300	3.9	-0.2	1.40 ± 0.32	$0.28^{+0.23}_{-0.05}$
310176634	5000	5.5	+0.5	1.07 ± 0.26	$0.10^{+0.07}_{-0.02}$
105336757	6500	4.6	-0.2	1.16 ± 0.15	$0.26^{+0.20}_{-0.04}$
105712106	6300	4.6	-0.0	1.15 ± 0.15	$0.48^{+0.43}_{-0.08}$
105403147	6700	4.5	-0.2	1.24 ± 0.17	$0.30^{+0.24}_{-0.05}$
105706604	6300	4.5	-0.1	1.15 ± 0.16	$0.26^{+0.20}_{-0.04}$
105714214	6200	5.1	0.2	1.19 ± 0.17	$0.33^{+0.27}_{-0.05}$
104295292	6200	4.7	-0.0	1.12 ± 0.14	$0.22^{+0.17}_{-0.03}$
110567660	6500	4.5	0.1	1.24 ± 0.17	$0.32^{+0.26}_{-0.05}$
101177265	6700	4.2	0.0	1.42 ± 0.27	$0.17^{+0.12}_{-0.03}$
101014035	6100	4.2	-0.0	1.24 ± 0.24	$0.25^{+0.19}_{-0.04}$
100889978	6300	5.0	-0.2	1.11 ± 0.14	$0.39^{+0.33}_{-0.06}$
105661774	8900	4.0	-0.5	1.96 ± 0.40	$0.20^{+0.15}_{-0.04}$
105618890	6300	4.4	0.0	1.20 ± 0.18	$0.34^{+0.28}_{-0.05}$
105802223	6400	4.6	0.0	1.20 ± 0.16	$0.11^{+0.08}_{-0.02}$
100880613	7300	4.5	+0.4	1.60 ± 0.22	$0.18^{+0.13}_{-0.03}$
105760939	6200	4.2	0.1	1.28 ± 0.23	$0.14^{+0.10}_{-0.02}$
104113878	6700	4.7	0.1	1.27 ± 0.15	$0.11^{+0.07}_{-0.02}$
103782315	5900	4.6	+0.3	1.12 ± 0.15	$0.16^{+0.11}_{-0.02}$
310169750	6500	3.6	+0.4	1.96 ± 0.52	$0.17^{+0.12}_{-0.03}$
103922738	6000	4.7	0.1	1.09 ± 0.14	$0.07^{+0.05}_{-0.01}$
104648865	8700	3.3	-0.4	2.89 ± 0.83	$0.15^{+0.12}_{-0.06}$
104536524	6400	4.4	0.1	1.25 ± 0.20	$0.08^{+0.06}_{-0.01}$
101058035	6500	4.7	0.1	1.23 ± 0.15	$0.11^{+0.07}_{-0.02}$
105378453	6300	5.0	-0.1	1.13 ± 0.14	$0.17^{+0.12}_{-0.02}$
105597526	6200	3.0	-0.0	2.47 ± 0.78	$0.17^{+0.13}_{-0.04}$
104667709	6200	3.6	-0.0	1.70 ± 0.46	$0.11^{+0.07}_{-0.02}$
105154613	6300	4.8	-0.2	1.08 ± 0.13	$0.09^{+0.06}_{-0.01}$
100537909	6500	5.0	-0.1	1.19 ± 0.15	$0.24^{+0.19}_{-0.04}$
105659320	6500	4.6	-0.1	1.16 ± 0.15	$0.03^{+0.02}_{-0.01}$
101044188	5900	4.8	0.1	1.07 ± 0.13	$0.05^{+0.03}_{-0.01}$
104279119	6200	5.1	+0.3	1.24 ± 0.18	$0.18^{+0.13}_{-0.03}$
104598628	6500	3.7	0.2	1.79 ± 0.46	$0.13^{+0.09}_{-0.03}$
105164611	8500	4.5	-0.1	1.75 ± 0.23	$0.18^{+0.13}_{-0.04}$
100851348	6300	3.9	+0.3	1.58 ± 0.36	$0.06^{+0.04}_{-0.02}$
105472536	5500	3.9	-0.0	1.20 ± 0.28	$0.14^{+0.10}_{-0.03}$

period histogram shows the log-normal fit of [Raghavan et al. \(2010\)](#) to the period distribution of stellar binaries in the solar neighborhood, scaled to best fit the histogram.

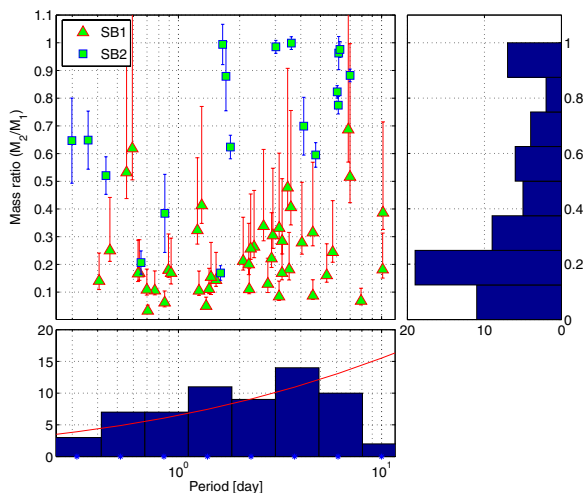


Fig. 11. Assigned mass ratio of the 45 confirmed SB1s and estimated mass ratio of the 18 confirmed SB2s versus orbital period. For the SB1s we assumed an isotropic inclination distribution (see text). *Bottom panel:* period histogram. The solid red line shows the log-normal fit reported by Raghavan et al. (2010) to the period distribution of stellar binaries, scaled to best fit the histogram. *Right panel:* mass-ratio histogram.

Table 11. Spectral parameters, primary mass, and mass ratio of the 18 confirmed BEER SB2s.

CoRoT ID	T_{eff} (K)	$\log g$ (cgs)	[m/H] (dex)	Primary mass (M_{\odot})	Mass ratio (M_2/M_1)
105962436	8200	4.4	-0.2	1.68 ± 0.26	0.62 ± 0.04
106024478	6000	3.2	-0.1	2.04 ± 0.63	0.99 ± 0.02
105649738	5800	3.1	+0.3	2.26 ± 0.71	1.00 ± 0.02
105928477	6300	4.4	-0.0	1.19 ± 0.18	0.99 ± 0.07
100688131	6100	4.7	0.1	1.14 ± 0.14	0.88 ± 0.02
310198235	6500	3.9	+0.3	1.66 ± 0.39	0.88 ± 0.12
100976101	7400	4.7	0.1	1.48 ± 0.16	0.60 ± 0.04
104369937	6400	5.0	0.1	1.18 ± 0.14	0.77 ± 0.03
105963904	6100	4.7	0.1	1.11 ± 0.14	0.82 ± 0.02
104181232	6500	5.0	-0.0	1.19 ± 0.15	0.70 ± 0.10
105506915	6500	3.8	0.0	1.62 ± 0.40	0.21 ± 0.04
310136399	5900	3.3	+0.5	2.04 ± 0.60	0.96 ± 0.06
101177998	7200	4.3	-0.0	1.50 ± 0.24	0.17 ± 0.03
310212616	6100	4.5	+0.3	1.22 ± 0.17	0.65 ± 0.11
103838038	6300	4.5	-0.1	1.13 ± 0.16	0.98 ± 0.03
310173237	5200	4.5	0.2	0.92 ± 0.14	0.65 ± 0.15
104432741	5800	2.9	+0.4	2.74 ± 0.90	0.52 ± 0.07
105583867	7300	3.8	0.0	1.92 ± 0.47	0.38 ± 0.14

One feature in Figure 11 is that for periods of >1 day, there seems to be a transition from SB1s to SB2s at $q \sim 0.6$. A similar transition was pointed out by Halbwachs et al. (2003) in their unbiased sample of solar-like spectroscopic binaries. In our sample this transition can be explained by the mass-luminosity relation of normal stars that is expected to be $L \sim M^4$ (e.g., Torres et al. 2010; Cox 2000, p. 382). Since the lowest significant α we could detect was ~ 0.1 (see Table 5), we did not expect detached binaries with $q \lesssim 0.6$ to be classified as SB2s. For periods of $\lesssim 1$ day

this transition is less evident, since at such short periods some of these binaries could experience mass transfer via Roche-lobe overflow (e.g., Eggleton 1983), and the mass-luminosity relation deviates from that of isolated normal stars (e.g., Batten 1973, p. 154).

The period histogram clearly shows a rise in the number of binaries per $\Delta \log P$ from ~ 0.3 to ~ 6 days, followed by a sharp drop at periods of >8 days. Since the detection probability of BEER binaries decreases with orbital period (see Fig. 7), this rise is probably real. In the past three decades, several studies reported a log-normal period distribution of solar-like binaries, with a peak at $\log P \sim 5$ (e.g., Duquennoy & Mayor 1991; Raghavan et al. 2010), and Fig. 11 shows that our period histogram fits well the log-normal fit of Raghavan et al. (2010) out to $P \sim 8$ days. The scaling factor between the two samples is 1.61, which means that for a bin size of $\Delta \log P = 0.214$, as we use here, we would obtain ~ 74 binaries at the peak of the distribution at $\log P = 5.03$. The histogram sharply drops at periods of >8 days both because at such periods BEER approaches its sensitivity limit when applied to CoRoT long-run light curves and because the AAOmega observing run was limited to seven nights.

The mass-ratio distribution of short-period binaries was the subject of several in-depth studies in the last three decades (e.g., Halbwachs 1987; Duquennoy & Mayor 1991; Mazeh et al. 1992; Halbwachs et al. 2003; Goldberg et al. 2003; Fisher et al. 2005). The main debates regarding the mass-ratio distribution of spectroscopic binaries are about the existence of peaks at $q \sim 1$ and/or at $q \sim 0.2$ and about the shape of the distribution toward lower q values – whether it is monotonically increasing, decreasing, or flat. It is therefore of interest to plot the distribution of the assigned mass ratios of our sample, as was done in Fig. 11.

The histogram presents three features, which we describe from top to bottom. (1) A clear peak at $q \sim 1$. (2) The number of binaries increases with decreasing q . (3) The histogram peaks at $q \sim 0.2$ and then falls sharply towards $q \sim 0.1$. However, correcting our sample for the Öpik (1924) effect might have significantly diminished the $q \sim 1$ peak (e.g., Goldberg et al. 2003; Halbwachs et al. 2003). In addition, at $q < 0.6$ our histogram is dominated by SB1s, and Mazeh & Goldberg (1992) have already shown that using an average $\sin i$ value to all SB1s, like we did here, might produce a monotonically increasing q distribution when the actual true distribution is flat. Lastly, the drop toward $q \sim 0.1$ can be explained both by BEER’s sensitivity for CoRoT long-run light curves, which probably approaches its limit at such low mass-ratios, and by the limited RV precision of our AAOmega data. Therefore, before reaching any definite conclusion, our data need an in-depth analysis to derive a real mass-ratio distribution of the CoRoT BEER sample (Shahaf et al., in prep.).

8. Summary

We have presented AAOmega RV confirmation of seventy new non-eclipsing short-period binaries found by BEER in CoRoT light curves. The confirmed binaries span a range of 0.3–10 days in orbital period, showing a clear rise in the number of binaries per $\Delta \log P$ toward longer periods. Our spectral analysis shows that the primary stars in the detected binaries are typically of spectral type G or earlier, and the mass ratio (including the mass ratio assigned to SB1s) spans a range of 0.03–1. The mass-ratio histogram resembles a double-peak distribution (e.g., Halbwachs et al. 2003), but since we did not correct our results,

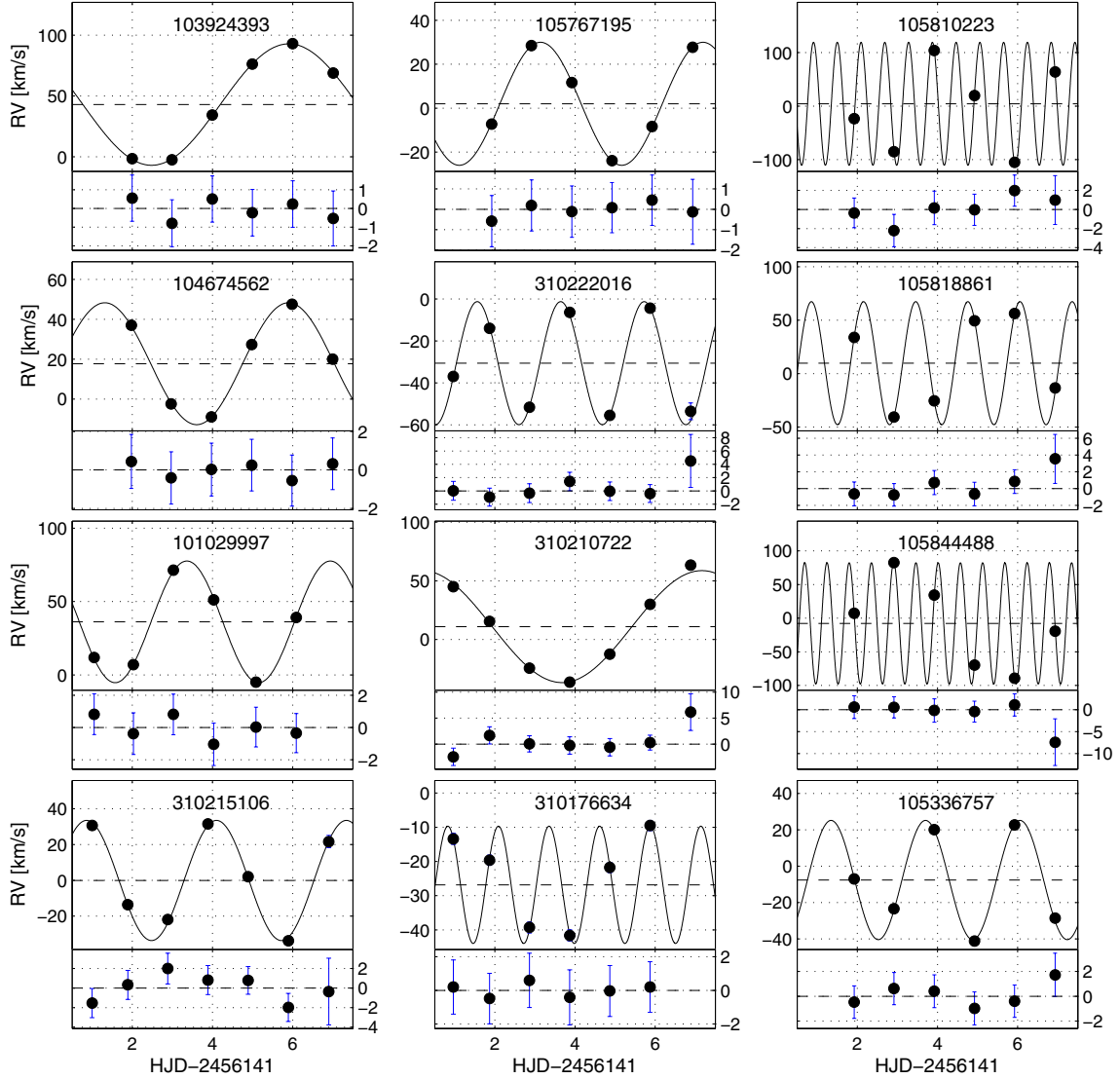
L. Tal-Or et al.: Seventy new *CoRoT* BEER binaries


Fig. 12. AAOmega RVs (black circles) and the best-fit Keplerian models (solid lines) of the confirmed BEER SB1s listed in Table 6.

neither for some well-known selection effects (e.g., Öpik 1924) nor for the non-isotropic inclination distribution (e.g., Mazeh & Goldberg 1992), the underlying true distribution might also be flat. Nevertheless, the orbital solutions presented here can be used in the future for an in-depth study of the mass-ratio distribution of short-period binaries, similar to the study presented by Goldberg et al. (2003).

On the lower end of our detection capability, we have detected two BD candidates on a ~ 1 day period orbit around F-G stars. We considered them as BD candidates and not bona fide BDs for two reasons: (1) the true inclination is not known; and (2) higher resolution and/or S/N spectroscopic observations might reveal a faint companion that could not have been found in the AAOmega spectra.

Relativistic beaming was already detected in *CoRoT* light curves (e.g., Mazeh & Faigler 2010), but this is the first time that BEER detected non-eclipsing binaries in *CoRoT* light curves. To roughly estimate the expected number of such binaries that can potentially be detected with BEER in *CoRoT* long-run light

curves we first need to correct for the 200 binaries that were selected for follow-up, but were not observed, taking into account their BEER priorities, and then for the total number of *CoRoT* long-run light curves ($\sim 110\,000$), assuming that short-period binaries do not have a preference for center or anticenter fields. Doing so, we estimate that observing all 481 selected candidates would have brought the number of confirmed binaries to ~ 110 , and that the expected number of beaming binaries that can be detected in *CoRoT* long-run light curves is ~ 300 . This confirms the prediction made by Zucker et al. (2007): *CoRoT* and *Kepler* will be capable of detecting hundreds of non-eclipsing beaming binaries.

Investigating BEER’s false-alarm probability and nature in *CoRoT* long-run light curves, we showed that red giants introduce a major source of false candidates and demonstrated a way to improve BEER’s performance in extracting higher fidelity samples from future searches. Understanding the dependence of the fidelity and completeness of such future samples on parameters such as period, spectral type, and BEER-model

A&A 580, A21 (2015)

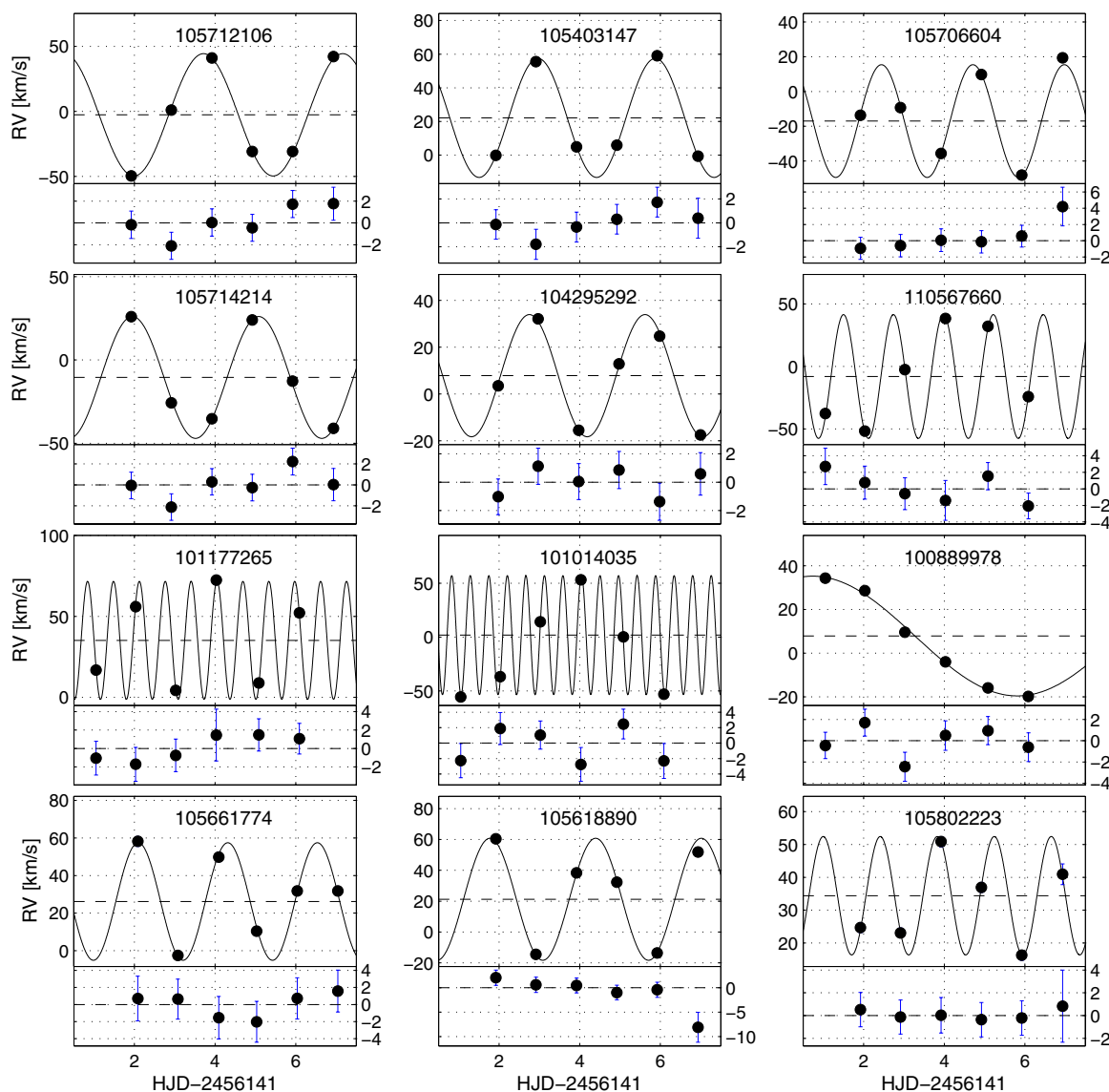


Fig. 12. continued.

score might enable using these samples to derive some statistical properties of the short-period binary population, like the period distribution, even before RV follow-up is done. Merging well-corrected large samples of *CoRoT* and *Kepler* beaming binaries with equivalent EB samples (e.g., Prša et al. 2011) might create large and well-defined samples of short-period binaries, which may shed some light on binary formation and evolution.

Radial-velocity follow-up observations of beaming and eclipsing binaries will continue to play a key role in these efforts because in most cases this is the only way to measure their mass ratio and the mass of the secondary companion. Scaling the AAOmega time that was required to make the detections reported here, we estimate that only three additional such runs would be required to detect virtually all beaming binaries that can be detected in *CoRoT* long-run light curves. This again demonstrates the efficiency of using multi-object spectrographs for this task (e.g., Zucker et al. 2007). One advantage of the beaming binaries over the EBs is the ability of detecting binaries

not only at edge-on inclinations, which widens the window for detecting intrinsically rare systems such as BD and massive-planetary companions to main-sequence stars (e.g., Halbwachs et al. 2000; Faigler et al. 2013).

Acknowledgements. We thank Gary Da Costa and Simon O’Toole for their help with preparing the AAOmega proposal and observations. We are grateful for the invaluable assistance of the AAOmega technical staff and support astronomers. Particularly, we thank Sarah Brough for her help with preparing, performing, and reducing the observations. We thank Gil Sokol for his help with the observations and the spectral analysis. We also thank Slavek M. Rucinski, the referee, for his fruitful comments and suggestions. The research leading to these results has received funding from the European Community’s Seventh Framework Programme (FP7/2007-2013) under grant-agreement numbers 291352 (ERC) and RG226604 (OPTICON). This research was also supported by the Israel Science Foundation (grant No. 1423/11), and by the Israeli Centers of Research Excellence (I-CORE, grant No. 1829/12). The *CoRoT* space mission, launched on 2006 December 27, was developed and operated by the CNES, with participation of the Science Programs of ESA, ESA’s RSSD, Austria, Belgium, Brazil, Germany, and Spain.

L. Tal-Or et al.: Seventy new *CoRoT* BEER binaries

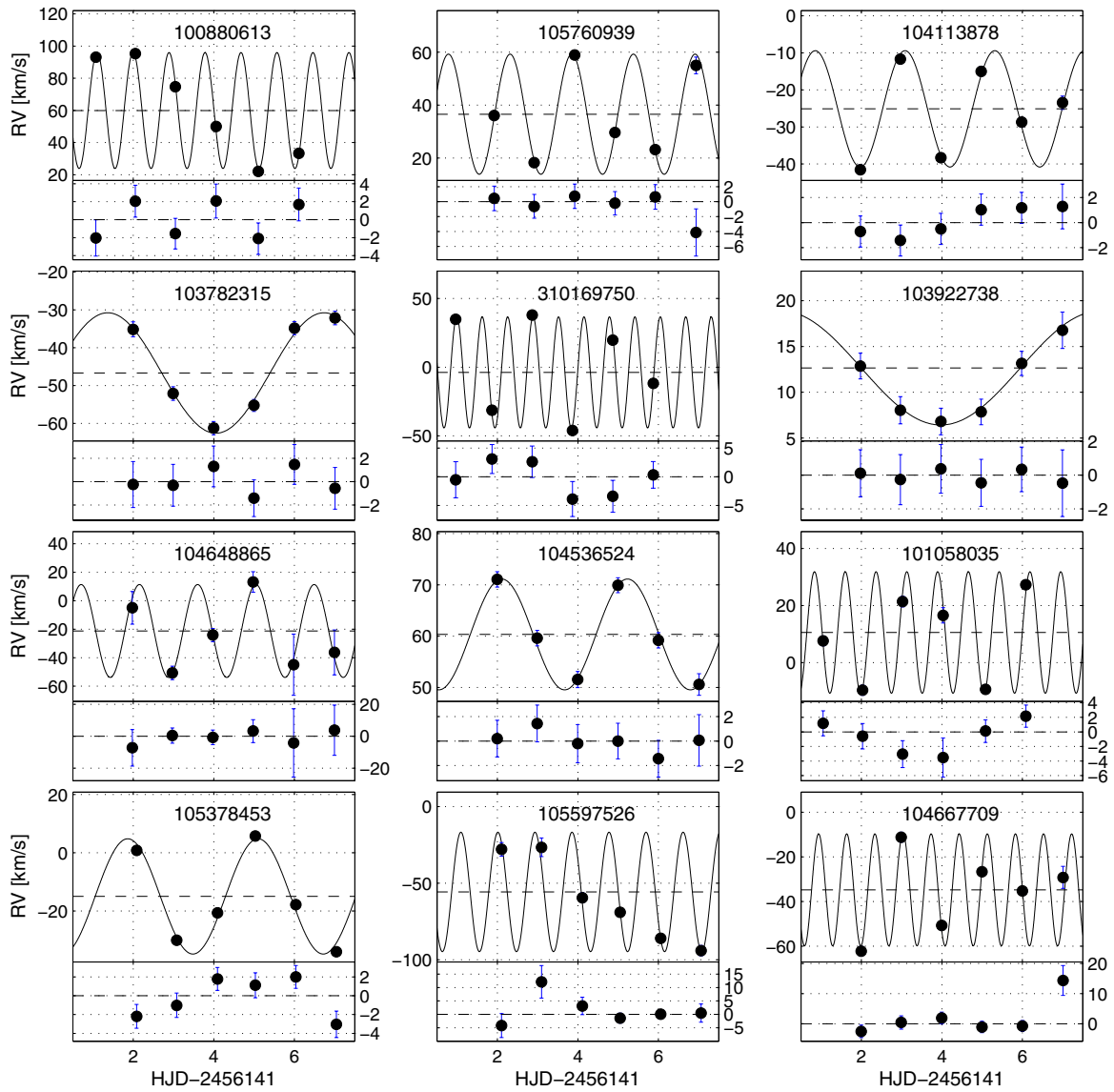


Fig. 12. continued.

A&A 580, A21 (2015)

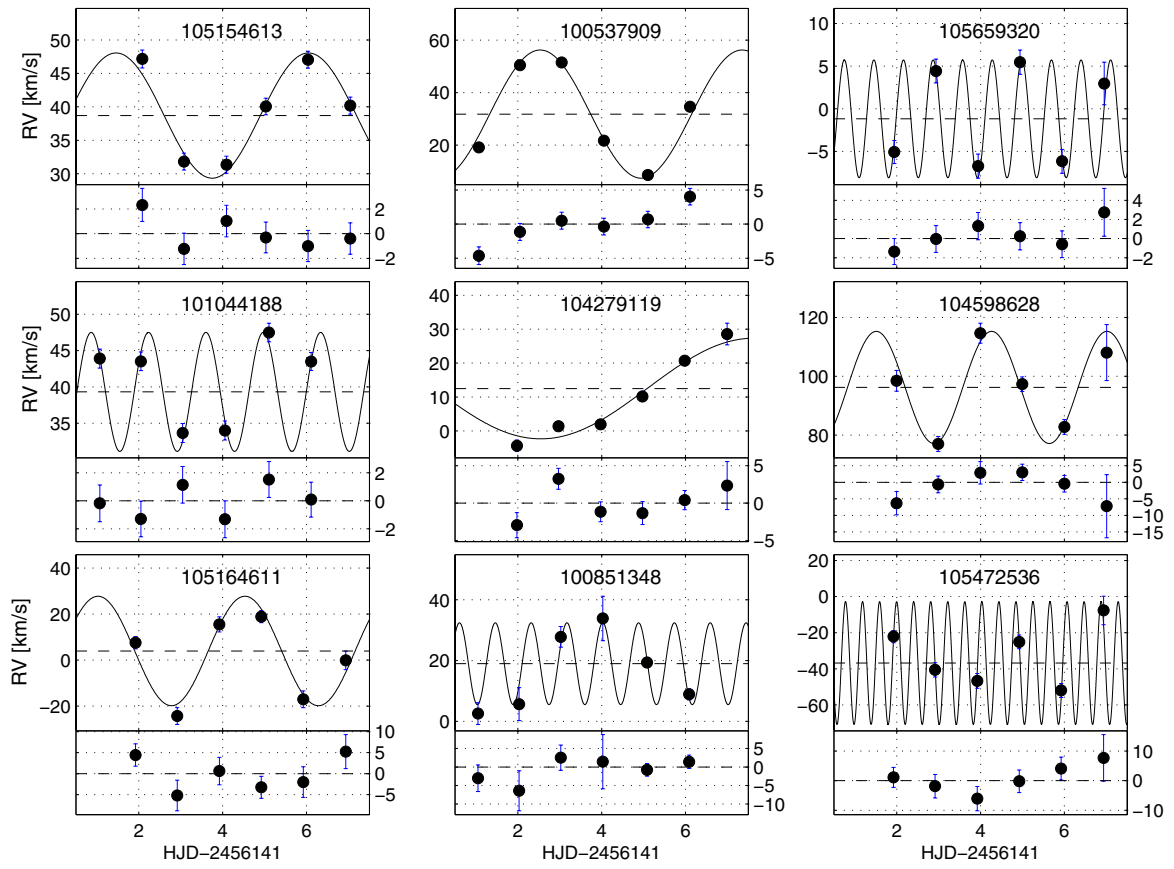


Fig. 12. continued.

L. Tal-Or et al.: Seventy new *CoRoT* BEER binaries

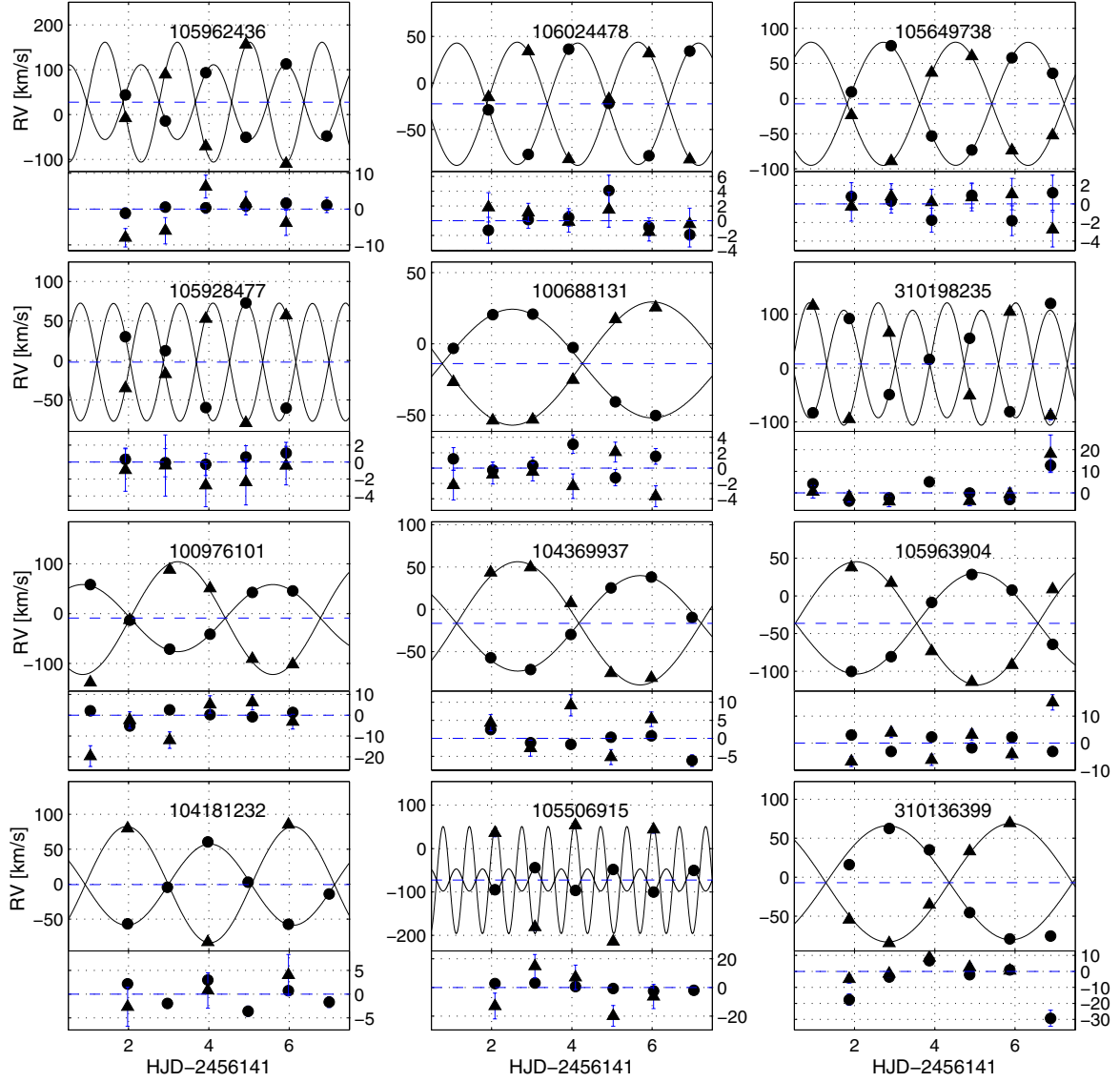


Fig. 13. AAOmega RVs and the best-fit Keplerian models (solid lines) of the confirmed BEER SB2s listed in Table 7. Primary RVs are marked with circles and secondary RVs with triangles.

A&A 580, A21 (2015)

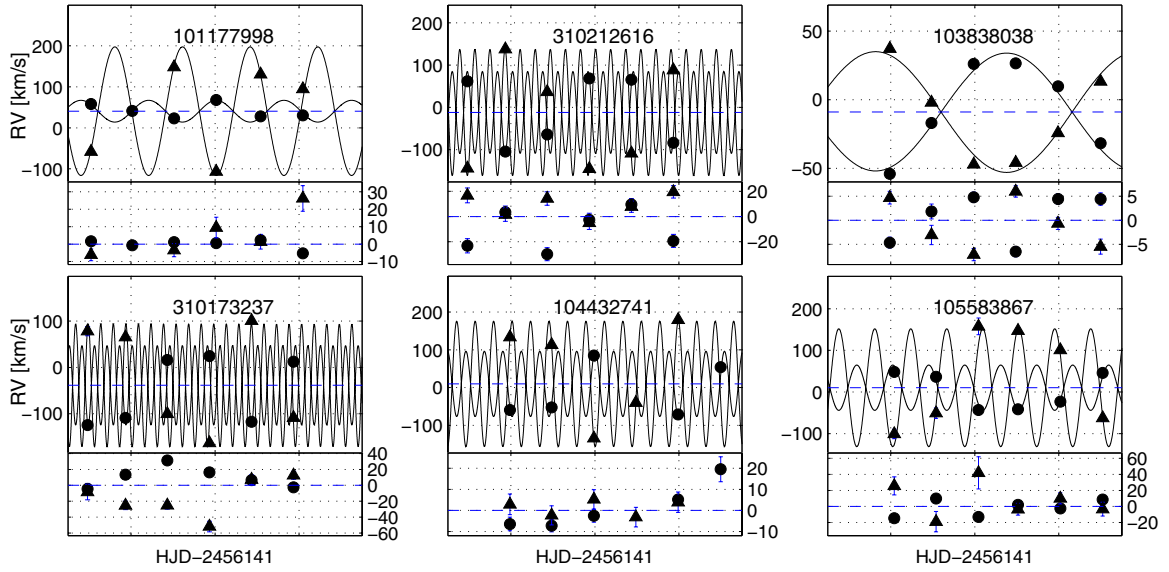


Fig. 13. continued.

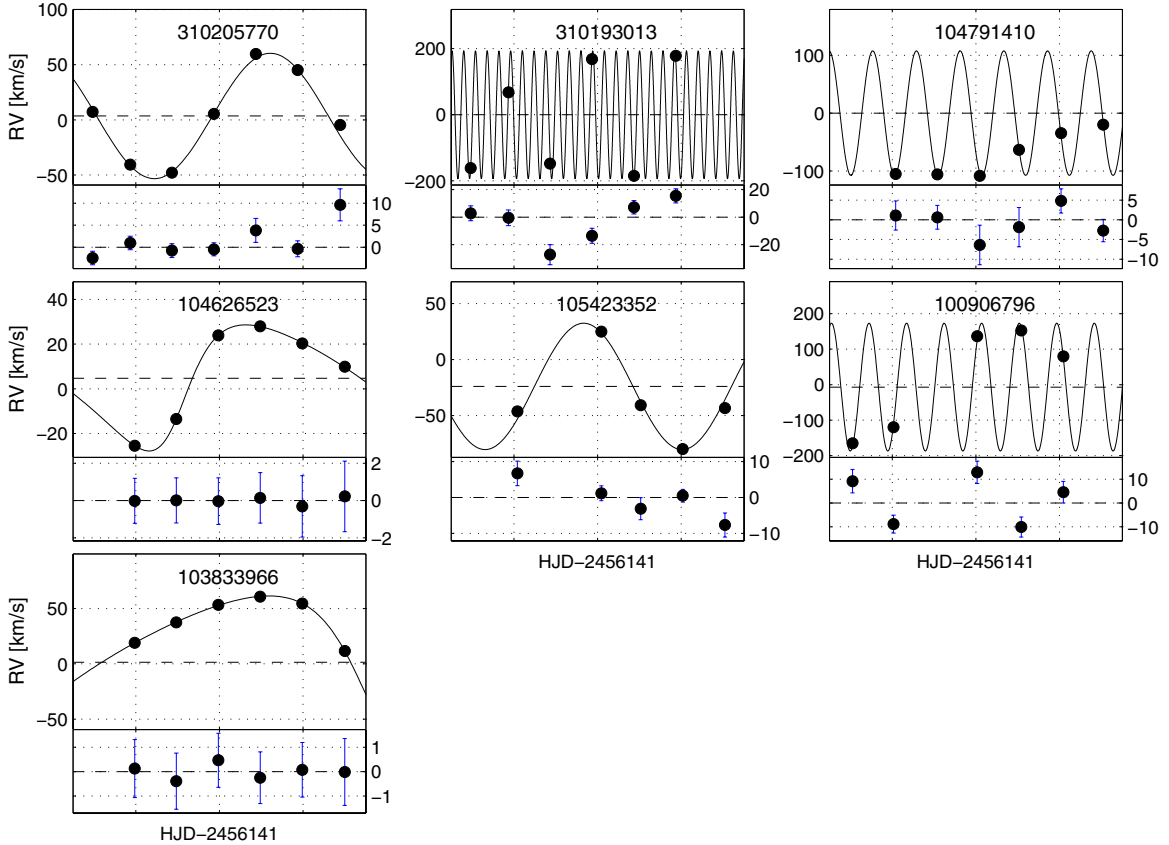


Fig. 14. AAOmega RVs (black circles) and the best-fit Keplerian models (solid lines) of the variable components in the confirmed BEER diluted binaries listed in Table 8.

L. Tal-Or et al.: Seventy new *CoRoT* BEER binaries

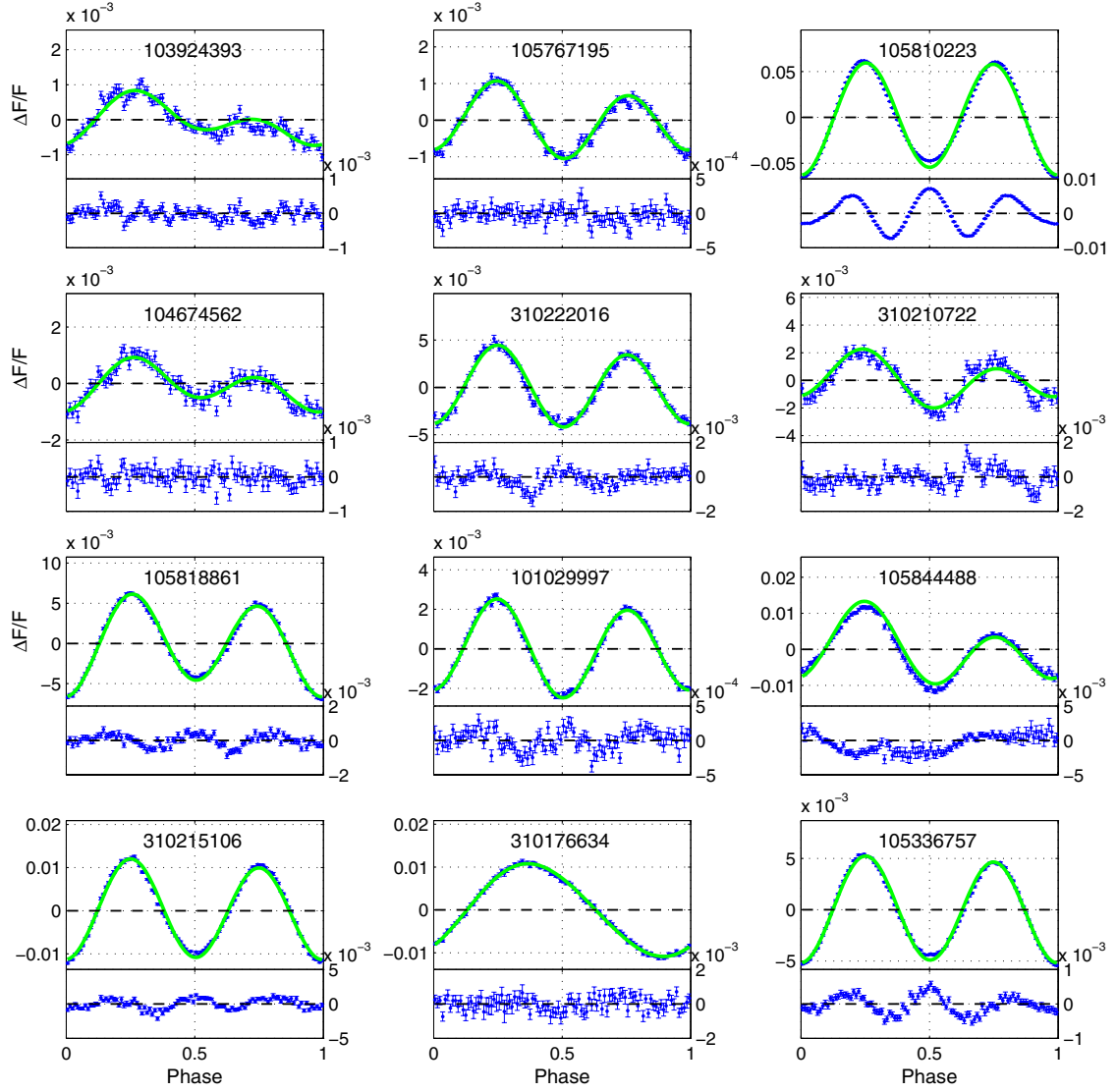


Fig. 15. Phase-folded and binned light curves (blue) and the best-fit BEER models assuming a circular orbit (green) of the 70 BEER binaries confirmed by AAOmega.

A&A 580, A21 (2015)

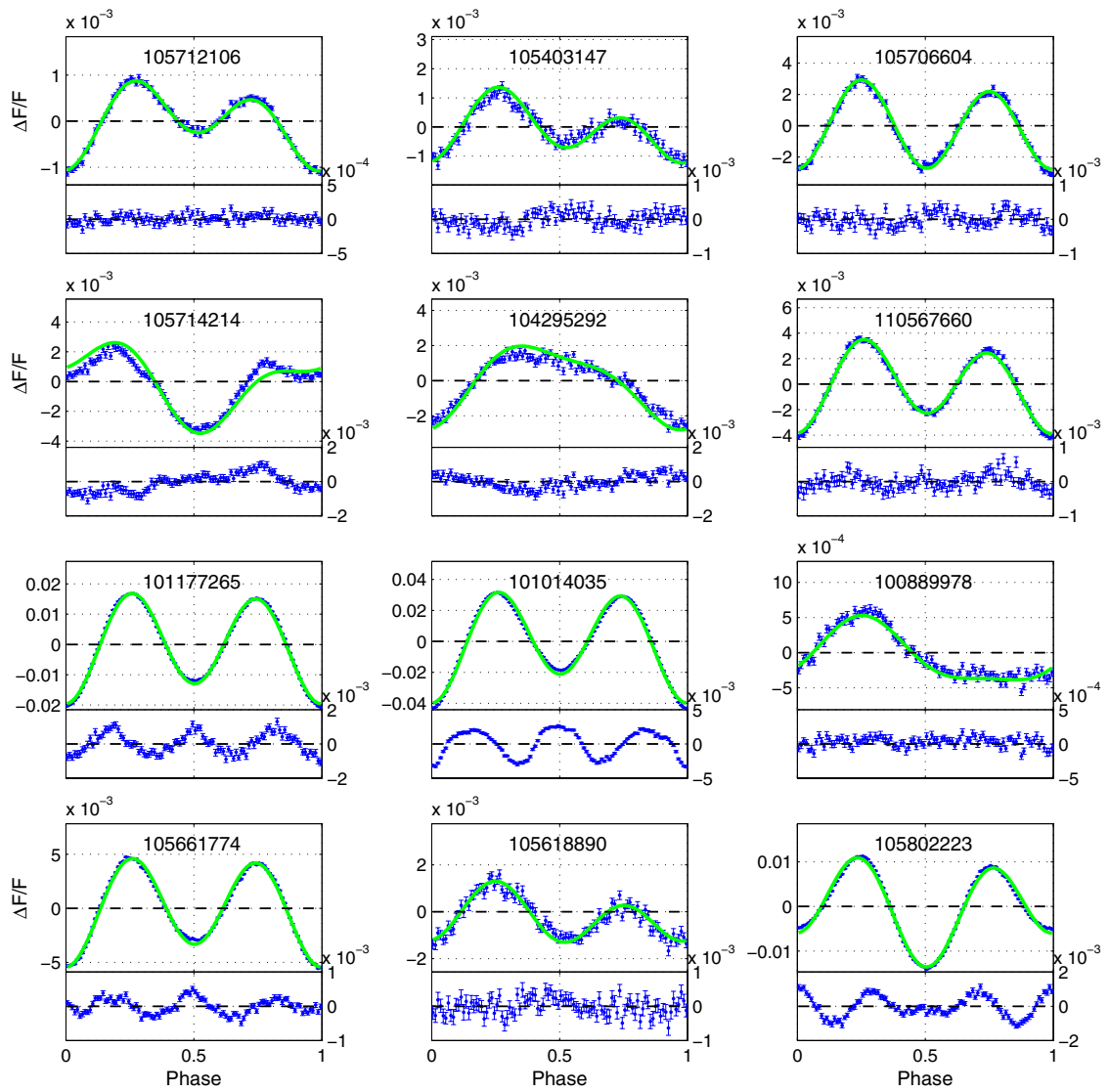


Fig. 15. continued.

L. Tal-Or et al.: Seventy new *CoRoT* BEER binaries

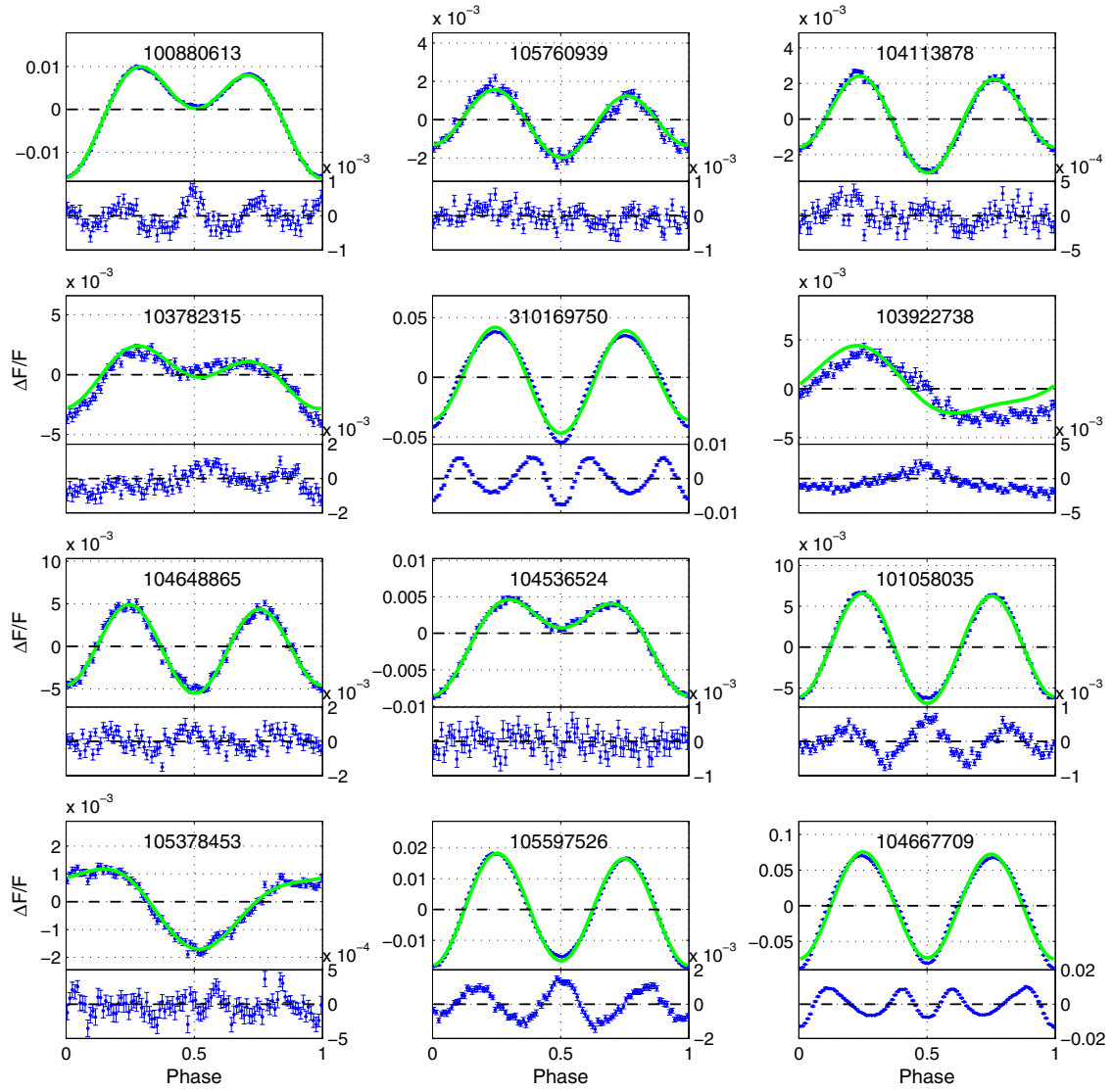


Fig. 15. continued.

A&A 580, A21 (2015)

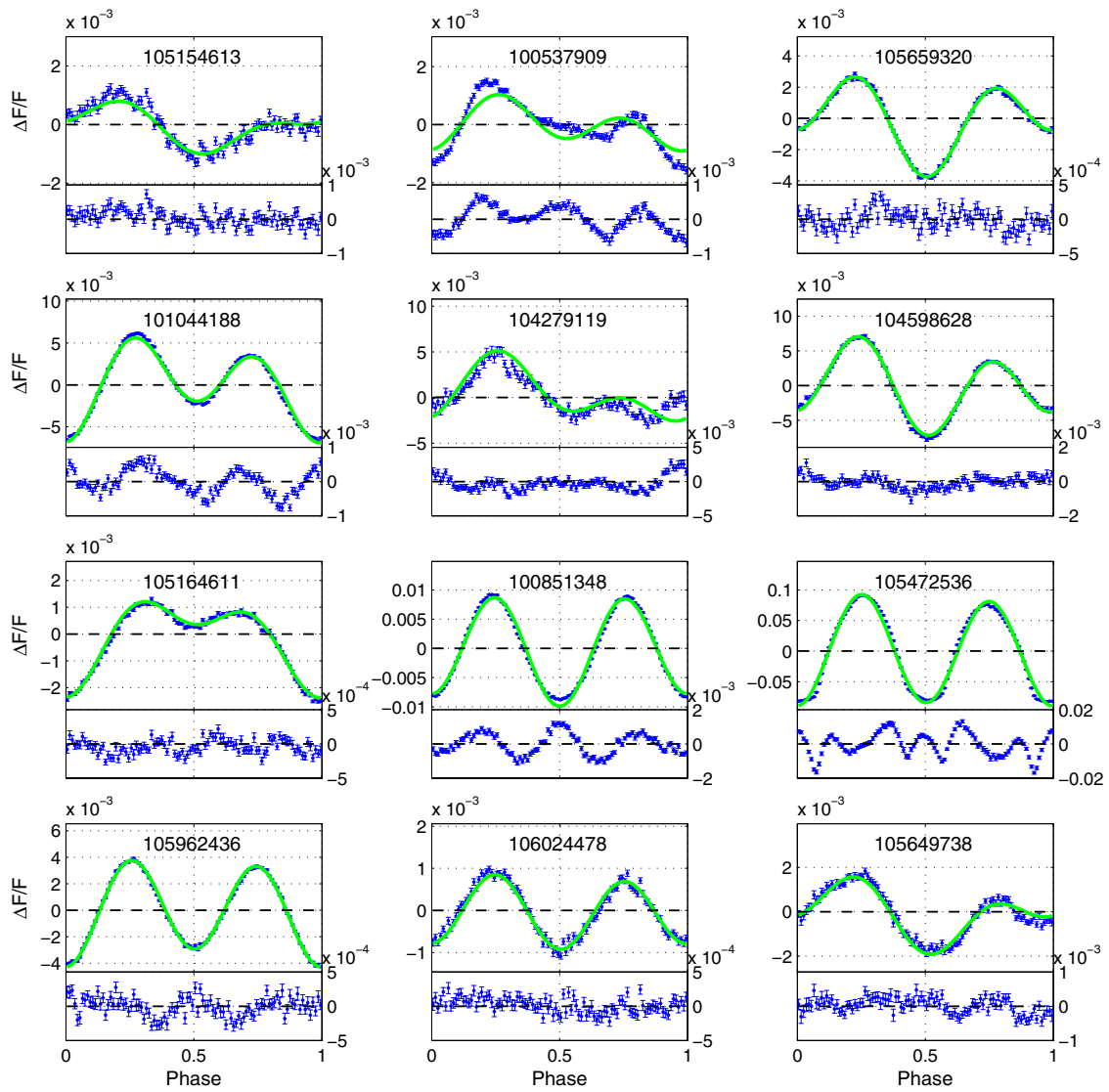


Fig. 15. continued.

L. Tal-Or et al.: Seventy new *CoRoT* BEER binaries

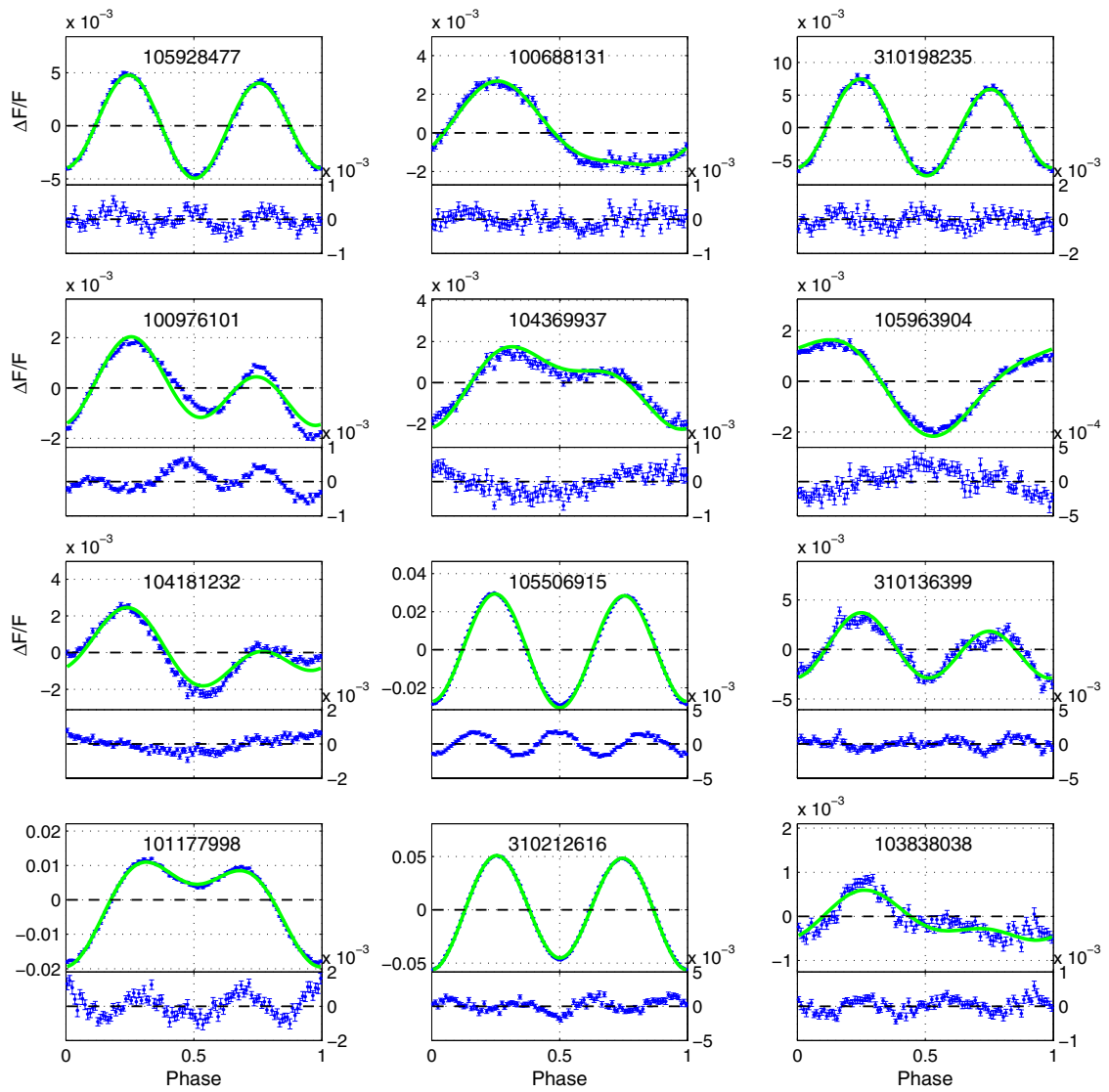


Fig. 15. continued.

A&A 580, A21 (2015)

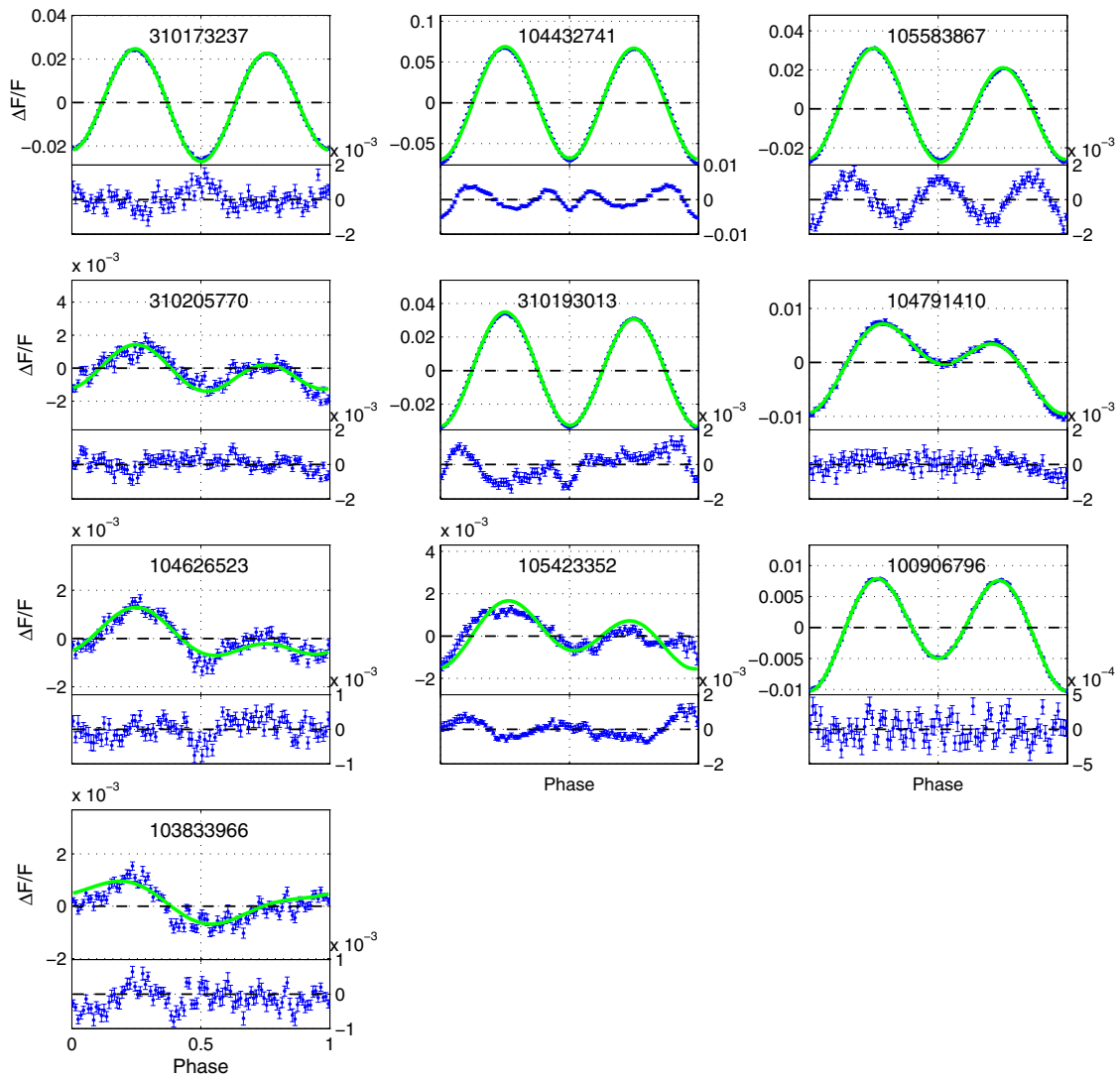


Fig. 15. continued.

References

- Aigrain, S., Favata, F., & Gilmore, G. 2004, *A&A*, **414**, 1139
- Aigrain, S., Barge, P., Deleuil, M., et al. 2008, in 14th Cambridge Workshop on Cool Stars, Stellar Systems, and the Sun, *ASP Conf. Ser.*, **384**, 270
- Auvergne, M., Bodin, P., Boissard, L., et al. 2009, *A&A*, **506**, 411
- Baglin, A. 2003, *Adv. Space Res.*, **31**, 345
- Batten, A. H. 1973, *Binary and multiple systems of stars* (New York: Pergamon Press)
- Borucki, W. J., Koch, D., Basri, G., et al. 2010, *Science*, **327**, 977
- Carter, J. A., Rappaport, S., & Fabrycky, D. 2011, *ApJ*, **728**, 139
- Cox, A. N. 2000, *Allen's astrophysical quantities* (New York: AIP Press)
- Deleuil, M., Meunier, J. C., Moutou, C., et al. 2009, *AJ*, **138**, 649
- Deleuil, M., Moutou, C., & Bordé, P. 2011, *Detection and Dynamics of Transiting Exoplanets*, St. Michel l'Observatoire, France, eds. F. Bouchy, R. Díaz, & C. Moutou, *EPJ Web of Conferences*, **11**, 1001
- Duquenooy, A., & Mayor, M. 1991, *A&A*, **248**, 485
- Eggleton, P. P. 1983, *ApJ*, **268**, 368
- Faigler, S., & Mazeh, T. 2011, *MNRAS*, **415**, 3921
- Faigler, S., & Mazeh, T. 2015, *ApJ*, **800**, 73
- Faigler, S., Mazeh, T., Quinn, S. N., Latham, D. W., & Tal-Or, L. 2012, *ApJ*, **746**, 185
- Faigler, S., Tal-Or, L., Mazeh, T., Latham, D. W., & Buchhave, L. A. 2013, *ApJ*, **771**, 26
- Fisher, J., Schröder, K.-P., & Smith, R. C. 2005, *MNRAS*, **361**, 495
- Gazzano, J.-C., de Laverny, P., Deleuil, M., et al. 2010, *A&A*, **523**, A91
- Goldberg, D., Mazeh, T., & Latham, D. W. 2003, *ApJ*, **591**, 397
- Gray, D. F. 2005, *Observation and Analysis of Stellar Photospheres*, 3rd edn. (UK: Cambridge University Press), 465
- Halbwachs, J. L. 1987, *A&A*, **183**, 234
- Halbwachs, J. L., Arenou, F., Mayor, M., Udry, S., & Queloz, D. 2000, *A&A*, **355**, 581
- Halbwachs, J. L., Mayor, M., Udry, S., & Arenou, F. 2003, *A&A*, **397**, 159
- Harrison, T. E., Howell, S. B., Huber, M. E., et al. 2003, *AJ*, **125**, 2609
- Hauschildt, P. H., Allard, F., & Baron, E. 1999, *ApJ*, **512**, 377
- Ho, S., & Turner, E. L. 2011, *ApJ*, **739**, 26
- Holland, P. W., & Welsch, R. E. 1977, *Commun. Statist. – Theor. Meth.*, **6**, 813
- Jackson, B. K., Lewis, N. K., Barnes, J. W., et al. 2012, *ApJ*, **751**, 112
- Koch, D. G., Borucki, W. J., Basri, G., et al. 2010, *ApJ*, **713**, L79
- Kramida, A., Yu. Ralchenko, Reader, J., & NIST ASD Team. 2013, NIST Atomic Spectra Database (ver. 5.1), [Online]. Available: <http://physics.nist.gov/asd> [2014, August 11]
- Lane, R. R., Kiss, L. L., Lewis, G. F., et al. 2011, *A&A*, **530**, A31
- Lewis, I. J., Cannon, R. D., Taylor, K., et al. 2002, *MNRAS*, **333**, 279
- Loeb, A., & Gaudi, B. S. 2003, *ApJ*, **588**, L117
- Lopez, S., & Jenkins, J. S. 2012, *ApJ*, **756**, 177
- Lucy, L. B., & Sweeney, M. A. 1971, *AJ*, **76**, 544
- Mazeh, T. 2008, *EAS Publ. Ser.*, **29**, 1
- Mazeh, T., & Faigler, S. 2010, *A&A*, **521**, L59
- Mazeh, T., & Goldberg, D. 1992, *ApJ*, **394**, 592
- Mazeh, T., & Zucker, S. 1994, *Ap&SS*, **212**, 349
- Mazeh, T., Goldberg, D., Duquenooy, A., & Mayor, M. 1992, *ApJ*, **401**, 265
- Mazeh, T., Nachmani, G., Sokol, G., Faigler, S., & Zucker, S. 2012, *A&A*, **541**, A56
- Mislis, D., Heller, R., Schmitt, J. H. M. M., & Hodgkin, S. 2012, *A&A*, **538**, A4
- Miszalski, B., Shorridge, K., Saunders, W., Parker, Q. A., & Croom, S. M. 2006, *MNRAS*, **371**, 1537
- Morris, S. L. 1985, *ApJ*, **295**, 143
- Mosser, B., Dziembowski, W. A., Belkacem, K., et al. 2013, *A&A*, **559**, A137
- Moutou, C., Deleuil, M., Guillot, T., et al. 2013, *Icarus*, **226**, 1625
- Öpik, E. 1924, *Publications of the Tartu Astrofizica Observatory*, **25**, 6
- Prša, A., Batalha, N., Slawson, R. W., et al. 2011, *AJ*, **141**, 83
- Raghavan, D., McAlister, H. A., Henry, T. J., et al. 2010, *ApJS*, **190**, 1
- Rouan, D., Baglin, A., Copet, E., et al. 1998, *Earth Moon Planet.*, **81**, 79
- Rowe, J. F., Bryson, S. T., Marcy, G. W., et al. 2014, *ApJ*, **784**, 45
- Rybicki, G. B., & Lightman, A. P. 1979, *Radiative processes in astrophysics* (New York: Wiley Interscience)
- Santerne, A., Moutou, C., Barros, S. C. C., et al. 2012, *A&A*, **544**, L12
- Saunders, W., Bridges, T., Gillingham, P., et al. 2004, in *SPIE Conf. Ser.* 5492, eds. A. F. M. Moorwood, & M. Iye, 389
- Sebastian, D., Guenther, E. W., Schaffnerroth, V., et al. 2012, *A&A*, **541**, A34
- Shporer, A., Jenkins, J. M., Rowe, J. F., et al. 2011, *AJ*, **142**, 195
- Smith, G. A., Saunders, W., Bridges, T., et al. 2004, in *SPIE Conf. Ser.* 5492, eds. A. F. M. Moorwood, & M. Iye, 410
- Surace, C., Alonso, R., Barge, P., et al. 2008, in *SPIE Conf. Ser.*, 7019
- Taylor, K., Bailey, J., Wilkins, T., Shorridge, K., & Glazebrook, K. 1996, in *Astronomical Data Analysis Software and Systems V*, eds. G. H. Jacoby, & J. Barnes, *ASP Conf. Ser.*, **101**, 195
- Torres, G., Andersen, J., & Giménez, A. 2010, *A&ARv*, **18**, 67
- Torres, G., Fischer, D. A., Sozzetti, A., et al. 2012, *ApJ*, **757**, 161
- van Kerkwijk, M. H., Rappaport, S. A., Breton, R. P., et al. 2010, *ApJ*, **715**, 51
- Wilson, R. E. 1990, *ApJ*, **356**, 613
- Zucker, S., & Mazeh, T. 1994, *ApJ*, **420**, 806
- Zucker, S., Mazeh, T., & Alexander, T. 2007, *ApJ*, **670**, 1326

BEER ANALYSIS OF *KEPLER* AND *CoRoT* LIGHT CURVES. IV. DISCOVERY OF FOUR NEW LOW-MASS WHITE DWARF COMPANIONS IN THE *KEPLER* DATAS. FAIGLER¹, I. KULL¹, T. MAZEH¹, F. KIEFER¹, D. W. LATHAM², AND S. BLOEMEN³¹ School of Physics and Astronomy, Raymond and Beverly Sackler Faculty of Exact Sciences, Tel Aviv University, Tel Aviv 69978, Israel² Harvard-Smithsonian Center for Astrophysics, 60 Garden Street, Cambridge, MA 02138, USA³ Department of Astrophysics, IMAPP, Radboud University Nijmegen, P.O. BOX 9010, NL-6500 GL Nijmegen, The Netherlands

Received 2015 June 18; accepted 2015 October 28; published 2015 December 3

ABSTRACT

We report the discovery of four short-period eclipsing systems in the *Kepler* light curves, consisting of an A-star primary and a low-mass white dwarf (WD) secondary (dA+WD)—KIC 4169521, KOI-3818, KIC 2851474, and KIC 9285587. The systems show BEaming, Ellipsoidal and Reflection (BEER) phase modulations together with primary and secondary eclipses. These add to the 6 *Kepler* and 18 WASP short-period eclipsing dA+WD binaries that were previously known. The light curves, together with follow-up spectroscopic observations, allow us to derive the masses, radii, and effective temperatures of the two components of the four systems. The orbital periods, of 1.17–3.82 days, and WD masses, of 0.19–0.22 M_{\odot} , are similar to those of the previously known systems. The WD radii of KOI-3818, KIC 2851474, and KIC 9285587 are 0.026, 0.035, and 0.026 R_{\odot} , respectively, the smallest WD radii derived so far for short-period eclipsing dA+WD binaries. These three binaries extend the previously known population to older systems with cooler and smaller WD secondaries. KOI-3818 displays evidence for a fast-rotating primary and a minute but significant eccentricity, $\sim 1.5 \times 10^{-3}$. These features are probably the outcome of the mass-transfer process.

Key words: stars: individual (KIC 4169521, KIC 6515722, KOI-3818, KIC 2851474 KIC 9285587) – white dwarfs

1. INTRODUCTION

The *Kepler* spacecraft was launched in order to detect shallow transits produced by planets, which are characterized by their small radii, of the order of 0.1–0.01 R_{\odot} , and therefore induce transits with shallow depth, of the order of 10^{-2} – 10^{-4} of the stellar flux (Borucki et al. 2010). As of 2015 May, *Kepler* indeed produced more than 4600 planet candidates, with orbital periods of 0.3–1295 days (Mullally et al. 2015). As a by-product of this effort, the *Kepler* mission has also identified more than 2700⁴ eclipsing binary (EB) systems (Slawson et al. 2011), most of which exhibit much deeper eclipses.

However, white dwarfs (WDs) residing in binary systems are also expected to produce shallow eclipses, mimicking the transits of small planets. In fact, there are nine known EBs with WD secondaries in the *Kepler* data (Rowe et al. 2010; Bloemen et al. 2011; Carter et al. 2011; Breton et al. 2012; Muirhead et al. 2013; Kruse & Agol 2014; Rappaport et al. 2015). Six of these were identified as short-period binaries of an F/A-type primary and a pre-Helium WD secondary (dA+pre-He-WD), with radii of 0.04–0.28 R_{\odot} . The remaining three systems belong to different categories and had more “standard” derived WD radii of 0.012–0.014 R_{\odot} .

Other than the *Kepler* discoveries, the stars V209, 1SWASP J024743.37–251549.2 (hereafter WASP0247–25), OGLE-BLG-RRLYR-02792, and possibly AW UMa, are EBs that are believed to accommodate pre-He-WD secondaries (Kaluzny et al. 2007; Pribulla & Rucinski 2008; Maxted et al. 2011, 2013; Pietrzyński et al. 2012). Of these, only WASP0247–25 was identified as a short-period detached dA+pre-He-WD EB, which we consider as the binary type associated with the discoveries reported here. A significant recent contribution to the known population of short-period dA+pre-He-WD EBs was made by

Maxted et al. (2014), who discovered 17 such systems in the WASP photometry database (Pollacco et al. 2006). Two of these have accurate measurements of the secondaries’ masses, radii, and T_{eff} , confirming that they are pre-He-WDs.

WDs in short-period binaries are expected to be hotter than their primary stars, resulting in a light curve with a flat-bottom secondary eclipse that is deeper than the primary eclipse. This is because for a circular orbit, the primary-to-secondary eclipses depth ratio approximates the primary-to-secondary surface-brightness ratio in the observed band. Indeed, except for the special case of KPD 1946 + 4340, with a subdwarf B star primary (Bloemen et al. 2011), the other eight WD systems in the *Kepler* data exhibit a secondary eclipse that is deeper than the primary one.

Unfortunately, just from the primary and secondary eclipse depths, one cannot tell if the companion is a low-mass star or a WD, as the primary and secondary eclipses can be interchanged. To overcome this ambiguity, Maxted et al. (2014) looked in the WASP catalog for EB systems that show a *deeper flat-bottom* eclipse, indicating a hotter WD companion. Using this method they discovered 17 short-period EBs with pre-He-WD secondaries. More recently, Rappaport et al. (2015) used a similar approach for the *Kepler* EB catalog. They visually inspected the light curves of EBs with the *Kepler* Input Catalog (KIC) $T_{\text{eff}} > 7000$ K and discovered two new short-period dA+pre-He-WD EBs.

Alternatively, one can use three photometric phase modulation effects, BEaming, Ellipsoidal and Reflection (BEER), to distinguish between low-mass stellar and WD companions. The beaming effect, sometimes called Doppler boosting, causes an increase (decrease) of the brightness of any light source approaching (receding from) the observer (Rybicki & Lightman 1979; Loeb & Gaudi 2003), with an amplitude that is proportional to the radial velocity (RV) of the source. Therefore, the stellar RV modulation due to a circular-orbit

⁴ <http://keplerebs.villanova.edu/>

companion will produce a sine-like beaming modulation at the orbital period, if the middle of the primary eclipse is defined as the phase zero point. The semi-amplitude of such a modulation is on the order of 100–400 parts-per-million (ppm) for low stellar-mass companions, compared to an order of 10 ppm for Jupiter-mass planets (Loeb & Gaudi 2003; Faigler et al. 2012). More importantly, the phase of the beaming effect reveals which object is being eclipsed, and thus it enables distinguishing between a low-mass stellar companion and a WD companion, based on the eclipses’ relative depths. It is the same as the information that is provided by the phases when the RV of the primary is blueshifted or redshifted.

The second effect is the well-known ellipsoidal variation (Kopal 1959; Morris 1985) that is due to the tidal distortion of the star by the gravity of the companion (e.g., Loeb & Gaudi 2003; Zucker et al. 2007; Mazeh 2008), resulting in a cosine-like phase modulation at half the orbital period, for a circular-orbit companion under the same phase zero definition. The semi-amplitude of the ellipsoidal modulation for orbital periods of a few days is on the order of 1000 ppm for low stellar-mass companions, compared to an order of 10 ppm for Jupiter-mass planets (Loeb & Gaudi 2003; Faigler et al. 2012).

The third effect is the reflection/emission variation, the result of light emitted by one component, scattered off of or thermally re-emitted from the dayside of the other component (Vaz 1985; Wilson 1990; Maxted et al. 2002; Harrison et al. 2003; For et al. 2010; Reed et al. 2010). This effect depends on properties that are associated with the response of the object’s atmosphere to its companion’s radiation, such as the Bond albedo, the scattered light geometric albedo, and heat redistribution parameters. The reflection/emission modulation is expected to behave approximately as a cosine wave at the orbital period for a circular orbit, and can have different signs depending on the luminosity ratio and radius ratio of the two components of the binary. In the known *Kepler* systems with large-radii WD secondaries, this effect is dominated by light originating from the WD, scattered off of or thermally re-emitted by the primary star atmosphere (Carter et al. 2011; Breton et al. 2012; Rappaport et al. 2015).

To take advantage of the information provided by the BEER modulations, the BEER algorithm (Faigler & Mazeh 2011) searches for stars whose light curves show a combination of the three effects’ amplitudes and phases that is consistent with a short-period companion. This work reports on the discovery of four additional short-period EBs of an A-type primary and a low-mass WD secondary (dA+WD) in the *Kepler* field, identified among the BEER compact companion candidates as having a secondary eclipse deeper than the primary one. One system includes a pre-Helium WD, similar to those in the previously known systems, while the other secondaries are well-developed WDs, which were not observed before in short-period dA+WD binaries.

This paper is organized as follows. Section 2 presents the BEER search and the resulting four detections, and Section 3 describes the spectroscopic follow-up observations. Section 4 then presents detailed modeling of the *Kepler* photometry, and Section 5 describes the parameters resulting from the analyses of the photometric and spectroscopic observations. Section 6 further reviews specific features of each of the four discovered systems, and Section 7 summarizes and discusses the results of this work.

2. THE PHOTOMETRIC BEER SEARCH

To identify WD secondaries, we applied the BEER search algorithm, after adaptation for a compact object companion, to the *Kepler* Q2–Q16 raw long-cadence light curves of 40,728 stars that were brighter than 13.5 mag. The BEER search assigned to each light curve a likelihood that the star hosts a compact companion, while identifying the inferior conjunction from the amplitudes and phases of the BEER modulations. After sorting the stars based on their BEER likelihoods, we visually inspected the 100 highest-scoring light curves and identified four systems, KIC 4169521, KOI-3818 = KIC 6515722, KIC 2851474, and KIC 9285587, in which there were two eclipses and the secondary was deeper than the primary. As indicated by its name, KOI-3818 was a member of the KOI catalog, listed as a false positive, but with an orbital period of ~ 1.9 days that is half the orbital period we detected, while the remaining three systems appeared in the *Kepler* EB catalog.

Figure 1 presents a short section of the raw *Kepler* light curve of each of the systems, Figure 2 shows the amplitude spectrum of the light curves, and Figure 3 presents the four cleaned and detrended light curves folded at their respective orbital periods. Cleaning of outliers and jumps and detrending were performed following Faigler et al. (2013). In the four systems the amplitude spectrum clearly shows the BEER frequency peaks at the orbital frequency and its first harmonic, associated mainly with the beaming and the ellipsoidal modulations, respectively. The KOI-3818 spectrum also shows peaks at frequencies of ~ 2.1 cycles day $^{-1}$ and its harmonics; KIC 9285587 displays peaks in the 19–24 cycles day $^{-1}$ range. Therefore in these two cases, cleaning also included fitting and subtracting several high-frequency sine functions, associated with the high-frequency spectra peaks (see Section 4 for more details about the cleaning and detrending process). Each of the resulting folded light curves in Figure 3 shows ellipsoidal and beaming phase modulation, a curved bottom primary eclipse at phase zero, and a deeper flat-bottom secondary eclipse at phase 0.5, all being consistent with a fully occulted, compact hot companion.

3. SPECTROSCOPIC OBSERVATIONS

Follow-up spectroscopic observations of the four stars were obtained with the Tillinghast Reflector Echelle Spectrograph (TRES; Fűrész 2008) mounted on the 1.5 m Tillinghast Reflector at the Fred Lawrence Whipple Observatory operated by the Smithsonian Astrophysical Observatory (SAO) on Mount Hopkins in Southern Arizona. The TRES instrument spans the wavelength range 3850–9096 Å, with a nominal resolving power of $R \sim 44,000$. The instrumental setup and observing procedures were as described in Faigler et al. (2013). The spectra were extracted and rectified to intensity versus wavelength using the standard procedures developed by Buchhave et al. (2010).

For each target, the pseudo-continuum of each spectrum was derived using a large-window p -percentile filter (Hodgson et al. 1985). For such a filter, a value of $p = 0.5$ corresponds to a median filtering, while for $p > 0.5$ the filter selects flux larger than the median. We empirically chose $p = 0.8$ and a filtering window w from the orders’ edge to the center of around 200–1000 pixels, in order to obtain the best compromise on continuum matching for both narrow and wide lines.

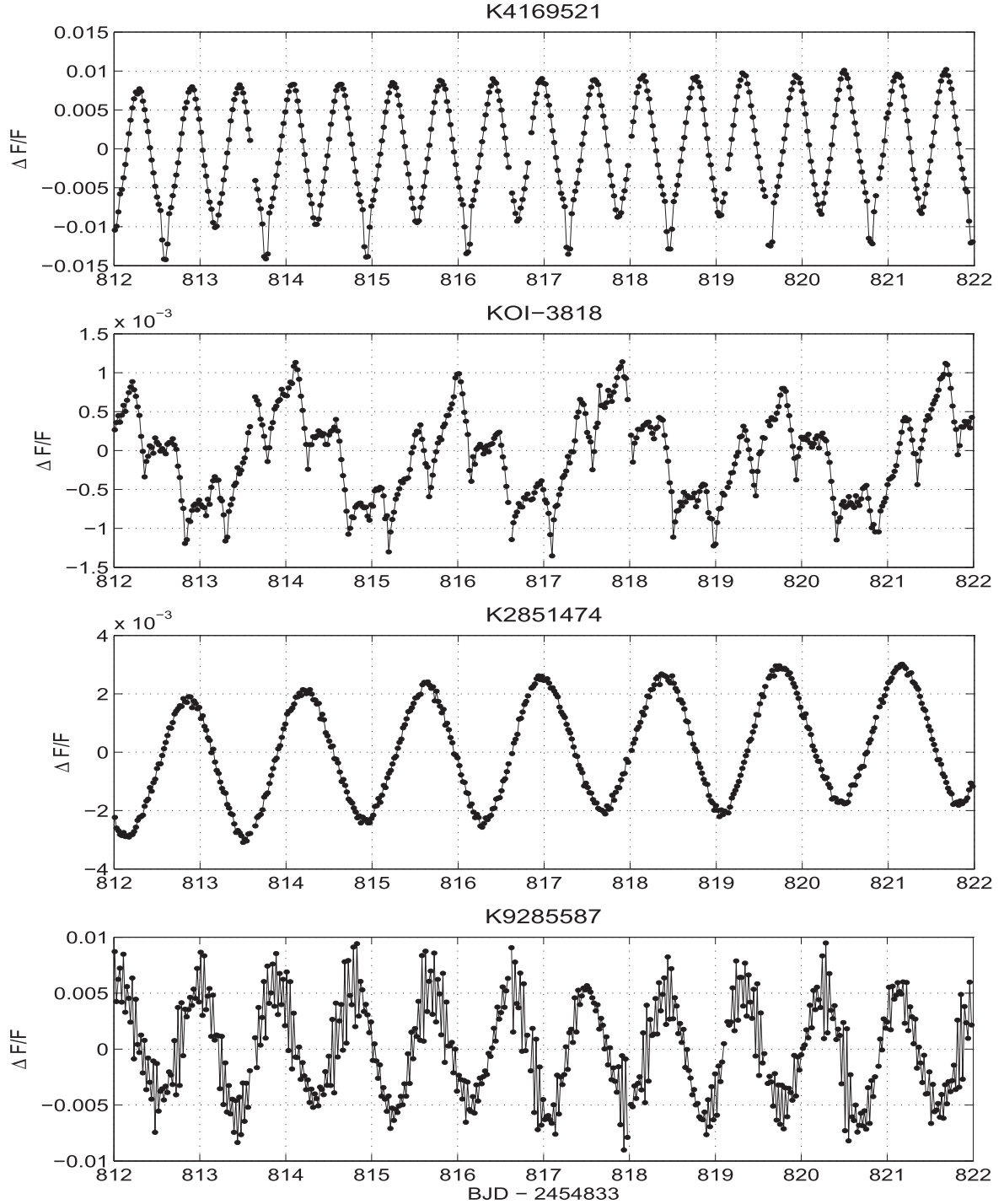


Figure 1. Light curves of the four systems for a selected time span of 10 days. Note the different Y axis scales of the four plots.

The same continuum derivation procedure was also applied to a library of synthetic spectra, with the parameters adjusted visually to $p = 0.95$ and $w = 500$ pixels so that the model spectra gave better fitted of the Balmer lines. We later verified that varying these parameters by 10% had a negligible effect on the derived radial velocities and orbital solutions. The synthetic

spectra were also broadened to match the TRES line spread function, on the $\ln(\lambda)$ scale, and assuming a constant $R \sim 44,000$ through all orders.

As our targets are hot stars ($T_{\text{eff}} > 6000$ K) with wide and prominent Balmer lines and narrower Ca II H and K lines and Mg II at 4481 Å, we tried χ^2 fitting the different lines to the

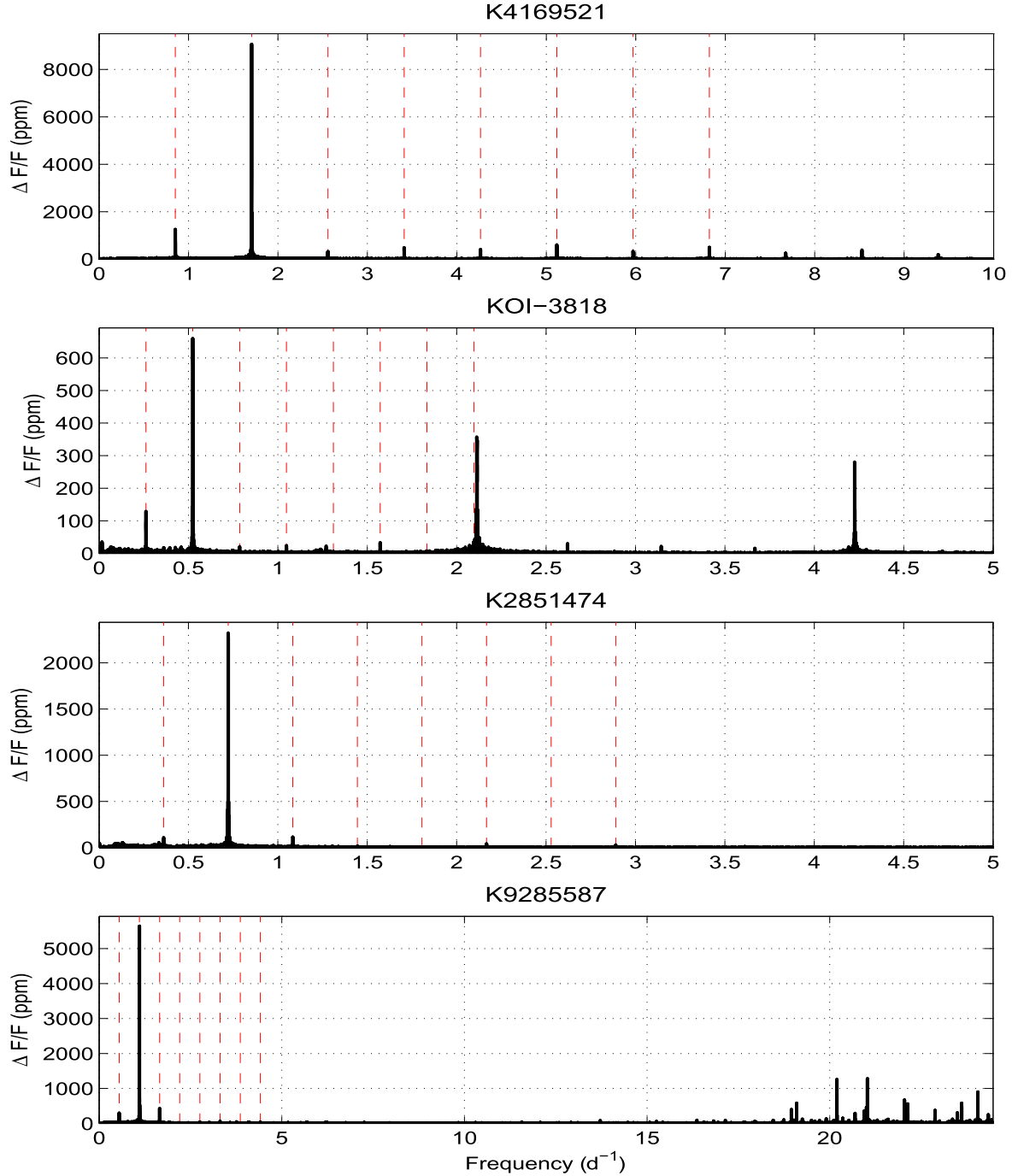


Figure 2. Amplitude spectra of the four systems. Dashed lines mark the orbital frequency and its harmonics, determined from the eclipses’ timings. The frequency axis range is different for each system for improved visualization of specific spectral features of that system.

library of synthetic spectra, using an approach similar to Bloemen et al. (2012). We did not observe a strong dependence of the surface gravity and metallicity on the χ^2 , so we fixed them to fiducial estimates of $\log(g) = 4.0$ dex and $[\text{Fe}/\text{H}] = 0.0$. Optimizing the stellar rotation $v \sin i$ over the different lines gave consistent results that are listed in the upper section of Table 2. We could not constrain the effective

temperature using this method, as different lines gave different optimized temperatures with deviations on the order of 1000–2000 K between the lines. We therefore kept T_{eff} as a free parameter when finding the optimized synthetic spectrum. For our subsequent analysis, described in the next section, we adopted the most recent KIC effective temperatures of Q1–Q17 DR 24 from the *Kepler* Exoplanets Archive

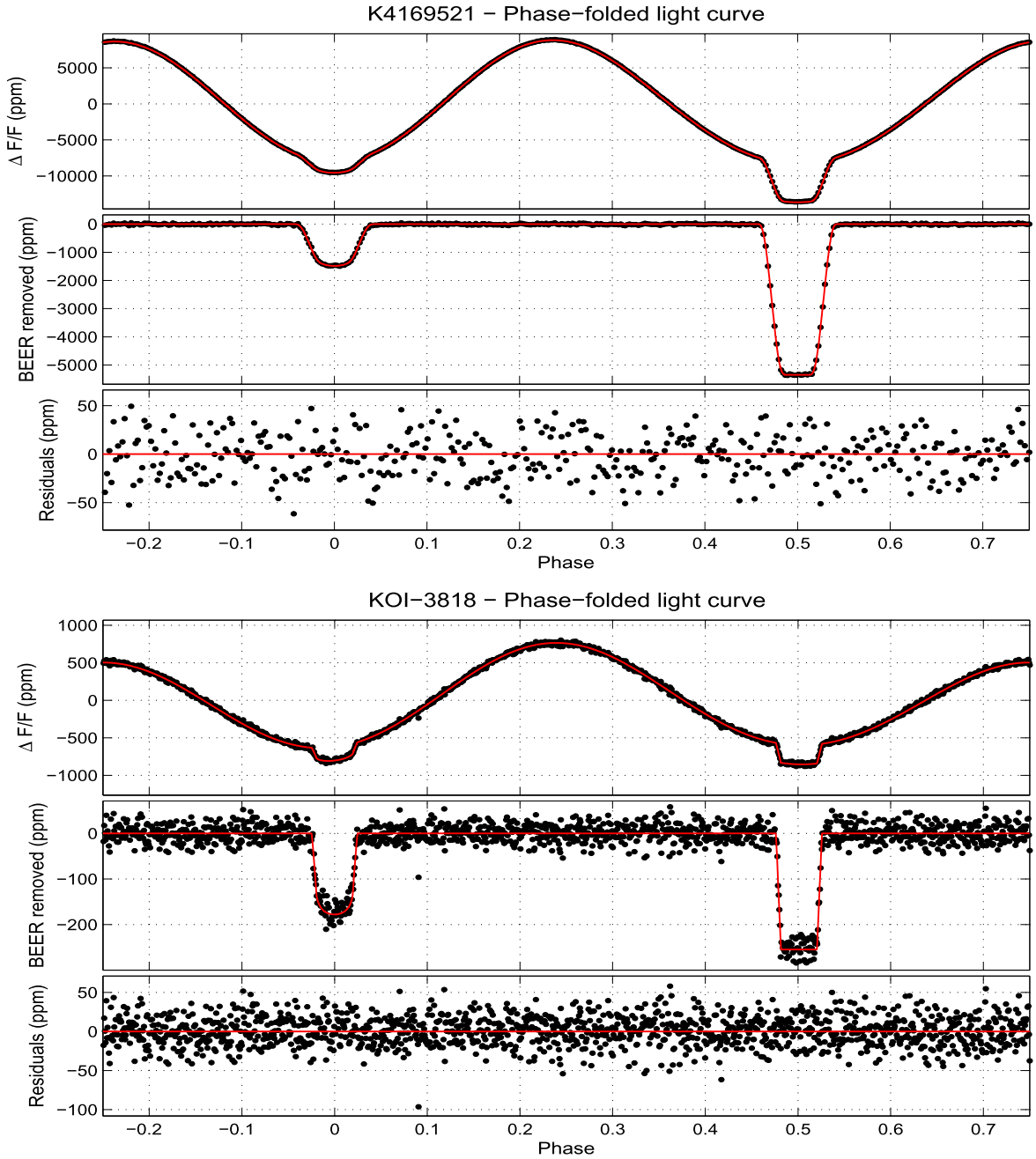


Figure 3. Folded cleaned and detrended light curves of the four systems. The upper panels present the folded data, the middle panels show the folded data after the removal of the BEER modulation, and the lower panels present the residuals. The black points are the folded data in 4 minute bins, and the red curve is the model fit described in Section 4.

(2015), which were determined using a variety of methods (Huber et al. 2014).

Radial velocities were derived by cross-correlating the multi-order spectra of each target with the synthetic spectrum that gave the highest peak correlation value (e.g., Mazeh & Zucker 1992; Zucker 2003; Tal-Or et al. 2015) chosen from the PHOENIX library of synthetic spectra (Hauschildt et al. 1999). We excluded all orders with telluric lines and known problems (e.g., broad line on the order’s edge, low

signal-to-noise ratio, no lines). The resulting RV points are listed in Table 1.

The radial velocities were used to derive orbital solutions, while taking into account the photometric period and primary eclipse time estimates and their uncertainties. This was done by adding the χ^2 of the photometric period and ephemeris to the χ^2 of the RV points. To find the orbital solution we searched the parameter space for χ^2_{\min} , the minimum combined χ^2 . The uncertainties of the parameters were derived by calculating the

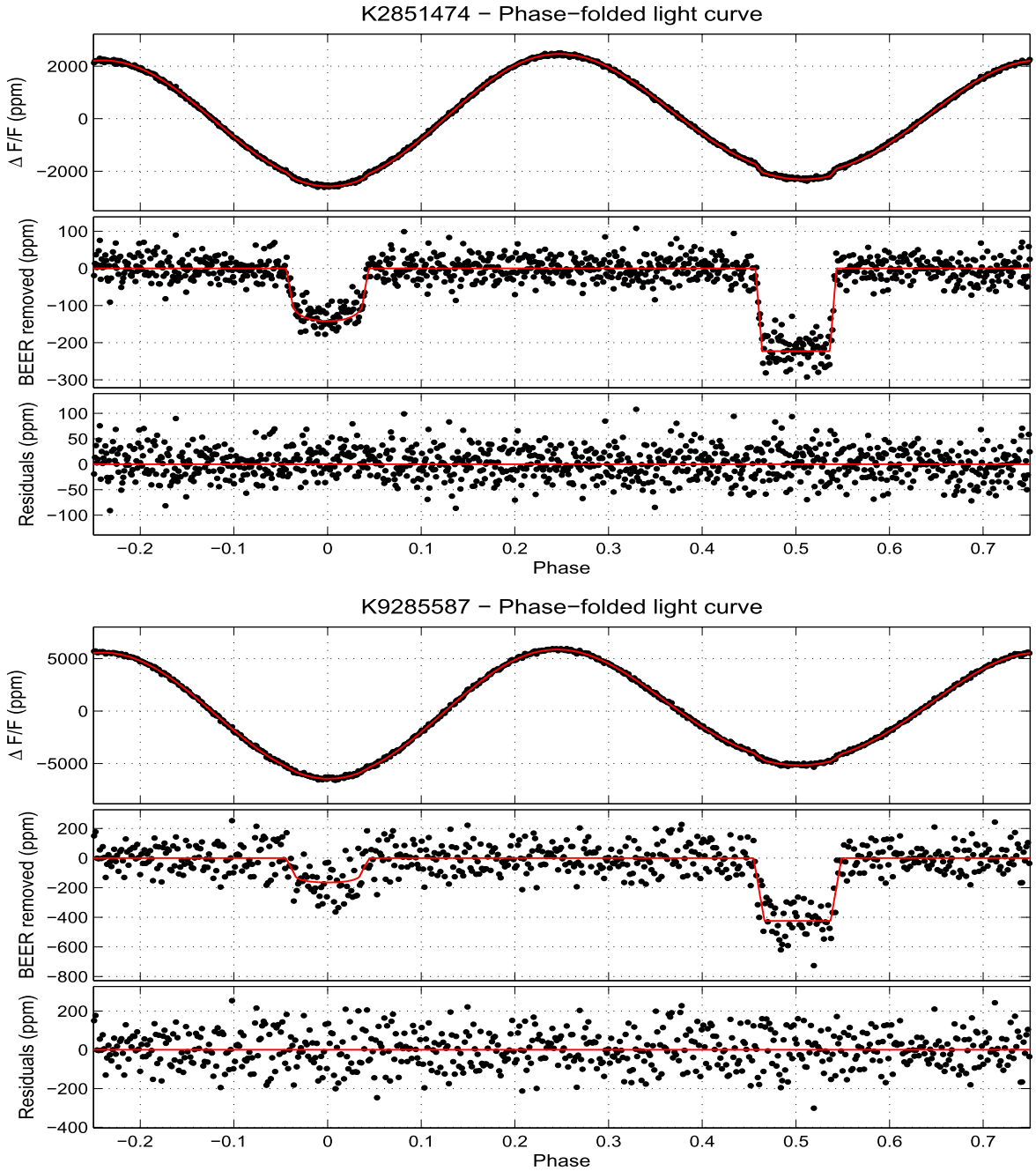


Figure 3. (Continued.)

locus of $\chi^2 = \chi_{\min}^2 + \Delta$, where Δ corresponds to 1σ uncertainty. In order to get more realistic uncertainties for the orbital parameters, we inflated only the RV uncertainties by a common multiplicative factor, so that the reduced χ^2 became unity.

We first derived eccentric orbital solutions, but these were not found by an F-test to be preferable over circular-orbit solutions, so here we present the circular-orbit solutions. The orbital elements of the four systems are listed in Table 2 and the RV points and orbital models are presented in Figure 4.

4. MODELING THE LIGHT CURVES

For a more complete photometric analysis of these eclipsing WD companion systems we re-analyzed the *Kepler* data while trying to minimize the data preparation stages. We first removed data segments with instrumental artifacts (Faigler et al. 2013) and subtracted a third light constant from each quarter’s data using its light curve crowding ratio (Jenkins et al. 2010). Removal of the long-term trend, periodic modulations, and outliers was performed for each *Kepler*

Table 1
Radial Velocities of the Four Systems

Time (BJD –2450000)	RV (km s ^{–1})	Time (BJD –2450000)	RV (km s ^{–1})
KIC 4169521:		KOI-3818:	
7092.999960	11.7(1.0)	6610.588231	20.0(1.3)
7113.939043	22.3(1.0)	6621.603852	14.8(1.4)
7123.933711	–26.73(93)	7079.014413	0.1(1.8)
7143.946135	–17.31(87)	7091.986663	26.4(1.4)
7146.896942	17.63(93)	7092.975399	–1.8(2.0)
7150.931177	–17.72(94)	7094.986119	20.6(1.3)
7152.914603	–3.0(1.0)	7110.958442	20.6(2.1)
7153.931701	16.86(75)	7114.916440	24.3(1.1)
	...	7116.952376	–7.1(1.4)
	...	7117.944316	17.2(1.2)
KIC 2851474:		KIC 9285587:	
7087.024901	–16.87(43)	7140.884898	2.72(93)
7095.000035	–22.33(53)	7143.872021	–29.67(60)
7143.843575	6.54(29)	7149.956001	–0.35(83)
7145.960435	9.28(35)	7150.959942	–37.33(99)
7149.829697	–8.03(47)	7152.946544	–29.59(79)
7150.842479	–13.38(53)	7165.918995	–11.50(71)
7153.903532	–3.81(28)	7170.789666	–38.18(67)
	...	7175.763105	–20.56(62)

quarter by a *single* simultaneous robust linear fit (Holland & Welsch 1977) to the data after masking out the eclipses. The simultaneous fit was to four sets of functions: long-term cosine-trend functions of periods down to a minimum of twice the orbital period (Mazeh & Faigler 2010), BEER cosine and sine functions of the first four orbital-period harmonics, jump functions at predefined *Kepler* times (Faigler et al. 2013), and high-frequency stellar-activity sine and cosine functions.

The high-frequency functions were incorporated only for KOI-3818 and KIC 9285587, for which the light curve and amplitude spectrum show significant high-frequency modulations. The high-frequencies list of KOI-3818 was constructed manually because its modulation spectrum showed a simple structure of peaks at ~ 2.113 cycles day^{–1} and its harmonics. Consequently, we included the ~ 2.113 cycles day^{–1} frequency in the list, along with its three first harmonics, and added two and one side-lobe frequencies on each side of the base frequency and its first harmonic, respectively. The side-lobe frequencies were separated by 1/90 cycles day^{–1}, which is the natural frequency separation for a fit performed on a single *Kepler* quarter of a typical duration of 90 days.

The high-frequency modulation spectrum of KIC 9285587 showed no clear structure, so we constructed its frequency list through a pre-whitening iterative process. At each iteration, we fitted the data to sine and cosine functions of the previous frequency list, and derived the spectrum of the fit residuals. The frequency of the highest residuals-spectrum peak was then added to the previous list, and the updated list was used in the next iteration. This process was stopped based on a Bayesian information criteria.

The resulting frequency lists of KOI-3818 and KIC 9285587 were then used in the simultaneous robust fit of each *Kepler* quarter data to the detrend, jumps, BEER, and high-frequency functions. As the fit results we report an amplitude and its uncertainty as that amplitude’s median and its median absolute deviation across the *Kepler* quarters, respectively (Faigler &

Mazeh 2015). The fitted high frequencies and amplitudes of these two systems are listed in Table 3. For each frequency, the listed amplitude is the 2-norm of that frequency’s sine and cosine fitted amplitudes (i.e., $\sqrt{A_{\cos}^2 + A_{\sin}^2}$, where A_{\cos} is the cosine amplitude, and A_{\sin} is the sine amplitude, of that frequency). It may seem strange that for most frequencies the fitted amplitudes are much smaller than their uncertainties. However, this only means that the amplitudes vary wildly across the quarters, which is indicative of the non-periodic nature of these modulations.

For the shortest period system, KIC 4169521, we had to fit *five* BEER harmonics in order to get a good fit to the data. This is probably due to the significance of higher orders of the ellipsoidal modulation, resulting from the proximity of the two binary objects. The simultaneous robust fit was performed after taking the logarithm of the data to account for the multiplicative nature of the eclipses and the phase modulations (Huang et al. 2013). The fitted BEER amplitudes, with their uncertainties derived from the quarter-to-quarter scatter (Faigler & Mazeh 2015), are listed in Table 4.

Next, we subtracted the fitted trend model from the *unmasked* data and analyzed the detrended eclipses. For that we ran a Markov chain Monte Carlo (MCMC) analysis, using the Ensemble Samplers method (Goodman & Weare 2010) that is invariant to affine transformations of the parameter space, making it much more efficient for problems with correlated parameters. The MCMC analysis was performed by simultaneously fitting the primary and secondary eclipses using a *Kepler* long-cadence integrated Mandel & Agol (2002) model with quadratic limb darkening, assuming a circular orbit. The model limb-darkening coefficients could not be constrained from the data, so we estimated their values and uncertainties by interpolating the Claret & Bloemen (2011) limb-darkening tables, using the KIC effective temperatures and the fiducial estimates of $\log(g) = 4.0$ dex and $[\text{Fe}/\text{H}] = 0.0$.

The model we fitted to the data had 8 free parameters: orbital period P , middle of primary eclipse time T_0 , radius ratio R_2/R_1 , scaled separation a/R_1 , flux ratio F_2/F_1 , impact parameter b , secondary-eclipse time shift ΔT_{sec} , and secondary-to-primary eclipses durations ratio $\tau_{\text{sec}}/\tau_{\text{prim}}$. The secondary-eclipse time shift was added to the model in order to account for the Rømer delay (Kaplan 2010; Bloemen et al. 2012) and the $e \cos \omega$ component of a possible small eccentricity, while the secondary-to-primary eclipses durations ratio was added to account for the $e \sin \omega$ component of such a possible eccentricity.

Figure 3 presents the cleaned and detrended binned data and the best-fit Mandel & Agol (2002) model combined with, and without, the BEER phase modulation, folded at the orbital period. The three upper sections of Table 4 summarize the results of the photometric analysis. The first section of the table lists the third light fraction and the limb-darkening coefficients; the second lists the MCMC medians and 1σ uncertainties of the model parameters; and the third section lists the BEER amplitudes with their uncertainties.

5. THE PARAMETERS OF THE SYSTEMS

5.1. Masses and Radii

To estimate the primary mass, we used a method similar to the one used by Rappaport et al. (2015). We first estimated the primary density by using *Kepler*’s third law with the

Table 2
Stellar Properties and RV Orbital Elements

	KIC 4169521	KOI-3818	KIC 2851474	KIC 9285587	
R.A.	19 ^h 37 ^m 32 ^s .02	19 ^h 18 ^m 57 ^s .40	19 ^h 24 ^m 59 ^s .78	19 ^h 34 ^m 59 ^s .84	J2000 R.A.
Decl.	39 ^d 15 ^m 18 ^s .94	41 ^d 57 ^m 54 ^s .97	38 ^d 02 ^m 33 ^s .65	45 ^d 45 ^m 42 ^s .26	J2000 Decl.
K_p (mag)	13.4	11.7	12.6	12.9	<i>Kepler</i> magnitude
$v \sin i$ (km s ⁻¹)	60(15)	130(15)	32(10)	65(15)	Projected rotation velocity
P (d)	1.172555673(89)	3.8170427(48)	2.7682949(87)	1.8119598(58)	Orbital period
T (BJD-2457000)	113.91450(15)	91.8111(19)	146.2347(50)	140.8392(58)	Maximum RV time
K (km s ⁻¹)	23.7(1.5)	16.8(1.7)	16.81(90)	19.8(1.4)	RV semi-amplitude
V_γ (km s ⁻¹)	0.0(1.1)	8.1(1.3)	-4.74(55)	-19.68(95)	Systemic velocity
$f(m_2)$ (M_\odot)	0.00162(30)	0.00189(58)	0.00136(22)	0.00146(31)	Mass function
N_{RV}	8	10	7	8	Number of RV points
F_{RV_err}	2.59	1.93	2.84	2.77	RV uncertainties rescale factor

photometric period, the scaled separation a/R_1 , and a rough initial estimate of 0.1 for the mass ratio (Seager & Mallén-Ornelas 2003). We then used the Dartmouth stellar evolution tracks (Dotter et al. 2008) in the mean stellar density ρ and effective temperature T_{eff} plane, to estimate the primary mass. Next, using the RV mass function, we derived the secondary mass and thus got a better estimate for the mass ratio. We repeated this process with the updated mass ratio until the primary and secondary mass estimates converged to stable values, which required only two iterations for each of the four systems. To test this process, we also tried initial mass-ratio values of 0.2 or 0.05, and in both cases it converged to the same final parameters estimates within only two iterations. Figure 5 presents the location of the four systems on stellar evolution tracks, for stars of a range of initial masses, in the density-temperature plane.

Using the masses of the two components of the binary we then derived the semimajor axis and the two radii using *Kepler*'s third law and the photometry derived parameters. The WD radius R_2 was estimated while also taking into account the gravitational-lensing effect on the primary eclipse depth (Marsh 2001; Agol 2003; Bloemen et al. 2011; Muirhead et al. 2013; Kruse & Agol 2014). This effect is expected to be almost negligible for short-period low-mass WD companions. Indeed, the effect was most prominent in our longest period system, KOI-3818, for which it inflated the estimated WD radius by only $\sim 4\%$, or $\sim 0.4 \sigma$.

5.2. Photometric Beaming RV

For a negligible luminosity companion, the beaming phase modulation amplitude is proportional to the primary RV amplitude, with a proportionality constant of $4 \alpha_{\text{beam}}/c$, where c is the speed of light, and α_{beam} is mainly a function of the primary effective temperature (Loeb & Gaudi 2003; Zucker et al. 2007; Bloemen et al. 2011). We note that $\alpha_{\text{beam}} = \frac{3-\alpha}{4} = \frac{\langle B \rangle}{4}$, where α is the power-law index used by Loeb & Gaudi (2003) and $\langle B \rangle$ is the photon weighted bandpass-integrated beaming factor used by Bloemen et al. (2011). Using this relation, we estimated the expected RV semi-amplitude from the photometric beaming semi-amplitude, K_{beam} , following the same method used by Faigler et al. (2013).

For KOI-3818, KIC 2851474, and KIC 9285587, our K_{beam} estimates are consistent with the spectroscopic RV estimates, K_{RV} , with deviations of 0.3σ , 0.7σ and 1.4σ respectively. For

KIC 4169521 our K_{beam} estimate is significantly lower than the spectroscopic K_{RV} . This may be explained by the fact that for this system the orbital-period cosine reflection-phase-modulation is more than 10 times larger than the corresponding sine modulation. In such a case, a small phase shift in the cosine reflection modulation, due to stellar atmospheric effects, can significantly modify the sine phase modulation semi-amplitude, which we interpret as the beaming semi-amplitude. Similar effects were previously observed for the WD secondary system KIC 9164561 (Rappaport et al. 2015) and for the hot-Jupiter system *Kepler*-76 (Faigler et al. 2013).

5.3. Photometric Ellipsoidal Mass Ratio and Amplitudes

In theory, for a co-rotating primary the mass ratio can be photometrically derived from the ellipsoidal amplitude combined with the scaled separation a/R_1 , the inclination, and the estimated effective temperature (Equation (1) in Morris & Naftilan 1993; Zucker et al. 2007). However, in practice this calculation usually results in large uncertainties that give little meaning for the resulting mass ratio. In addition, it has been shown theoretically and through observations in multiple cases that for a massive star with a radiative envelope, or for asynchronous primary rotation, the ellipsoidal derived mass ratio can be significantly different from the real one (e.g., Pfahl et al. 2008; Carter et al. 2011; Bloemen et al. 2012, and references therein). For these reasons we chose not to use the ellipsoidal modulation amplitude in order to derive the systems' parameters. It is interesting, though, to compare the ellipsoidal derived mass ratio q_{ellip} , with the mass ratio we derive from the combination of primary and secondary eclipses fitting, RV solutions, and stellar evolution models. For KOI-3818, KIC 2851474, and KIC 9285587, the ellipsoidal derived mass ratios are consistent with our mass-ratio estimates, at the levels of 1.0σ , 0.7σ , and 1.1σ respectively. We note, though, that this is merely due to the large relative uncertainty of 29%–40% in the derived q_{ellip} of these systems, making it of little importance. For KIC 4169521, q_{ellip} , with a much smaller relative uncertainty of $\sim 4\%$, is still consistent with our derived mass ratio at the 1.2σ level. This result, which assumes a co-rotating primary, fits well with the consistency of the orbital period and the stellar rotation period of KIC 4169521 (Section 5.4).

It is also interesting to derive the expected first four BEER amplitudes using Equation (1) of Morris & Naftilan

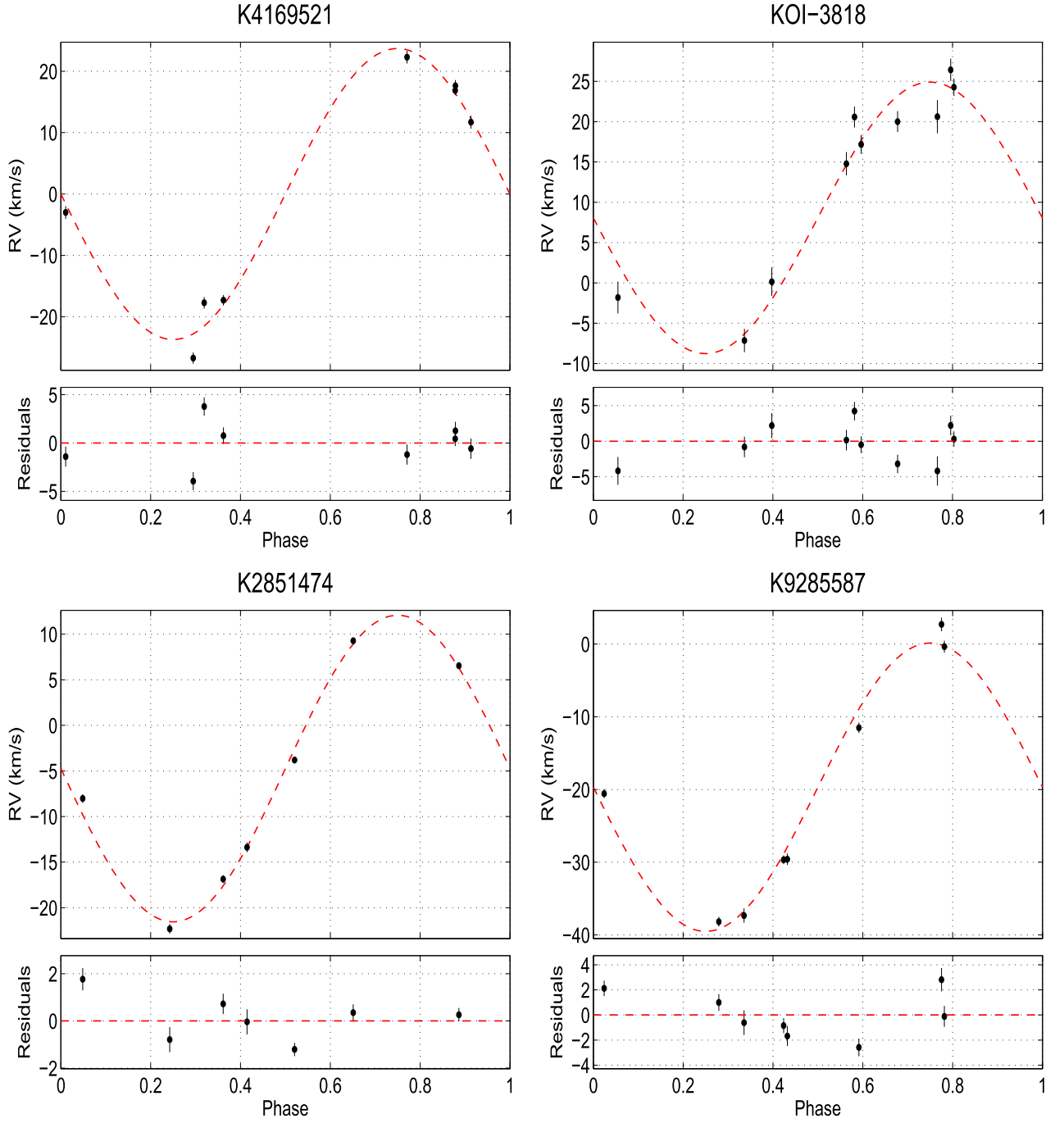


Figure 4. RV data and solutions of the four systems. Dashed lines present the circular velocity curve solutions using the orbital elements listed in Table 2. Note the different scales of the lower panels of residuals.

(1993), and compare them to the amplitudes measured from the data. Again, for KOI-3818, KIC 2851474, and KIC 9285587, the resulting uncertainties are too high to provide any meaningful result. For KIC 4169521, however, for the 2nd, 3rd, and 4th cosine amplitudes (a_{2c} , a_{3c} and a_{4c}) we find -8070 ± 820 , -750 ± 90 , and 213 ± 27 ppm, respectively. These are very consistent with the BEER amplitudes derived from the light curve

(Table 4), which again supports the co-rotation scenario of this system.

5.4. Stellar Rotation Period

In general, given enough time, tidal interaction in short-period binaries leads to synchronization, circularization and alignment of the system (e.g., Mazeh 2008). The data that we

Table 3
Fitted Frequencies and Amplitudes of High-frequency Modulations

Frequency (cycles day ⁻¹)	Amplitude (ppm)	Frequency (cycles day ⁻¹)	Amplitude (ppm)
KOI-3818:		KIC 9285587:	
2.090690	7 ± 35	18.948908	99 ± 454
2.101801	11 ± 70	19.091935	198 ± 633
2.112913	93 ± 560	20.195763	249 ± 1685
2.124024	16 ± 106	20.693235	151 ± 292
2.135135	12 ± 44	20.941710	44 ± 438
4.214714	10 ± 18	21.006874	22 ± 635
4.225825	101 ± 322	21.031024	689 ± 1486
4.236936	9 ± 29	21.596262	51 ± 162
6.338738	15 ± 41	22.045434	189 ± 893
8.451650	4 ± 31	22.134748	192 ± 653
	...	22.880592	187 ± 493
	...	23.362137	105 ± 106
	...	23.493714	96 ± 284
	...	23.611342	95 ± 732
	...	24.052498	205 ± 1236
	...	24.341467	35 ± 222

have at hand allow us to check if our four dA+WD reached such a stable dynamical configuration. If true, we can assume alignment and test synchronization by using the spectroscopic projected rotation velocity $v \sin i$, with the derived impact parameter and stellar radius, to estimate the stellar rotation period. Table 4 lists the resulting stellar rotation periods of the four systems, under these assumptions. For KIC 4169521, KIC 2851474, and KIC 9285587, the resulting rotation periods are consistent with the orbital periods, but this may be attributed to their large relative uncertainty of $\sim 40\%$. For KOI-3818 this exercise gives a rotation period of 0.79 ± 0.14 days, far from being consistent with the 3.82 days orbital period, suggesting a fast-rotating primary.

5.5. Eccentricities

In addition, the precise *Kepler* data allow us to look for small orbital eccentricity, another aspect of the tidal interaction. This is done by deriving the secondary-eclipse time shift ΔT_{sec} , and the secondary-to-primary eclipses duration ratio $\tau_{\text{sec}}/\tau_{\text{prim}}$. We estimated $e \cos \omega$ from the secondary-eclipse time shift by taking the first order in e of Equation (1) in Dong et al. (2013), after subtracting from it the expected Rømer delay (Kaplan 2010; Bloemen et al. 2012). Next, $e \sin \omega$ was derived from the secondary-to-primary eclipse duration ratio, using the first order approximation in e of Equation (7) in Tingley & Sackett (2005). Again, for KOI-3818 we identify a small but significant eccentricity component of $e \cos \omega = -0.00146(33)$. The data of KIC 4169521 are precise enough to rule out even such a small eccentricity, with a 2σ upper limit of 0.0005. Unfortunately, the light curves of the other two systems, KIC 2851474 and KIC 9285587, yielded larger upper limits, 0.002 and 0.008, respectively, and therefore do not allow us to rule out eccentricities of the order of 0.001.

6. REVIEW OF THE INDIVIDUAL SYSTEMS

In this section we review specific features of each of the four systems.

6.1. KIC 4169521

This system is listed in the *Kepler* EB catalog with an orbital period that is consistent with what we find, but with a primary eclipse time BJD_0 that is shifted by half a period, because the catalog defines BJD_0 as the time of the deeper eclipse. This system’s orbital period of 1.17 days is the shortest among the dA+WD EBs discovered so far in *Kepler*. It is, though, within the period range of 0.67–2.2 days of the previously discovered systems in WASP. It is also the hottest WD with the largest radius of the four systems reported here. It is then not a surprise that the light curve of this system shows a significant reflection/emission modulation of $+818.7(8.9)$ ppm. This is likely due to light originating from the WD, which is scattered off of or thermally reprocessed and later emitted from the atmosphere of the A star. It is similar to the reflection/emission modulation observed for the WD secondaries systems KIC 10657664, KOI-1224, and KIC 9164561 (Carter et al. 2011; Breton et al. 2012; Rappaport et al. 2015). Such a modulation, in turn, can significantly modify the derived beaming amplitude, which is likely the case here (see Section 5.2).

6.2. KOI-3818

Our analysis detects small but significant orbital eccentricity (Section 5.5) and fast rotation of the primary, which highly deviates from synchronization (Section 5.4), indicating an incomplete tidal interaction.

In addition, the light curve of this system shows significant modulations at frequencies of ~ 2.1 cycles day⁻¹ and its harmonics (Figures 1 and 2). With a secondary-to-primary *Kepler*-band flux ratio of $\sim 2.5 \times 10^{-4}$, it is safe to assume that the A-star is the source of this variability. This is similar to the photometric modulations, termed “low-frequencies,” seen in many A-type stars in the *Kepler* data (Balona 2011, 2014; Balona et al. 2015; Guzik et al. 2015). There is active ongoing research trying to explain the source of such modulations, with no clear conclusions. Based on the harmonic structure of the modulation, and the consistency of its frequency with our derived stellar rotation period (Section 5.4), we speculate that it may be associated with the A-star rotation.

6.3. KIC 2851474

This system appears in the *Kepler* EB catalog, with an orbital period and a BJD_0 consistent with our findings, but the catalog folded light curve mainly shows an ellipsoidal variation, with no visible eclipses. This binary features the most massive primary A-star of the four systems. For the A-star we derive a mass of $2.3 M_{\odot}$ and a radius of $3.1 R_{\odot}$, suggesting that the primary has already started to evolve away from the main sequence. This is also indicated by its position on the stellar evolution tracks illustrated in Figure 5.

6.4. KIC 9285587

The light curve of this system shows significant modulations at the 19–24 cycles day⁻¹ frequency range (Figures 1 and 2). Similar to KOI-3818, the small secondary-to-primary *Kepler*-band flux ratio of $\sim 4 \times 10^{-4}$ suggests that the A-star is the source of this variability. These δ Scuti-like pulsations are similar to high-frequency modulations seen in many A-type stars in the *Kepler* data (Breger 2000; Balona et al. 2015; Guzik et al. 2015).

Table 4
 System Parameters

	KIC 4169521	KOI-3818	KIC 2851474	KIC 9285587	
f_3	0.042	0.017	0.109	0.027	Average <i>Kepler</i> third light fraction
γ_1	0.274(19)	0.230(16)	0.254(20)	0.258(27)	linear limb-darken coeff.
γ_2	0.317(21)	0.2919(74)	0.297(17)	0.305(28)	quad. limb-darken coeff.
P (days)	1.17255671(69)	3.8170428(39)	2.7682925(66)	1.8119579(48)	Orbital period
T_0 (BJD-2454833)	863.598047(83)	862.73788(72)	907.6432(17)	864.1697(30)	Middle of primary eclipse time
R_2/R_1	0.04131(22)	0.01256(22)	0.01118(31)	0.01206(57)	Radius ratio
a/R_1	2.704(26)	6.85(75)	3.69(56)	3.77(62)	Normalized separation
F_2/F_1	0.0053785(52)	0.0002546(24)	0.0002227(35)	0.000425(11)	<i>Kepler</i> -band flux ratio
b	0.8564(19)	0.31(0.22)	0.37(0.26)	0.38(0.26)	Impact parameter
ΔT_{sec} (minutes)	0.02(12)	6.0(1.2)	0.7(2.7)	4.6(4.5)	Secondary eclipse time delay
$\tau_{\text{sec}}/\tau_{\text{prim}}$	0.9921(39)	1.001(10)	0.976(18)	1.039(48)	Eclipses duration ratio
BEER harmonics semi-amplitudes (ppm):					
a_{1c}	818.7(8.9)	13.0(4.5)	-39(23)	-312(13)	$\cos\phi$ semi-amplitude
a_{1s} (beaming)	78.5(7.3)	132.3(3.4)	126(11)	138(16)	$\sin\phi$ semi-amplitude
a_{2c} (ellipsoidal)	-8402(18)	-621.8(3.7)	-2296(157)	-5601(30)	$\cos 2\phi$ semi-amplitude
a_{2s}	67.0(6.3)	45.9(3.3)	-112(16)	-153(78)	$\sin 2\phi$ semi-amplitude
a_{3c}	-738.1(6.0)	-26.4(1.7)	-139(14)	-465(13)	$\cos 3\phi$ semi-amplitude
a_{3s}	-4.7(4.7)	4.7(2.8)	-4.5(3.1)	-23(12)	$\sin 3\phi$ semi-amplitude
a_{4c}	207.0(7.8)	10.3(2.1)	37.8(3.0)	94.9(9.0)	$\cos 4\phi$ semi-amplitude
a_{4s}	-5.2(3.9)	-0.3(2.6)	0.9(3.3)	7.1(6.2)	$\sin 4\phi$ semi-amplitude
α_{beam}	0.643(49)	0.570(34)	0.614(47)	0.650(52)	Beaming factor
K_{beam} (km s ⁻¹)	9.1(1.1)	17.4(1.2)	15.4(1.9)	15.9(2.4)	RV semi-amplitude from beaming
q_{ellip}	0.1191(51)	0.144(42)	0.078(28)	0.191(76)	Mass ratio from ellipsoidal
T_{eff} (K)	8290 ⁺²⁵⁰ ₋₃₂₀	9170 ⁺²⁸⁰ ₋₃₉₀	8580 ⁺²⁴⁰ ₋₃₇₀	8230 ⁺²³⁰ ₋₃₅₀	KIC effective temperature
M_1 (M_{\odot})	1.982(92)	2.14(12)	2.34(19)	1.94(16)	Primary mass
R_1 (R_{\odot})	2.247(40)	1.99(28)	3.06(64)	2.13(48)	Primary radius
ρ_1 (g/cc)	0.2460(72)	0.38(11)	0.114(44)	0.28(12)	Primary density
Age (Gyr)	0.74(0.13)	0.42(0.1)	0.6(0.1)	0.72(0.14)	Age
K_{RV} (km s ⁻¹)	23.7(1.5)	16.8(1.7)	16.81(90)	19.8(1.4)	Spectroscopic RV semi-amplitude
P_{rot} (days)	1.79(60)	1.79(14)	5.0(2.4)	1.71(62)	Primary rotation period
T_2 (K)	12114(629)	10854(617)	10306(545)	11748(707)	Secondary temperature
M_2 (M_{\odot})	0.210(15)	0.220(26)	0.210(18)	0.191(19)	Secondary mass
R_2 (R_{\odot})	0.0929(19)	0.0260(39)	0.0346(83)	0.0260(68)	Secondary radius
ρ_2 (g/cc)	372(28)	19388(6470)	7365(3265)	15847(7559)	Secondary density
q	0.1064(74)	0.103(11)	0.0894(54)	0.0979(76)	Mass ratio
$\Delta T_{\text{Rømer}}$ (minutes)	0.3570(77)	0.856(24)	0.726(26)	0.506(12)	Rømer delay
$e \cos \omega$	0.00030(11)	-0.00146(33)	0.0000(11)	-0.0025(27)	Eccentricity cosine component
$e \sin \omega$	0.0039(20)	-0.0004(50)	0.0123(90)	-0.019(23)	Eccentricity sine component

7. SUMMARY AND DISCUSSION

We report the discovery of four short-period dA+WD EBs in the *Kepler* light curves. The 4 systems add to the 6 previously known short-period dA+pre-He-WD EBs in the *Kepler* data (Rowe et al. 2010; van Kerkwijk et al. 2010; Carter et al. 2011; Bloemen et al. 2012; Breton et al. 2012; Matson et al. 2015; Rappaport et al. 2015), and the 18 such WASP systems (Maxted et al. 2011, 2013, 2014). All of the 6 *Kepler* systems and 3 of the WASP systems have accurate measurements of the primary and secondary mass, radius, and T_{eff} . The new systems' orbital-period range is 1.17–3.82 days, well within the 0.67–23.9 days range of the previously known systems. The masses of the WD secondaries of the new systems range from 0.19 to 0.22 M_{\odot} , somewhat overlapping the lower edge of the 0.19–0.3 M_{\odot} mass range of the known systems with derived secondary masses.

Each dA+WD binary that we currently observe has evolved from a system in which the primordial primary was the progenitor of the current WD. Such systems are believed to have gone through a mostly stable mass transfer from the WD progenitor to the current primary star, which gained a significant part of its current mass through this process (Podsiadlowski et al. 2002; Panei et al. 2007; Rappaport et al. 2009; van Kerkwijk et al. 2010). The WD evolution could involve several hydrogen shell flashes of the degenerate remnant, before it settles on the He WD cooling track (Podsiadlowski et al. 2002; Panei et al. 2007; Althaus et al. 2013).

Mass-transfer models predict a direct dependence of the final orbital period on the WD mass. To check this dependence, we follow Carter et al. (2011) and plot in Figure 6 the current orbital period as a function of the WD mass of the four new and nine previously known systems with derived masses, on top of

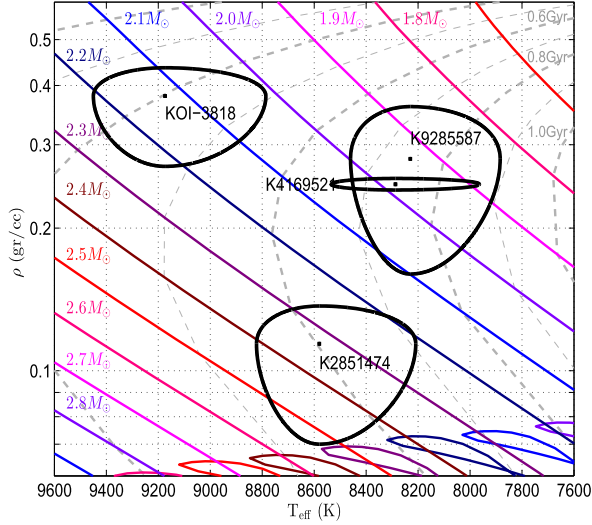


Figure 5. Location of the four systems on Dartmouth density-temperature plane stellar evolutionary tracks. Black contours show the 1σ uncertainties’ boundaries.

the expected mass–period relation from Lin et al. (2011; see also e.g., Joss & Rappaport 1983; Savonije 1983; Rappaport et al. 1995). Indeed, all systems seem consistent with the mass–period relation, supporting the stable mass-transfer scenario.

It is also interesting to examine the WD radii of the newly discovered systems. For KIC 4169521 we derive a bloated WD radius of $0.09 R_\odot$, well within the WD radius range of 0.04 – $0.33 R_\odot$ of the already known dA+pre-He-WD systems. However, the WD radii of the other three new systems are in the range of 0.026 – $0.035 R_\odot$, the smallest WD radii discovered so far in short-period eclipsing dA+WD binaries. This is reflected by the very shallow eclipses of these three systems, with depths on the order of 100–400 ppm, well below those of the previously detected dA+pre-He-WD systems.

Figure 7 shows the derived radii as a function of the T_{eff} of the newly discovered WDs, together with those of the previously known systems with derived radii, on top of WD evolution tracks of a set of WD masses from Althaus et al. (2013). Although Althaus et al. (2013) derived the tracks for WD orbiting a neutron star, they suggest that this evolutionary stage of the WD does not depend on the nature of its companion. The figure shows that the known systems, together with KIC 4169521, all with hot and bloated WD secondaries, represent young systems probably at the pre-He-WD, or the initial WD cooling track stage (van Kerkwijk et al. 2010; Rappaport et al. 2015). The three new systems—KOI-3818, KIC 2851474, and KIC 9285587, are probably positioned further along the WD cooling track. Reading from the evolutionary tracks of Figure 7, we estimate the ages of the systems, measured from the end of the mass-transfer epoch, to be at the range of 0.2–0.8 Gyr. These are roughly consistent with the ages of the A-star primaries that we derive from the stellar evolutionary tracks (see Figure 5 and Table 4).

The KOI-3818 system, with its fast-rotating primary and very small eccentricity, can shed some light on the dynamical evolution of the binary. On one hand, the fast rotation of KOI-3818 might indicate that the synchronization timescale is much longer than the age of the binary, measured from the end of the

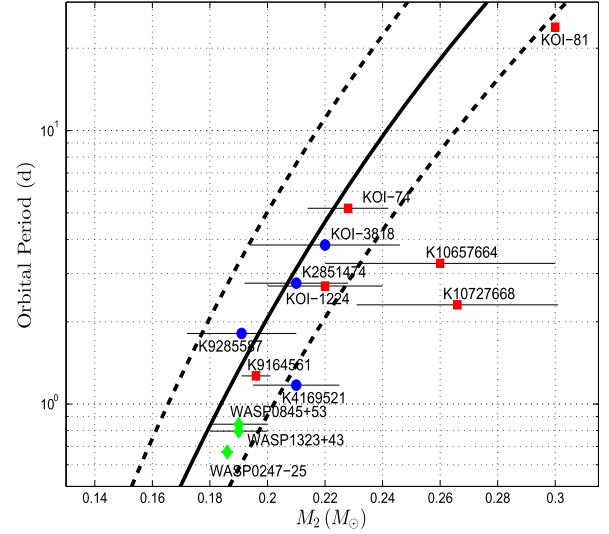


Figure 6. WD mass–period relation of the four new and nine previously known systems. The solid curve shows the expected relation from Lin et al. (2011) and the dashed lines show the $\pm 10\%$ uncertainties of the model. Red squares are the six previously known *Kepler* systems, green diamonds are the three previously known WASP systems, and blue circles are the four newly discovered systems.

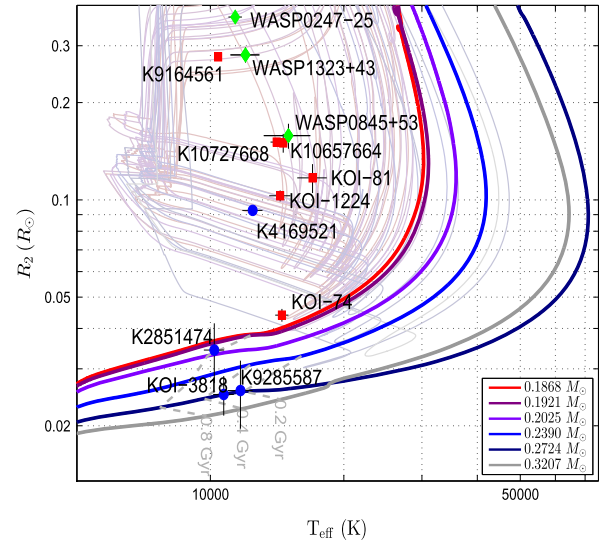


Figure 7. WD evolution tracks for binary systems that have gone through stable mass transfer, for a selected set of WD masses from Althaus et al. (2013). Colored curves show the final cooling track of the WDs evolution, while grayed out tracks show the pre-He-WDs evolution that goes through multiple Hydrogen flash cycles. Red squares are the six previously known *Kepler* systems, green diamonds are the three previously known WASP systems, and blue circles are the four newly discovered systems. Gray dashed lines show isochrones of 0.2, 0.4 and 0.8 Gyr, measured from the end of the mass-transfer epoch.

mass-transfer phase. On the other hand, tidal evolutionary models of short-period binaries predict synchronization and alignment timescales to be two to three orders of magnitude shorter than the circularization timescale (Zahn & Bouchet 1989; Witte & Savonije 2002). We can therefore conclude that the present small eccentricity is not a product of tidal

circularization at the present phase, but instead is the result of the mass-transfer process. Evolutionary models of the mass-transfer phase do predict fast-rotating primaries and very small eccentricities (e.g., Toonen et al. 2014).

The minute eccentricity component of $e \cos \omega = -0.00146$ (33) that we derive for KOI-3818 is about half of the eccentricity component of $e \cos \omega = 0.0029(5)$ derived by Carter et al. (2011) for KIC 10657664. Such small eccentricities are impossible to obtain from RV measurements alone, due to the small line-profile distortion expected for short-period binaries (e.g., Lucy 2005; Komonjinda et al. 2007). Small eccentricities have been measured previously for pulsars,⁵ with WD secondaries in particular (e.g., Manchester et al. 2005), utilizing the precise timing of the observed radio pulses. Obviously, evolutionary models (Toonen et al. 2014) that include tidal interaction (e.g., Antoniadis 2014) should account for these non-zero eccentricities.

It is also interesting to note that out of the four systems, only the primary of KOI-3818 is a fast rotator, while the other three derived rotation periods of the A-stars are consistent with being synchronized. This may be because the binary separation to primary radius ratio, (a/R_1), of KOI-3818 is relatively large, 6.9, while it is much smaller for the other three binaries—2.7, 3.7, and 3.8 for KIC 4169521, KIC 2851474, and KIC 9285587, respectively. As we can estimate the age of the four systems from their WD radii and temperatures (Figure 7), we might be able to constrain the calibration of the synchronization timescale for stars with radiative envelopes.

The exquisite *Kepler* photometry led to the discovery of 10 short-period dA+WD EBs, and has enabled us to derive the masses, radii, and effective temperatures of both components of each system. Together with the 18 similar WASP systems these open a unique window into the end products of binaries. In particular, we have discovered three dA+WD systems with small, $\lesssim 0.04 R_\odot$, WDs, extending the known population to older systems with cooler and smaller WD secondaries.

Finally, the identified sample of 10 short-period dA+WD eclipsing binaries in the *Kepler* stars should enable us to estimate the statistics of this population and the fraction of A-stars with compact companions. The BEER search might help us to detect such non-eclipsing binaries lurking in the *Kepler* light curves.

We are thankful to the anonymous referee for comprehensive and valuable remarks that significantly improved this manuscript. We thank Donald W. Kurtz for his review and advice regarding the high-frequency photometric modulations that we report here. We are indebted to Andrew H. Szentgyorgyi, who led the TRES project, and to Gabor Fűrész for his many contributions to the success of the instrument. We thank Perry Berlind, Gilbert A. Esquerdo, and Michael L. Calkins for obtaining the TRES observations, and Allyson Bieryla and Jessica Mink for help with the data analysis. We feel deeply indebted to the team of the *Kepler* mission, who enabled us to search and analyze their unprecedentedly accurate photometric data. The research leading to these results has received funding from the European Research Council under the EU's Seventh Framework Programme (FP7/(2007-2013)/ ERC Grant Agreement No. 291352). This research was supported by the ISRAEL SCIENCE FOUNDATION (grant No. 1423/11) and

the Israeli Centers Of Research Excellence (I-CORE, grant No. 1829/12). All of the photometric data presented in this paper were obtained from the Mikulski Archive for Space Telescopes (MAST). STScI is operated by the Association of Universities for Research in Astronomy, Inc., under NASA contract NAS5-26555. Support for MAST for non-*HST* data is provided by the NASA Office of Space Science via grant NNX09AF08G and by other grants and contracts. We thank the *Kepler* mission for partial support of the spectroscopic observations under NASA Cooperative Agreement NNX13AB58A with the Smithsonian Astrophysical Observatory, DWL PI.

Facility: FLWO:1.5m (TRES).

REFERENCES

- Agol, E. 2003, *ApJ*, 594, 449
- Althaus, L. G., Miller Bertolami, M. M., & Córscico, A. H. 2013, *A&A*, 557, A19
- Antoniadis, J. 2014, *ApJL*, 797, L24
- Balona, L. A. 2011, *MNRAS*, 415, 1691
- Balona, L. A. 2014, *MNRAS*, 437, 1476
- Balona, L. A., Daszyńska-Daszkiewicz, J., & Pamyatnykh, A. A. 2015, *MNRAS*, 452, 3073
- Bloemen, S., Marsh, T. R., Degroote, P., et al. 2012, *MNRAS*, 422, 2600
- Bloemen, S., Marsh, T. R., Østensen, R. H., et al. 2011, *MNRAS*, 410, 1787
- Borucki, W. J., Koch, D., Basri, G., et al. 2010, *Sci*, 327, 977
- Breger, M. 2000, in ASP Conf. Ser. 210, Delta Scuti and Related Stars, Reference Handbook and Proceedings of the 6th Vienna Workshop in Astrophysics, ed. M. Breger & M. Montgomery (San Francisco, CA: ASP), 3
- Breton, R. P., Rappaport, S. A., van Kerkwijk, M. H., & Carter, J. A. 2012, *ApJ*, 748, 115
- Buchhave, L. A., Bakos, G. Á., Hartman, J. D., et al. 2010, *ApJ*, 720, 1118
- Carter, J. A., Rappaport, S., & Fabrycky, D. 2011, *ApJ*, 728, 139
- Claret, A., & Bloemen, S. 2011, *A&A*, 529, A75
- Dong, S., Katz, B., & Socrates, A. 2013, *ApJL*, 763, L2
- Dotter, A., Chaboyer, B., Jevremović, D., et al. 2008, *ApJS*, 178, 89
- Faigler, S., & Mazeh, T. 2011, *MNRAS*, 415, 3921
- Faigler, S., & Mazeh, T. 2015, *ApJ*, 800, 73
- Faigler, S., Mazeh, T., Quinn, S. N., Latham, D. W., & Tal-Or, L. 2012, *ApJ*, 746, 185
- Faigler, S., Tal-Or, L., Mazeh, T., Latham, D. W., & Buchhave, L. A. 2013, *ApJ*, 771, 26
- For, B.-Q., et al. 2010, *ApJ*, 708, 253
- Fűrész, G. 2008, Ph.D. thesis, Univ. Szeged
- Goodman, J., & Weare, J. 2010, *Communications in Applied Mathematics and Computational Science*, 5, 65
- Guzik, J. A., Bradley, P. A., Jackiewicz, J., et al. 2015, arXiv:1502.00175
- Harrison, T. E., Howell, S. B., Huber, M. E., et al. 2003, *AJ*, 125, 2609
- Hauschildt, P. H., Allard, F., & Baron, E. 1999, *ApJ*, 512, 377
- Hodgson, R. M., Bailey, D. G., Naylor, M. J., Ng, A. L. M., & McNeil, S. J. 1985, *Image Vision Comput.*, 3, 4
- Holland, P. W., & Welsch, R. E. 1977, *Communications in Statistics: Theory and Methods*, A6, 813
- Huang, X., Bakos, G. Á., & Hartman, J. D. 2013, *MNRAS*, 429, 2001
- Huber, D., Silva Aguirre, V., Matthews, J. M., et al. 2014, *ApJS*, 211, 2
- Jenkins, J. M., Caldwell, D. A., Chandrasekaran, H., et al. 2010, *ApJL*, 713, L87
- Joss, P. C., & Rappaport, S. A. 1983, *Natur*, 304, 419
- Kaluzny, J., Rucinski, S. M., Thompson, I. B., Pych, W., & Krzeminski, W. 2007, *AJ*, 133, 2457
- Kaplan, D. L. 2010, *ApJL*, 717, L108
- Kepler* Exoplanets Archive 2015, <http://exoplanetarchive.ipac.caltech.edu/>
- Komonjinda, S., Hearnshaw, J. B., & Ramm, D. J. 2007, in IAU Symp., 240, Binary Stars as Critical Tools and Test in Contemporary Astrophysics (Paris: IAU), 118
- Kopal, Z. 1959, The International Astrophysics Series: Close binary systems (London: Chapman & Hall)
- Kruse, E., & Agol, E. 2014, *Sci*, 344, 275
- Lin, J., Rappaport, S., Podsiadlowski, P., et al. 2011, *ApJ*, 732, 70
- Loeb, A., & Gaudi, B. S. 2003, *ApJL*, 588, L117
- Lucy, L. B. 2005, *A&A*, 439, 663

⁵ <http://www.atnf.csiro.au/people/pulsar/psrcat/>

- Manchester, R. N., Hobbs, G. B., Teoh, A., & Hobbs, M. 2005, *AJ*, **129**, 1993
- Mandel, K., & Agol, E. 2002, *ApJL*, **580**, L171
- Marsh, T. R. 2001, *MNRAS*, **324**, 547
- Matson, R. A., Gies, D. R., Guo, Z., et al. 2015, *ApJ*, **806**, 155
- Maxted, P. F. L., Anderson, D. R., Burleigh, M. R., et al. 2011, *MNRAS*, **418**, 1156
- Maxted, P. F. L., Bloemen, S., Heber, U., et al. 2014, *MNRAS*, **437**, 1681
- Maxted, P. F. L., Marsh, T. R., Heber, U., et al. 2002, *MNRAS*, **333**, 231
- Maxted, P. F. L., Serenelli, A. M., Miglio, A., et al. 2013, *Natur*, **498**, 463
- Mazeh, T. 2008, in *EAS Publications Series*, 29, Tidal Effects in Stars, Planets and Disks, ed. M.-J. Goupil & J.-P. Zahn (Noordwijk: EAS), 1
- Mazeh, T., & Faigler, S. 2010, *A&A*, **521**, L59
- Mazeh, T., & Zucker, S. 1992, in *IAU Coll. 135, Complementary Approaches to Double and Multiple Star Research*, ed. H. A. McAlister & W. I. Hartkopf (San Francisco, CA: ASP), 164
- Morris, S. L. 1985, *ApJ*, **295**, 143
- Morris, S. L., & Naftilan, S. A. 1993, *ApJ*, **419**, 344
- Muirhead, P. S., Vanderburg, A., Shporer, A., et al. 2013, *ApJ*, **767**, 111
- Mullally, F., Coughlin, J. L., Thompson, S. E., et al. 2015, *ApJS*, **217**, 31
- Panei, J. A., Althaus, L. G., Chen, X., & Han, Z. 2007, *MNRAS*, **382**, 779
- Pfahl, E., Arras, P., & Paxton, B. 2008, *ApJ*, **679**, 783
- Pietrzyński, G., Thompson, I. B., Gieren, W., et al. 2012, *Natur*, **484**, 75
- Podsiadlowski, P., Rappaport, S., & Pfahl, E. D. 2002, *ApJ*, **565**, 1107
- Pollacco, D. L., Skillen, I., Collier Cameron, A., et al. 2006, *PASP*, **118**, 1407
- Pribulla, T., & Rucinski, S. M. 2008, *MNRAS*, **386**, 377
- Rappaport, S., Nelson, L., Levine, A., et al. 2015, *ApJ*, **803**, 82
- Rappaport, S., Podsiadlowski, P., & Horev, I. 2009, *ApJ*, **698**, 666
- Rappaport, S., Podsiadlowski, P., Joss, P. C., Di Stefano, R., & Han, Z. 1995, *MNRAS*, **273**, 731
- Reed, M. D., Terndrup, D. M., Østensen, R., et al. 2010, *Ap&SS*, **329**, 83
- Rowe, J. F., Borucki, N. J., Koch, D., et al. 2010, *ApJL*, **713**, L150
- Rybicki, G. B., & Lightman, A. P. 1979, *Radiative Processes in Astrophysics* (New York: Wiley)
- Savonije, G. J. 1983, *Natur*, **304**, 422
- Seager, S., & Mallén-Ornelas, G. 2003, *ApJ*, **585**, 1038
- Slawson, R. W., Prša, A., Welsh, W. F., et al. 2011, *AJ*, **142**, 160
- Tal-Or, L., Faigler, S., & Mazeh, T. 2015, *A&A*, **580**, A21
- Tingley, B., & Sackett, P. D. 2005, *ApJ*, **627**, 1011
- Toonen, S., Claeys, J. S. W., Mennekens, N., & Ruiter, A. J. 2014, *A&A*, **562**, A14
- van Kerkwijk, M. H., Rappaport, S. A., Breton, R. P., et al. 2010, *ApJ*, **715**, 51
- Vaz, L. P. R. 1985, *Ap&SS*, **113**, 349
- Zahn, J.-P., & Bouchet, L. 1989, *A&A*, **223**, 112
- Wilson, R. E. 1990, *ApJ*, **356**, 613
- Witte, M. G., & Savonije, G. J. 2002, *A&A*, **386**, 222
- Zucker, S. 2003, *MNRAS*, **342**, 1291
- Zucker, S., Mazeh, T., & Alexander, T. 2007, *ApJ*, **670**, 1326

Chapter 3

Discussion

In this chapter I summarize the findings of the seven papers and briefly discuss their astrophysical implications.

3.1 The Papers

Paper I (Mazeh & Faigler, 2010) presents the detection of the beaming and the ellipsoidal modulations in the light curve of CoRoT-3, a system of a $22M_{\text{Jup}}$ brown dwarf orbiting an F3 star in an orbital period of 4.3 days (Deleuil et al., 2008). This was the first time the beaming effect was detected for a substellar companion. The paper suggests that had this analysis been performed immediately after the discovery of the light-curve transits, the mass of the companion could have been estimated from the observed beaming and ellipsoidal amplitudes, thus reducing the number of RV points needed to confirm the mass of the transiting object. The detection of the effects also means that the same effects can be detected in the *CoRoT* and *Kepler* light curves of stars with massive-planet/brown-dwarf companions, even without any transits, as suggested by Loeb & Gaudi (2003) and Zucker, Mazeh & Alexander (2007). The ability to detect some combination of the

three effects in space-missions light curves, even for non-eclipsing systems, lays the grounds for the BEER search algorithm for non-eclipsing binaries.

As a natural development following Paper I, Paper II (Faigler & Mazeh, 2011) presents the BEER algorithm for detection of *non-transiting* short-period low-mass companions, through the beaming, ellipsoidal and reflection effects, in *Kepler* and *CoRoT* light curves. After describing the search algorithm and analyzing its expected performance, the paper predicts that when more *Kepler* data is available it may be possible to find in it candidates for planets of mass as small as $5\text{--}10M_{\text{Jup}}$. This claim was later confirmed by the discovery of Kepler-76b (Paper IV). The paper also suggests that the long time span of the *Kepler* mission enables using not only the period, but also the phase of the BEER modulations, so that very few RV follow-up observations are needed to confirm the existence of a companion. This method was later used in the RV confirmations presented in Papers III, IV and VII.

To illustrate the effectiveness of the BEER method, Paper III (Faigler et al., 2012) presents the discovery and RV confirmation of seven non-eclipsing binaries, with minimum secondary masses of $0.07\text{--}0.4M_{\odot}$, in the *Kepler* data. The paper emphasizes that unlike eclipses searches, the BEER algorithm searches for *non-eclipsing* companions, and therefore can detect additional systems with lower inclination angles. It is thus effectively equivalent to performing an RV survey on hundreds of thousands of stars through scanning their *Kepler* and *CoRoT* light curves. Therefore, the paper predicts that BEER can discover hundreds of new short-period binaries. As also stated by Paper I, Paper III predicts that once the full *Kepler* data is available, we should be able to detect in it brown-dwarf secondaries and even massive planets.

As envisioned by the previous papers, Paper IV (Faigler et al., 2013)

presents the discovery of Kepler-76b, a $2M_{\text{Jup}}$ transiting hot Jupiter orbiting a 13.3 mag F star with orbital period of 1.54 days. This planet was first identified by the BEER algorithm, and then confirmed by RV follow-up observations. Interestingly, the paper finds inconsistency between the beaming amplitude and the spectroscopically measured RV. This apparent discrepancy is explained by a phase shift of the planetary thermal modulation, due to equatorial superrotating jets in the planet atmosphere. This phenomenon was predicted by Showman & Guillot (2002) and later observed by Knutson et al. (2007, 2009) in the infrared for HD 189733. The discovery illustrates that atmospheric phenomena, such as thermal winds or reflective clouds, can be probed not only by IR observations, but also by the high-precision visual-band light curves of *Kepler*.

Next, Paper V (Faigler & Mazeh, 2015) extends the discovery of superrotation in Kepler-76b to two additional known hot Jupiters, HAT-P-7b and KOI-13b. The paper presents the Lambert superrotation BEER model and shows that its planet-mass estimates are highly consistent with the planetary masses derived or constrained by RV observations. It then discusses and shows that close-in hot Jupiters are expected to show the most apparent beaming amplitude inconsistency. It is then not a surprise that this phenomenon was initially discovered in hot Jupiters, and is in agreement with the phase-shifted reflection/emission modulations of Kepler-76, HAT-P-7 and KOI-13 reported by this study. The paper concludes that detailed phase-curve studies of the precise light curve of *CoRoT*, *Kepler*, and future space missions, as this paper and alike (e.g., Esteves et al., 2014), open the opportunity to estimate the mass, and investigate the atmospheric properties of multiple close-in exoplanets.

To further establish the effectiveness of the BEER method, Paper VI (Tal-

Or, Faigler & Mazeh, 2015) describes the discovery and RV confirmation of *seventy non-eclipsing binaries* in the *CoRoT* data, using the AAOmega multi-object spectrograph (Smith et al., 2004; Saunders et al., 2004). Medium-resolution spectra of 281 BEER candidates were obtained in a seven-night AAOmega RV campaign, with a precision of ~ 1 km/s. The measured RVs confirmed the binarity of seventy of the candidates, with periods of 0.3–10 days. The mass ratio of the confirmed binaries spanned a range of 0.03–1. The paper also shows that red giants introduce a major source of false candidates, and suggests a method to improve BEER’s performance in extracting higher-fidelity samples from future searches of *CoRoT* light curves.

The last study, Paper VII (Faigler et al., 2015), demonstrates a different strength and utility of the BEER search algorithm. It presents the discovery of four short-period eclipsing dA+WD systems in the *Kepler* light curves. The systems show BEER phase modulations together with primary and secondary eclipses. These add to the 6 *Kepler*, and 18 WASP, previously known short-period eclipsing dA+WD binaries. The paper shows that the new, and the previously known systems, are consistent with the mass-period relation expects for such binaries, that have gone through a mostly stable mass transfer from the WD progenitor to the current primary star. It then shows that three of the new systems harbor the smallest WDs detected so far in short-period eclipsing dA+WD binaries. These three binaries extend the previously known population to older systems with cooler and smaller WD secondaries. In addition the paper points to the interesting KOI-3818 system that displays evidence for a fast-rotating primary and a minute but significant eccentricity. These features are probably the outcome of the mass-transfer process.

3.2 Astrophysical contributions

Within the scope of this thesis I can mark three main astrophysical contributions.

First, we have developed the BEER algorithm for detection of *non-eclipsing* short-period companions, through the beaming, ellipsoidal and reflection effects, in high-precision light curves. The effectiveness of this new method was shown through the detection and RV confirmation of a large number of common stellar binaries (Paper III,VI). The algorithm also allowed the detection and confirmation of rare objects, the hot Jupiter Kepler-76b (Paper IV) and four eclipsing dA+WD binaries (Paper VII). On one hand, the discovery of many stellar binaries shows that the BEER method can serve as a high-throughput photometric detection tool of non-eclipsing binaries, with numbers comparable to those achieved by the eclipse method. On the other hand, the discovery of a planet, and four systems harboring WDs, illustrate that the new algorithm complements the known eclipse/transit method, and enables the discovery of important astrophysical systems missed by other methods.

Next, we detected the superrotation phenomenon in the visual light curves of Kepler-76, HAT-P-7 and KOI-13 (Paper IV, V). This phenomenon, that involves a phase shift of the planetary thermal modulation, due to equatorial superrotating winds in the planet atmosphere (Showman & Guillot, 2002), was previously observed only in the infrared (Knutson et al., 2007, 2009). These discoveries illustrate that detailed phase-curve studies of precise space-surveys light curves (e.g., Paper V; Esteves et al., 2014) open the opportunity to investigate atmospheric phenomena, such as thermal winds or reflective clouds, in multiple close-in exoplanets.

Finally, Using the BEER algorithm, we detected four short-period eclipsing dA+WD systems in the *Kepler* data, three of which harbor the smallest WDs detected so far in such binaries (Paper VII). The three binaries extend the previously known population of such systems, to older systems with cooler and smaller WD secondaries. The new discoveries allow comparing the small WDs properties to those predicted by binary evolution models, in a parameter region not observed before.

3.3 Into the future

In recent years, a few large photometric surveys were initiated, and more are planned for, motivated by various astrophysical research fields such as exoplanets, supernovae, gravitational-lensing and more. Looking into the future, we can use the BEER algorithm to search the data of such large ground and space based photometric surveys. To illustrate the potential of this approach, Table 3.1 lists current and future large photometric surveys that are applicable for our purposes.

Similarly to the *CoRoT* binary catalog constructed in Paper VI, we can search the data of each space survey and build a catalog of non-eclipsing stellar binaries, of up to *several million systems* for the largest surveys — GAIA and PLATO. Such a uniform catalog, with well-defined observational biases, allows studying the binary population and its statistical characteristics, which in turn can serve as an important observational reference for binary formation and evolution theories.

In addition, the BEER method allows for searching the surveys for rare companions such as planets, brown dwarfs, white dwarfs, neutron stars and black holes. As demonstrated in Papers IV and VII, the combination of the

Table 3.1. Main properties of large photometric surveys

	OGLE-IV ¹	WASP ²	<i>CoRoT</i> ³	<i>Kepler</i> ⁴	GAIA ⁵	TESS ⁶	PLATO ⁷	LSST ⁸
Stars ($\times 10^6$)	1000	18	0.17	0.17	1000	0.2	1000	~ 40000
Cadence	1-3 d	~ 10 min.	8.5 min. ^b	30 min. ^b	N/A	2 min.	25 sec. ^b	~ 4 d
Points/star	300-700	6700	3000-25000 ^b	60000 ^b	70	19000 ^c	2.5×10^{6b}	825
Time span (days)	1500	830	20-150	1400	1800	27	730	3650
Precision ^a	1%	1%	0.1%	0.01%	0.3%	0.02%	0.001%	1%
Band (nanometer)	700-900 (I)	400-700	450-900	400-900	330-1050	600-1000	500-1000	320-1050 (5 bands)
Magnitude range	12-22	7-15	11-16	7-17	6-20	4-13	4-16	16-27
Measurements	Ground	Ground	Space	Space	Space	Space	Space	Ground
Availability	at present	at present	at present	at present	2016-22	2017-19	2024-29	2023-2033

¹ Udalski et al. (2015)

² Butters et al. (2010)

³ Auvergne et al. (2009)

⁴ Koch et al. (2010)

⁵ Lindgren (2010)

⁶ Ricker et al. (2015)

⁷ Rauer et al. (2014)

⁸ LSST Science Collaboration et al. (2009)

^a Typical precision per long-cadence data point.

^b Typical for long-cadence light curves.

^c Typical for 2 min. cadence *TESS* light curves.

BEER algorithm with the eclipse method can be used for finding transiting planets, brown dwarfs and white dwarfs, in the data of precise future surveys such as TESS and PLATO. Even more interesting will be to search for neutron stars and black holes. Such searches can be conducted on both ground and space photometry, as the ellipsoidal, and maybe even the beaming, caused by such massive companions, may be detectable even by ground surveys.

With the vast amount of astronomical data made publicly available in recent years, and the increased importance of virtual astronomy, robust and efficient search algorithms are critical for the astronomical community. This thesis presents the BEER algorithm for searching the data of large photometric surveys, and illustrates its effectiveness in finding both common stellar binaries and rare astrophysical objects. I believe that the BEER tool can become an important component in the virtual astronomy toolbox for mining the vast astronomical data produced by current and future photometric surveys.

Bibliography

- Aigrain, S., Favata, F., & Gilmore, G. 2004, *A&A*, 414, 1139
- Auvergne, M., et al. 2009, *A&A*, 506, 411
- Baglin, A., et al. 2006, 36th COSPAR Scientific Assembly, 36, 3749
- Barclay, T., Huber, D., Rowe, J. F., et al. 2012, *ApJ*, 761, 53
- Batalha, N. M., Borucki, W. J., Bryson, S. T., et al. 2011, *ApJ*, 729, 27
- Batalha, N. M., Rowe, J. F., Bryson, S. T., et al. 2013, *ApJS*, 204, 24
- Bloemen, S., et al. 2011, *MNRAS*, 410, 1787
- Bloemen, S., Marsh, T. R., Degroote, P., et al. 2012, *MNRAS*, 422, 2600
- Borucki, W. J., et al. 2010, *Science*, 327, 977
- Bouchy, F., Hébrard, G., Udry, S., et al. 2009, *A&A*, 505, 853
- Bouchy, F., Díaz, R. F., Hébrard, G., et al. 2013, *A&A*, 549, A49
- Breton, R. P., Rappaport, S. A., van Kerkwijk, M. H., & Carter, J. A. 2012, *ApJ*, 748, 115
- Butters, O. W., West, R. G., Anderson, D. R., et al. 2010, *A&A*, 520, L10
- Carter, J. A., Rappaport, S., & Fabrycky, D. 2011, *ApJ*, 728, 139
- Deleuil, M., Deeg, H. J., Alonso, R., et al. 2008, *A&A*, 491, 889
- Drake, A. J. 2003, *ApJ*, 589, 1020
- Esteves, L. J., De Mooij, E. J. W., & Jayawardhana, R. 2014, arXiv:1407.2245
- The Extrasolar Planets Encyclopaedia, <http://exoplanet.eu/>
- The *Kepler* Exoplanets Archive, <http://exoplanetarchive.ipac.caltech.edu/>
- Faigler, S., & Mazeh, T. 2011, *MNRAS*, 415, 3921

- Faigler, S., Mazeh, T., Quinn, S. N., Latham, D. W., & Tal-Or, L. 2012, *ApJ*, 746, 185
- Faigler, S., Tal-Or, L., Mazeh, T., Latham, D. W., & Buchhave, L. A. 2013, *ApJ*, 771, 26
- Faigler, S., & Mazeh, T. 2015, *ApJ*, 800, 73
- Faigler, S., Kull, I., Mazeh, T., Kiefer, F., Latham, D. W., & Bloemen, S. 2015, submitted to *ApJ*
- For, B.-Q., et al. 2010, *ApJ*, 708, 253
- Fűrész, G., Ph.D. thesis, University of Szeged, Hungary
- Harrison, T. E., Howell, S. B., Huber, M. E., Osborne, H. L., Holtzman, J. A., Cash, J. L., & Gelino, D. M. 2003, *AJ*, 125, 2609
- Herrero, E., Lanza, A. F., Ribas, I., et al. 2014, *A&A*, 563, A104
- Knutson, H. A., Charbonneau, D., Allen, L. E., et al. 2007, *Nature*, 447, 183
- Knutson, H. A., Charbonneau, D., Cowan, N. B., et al. 2009, *ApJ*, 690, 822
- Koch, D. G., et al. 2010, *ApJ*, 713, L79
- Kopal, Z. 1959, *The International Astrophysics Series: Close binary systems*, London: Chapman & Hall, 1959,
- Léger, A., Rouan, D., Schneider, J., et al. 2009, *A&A*, 506, 287
- Lindgren, L. 2010, *IAU Symposium*, 261, 296
- Loeb, A., & Gaudi, B. S. 2003, *ApJ*, 588, L117
- LSST Science Collaboration, Abell, P. A., Allison, J., et al. 2009, arXiv:0912.0201
- Maxted, P. F. L., Marsh, T. R., & North, R. C. 2000, *MNRAS*, 317, L41
- Maxted, P. F. L., Marsh, T. R., Heber, U., Morales-Rueda, L., North, R. C., & Lawson, W. A. 2002, *MNRAS*, 333, 231
- Mazeh, T. 2008, *EAS Publications Series*, 29, 1
- Mazeh, T., & Faigler, S. 2010, *A&A*, 521, L59
- Mazeh, T., Nachmani, G., Sokol, G., Faigler, S., & Zucker, S. 2012, *A&A*, 541, A56
- Morris, S. L. 1985, *ApJ*, 295, 143

- Mullally, F., Coughlin, J. L., Thompson, S. E., et al. 2015, *ApJS*, 217, 31
- Perruchot, S., Kohler, D., Bouchy, F., et al. 2008, *Proc. SPIE*, 7014,
- Rappaport, S., Nelson, L., Levine, A., et al. 2015, *ApJ*, 803, 82
- Rauer, H., Catala, C., Aerts, C., et al. 2014, *Experimental Astronomy*, 38, 249
- Reed, M. D., et al. 2010, *Ap&SS*, 329, 83
- Ricker, G. R., Winn, J. N., Vanderspek, R., et al. 2015, *Journal of Astronomical Telescopes, Instruments, and Systems*, 1, 014003
- Rouan, D., Baglin, A., Copet, E., Schneider, J., Barge, P., Deleuil, M., Vuillemin, A., & Léger, A. 1998, *Earth Moon and Planets*, 81, 79
- Rybicki, G. B., & Lightman, A. P. 1979, *Radiative Processes in Astrophysics* (New York: Wiley)
- Saunders, W., Bridges, T., Gillingham, P., et al. 2004, *Proc. SPIE*, 5492, 389
- Seager, S., & Mallén-Ornelas, G. 2003, *ApJ*, 585, 1038
- Showman, A. P., & Guillot, T. 2002, *A&A*, 385, 166
- Shporer, A., Jenkins, J. M., Rowe, J. F., et al. 2011, *AJ*, 142, 195
- Slawson, R. W., Prša, A., Welsh, W. F., et al. 2011, *AJ*, 142, 160
- Smith, G. A., Saunders, W., Bridges, T., et al. 2004, *Proc. SPIE*, 5492, 410
- Snellen, I. A. G., de Mooij, E. J. W., & Albrecht, S. 2009, *Nature*, 459, 543
- Tal-Or, L., Faigler, S., & Mazeh, T. 2015, *A&A*, 580, A21
- Udalski, A., Szymański, M. K., & Szymański, G. 2015, *Acta Astron.*, 65, 1
- Wilson, R. E. 1990, *ApJ*, 356, 613
- van Kerkwijk, M. H., Rappaport, S. A., Breton, R. P., Justham, S., Podsiadlowski, P., & Han, Z. 2010, *ApJ*, 715, 51
- Vaz, L. P. R. 1985, *Ap&SS*, 113, 349
- Welsh, W. F., Orosz, J. A., Seager, S., Fortney, J. J., Jenkins, J., Rowe, J. F., Koch, D., & Borucki, W. J. 2010, *ApJ*, 713, L145
- Zucker, S., Mazeh, T., & Alexander, T. 2007, *ApJ*, 670, 1326

Acknowledgments

First and foremost I wish to deeply thank my thesis advisor, Professor Tsevi Mazeh, for his guidance and support in the course of this work.

During the years of my Ph.D. study I have benefited from the collaboration and assistance of many faculty members, postdocs, students and other astronomers (in alphabetical order): Suzanne Aigrain, Steven Bloemen, Lars Buchhave, Joshua Carter, Michael Engel, Avishay Gal-Yam, Tomer Holczer, Flavien Kiefer, Ilya Kull, Donald Kurtz, Dave Latham, Dan Maoz, Gil Nachmani, Ehud Nakar, Dovi Poznanski, Sahar Shahaf, Avi Shporer, Gil Sokol, Amiel Sternberg, Lev Tal-Or, Sam Quinn, Ignasi Ribas, William Welsh & Shay Zucker.

The research leading to these results has received funding from the European Research Council under the EU's Seventh Framework Programme (FP7/(2007-2013)/ ERC Grant Agreement No. 291352), the ISRAEL SCIENCE FOUNDATION (grant No. 1423/11) and the Israeli Centers Of Research Excellence (I-CORE, grant No. 1829/12).

superrotation ב-Kepler-76b לשני יופיטרים-חמים ידועים נוספים, HAT-P-7b ו- KOI-13b. תגליות אלה מדגימות שניתוחים מפורטים של עקומות הפאזה של עקומות אור חלליות מדוייקות, מאפשרים לחקור תופעות אטמוספירות, כגון רוחות תרמיות או עננים מחזירי אור, בכוכבי לכת קצרי-מחזור רבים.

העבודה האחרונה, מאמר VII, מדגים חוזקה ושימוש שונים של אלגוריתם ה-BEER. המאמר מציג גילוי של 4 כוכבים כפולים קצרי-מחזור בעקומות האור של *Kepler*, המורכבים מכוכב ראשי מסוג A ומישני מסוג ננס לבן קל (dA+WD). המערכות מראות מודולציות BEER ביחד עם ליקויים ראשיים ומשניים. מערכות אלה נוספות ל-6 מערכות ב-*Kepler*, ו-18 ב-WASP, הידועות ככוכבים כפולים מלקים קצרי-מחזור מסוג dA+WD. המאמר מראה ש-3 מהמערכות החדשות מכילות את הננסים הלבנים הקטנים ביותר שהתגלו עד-עתה בכוכבים כפולים כאלה. 3 כוכבים כפולים אלה מרחיבים את האוכלוסיה הידועה, למערכות בוגרות יותר עם ננסים לבנים קטנים וקרים יותר, ובכך מאפשרים לבחון תאוריות של התפתחות כוכבים כפולים בתחום פרמטרים שלא ניצפה קודם לכן.

שבעת המאמרים מדגימים את האפקטיביות של אלגוריתם ה-BEER במציאת הן כוכבים כפולים רגילים, והן אובייקטים אסטרופיזיקאליים נדירים. ככזה, אלגוריתם ה-BEER יכול לשמש כמרכיב חשוב בארגז הכלים של האסטרונומיה הוירטואלית, לחיפוש במידע האסטרונומי הרב שמיוצר/ייוצר ע"י סקרים פוטומטריים נוכחיים ועתידיים.

תקציר

תזה זו מורכבת משבעה מאמרים מדעיים המתארים את הוכחת ההיתכנות, הפיתוח, והתגליות שהתגלו באמצעות אלגוריתם ה-*BEER* (*BEaming, Ellipsoidal, and Reflection*) לחיפוש אובייקטים משניים בעקומות האור של טלסקופי החלל *Kepler* ו-*CoRoT*.

מאמר I מציג את גילוי ה-*ellipsoidal* וה-*beaming* בעקומת האור של *CoRoT-3*, מערכת הכוללת ננס חום במסה $22M_{Jup}$ הסובב כוכב מסוג F בזמן מחזור של 4.3 יום. עבודה זו הייתה הוכחת היתכנות שאפקטים אלה אכן ניתנים לגילוי בפוטומטריית חלל של מערכות עם ננסים חום או כוכבי לכת, ובכך סיפקה אינדיקציה שמודולציות דומות אולי ניתנות לגילוי בעקומות האור של מערכות לא מלקות. בהמשך למאמר הראשון, מאמר II מתאר את אלגוריתם ה-*BEER* לגילוי כוכבים משניים קלים קצרי-מחזור שאינם מלקים, באמצעות אפקטי ה-*BEaming, Ellipsoidal, Reflection* ו- בעקומות האור של *Kepler* ו-*CoRoT*.

כמו כן, המאמר מנתח את ביצועי האלגוריתם הצפויים ומנבא שהוא אמור לאפשר גילוי של אובייקטים משניים עד למסות קטנות של $5-10M_{Jup}$.

לביסוס יעילות האלגוריתם, מאמר III, ומאוחר יותר מאמר VI, מציגים את הגילוי, ואימות באמצעות מדידות מהירות רדיאלית (RV), של שבעה, ושבעים, כוכבים כפולים קצרי-מחזור שאינם מלקים, במידע של *Kepler* ו-*CoRoT*, בהתאמה. מאמרים אלה מדגימים שבניגוד לשיטת חיפוש הליקויים, אלגוריתם ה-*BEER* מחפש אחר משניים שאינם מלקים, ולכן מאפשר גילוי של מערכות נוספות עם זוויות הטייה נמוכות יותר.

כפי שנובא ע"י המאמרים הקודמים, מאמר IV מציג את הגילוי של *Kepler-76b*, יופיטר-חם מלקה בעל מסה של $2M_{Jup}$, הסובב סביב כוכב מסוג F בזמן מחזור של 1.54 יום. כוכב לכת זה התגלה תחילה ע"י אלגוריתם ה-*BEER*, ולאחר מכן אומת באמצעות מדידות RV. כמו כן, עקומת האור של *Kepler-76* הראתה עדות ראשונה ל-*superrotation* בתחום התדר של *Kepler*. תופעה זו מתבטאת כהסחת פאזה של מודלציית הפליטה התרמית של כוכב הלכת, כתוצאה מרוחות משווניות על-סיבוביות באטמוספירה שלו, שניצפו קודם לכן רק באינפרה-אדום. מאמר V מרחיב את גילוי ה-

אנליזת BEER של עקומות האור של *Kepler* ו-*CoRoT*:

גילוי כוכבים כפולים וכוכבי לכת

חיבור לשם קבלת התואר "דוקטור לפילוסופיה"

מאת

שמחון פייגלר

הוגש לסנאט של אוניברסיטת ת"א

שבט תשע"ו

העבודה הוכנה בהנחייתו של

פרופסור צבי מזא"ה